國立交通大學

應用化學所

博士論文

多面體聚矽氧烷為建構單元的嵌段式共聚物奈米複合材料及金屬晶粒複合奈米粒子

Diblock Copolymer Nanocomposites and Metal Nanocrystal Hybrid Nanoparticles Incorporating Polyhedral Oligomeric Silsesquioxane Building Blocks

研究生：呂居樺

指導教授：張豐志 教授

中華民國九十八年二月

多面體聚矽氧烷為建構單元的嵌段式共聚物奈米複合材料及金屬晶粒複合奈米粒子

Diblock Copolymer Nanocomposites and Metal Nanocrystal Hybrid Nanoparticles Incorporating Polyhedral Oligomeric Silsesquioxane Building Blocks

研究生：呂居樺　　Student：Chu-Hua Lu

指導教授：張豐志　　Advisor：Feng-Chih Chang

國立交通大學

應用化學所

博士論文

A Dissertation
Submitted to Department of Applied of Chemistry
College of Science
National Chiao Tung University
in Partial Fulfillment of the Requirements
for the Degree of
Doctor of Philosophy
in

Applied Chemistry

February 2009

Hsinchu, Taiwan, Republic of China

中華民國九十八年二月

國立交通大學

論文口試委員會審定書

本校 **應用化學** 學系博士班 **呂居樺** 君

所提論文 多面體聚矽氧烷為建構單元的嵌段式共聚物奈米複合材料及金屬晶粒複合奈米粒子

Diblock Copolymer Nanocomposites and Metal Nanocrystal Hybrid Nanoparticles Incorporating Polyhedral Oligomeric Silsesquioxane Building Blocks

合於博士資格標準、業經本委員會評審認可。

口試委員：張豐志教授 張豐志 Feng-Chih Chang

戴憲弘教授 戴憲弘 Shenghong A. Dai

林宏洲教授 林宏洲 Hong-Cheu Lin

邱文英教授 邱文英 Wen-Yen Chiu

林江珍教授 林江珍 Jiang-Jen Lin

陳志勇教授 陳志勇 Chih-Yung Chen

指導教授：張豐志

系主任：陳登銘 教授

中華民國 九十八年 二 月 十三 日

誌謝

學生在中興大學學習，很早就發現對化學有很高的興趣，雖然是主修化學工程，課餘去修許多化學系的主修課程，博聞強記之下，對化學基本學問有充份的了解；大學專題也和化學相關的教授學習，在何榮銘老師實驗室，讓學生了解高分子材料，在鄭文桐老師實驗室，學習高分子在光阻劑的應用，幾年來對高分子有基本的了解，特別在大四較空閒的那一年，和戴憲弘老師學習學生最感興趣的高分子化學-異氰酸塩；學生能累積在高分子這方面的知識，十分感謝，中興化工系的培養，尤其三位老師對學生的教育。

碩士學程，有機會進入交通大學應用化學系，跟張豐志老師更深入研究高分子科學，這幾年來，學生很佩服張老師帶實驗室的遠見，讓郭紹偉及黃智峯學長帶領實驗室，博士班學生自由發揮，張老師為學生找計劃，支持學生們的學術研究及論文發表；因此，學生在進實驗室不久就有想攻讀博士班，碩士班一年後如期直升博士班，想法很單純，只要我肯用時間、用心做，研究成果及論文發表不難取得，過兩年後庸庸碌碌，表現平凡，實驗做得多，沒能有效的整理發表，面臨四年博士班畢業期限將致的壓力，否定自己做研究的能力，甚致懷疑自己自身難保，怎還有閒時去幫助其它同學和學弟妹在學業研究和管理實驗室，長達半年時間，認真思考自己博士論文，實實在在去完成預定的目標-四篇研究論文；張老師給時間讓學生自己調適，針對這一點讓學生感激萬分，此事讓學生了解做研究，不僅只是在”做”而”寫”和”發表”同樣重要，欠一就顯得不足；雖然，學生很早就發現自己對做研究有天份，但對語言的天份就差多了，張老師沒多說什麼，多次幫學生修改論文，後來了解”參考”文獻對論文寫作的重要，論文寫作就順利多了，張老師對學生的不離不棄，學生感激在心；今年順利畢業，學生會決定留下來做博士後研究的最主要原因想回報老師的幫忙，其次完成幾篇尚未完成的研究論文；此外，學生很感謝工研院沈永清及蘇一哲學長提供學生長達四年的工讀，讓學生得以順利取得博士學位。

四年半來，除了張老師，學生還要感謝我的直屬學長-黃智峯學長和郭紹偉學長，雖然有時候會被學長凹，但兩位學長對我還是不錯，給我很多幫忙和指導，尤其黃智峯學長常常聽我發牢騷，學長去了美國做博士後進修才發現學長人不錯，沒有學長在實驗室還真得有點不習慣；郭紹偉學長人也不錯，和黃智峯學長不同，郭學長讓我看到做研究的積極，這點是學生要跟郭學長學習的；同樣很感謝實驗室學長姐、同學和學弟妹的幫忙；學生家境並不富裕，只算小康，家裡無條件支持，讓學生能無憂無慮，專心研讀博士班，感謝多年來家裡媽媽、姐姐和弟弟的支持；尤其姐姐，在多年前爸爸過世後，日夜兼差負責家計，讓學生在無憂無慮的環境中成長順利完成學業，在此並祝幫助與關心學生的人能永遠平安快樂。

居樺(didi)　2009年2月

Outline of Contents

Pages

Chapter 1 Introduction

Chapter 2 Synthesis and Characterization of Poly(ε-caprolactone-*b*-4-vinyl pyridine): Initiation, Polymerization, Solution Morphology, and Gold Metalation

Chapter 3 Syntheses and Characterizations of Star Polymers and Star Block Copolymers from Polyhedral Oligomeric Silesesquioxane Core through Nitroxide-mediated Radical Polymerization

Chapter 4 Self-Assembled Fernlike Microstructures of POSS/Gold Nanoparticle Hybrids

Chapter 5 Supramolecular Catalysts by Encapsulating Palladium Nanocrystals within POSS Colloids

List of Tables

List of Schemes

List of Figures

Pages

多面體聚矽氧烷為建構單元的嵌段式共聚物奈米複合材料及金屬晶粒複合奈米粒子

學生：呂居樺　　　　　　　　　　指導教授：張豐志

國立交通大學應用化學研究所　博士班

摘　　要

奈米材料(nanomaterials)泛指一維空間尺度在1到100奈米的材料，我們可以發現很多的零維奈米粒子(nanoparticles, NPs)可以有很多不同的組成及功能；在第一章檢閱目前的文獻，我們將奈米晶粒(nanocrystals, NCs)從奈米粒子(NPs)分類出來，因為它們的奈米結構是由原子或離子有序堆積組成。奈米晶粒(NCs)根據組成可再細分為金屬奈米晶粒(metal NCs)及離子奈米晶粒(ionic NCs)；同理，其它奈米粒子(NPs)可細分為無機(inorganic NPs)、有機(organic NPs)及無機有機混成(inorganic/organic hybrid NPs)的奈米粒子。有些奈米粒子(NPs)有特定單一的化學結構可在歸類為分子型奈米粒子(molecular NPs)，相較於其它的，凝聚或叢集型奈米粒子(aggregative or cluster NPs)。此研究的無機有機混成的奈米複合粒子(inorganic/organic hybrid NPs)包括：嵌段式共聚物微胞保護的奈米金晶粒(PCL-b-P4VP-protected Au NPs)、嵌段式共聚物接枝的多面體聚矽氧烷[POSS-(PS)$_8$, POSS-(PS-b-P4VP)$_8$, POSS-(PS-b-P4VP)$_8$]、多面體聚矽氧烷(POSS)保護奈米金晶粒(POSS-Au hybrid NPs)及鈀晶粒(POSS-Pd hybrid NPs)。

有很多有趣的研究討論雙親性嵌段式共聚物可自組裝成很多有序奈米結構做為奈米反應器或儲存器，對聚七環ε-型己內酯及聚對位乙烯吡啶的嵌段式共聚

物[poly(ε-caprolactone)-*block*-poly(4-vinylpyridine)，命名為PCL-b-P4VP]，二個互不相溶的長鏈高分子致使他們的混合焓(ΔH> 0)為正混合熵(ΔS~0)接近零，在熱力學上這兩鏈段會自組裝成明顯相分離的微結構，因為它們的混合自由能為正值[ΔG= ΔH-TΔS)> 0]。聚對位乙烯吡啶的吡啶單元可做為高分子型金屬螯合劑做為奈米儲存器用來穩定金屬離子或金屬奈米粒子，此研究的第二章，我們開發一種較簡易的方法用來製備雙官能基起始劑包含醇基(hydroxyl)及烷氧胺基(*N*-alkoxyamine)的基團用來活性開環聚合對聚七環ε-型己內酯及可控制氮氧化物為媒介自由基聚合對位乙烯吡啶。

多面體聚矽氧烷(POSS)有特定單一的化學結構$(RSiO_{1.5})_8$包含八個有機基團(R)共價性鍵結在矽烷氧的籠狀立方體的八個端點$(SiO_{1.5})_8$，這樣的結構可歸類為分子型無機有機混成奈米粒子(molecular inorganic and organic hybrid NPs)；與小分子相似，POSS的膠體(溶劑溶解的有機殼層包覆不可溶的無機核心)也能有序堆積成固態膠體結晶。可惜的是，用零價鉑催化的矽氫加成修飾的八官能基有不同構型的異構物分別為分枝的α型$(-Si-CH(CH_3)-R)$和線狀的β型$(-Si-CH_2CH_2-R)$，這樣的異構物會抑制POSS的有序堆積(膠體結晶)，讓八官能基的POSS產物呈現非晶型的液體或玻璃狀的固體。然而，含八個有機基團在1奈米大小的POSS膠體的八個方位，這樣的化合物可預期良好的反應特性(較少的立體阻礙)用來製備POSS為主的奈米複合材料。此研究的第三章，我們共價接枝八個烷氧胺基團(*N*-alkoxyamine)到矽烷氧的籠狀立方體的八個端點$(SiO_{1.5})_8$，做為八官能基起始劑製備星狀的聚苯乙烯$[POSS-(PS)_8]$，聚苯乙烯及聚對位乙烯吡啶的嵌段式共聚物$[POSS-(PS-b-P4VP)_8]$和聚苯乙烯及聚對位乙烯酚的嵌段式共聚物$[POSS-(PS-b-PVPh)_8]$。和線性聚苯乙烯比較，動力學分析星狀的聚苯乙烯有相似的趨勢，指出從較少立體阻礙多官能起始的POSS可得到良好星狀高分子聚合的特性。

在此研究的第二章，雙親性的嵌段式共聚物(PCL-b-P4VP)可以從水相把$HAuCl_4$的離子化合物轉移到有機相(dichloromethane)利用離子間作用力如

[NH(AuCl)$_4$]；借由NaBH$_4$的環原及大量選擇性溶劑(insoluble P4VP blocks in toluene)，可經由嵌段式共聚物微胞穩定分散金奈米晶粒在有機溶劑中。然而，用嵌段式共聚物微胞包覆的金奈米晶粒會降低表面反應活性;因此使用較大體積的保護基團,可利用基團間的空隙讓反應物分子進入與產物分子出去,如此可維持奈米晶粒表面原子的高反應性。就已報導的POSS膠體晶體，POSS膠體先堆積而後再脫附溶劑分子造成，晶格常數*a*略大於POSS膠體的尺寸，意即POSS膠體的堆積的晶體固體會有空隙。在此研究的第四章，我們利用硫醇基POSS(SH-POSS)製備POSS和金奈米晶粒複合的奈米粒子(POSS-Au hybrid NPs)；當1.3奈米大小的硫醇基POSS吸附在約2奈米的金奈米晶粒表面，可預期會抑制硫醇基POSS的結晶，造成非結晶性的複合奈米粒子(POSS-Au hybrid NPs)。加入過量的硫醇基POSS，可利用硫醇基POSS的結晶做為模板將複合奈米粒子(POSS-Au hybrid NPs)組裝在模板的表面，構成很特別的蕨葉狀微結構。此研究，可發現POSS是很好的保護劑可以將金奈米晶粒分散在固態或溶液中。

鈀的奈米晶粒(Pd NCs)常用來做為碳碳鍵隅合的觸媒像Suzuik或Heck的反應，因此，我們所製備POSS和鈀奈米晶粒複合的奈米粒子(POSS-Pd hybrid NPs)，針對第二章的發現，硫醇基POSS晶體間的空隙可預期會有很好的觸媒活性。在此研究的第五章，我們發現一種不用化學環原劑的方法製備POSS和鈀奈米晶粒複合的奈米粒子(POSS-Pd hybrid NPs)，製備方法是把醋酸鈀和硫醇基POSS或十二烷基硫醇在甲苯溶劑中共沸，可以觀察到溶液從紅色的鈀離子錯合物轉變到黑色的鈀奈米晶粒。在此研究的第一章回顧金、銀、鈀和鉑奈米晶粒的製備方法，可分為化學環原法(chemical reduction)和熱溶劑法(solvothermal reduction)；所製備的鈀奈米晶粒(Pd NCs)可用做Heck碳碳鍵隅合丙烯酸甲酯(methyl acryalte)和碘基苯(iodobenzene)，與十二烷基硫醇保護的鈀奈米晶粒(C12-Pd hybrid NPs)比較，POSS和鈀奈米晶粒複合的奈米粒子(POSS-Pd hybrid NPs)有較好的化學反應特性。

此研究的第六章，我們總結四項重要的研究結果：(i) 低溫製備烷氧胺基

(*N*-alkoxyamine)化合物做為氮氧化物為媒介自由基聚合；(ii) 活性自由基聚合星狀聚苯乙烯(star polystyrene)和其星狀-嵌段式共聚物；(iii) POSS結晶模板可用來自組裝POSS和金奈米晶粒複合的奈米粒子(POSS-Au hybrid NPs)，構成形狀特殊的蕨葉狀微結構和(iv) 低溫熱溶劑法環原製備POSS和鈀奈米晶粒複合的奈米粒子(POSS-Pd hybrid NPs)做為良好觸媒用在Heck隅合丙烯酸甲酯和碘基苯。

Diblock Copolymer Nanocomposites and Metal Nanocrystal Hybrid Nanoparticles Incorporating Polyhedral Oligomeric Silsesquioxane Building Blocks

Student：Chu-Hua Lu　　Advisors：Dr. Feng-Chih Chang

Institute of Applied Chemistry
National Chiao Tung University

ABSTRACT

Nanomaterials are defined as materials having at least one dimension ranging in size from 1 to 100 nm. One-dimensional NPs (NPs) have been prepared with many different compositions and functions. In our review of the literature in **Chapter 1** of this Thesis, we separate NPs from nanocrystals (NCs) that exhibit ordered packing of their compositional atoms or ions in confined nanodomains. Nanocrystals can be further divided, according to their compositions, into metal NCs and ionic NCs. Similarly, NPs can be further divided into inorganic, organic, and inorganic/organic hybrid NPs. In addition to aggregate or cluster NPs, some well-defined chemical structures can be regarded as molecular NPs. In this thesis, gold and palladium NCs (Au, Pd NCs) are classified as metal NCs and polyhedral oligomeric silsesquioxane (POSS) derivatives are classified as molecular inorganic/organic hybrid NPs; in addition, pure micelles of block copolymers and their metal NC-incorporated congeners are considered to be aggregate organic NPs and aggregate inorganic/organic hybrid NPs, respectively. Chemical and solvothermal reductions are

discussed in a reviewing of the methods of preparation of Au, Ag, Pd, and Pt NCs.

Amphiphilic block copolymers are the focus of a great deal of research because of their ability to self-assemble into well-defined nanostructures that have the potential to function as nanosized reactors or storage vessels. The two immiscible high-molecular-mass blocks of poly(ε-caprolactone)-*block*-poly(4-vinylpyridine) (PCL-*b*-P4VP) have a positive mixing enthalpy (ΔH) and nearly-zero mixing entropy (ΔS); as a result, PCL-*b*-P4VP can thermodynamically self-assemble into microstructures featuring regions of distinct phase separation [positive mixing free energy ($\Delta G = \Delta H - \mathrm{T}\Delta S$)]. The pyridine units of the P4VP block can function as a polymeric metal ligand for the stabilization of metal ions and for the nanoscale storage of metal NPs. **Chapter 2** describes the development of a simple difunctional initiator containing hydroxyl and *N*-alkoxyamine groups for the living ring-opening polymerization of ε-CL and the controllable nitroxide-mediated polymerization of 4-VP.

POSS derivatives have a well-defined chemical structure $(RSiO_{1.5})_8$ of eight alkyl or aryl chains (R) presented at the corners of a cubic siloxane cage (Si_8O_{12}). Similar to organic molecules, POSS colloids, with their insoluble siloxane cubes, can crystallize from organic solvents into ordered structures. Unfortunately, Pt(0)-mediated hydrosilylation of octakis-functionalized POSS derivatives yields products possessing both α- and β-isomeric linkages, which suppress the crystallization of POSS colloids, resulting in amorphous liquids and glasses. Nevertheless, such compound feature eight functional groups dispersed in eight directions from the corners of the 1-nm-diameter POSS core, providing POSS-based nanocomposites exhibiting high degree of chemical modification and low steric hindrance. **Chapter 3** describes the incorporation of eight *N*-alkoxyamine groups onto a POSS cage and its use in the preparation of eight-arm star polystyrene [POSS-$(PS)_8$] and star-block polystyrene-*block*-poly(4-vinylpyridine) [POSS-(PS-*b*-P4VP)$_8$] and polystyrene-*block*-poly(4-vinylphenol) [POSS-(PS-b-PVPh)$_8$] derivatives. The kinetics of the polymerization of POSS-(PS)$_8$ were similar to that of linear PS, indicating the ability to form excellent-quality star polymers from this low-steric-hindrance POSS-based multi-initiator.

Chapter 2 describes amphiphilic PCL-*b*-P4VP copolymers that are capable of transferring $HAuCl_4$ from water to dichloromethane in ionic form [NH($AuCl_4$)]. Subsequent reduction with $NaBH_4$ and micellization with excess toluene (a selective solvent for the P4VP blocks) provided micelle-protected gold NCs (Au NCs) that could be dispersed well in organic solvents. Because the organically encapsulated Au NCs exhibited decreased activity for their surface reactions, we employed bulky protective groups with relatively large interparticlar distances to improve the reactivity of the surface atoms of the NCs. In the reported structures of POSS crystal, the lattice constant *a* is usually larger than the diameter of the POSS molecule, suggesting that desolvation occurs after packing of the POSS colloids. **Chapter 4** describes POSS-Au hybrid NPs prepared from a thiol-monofunctionalized isobutyl-POSS (SH-POSS). As expected, the absorption of 1.3-nm-diameter SH-POSS colloids onto the surface of ca. 2-nm-diameter Au NPs through dynamic Au–S bonds suppressed the crystallization of the SH-POSS colloids, resulting in amorphous POSS-Au hybrid NPs. Excess SH-POSS colloids formed a crystalline POSS template for the surface self-assembly of POSS-Au hybrid NPs, resulting in novel fernlike microstructures. The use of such a POSS derivative as a protective agent provides an excellent dispersion of Au NCs in the condensed phase or in organic solvents.

Palladium NCs (Pd NCs) are well-known catalysts for many carbon–carbon bond-forming reactions, including Suzuki and Heck couplings. Thus, POSS-Pd hybrid

NPs are expected to be a highly reactive catalysts because of the large interstices between the absorbed SH-POSS colloids on the surfaces of the Pd NCs. **Chapter 5** describes a reductant-free method for preparing POSS-Pd hybrid NPs by refluxing a toluene solution containing palladium acetate and thiol compounds, namely SH-POSS and 1-dodecanthiol (SH-C12). The Heck couplings of methyl acrylate with iodobenzene using the POSS-Pd and C12-Pd hybrid NPs as catalysts revealed the better activity of the former hybrid NPs.

Chapter 6 presents a summary of the four major accomplishments described in this thesis: (i) the low-temperature preparation of *N*-alkoxyamine adducts for nitroxide-mediated radical polymerization, (ii) the living polymerization of a well-defined star PS and related star-block copolymers, (iii) a crystalline template of POSS colloids that incorporate POSS-Au hybrid NPs to give novel fernlike microstructures, and (iv) the low-temperature solvothermal reduction of POSS-Pd hybrid NPs that function as excellent catalysts for the Heck coupling of methyl acrylate and iodobenzene.

Chapter 1

Introduction

1-1 Nanomaterials

The *ISI Web Knowledge*, an academic search engine, lists 491 review papers that were published concerning the topic of “nanomaterials” from 1995 to 2008. Nanomaterials are defined by as materials having at least one dimensions in the range from 1 100 nm. Despite the fact that there is no consensus for the minimum and maximum sizes of nanomaterials, with some authors restricting their sizes to less than 30 nm, a logical definition would situate the nanoscale between the microscale (ca. 0.1 μm) and the atomic/molecular scale (ca. 0.2 nm). The properties of such materials are strongly dependant on their sizes and shapes. Nanomaterials include zero-dimensional NPs (NPs), one-dimensional nanowires and nanotubes, and two-dimensional nanofilms and nanowalls. In this Chapter, we focus on the zero-dimensional NPs because of their more interesting surface compositions in comparison with the bulk volume of nanomaterials. Herein, NCs (NCs), with their ordered packing of atoms or ions, are classified separately from NPs because they exhibit unique properties, such as optical absorbance and catalytic activity (**Fig. 1-1**). X-ray diffraction (XRD) and high-resolution transmission electron microscopy (HRTEM) analyses are very useful for displaying the ordered packing of atoms and ions within NCs. According to the composition of the nanomaterials, NCs can be further classified into metal NCs and ionic NCs. In addition, there are three classes of NPs: inorganic, organic, and inorganic/organic hybrids. These materials are all essential components of nanoscience and nanotechnology. Although nanomaterials can be generated through physical methods, such as laser ablation, arc-discharging, and evaporation, chemical methods have proved to be more effective because they provide better control over size, shape, and functionalization. The chemical synthesis of nanomaterials has been reviewed by several authors,[1–7] with improved methods being reported continually over the last few years. A large selection of reagents and strategies are available, in addition to a wide spectrum of reaction conditions, for the synthesis and manipulation of nanomaterials. In view of the intense research activity related to nanomaterials synthesis, this Chapter presents recent developments and new directions in this area. In doing so, we will deal with all classes of inorganic nanomaterials. Because it is impossible to do justice to the vast number of valuable contributions that have appeared in the literature in last three years, through necessity we will restrict ourselves to highlighting mostly recent results.

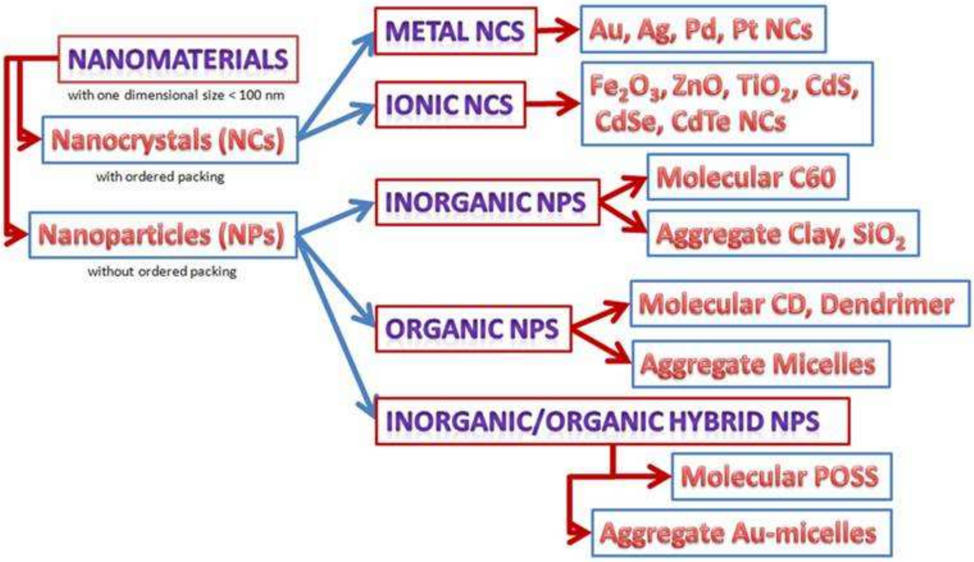

Figure 1-1. Dendritic distribution of Nanomaterials.

1-2 Nanocrystals (NCs)

Fahlman defined an NC as any nanomaterial having at least one dimension of 100 nm or less and having a single crystalline morphology regularly packed with ions, atoms, or molecules.[8] More properly, any material having a dimension of less than 1 μm, i.e., 1000 nm, should be referred to as an NP, not an NC. For example, any particle that exhibits regions of crystallinity should be termed an NP or nanocluster based on its dimensions. These materials are of huge technological interest because many of their electrical and thermodynamic properties display strong size dependence and can, therefore, be controlled through careful manufacturing. Crystalline NPs (NCs) are also of interest because they often provide single-domain crystalline systems that can be studied to provide information explaining the behavior of macroscopic samples of similar materials, without the complicating presence of grain boundaries and other defects. Semiconductor NCs, such as CdSe, CdTe, ZnO, and ZnS, in the sub-10-nm size range are often referred to as quantum dots (QDs). Depending on their composition, NCs can be classified as metal, metal salt, and nonmetal NCs.

1-2.1 Metal Nanocrystals (Metal NCs)

There are many difficulties to overcome when preparing monodisperse metal NCs. To data, only a few metal NCs, including Au, Ag, Pd, Pt, Fe, Cu, and Co NCs, have been prepared in the laboratory and not all of them can be obtained easily in monodisperse form. Thus, it remains a challenge to control the shape and the size of metal NCs. In general, it is easy to obtain monodisperse metal NCs having diameters less than 10 nm, but it is difficult to obtain them with diameters greater than 30 nm. The similar procedures of solvothermal and chemical reduction of metal salts with different protective groups are available for the preparation of Ag, Ag, Pd, and Pt NCs. The main difference between solvothermal and chemical reduction is that the weak reductant in the former needs a higher temperature to activate the reduction process.

Gold Nanocrystals (Au NCs).

Colloidal Au NCs can be synthesized through two methods for the reduction of tetrachloroauric acid ($HAuCl_4$) and can be stabilized in the confined domain by surrounding protective groups. Free Au atoms have a high interface free energy and are very unstable; therefore, they tend to pack into thermodynamically stable crystals. Because of absorption of a protective group on the surface, protective group/Au NC hybrid micelles having sizes of 1–100 nm can be stabilized in solution. **Figure 1-2**, for example, reveals that (i) $HAuCl_4$ salts can be reduced into Au atoms through solvothermal reduction with sodium citrate $[HOC(CH_2COO^-Na^+)_3]$ at 100 °C or through chemical reduction with sodium borohydride ($NaBH_4$) at 25 °C and (ii) 83 Au atoms having a diameter of 0.27 nm can be crystallized into 1.35-nm-diameter Au NCs. Hydrothermal reduction using sodium citrate was developed by Faraday in 1857[9] and later refined by Frens;[10] the two-phase method of chemical reduction using $NaBH_4$ was originally described by Wilcoxon et al.[11] and later modified by Brust et al.[12] $NaBH_4$ is a salt comprising a sodium cation (Na^+) and a borohydride anion (BH_4^-); the B–H bond of BH_4^- anion effectively serves as a reductant source of a hydride ion ($:H^-$). When using a water/toluene biphasic mixture, a phase transfer agent, such as tetraoctylammonium bromide (TOAB), is employed to transfer the hydrophilic $HAuCl_4$ and $NaBH_4$ species into the toluene phase in the presence of hydrophobic thiol compounds. Amphiphilic TOAB can form a hydrophilic nanosized reactor in toluene; the sizes of Au NPs are, therefore, limited by confinement in the nanoreactors to give small-size Au NCs. The thiol compound (RSH) plays an important role in stabilizing the Au NCs in toluene to form close-packed monolayers—stabilized by Au-S bonds—on their surfaces. In contrast, the hydrothermal reduction produces nearly monodisperse Au NPs in the size range from 2 to 100 nm.[13] Problems associated with the hydrothermal reduction originate from the fact that a low-concentration solution [<0.01 M (ca. 4 mg/mL) for Au NCs with the equimolar 1-dodecanethiol] is needed to stabilize the colloidal Au

NCs in water.[14] In addition, the charge-stabilized NPs readily undergo irreversible aggregation upon addition of electrolytes and nonpolar surfactants. Chemical reduction, on the other hand, allows the introduction of hydrophobic thiols as surfactants, but it suffers from (i) the limitation to small particle sizes (<10 nm) with greater polydispersity and (ii) difficult separation of the amphiphilic phase transfer agents. Similar to hydrothermal reduction with the hydroxyl groups of sodium citrate in water, Hiramastu et al. developed a novel solvothermal reduction method to prepare monodisperse 6–21-nm-diameter Au NCs and 8–32-nm-diameter Ag NCs through the refluxing of solvents such as toluene, hexane, and 1,2-dichlorobenzene containing $HAuCl_4$, AgOAc, and oleylamine (**Fig. 1-3**).[14] The reducing equivalents in the reaction are provided by the amino group (CH_2NH_2), which undergo metal ion-induced oxidation to form nitriles (-C≡N).[15,16] From high-resolution TEM images, Brust et al.[12] observed atomic packing of the Au NCs, with a layer-to-layer distance of 0.24 nm similar to the 0.27-nm-diameter of a Au atom (**Fig. 1-4**).

The size effect of NCs plays an important role in determining their physical and chemical properties. For example, bulk Au (>1 μm) is a shiny, yellow noble metal that does not tarnish, has a face-centered-cubic crystal structure composed of 0.27-nm-diameter atoms, is non-magnetic and melts at 1336 K (1063 °C). The properties of very small gold particles are, however, quite different: 10-nm-diameter particles absorb green light (λ = ca. 530 nm) and, thus, appear red. Meanwhile, the melting temperature decreases dramatically to 473K (200 °C) as the size decreases. Moreover, Au ceases to be noble at such small dimensions; for example, 2–3-nm-diameter NPs are excellent catalysts that also exhibit considerable magnetism. At this size they remain metallic, but smaller NPs are insulators. The ions or atoms on the surface of nanosized crystals are quite different from those of bulk materials because they cannot pack into a smooth surface and, therefore, leave active defects. Thus, an atom at the surface of a bulk material is different from an atom of the same element within that material. Moreover, an atom at the smooth surface of a sizable single crystal is different from an atom at the surface of a small cluster of the same element. Furthermore, the properties of a surface atom of a small metal cluster depend on the type of support on which it sits or whether the cluster is doped with one or a few atoms of a different element. A solution of Au NCs is usually either an intense red color (diameters < 100 nm) or a dirty yellowish color (for larger particles). The excitation of surface plasmons by light results in a surface plasmon resonance (SPR) for planar surfaces and a localized surface plasmon resonance (LSPR) for nanometer-sized metallic structures. This phenomenon is the basis of many standard tools (e.g., color-based biosensors and lab-on-a-chip sensors) for measuring the adsorption of materials onto planar metal (typically Au and Ag) surfaces and the surfaces of metal NPs. For example, Lim et al. demonstrated (**Fig. 1-5**) the color-tuning of a colloidal solution containing red Au NCs (520 nm), yellow Ag NCs (410 nm), and blue hollow Au (650 nm).[17] By necessity, there are proportionally more atoms on the surfaces of NCs that have smaller diameters than there are within them.[18] Mathematically, the surface of a sphere scales with the square of its radius (r), but its volume scales with r^3. The total number of atoms (N) in this sphere scales linearly with volume. The fraction of atoms at the surface is called the dispersion (F); it scales with the surface area divided by volume, i.e., with the inverse radius or diameter ($1/r$), and thus also with $N^{-1/3}$. As indicated in **Fig. 1-6**, the fraction F of atoms on the surface of NCs rapidly increases upon decreasing their size. In comparison with atoms in the internal region, the atoms on the surface facing the environment can serve as novel reactive sites for catalyzing reactions, even for inert metal NCs such as treasure gold.[19] Nanocatalysts made from small particles of metals such as Au, Ag, Pd, and Pt are used widely in the chemical and refining industries, as well as in catalytic converters in automobile tailpipes.

Over the last decade, after the pioneering work of Prati, Rossi, et al.,[20,21] much attention has been paid also to the activity of Au catalysts in the liquid phase In most cases, Au catalysts display higher catalytic activity and much higher selectivity at lower temperatures and better stability than do Pd and Pt catalysts. Ishida and Haruta et al. reviewed the field, highlighting the role of polymer-supported Au NCs as nanocatalysts.[19] Four examples of polymer-supported Au NCs are those stabilized by (a) grafting water-soluble polymers, (b) loading in the pores of a functionalized resin, (c) covering with a polymer particle, and (d) depositing on polymer surfaces (**Fig. 1-7**). **Table 1-1** lists the results obtained for several Au NC-catalyzed reactions.[23-26] These the ideal "green" processes are performed at atmospheric pressure and room temperature, in aqueous media or under solvent-free conditions, and using air as the oxidant or molecular hydrogen as the reductant. Gold NPs supported on activated carbon or metal oxides are active for some liquid-phase reactions, such as the selective oxidation (with O_2 in aqueous media) of alcohols into corresponding aldehydes, ketones, and carboxylic acid and the selective reduction (with H_2) of nitroarenes into amino arenes.[22]

Figure 1-2. Preparation of Au NCs through chemical reduction with $NaBH_4$ at 25 °C and solvothermal reduction with citric acid at 100 °C. The 1.35-nm-diameter Au NCs result from the aggregation of 83 Au atoms (diameter: 0.27 nm).

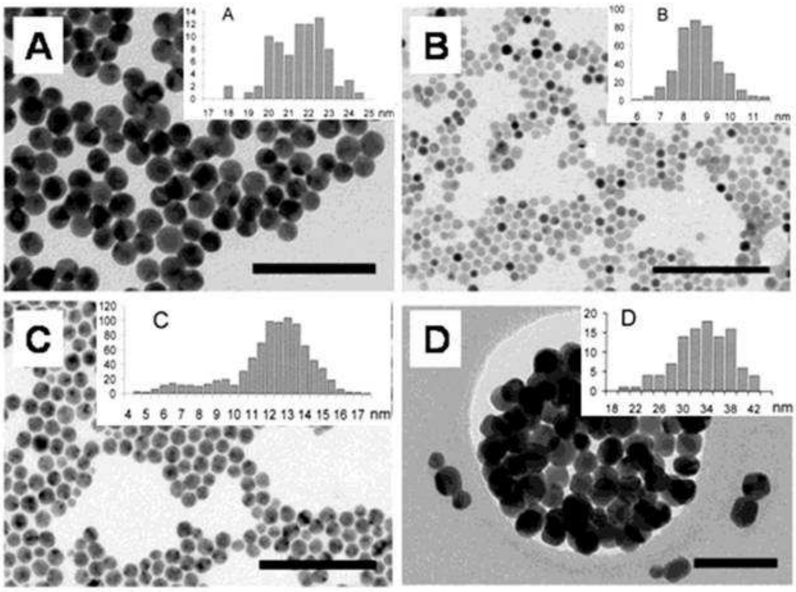

Figure 1-3. TEM images and DLS analyses of Au and Ag NC samples. (A) 21-nm-diameter Au NCs from toluene, (B) 9-nm-diameter Ag NCs from toluene, (C) 12-nm-diameter Ag NP nanocrystals from hexane, and (D) 32-nm-diameter Ag NCs from 1,2-dichlorobenzene. Scale bars: 100 nm.[14]

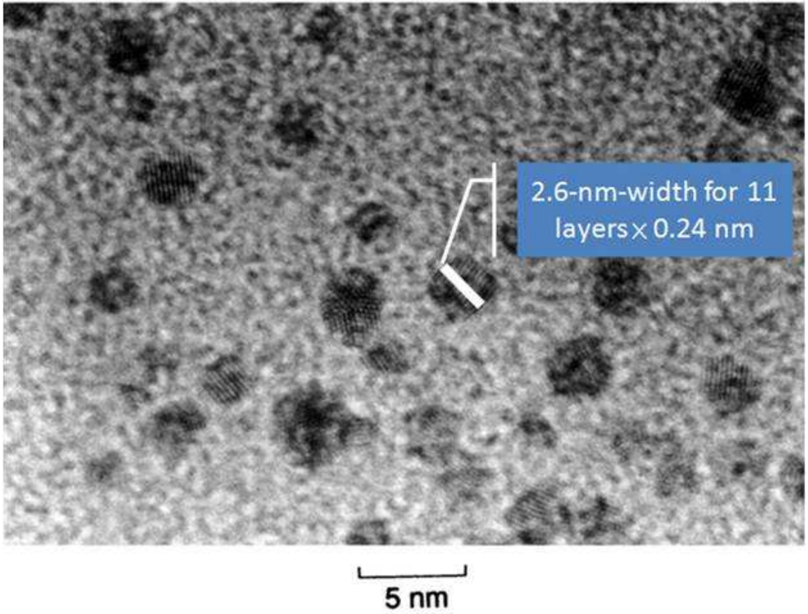

Figure 1-4. HRTEM images of 1-dodecanthiol-protected Au NCs. The thickness (0.24 nm) indicates the layer-to-layer distance of FCC Au NCs.[12]

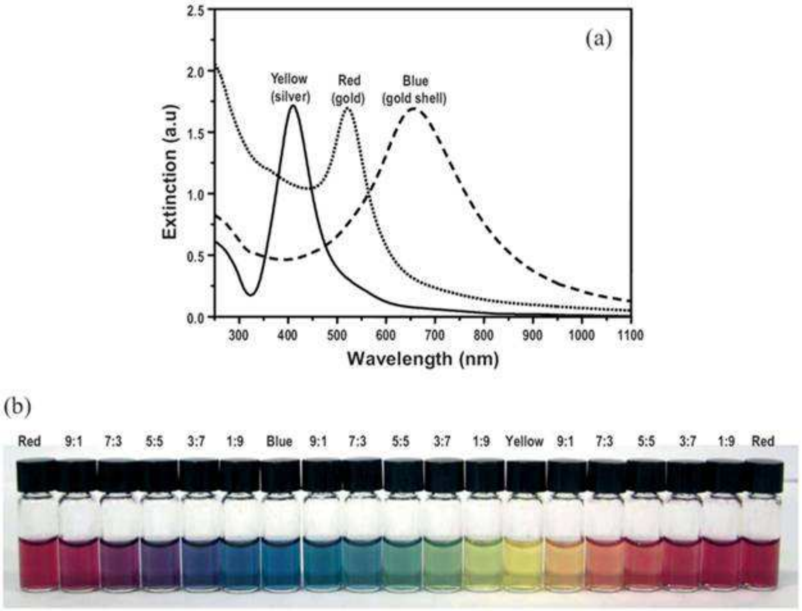

Figure 1-5. (a) Optical extinction spectra of Ag NCs (yellow), solid Au NCs (red), and hollow Au nanoshells (blue). The optical densities of the three differently colored samples have been matched to 1.8. (b) Photograph of aqueous dispersions of metal NP colloids, the SPR bands of which were tuned in terms of wavelength and intensity multiplexing.[17]

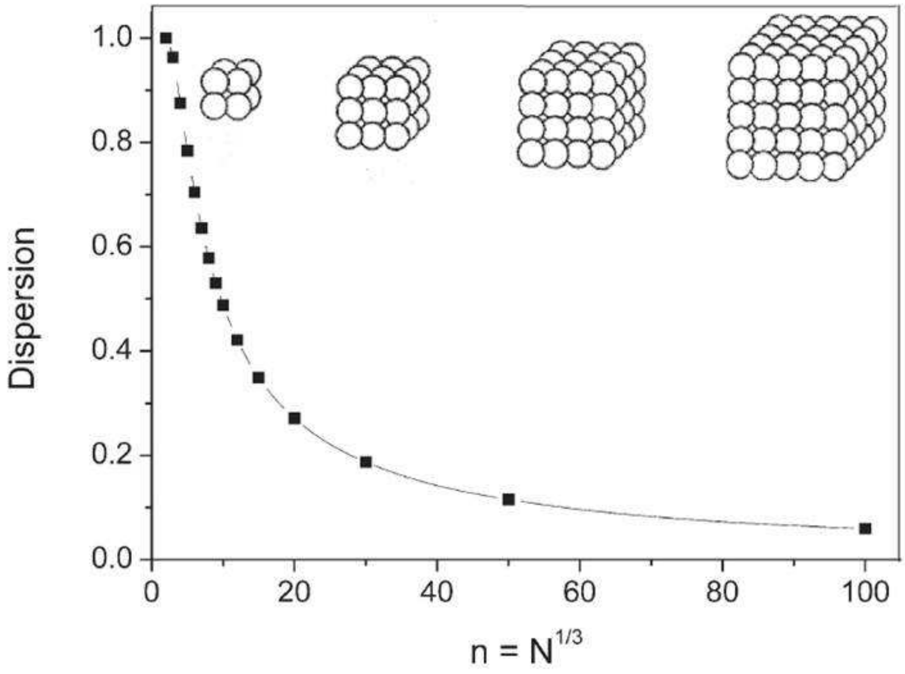

Figure 1-6. Evolution of the dispersion *F* as a function of *n* for cubic clusters up to *n* = 100 (*N* = 106). The structures of the first four clusters are displayed.[18]

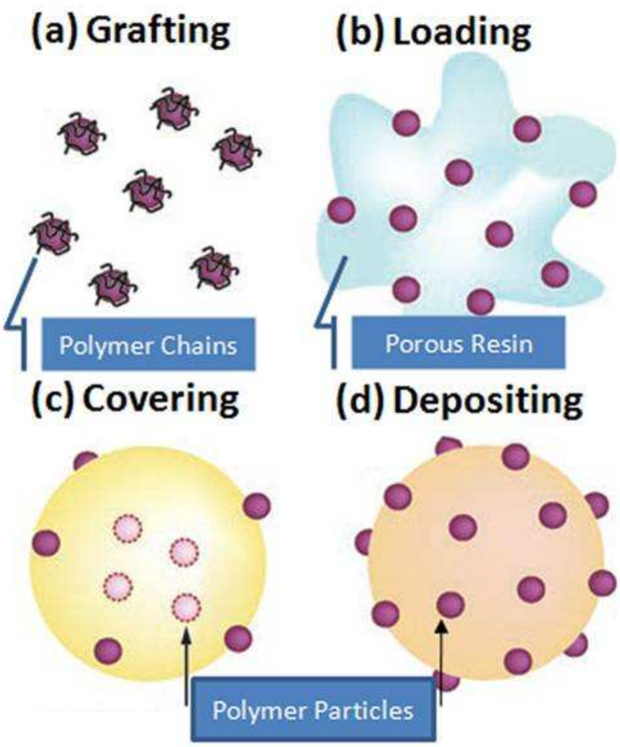

Figure 1-7. Cartoon representations of four polymer-stabilized Au NCs: (a) grafted with water-soluble polymers, (b) loaded in the pores of a functionalized resin, (c) covered with polymer particles, and (d) deposited on a polymer surface.[19]

Table 1-1. Representative reactions catalyzed by polymer-supported Au NPs.[19]

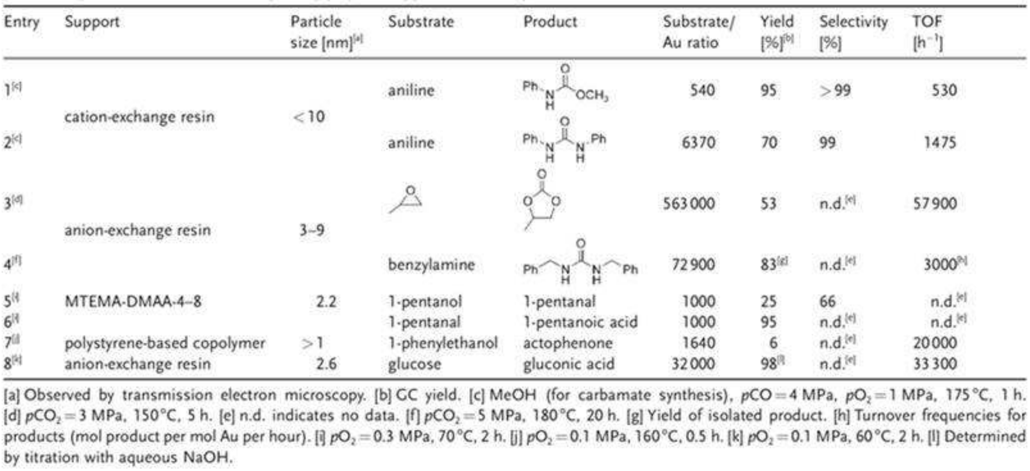

Entry	Support	Particle size [nm][a]	Substrate	Product	Substrate/ Au ratio	Yield [%][b]	Selectivity [%]	TOF [h^{-1}]
1[c]	cation-exchange resin	< 10	aniline	$\mathrm{PhNHC(O)OCH_3}$	540	95	> 99	530
2[c]			aniline	$\mathrm{PhNHC(O)NHPh}$	6370	70	99	1475
3[d]	anion-exchange resin	3–9			563000	53	n.d.[e]	57900
4[f]			benzylamine	$\mathrm{PhCH_2NHC(O)NHCH_2Ph}$	72900	83[g]	n.d.[e]	3000[h]
5[i]	MTEMA-DMAA-4–8	2.2	1-pentanol	1-pentanal	1000	25	66	n.d.[e]
6[i]			1-pentanal	1-pentanoic acid	1000	95	n.d.[e]	n.d.[e]
7[j]	polystyrene-based copolymer	> 1	1-phenylethanol	actophenone	1640	6	n.d.[e]	20000
8[k]	anion-exchange resin	2.6	glucose	gluconic acid	32000	98[l]	n.d.[e]	33300

[a] Observed by transmission electron microscopy. [b] GC yield. [c] MeOH (for carbamate synthesis), $pCO = 4$ MPa, $pO_2 = 1$ MPa, 175 °C, 1 h. [d] $pCO_2 = 3$ MPa, 150°C, 5 h. [e] n.d. indicates no data. [f] $pCO_2 = 5$ MPa, 180 °C, 20 h. [g] Yield of isolated product. [h] Turnover frequencies for products (mol product per mol Au per hour). [i] $pO_2 = 0.3$ MPa, 70 °C, 2 h. [j] $pO_2 = 0.1$ MPa, 160 °C, 0.5 h. [k] $pO_2 = 0.1$ MPa, 60 °C, 2 h. [l] Determined by titration with aqueous NaOH.

Silver Nanocrystals (Ag NCs).

Similar to Au NCs, Ag NCs can be also prepared through both solvothermal and chemical reduction. For example of chemical reduction, He et al. prepared monodisperse Ag NCs having an average diameter of 4.18 nm through a two-phase method, using $AgNO_3$, $NaBH_4$, TOAB, and 1-nonanethiol ($C_9H_{19}SH$) in water and dichloromethane (**Fig. 1-8**).[12,27] In addition, solvothermal reductions with ethanol or ethylene glycol are well established for the preparation of high quantities of Ag NC products.[28,29] During the past decade, Toshima's group developed and optimized an effective technique for the preparation of Ag NC colloidal dispersions through reduction with alcohols under reflux in the presence of a protecting agent of polymeric nature.[30-35] Poly(vinylpyrrolidone) (PVP), a useful stabilizing agent with polar cyclic amide groups, forms complexes with the surface atoms of Ag NCs. In an investigation of ethylene glycol-induced solvothermal reduction, Silvert et al. obtained a plot of the variation of the mean particle size by dynamic light scattering (DLS) and the concentration in solution (UV absorbance at 410 nm) as a function of time (**Fig. 1-9**);[29] it consists of three regions: Region 1 (up to 55 °C), Region 2 (up to 120 °C), and Region 3 (isotherm at 120 °C). In Region 1, the nucleation of 8% Ag salts predominates to produce small-size Ag colloids [95% of diameters < 10 nm; 5% diameters = ca. 20 nm (**Fig. 1-10a**)]. In Region 2, the growth of Ag salts becomes significant to produce a broad distribution with large and small Ag colloids [24% of diameters = ca. 20 nm (**Fig. 1-10b**); 92% of diameters = 20 nm (**Fig. 1-10c**)]. In Region 3, almost all of the Ag salt has been reduced into monodisperse Ag NCs having an average diameter of ca. 20 nm (**Fig. 1-10d**); therefore, in this region, stable-sized 20-nm-diameter-Au NCs are available when prepared using PVP protecting polymers.

Low-cost colloids of Ag NCs can function as precursors of conductive nanowires to fabricate patterns with at least one lateral dimension having a size between that of an individual atom and ca. 100 nm; this process is called nanolithography. For example, Wang et al. used atom force microscopy (AFM) to write Ag nanowires with a colloid ink followed by thermal sintering at 300 °C (**Fig.**

1-11).[36] **Figure 1-12** displays an AFM image and cross-sectional analysis of such well-defined nanowires having a width of 5 μm. Hydrazine (NH_2NH_2) is the best established reductant for the chemical reductions used to prepare Ag NCs. Li et al. developed a facile method for the synthesis of Ag NCs used in the fabrication of high-conductivity elements for printed electronics.[37] The acetate anions of AgOAc can be replaced with alkylamines to give silver complexes that are soluble in toluene (**Fig. 1-13**); monodisperse 5-nm-diameter Ag NCs can then be obtained through subsequent reduction with hydrazine hydrate (**Fig. 1-13a**). A continuous phase of sintered Ag NCs can be observed through scanning electron microscopy (SEM) (**Fig. 1-13b**) after heat treatment at 140 °C for 30 s. The conductivity of the sintered Ag NCs can be detected (**Fig. 1-13c**) after the deposition of Ag NCs colloids on a chip and subsequent thermal treatment. The electrical conductivity of the resulting Ag film was in the range from $2–4 \times 10^4$ S cm^{-1}, which is on the same order as that of a vapor-deposited Ag thin film of similar thickness ($4–6 \times 10^4$ S cm^{-1}). This high level of conductivity is more than sufficient for applications in electronic devices. In addition, the alkylamine-stabilized Ag NPs prepared using this procedure exhibit good shelf life, both in both powder form and in solution—a feature of critical importance in electronic circuit manufacturing.

Ag NCs also exhibit antibacterial (antimicrobial) activity, allowing their use in the surface modification of biomedical materials.[38] This antibacterial property has been known for thousands of years, with the ancient Greeks cooking from silver pots. Indeed, the old adage, “born with a silver spoon in his mouth,” refers to more than just wealth—eating with a silver spoon is also more hygienic. Lok et al. revealed that Ag^+ cations in $AgNO_3$ solutions can inhibit the growth of bacteria.[38] For nanosized Ag NCs, the fraction of Ag atoms on the surface of NCs increases rapidly upon decreasing the size (**Fig. 1-6**).[18] These surface Ag atoms present a free surface to contact the surroundings, showing high chemical reactivity to give Ag^+ ions in the oxidative form (Ag_2O). Thus, the antibacterial activities of Ag NPs are dependent on the presence of chemisorbed Ag^+, which is readily formed owing to extreme sensitivity to O_2. In addition, Lok et al. applied SPR techniques to quantitatively detect the level of chemisorbed Ag^+ on the surface of Ag NCs; it correlated well with the observed antibacterial activities (**Fig. 1-14**). The SPR spectra of Ag NCs indicate a shift in the absorbance from 375 nm for the Ag NCs to 398 nm for the Ag^+ ions (**Fig. 1-14a**). From a comparison of the reactions of untreated and oxidized Ag NCs with bovine serum albumin (BSA), it was found that BSA can convert oxidized Ag NCs into Ag^+, which significantly prohibits the growth of bacteria (**Fig. 1-14b,c**). BSA has a high affinity for fatty acids, hematin, and bilirubin and has a broad affinity for small negatively charged aromatic compounds. It forms covalent adducts with pyridoxyl phosphate, cysteine, glutathione, and various metal ions, such as Cu(II), Ni(II), Hg(II), Ag(II), and Au(I). Thus, highly active oxidized Ag ions on the surface could be release to form stable complexes with BSA. In addition, Chen et al. prepared an antibacterial and biocompatible substrate through sputter coating with a Ag NC-containing hydroxyapatite (Ag-HA).[39] **Figure 1-15** displays the significant improvement in the antibacterial properties of the Ag-HA in comparison with those of different substrates (e.g., Ti) and hydroxyapatite (HA). Moreover, Although Ag has a broad antibacterial effect, high concentrations of Ag are cytotoxic (maximum toxic concentration for human cells: 10 mg/L).[40] The toxicity of Ag ions affects the basic metabolic cellular functions common to all specialized mammalian cells. A concentration- and time-dependent depletion of intracellular ATP content has been attributed to the presence of Ag ions, thereby compromising the cell energy charge, which precedes cell death.[41] Therefore, it is prudent to incorporate only a minimum amount of Ag on implant surfaces to adequately reduce bacterial adhesion as well as minimize tissue cytotoxicity. Indeed, anti-bactericidal properties were observed without osteoblast-precursor cell cytotoxicity for co-sputtered Ag-HA coatings having a concentration of 2.05 ± 0.55 wt% Ag.

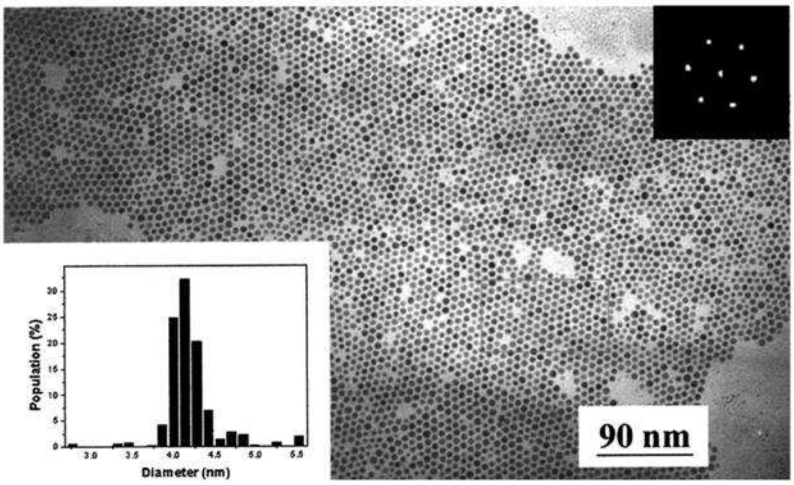

Figure 1-8. TEM images of a 2D superlattice containing 4.18-nm-diameter Ag NCs, (left insert) a histogram of the Au NCs, and (right insert) a 2D Fourier power spectrum of the TEM images.[27]

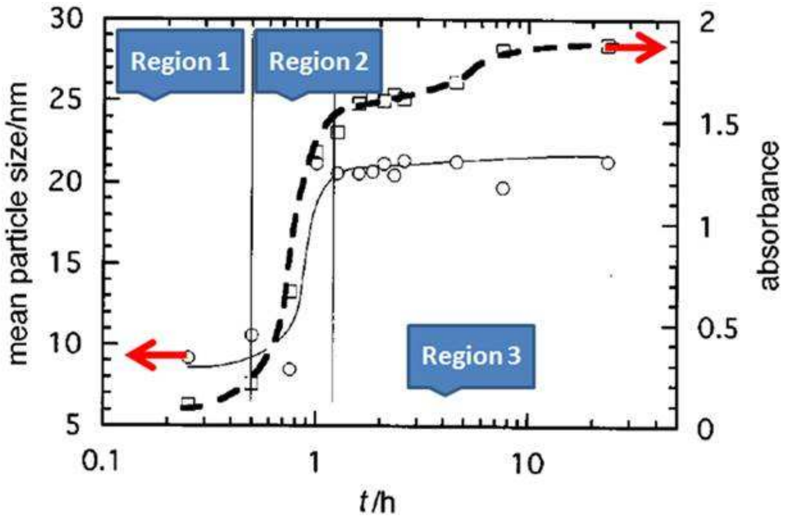

Figure 1-9. Evolution of the mean particle size (circle) and 410-nm-absorbance peak (square) during the formation of 21-nm-diameter monodisperse Ag colloids (400 mg $AgNO_3$; 10 g PVP; 75 mL EG; 1 °C/min from 25 to 120 °C, followed by isotherm).[29]

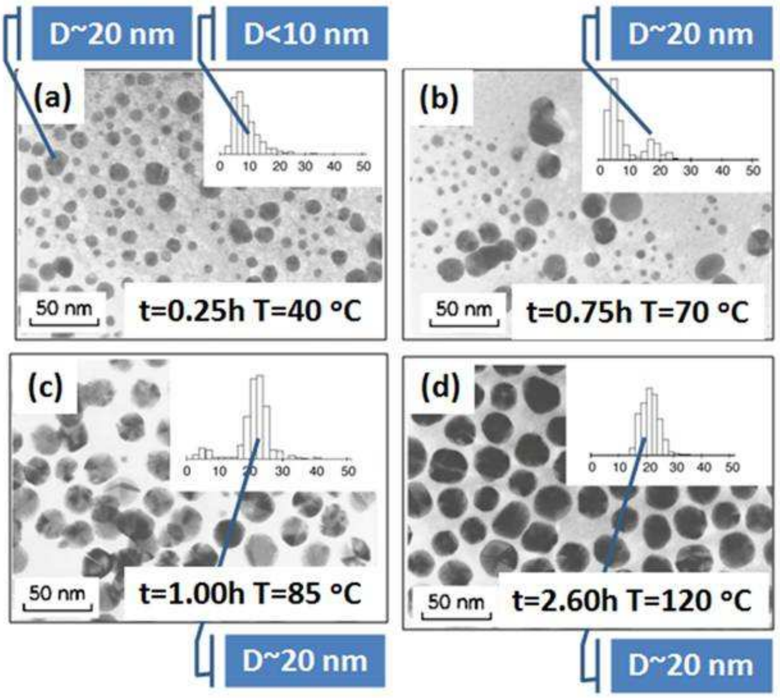

Figure 1-10. TEM images of a colloidal Ag dispersions: (a) t = 0.25 h and T = 40 °C, (b) t = 0.75 h and T = 70 °C, (c) t = 1.00 h and T = 85 °C, and (d) t = 2.60 h and T = 120 °C.[29]

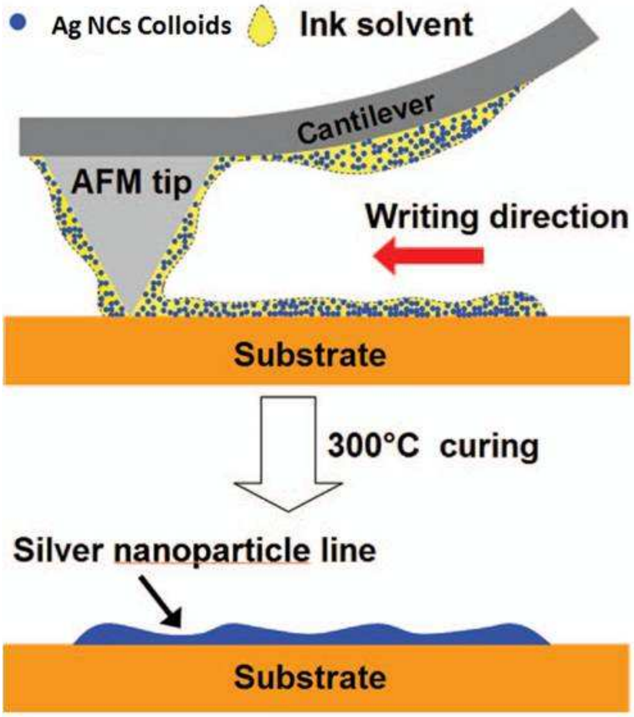

Figure 1-11. Schematic representation of the DPN procedure used to pattern a Ag NC ink on a glass substrate. This procedure is common to other substrates.[36]

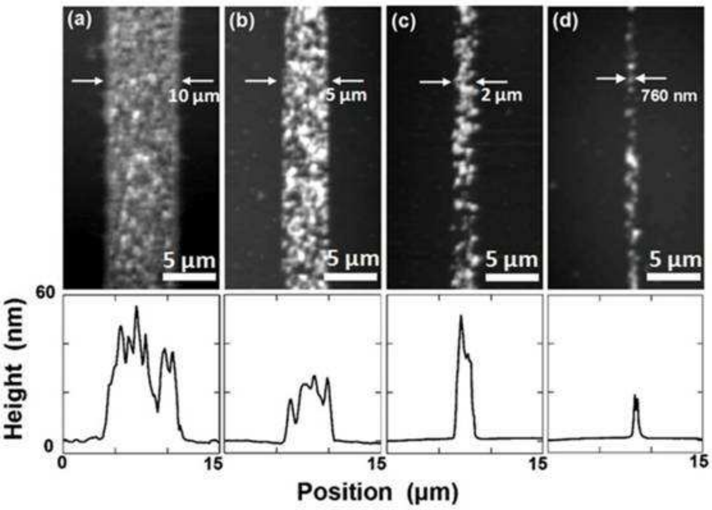

Figure 1-12. 2D AFM images and cross-sectional analysis of linewidths: (a) 10 µm, (b) 5 µm, (c) 2 µm, and (d) 760 nm.[36]

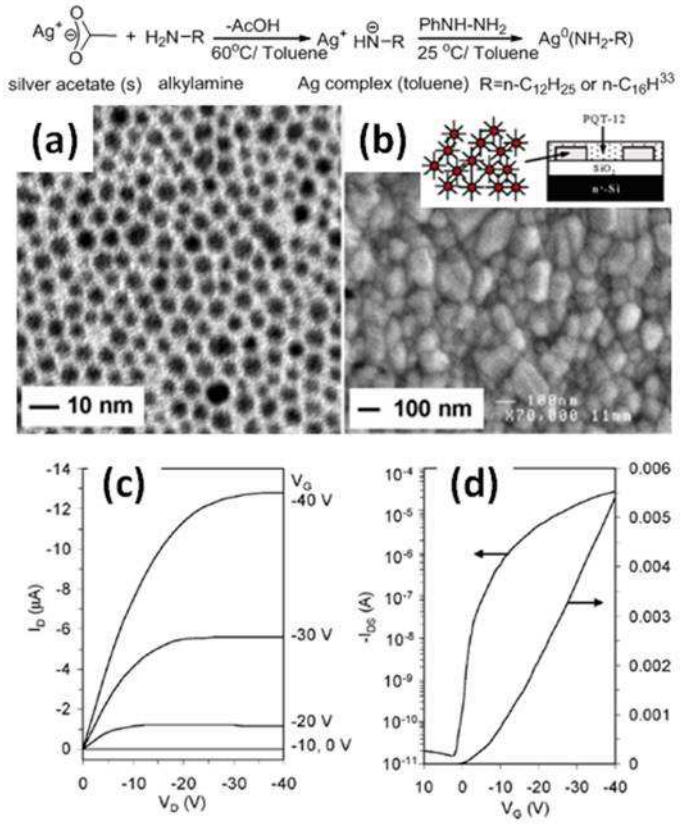

Figure 1-13. Single-phase preparation of Ag NCs and analytical results: (a) TEM image of Ag NCs having diameters of ca. 10 nm; (b) SEM image of Ag films after treatment at 140 °C for 30 s; (c) drain current (I_D) versus source-drain voltage (V_D) plotted as a function of the gate voltage (V_G) for a thin film transistor (TFT) with printed source/drain electrodes (channel length: 90 µm; channel width: 2250 µm); (d) I_D and $(-I_D)^{1/2}$ plotted versus V_G at a constant value of V_D (–40 V), used for calculation of the mobility and current on/off ratio.[37]

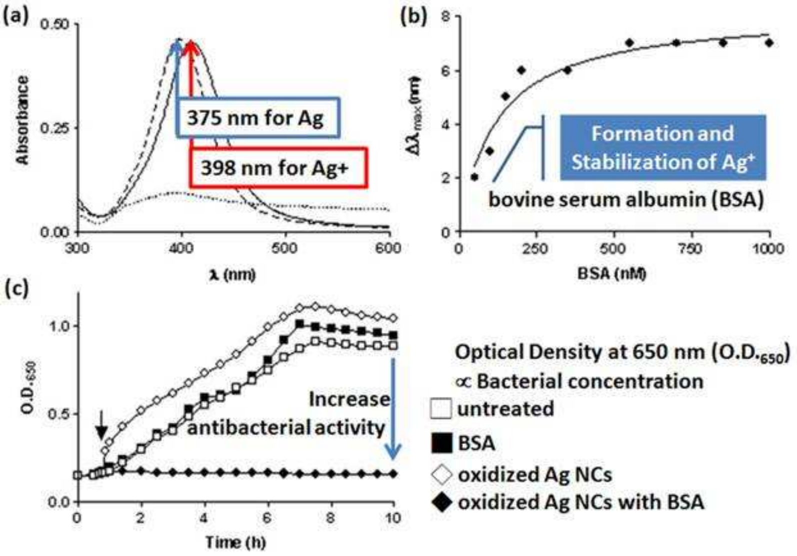

Figure 1-14. (a) SPR absorption of untreated and oxidized Ag NCs, (b) BSA-mediated shift of the SPR absorption, and (c) bacterial activity of untreated Ag NCs, oxidized Ag NCs, BSA-treated oxidized Ag NCs, and BSA.[38]

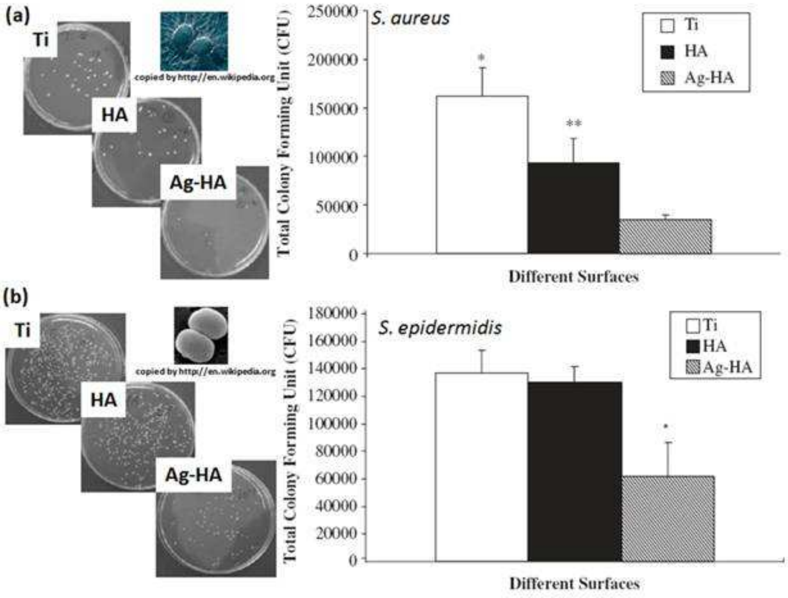

Figure 1-15. Photographs and statistical analyses of (a) *S. aureus* and (b) *S. epidemidis* on various substrates: Ti, HA, and Ag-HA.[39]

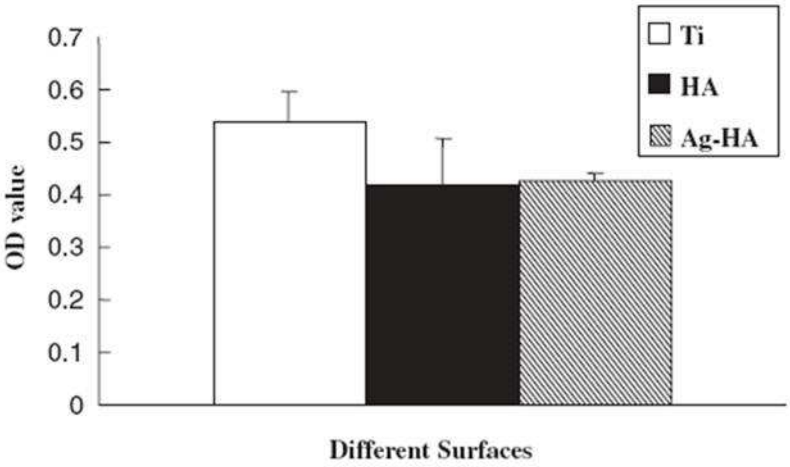

Figure 1-16. Cytotoxicity tests with human embryonic palatal mesenchyme (HEPM) cells on various surfaces after incubation for 24 h.[39]

Palladium Nanocrystals (Pd NCs).

In view of the preparation of Pd NCs, Quiros et al. obtained alkanethiol-protected Pd NCs with diameters of 1.3–3.9 nm through single-phase chemical reduction [$PdCl_2(CH_3CN)_2$, TOAB, and $LiBEt_3H$ in THF].[42] They stated several general rules for the isolation of obtain small clusters: use long thiols; increase the amounts of the surfactant and reducing agent; increase the stirring time after the addition of the reducing agent; and use a bulky surfactant, such as TOAB. In addition, Li and EI-Sayed used three different stabilizers—hydroxyl-terminated poly(amido-amine) (PAMAM) dendrimers (Gn-OH, where Gn represents the nth generation), the block copolymer polystyrene-*b*-poly(sodium acrylate), and poly(*N*-vinyl-2-pyrrolidone) (PVP)—for the $NaBH_4$-mediated reduction of Pd NCs used as catalysts for the Suzuki reactions in aqueous media.[43] In their approach, Pd^{2+} ions are absorbed into OH- or NH_2-terminated PAMAM dendrimers, where they complex strongly with the interior tertiary amino groups. Subsequent chemical reduction of the metal ions with BH_4^- results in dendrimer-encapsulated Pd NPs. Here, the dendrimers are used both as templates and stabilizers.[44-47] In addition to chemical reduction, Pd NCs can also be prepared through solvothermal reduction with ethanol in the presence of stabilizers, such as PVP[43] and amphiphilic copolymers. Kim et al. developed a novel method to prepare monodisperse Pd NCs through thermal decomposition of trioctylphosphine–Pd complexes at 300 °C for 0.5 h.[48] **Figure 1-17** displays the mechanism of the thermal decomposition of the metal complex into Pd NCs, TEM images of 5-nm-sized monodisperse Pd NPs, and a high-resolution TEM image of a single NC.

Pd NCs are catalysts for many carbon–carbon coupling reactions, such as Suzuki[49,50,52] and Heck reactions.[50,51] First published in 1979, the Suzuki reaction couples aryl or vinyl boronic acids with aryl or vinyl halides, catalyzed by a palladium(0) complex.[53,54] The reaction relies on a Pd catalyst, such as tetrakis(triphenylphosphine)palladium(0), to effect the transformation (**Fig. 1-18a**). The Pd catalyst (more strictly a pre-catalyst) is four-coordinate, usually involving phosphine supporting groups or sodium hydroxide-activated Pd catalysts (**Fig. 1-18b**). The reaction is used widely to synthesize polyolefins, styrenes, and substituted biphenyls, and has been extended to incorporate alkyl bromides.[53] As mentioned above, Li and El-Sayed[43] prepared PAMAM dendrimer-stabilized Pd NCs as catalysts for Suzuki coupling; they obtained high yields (90%) for the coupling of thiolphene and benzene units when using G3-OH(Pd)$_{10}$ and Na_3PO_4 (**Table 1-2**). The Heck reaction is the Pd-catalyzed C–C coupling of aryl or vinyl halides and activated alkenes in the presence of a base (**Fig. 1-19a**). Recent developments in the catalysts and reaction conditions have resulted in a much broader range of proton donors (acrylate esters or acrylonitrile) and proton acceptors (aryl, benzyl, or vinyl halides) being amenable to the Heck reaction (**Fig. 1-19b**).[55] The catalyst is commonly $(Ph_3P)_4Pd(0)$, $Pd(II)Cl_2$, or $Pd(II)(OAc)_2$, the ligand is commonly triphenylphosphine, and the base is commonly Et_3N, K_2CO_3, or NaOAc. The Heck coupling between iodobenzene and methyl acrylate occurs with high conversion (>99%) (**Table 1-3**).[51] Recently, Kobayashi et al. discovered strong hydrogen atom trapping behavior within Pd NCs, with applications in fuel cells.[56,57] XRD spectra revealed that H_2 absorbed within Pd NCs expanded the lattice constant (layer-to-layer distance) of NCs; the incorporation of H_2 can be detected in solid state ^2H NMR spectra (**Fig. 1-20**).

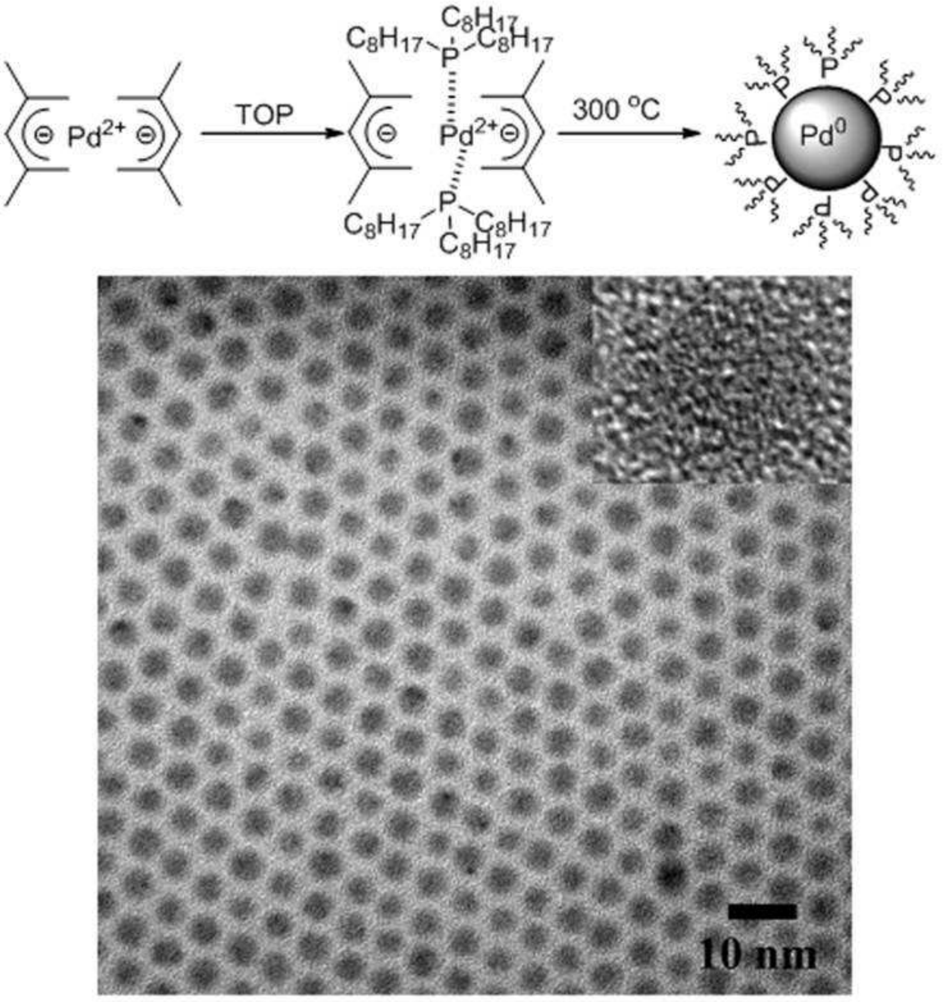

Figure 1-17. (a) Mechanism of thermal decomposition of metal complexes into Pd NCs and (b) TEM image of 5-nm-diameter monodisperse Pd NPs. Inset: HRTEM image of a single NC.[48]

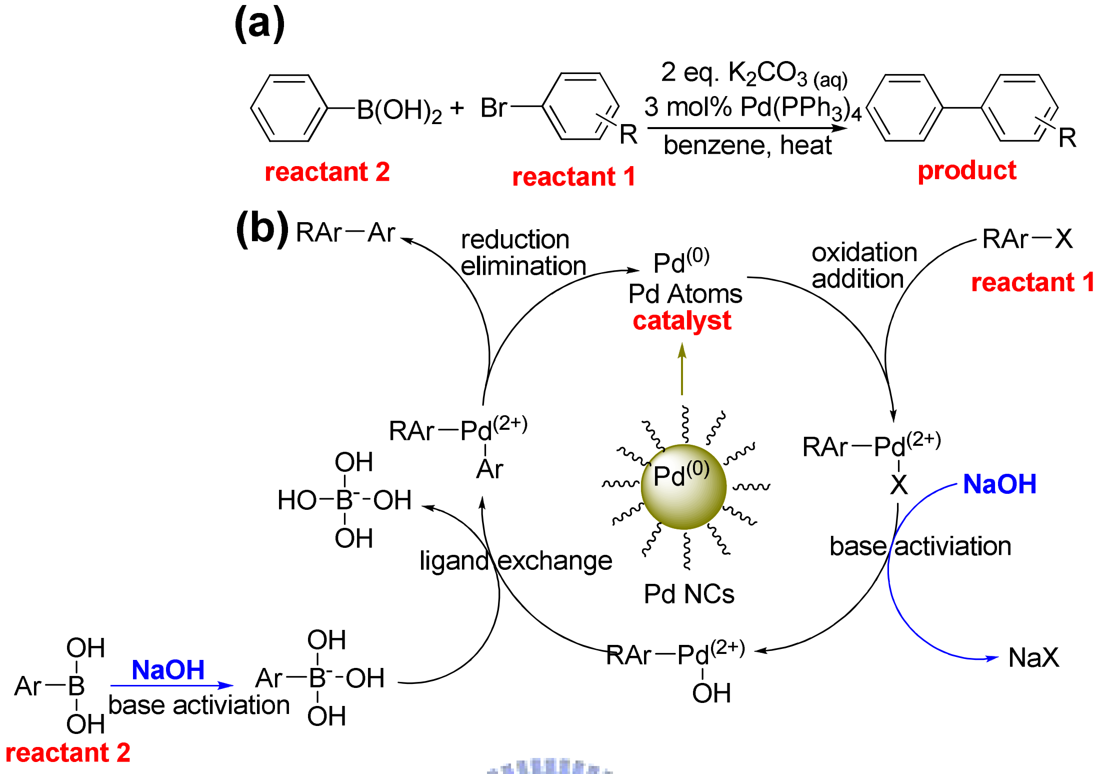

Figure 1-18. (a) Reaction scheme of the first published Suzuki coupling, the Pd-catalyzed cross-coupling between organoboronic acids and halides. (b) Reaction mechanism of the Pd NC-catalyzed Suzuki coupling of a NaOH-activated boronic acid.[53,54]

Table 1-2. Product yields for Suzuki couplings catalyzed by dendrimer-Pd NCs (1.5 mol% of metal) in 40% EtOH under reflux for 24 h[43]

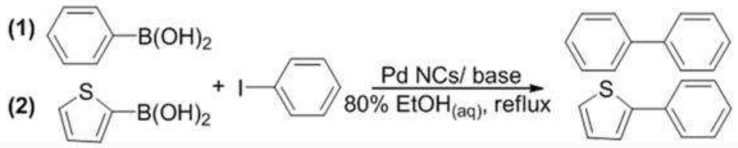

entry	reacn	catalyst	base	yield[a]	formation of Pd black	soln color after reacn
1	**(1)**	G4-OH(Pd)$_{10}$	Na_3PO_4	17%	no	light yellow
2	**(2)**	G4-OH(Pd)$_{10}$	Na_3PO_4	20%	no	light yellow
3	**(2)**	G4-OH(Pd)$_{10}$	NEt_3	35%	no	light yellow
4	**(2)**	G4-OH(Pd)$_{10}$	NaOAc	< 5%	yes	brown
5	**(1)**	G3-OH(Pd)$_{10}$	Na_3PO_4	71%	no	yellow/green
6	**(2)**	G3-OH(Pd)$_{10}$	Na_3PO_4	90%	yes	yellow/green[c]
7	**(1)**	yellow/green soln[b]	Na_3PO_4	40%	no	yellow/green
8	**(2)**	yellow/green soln[b]	Na_3PO_4	80%	yes	yellow/green[c]
9	**(1)**	G2-OH(Pd)$_5$	Na_3PO_4	69%	yes	yellow/green[c]
10	**(2)**	G2-OH(Pd)$_5$	Na_3PO_4	70%	yes	yellow/green[c]

[a] Isolated yield. [b] The clear yellow/green solution after extraction is used as the catalyst. See text for detail. [c] Solution color after filtering the Pd precipitates.

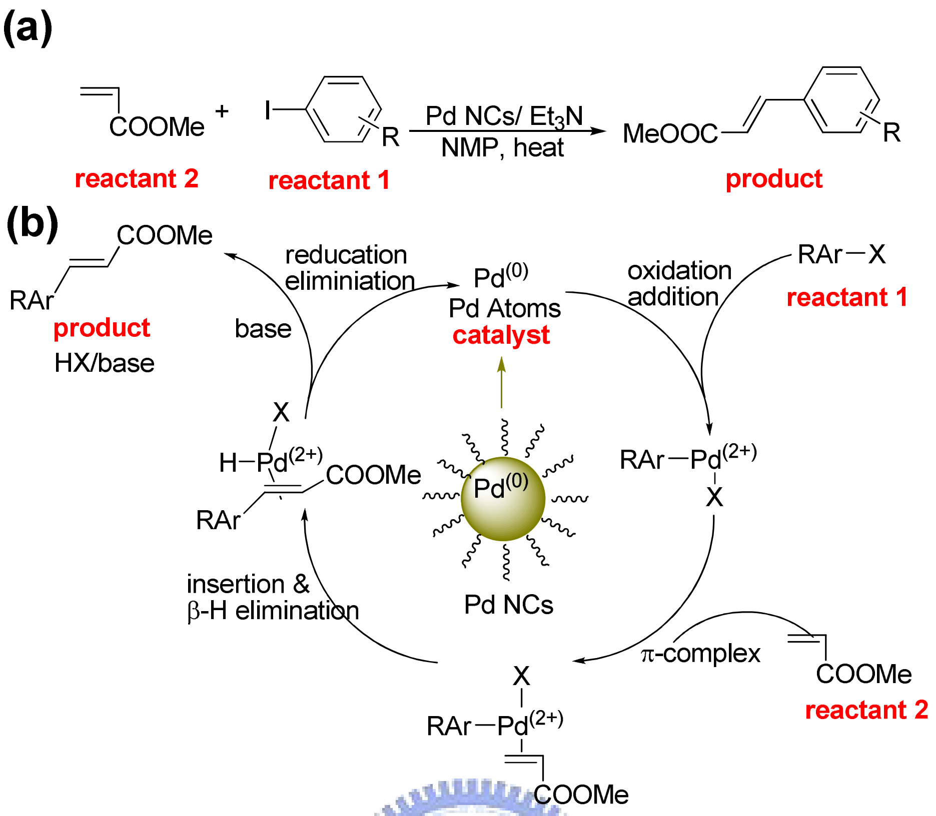

Figure 1-19. (a) Reaction scheme of Heck coupling, the Pd-catalyzed cross-coupling between acrylates and halides. (b) Reaction mechanism of the Pd NC-catalyzed Heck coupling with based-activation.[53,54]

Table 1-3. Comparison of the catalytic activities of various supported Pd catalysts in the Heck reaction of iodobenzene with methyl acrylate.[51]

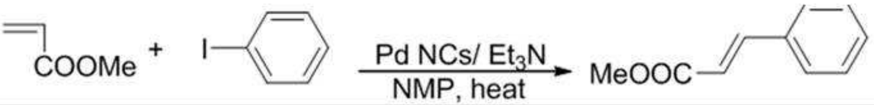

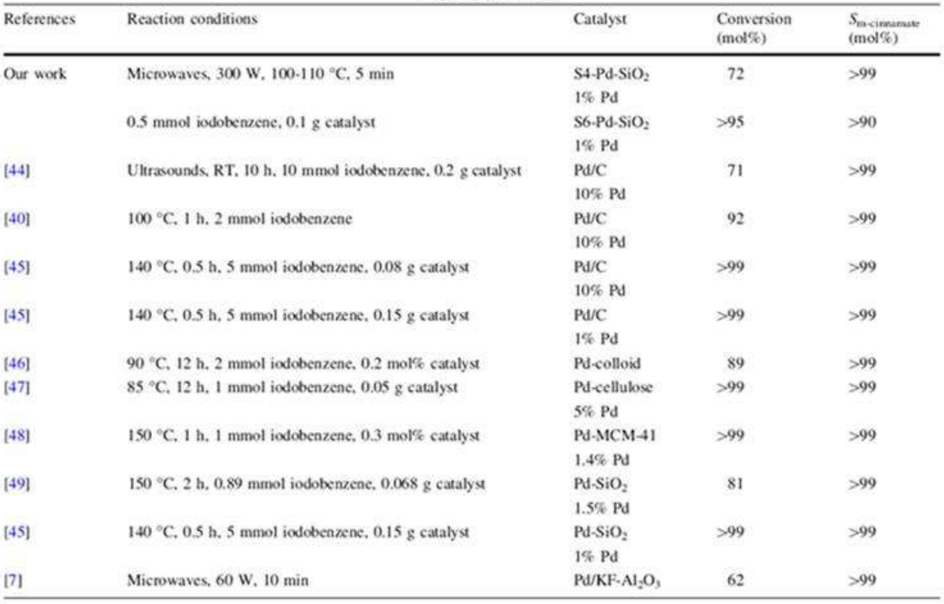

References	Reaction conditions	Catalyst	Conversion (mol%)	$S_{m\text{-cinnamate}}$ (mol%)
Our work	Microwaves, 300 W, 100-110 °C, 5 min	S4-Pd-SiO_2 1% Pd	72	>99
	0.5 mmol iodobenzene, 0.1 g catalyst	S6-Pd-SiO_2 1% Pd	>95	>90
[44]	Ultrasounds, RT, 10 h, 10 mmol iodobenzene, 0.2 g catalyst	Pd/C 10% Pd	71	>99
[40]	100 °C, 1 h, 2 mmol iodobenzene	Pd/C 10% Pd	92	>99
[45]	140 °C, 0.5 h, 5 mmol iodobenzene, 0.08 g catalyst	Pd/C 10% Pd	>99	>99
[45]	140 °C, 0.5 h, 5 mmol iodobenzene, 0.15 g catalyst	Pd/C 1% Pd	>99	>99
[46]	90 °C, 12 h, 2 mmol iodobenzene, 0.2 mol% catalyst	Pd-colloid	89	>99
[47]	85 °C, 12 h, 1 mmol iodobenzene, 0.05 g catalyst	Pd-cellulose 5% Pd	>99	>99
[48]	150 °C, 1 h, 1 mmol iodobenzene, 0.3 mol% catalyst	Pd-MCM-41 1.4% Pd	>99	>99
[49]	150 °C, 2 h, 0.89 mmol iodobenzene, 0.068 g catalyst	Pd-SiO_2 1.5% Pd	81	>99
[45]	140 °C, 0.5 h, 5 mmol iodobenzene, 0.15 g catalyst	Pd-SiO_2 1% Pd	>99	>99
[7]	Microwaves, 60 W, 10 min	Pd/KF-Al_2O_3	62	>99

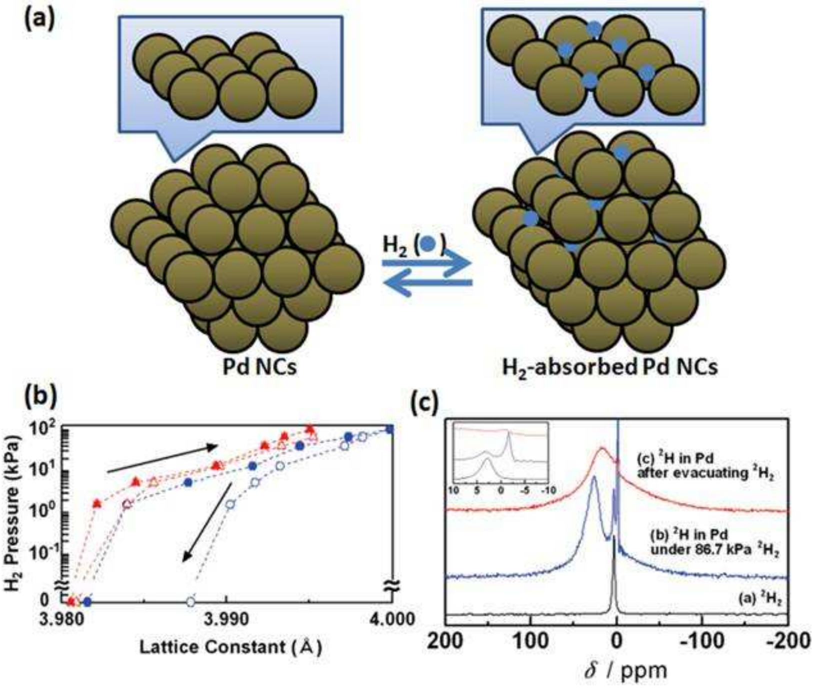

Figure 1-20. (A) Absorption and desorption of H_2 on Pd NCs. (B) XRD lattice constant of Pd NCs during absorption (filled) and desorption (opened) at 373 K (triangle) and 303 K (circle). (C) Solid state ^{2}H NMR spectra of (a) $^2H_2$ gas and (b, c) a sample of Pd NPs (b) under 86.7 kPa of $^2H_2$ gas and (c) after evacuating the $^2H_2$ gas at 303 K.[56]

Platinum Nanocrystals (Pt NCs).

For Pt NPs having sizes ranging between 2 and 3 nm, trillions of Pt NPs are suspended in brownish red- or black-colored colloidal solutions. Similar to Au, Ag, and Pd NCs, the Pt NCs can be prepared through both chemical and solvothermal reductions. For chemical reduction, Zhao and Crooks used the PAMAM dendrimer G4-OH to capture Pt^{2+} followed by reduction with $NaBH_4$.[44,45] **Figure 1-21a** provides spectroscopic evidence for Pt^{2+} sorption into G4-OH dendrimers. In the absence of the dendrimer, the spectrum of a freshly prepared solution of 3 mM $PtCl_4^{2+}$ consists of a strong absorption peak at 216 nm arising from a ligand-to-metal charge-transfer (LMCT) transition.[58] When 0.05 mM G4-OH is added to this solution, a new band emerges at 250 nm, while the band at 216 nm decreases in intensity and shifts slightly to 219 nm. The isosbestic point at 234 nm suggests the replacement of the chlorine ligands of $PtCl_4^{2+}$ with tertiary amino ligands from the dendrimer interior. This ligand exchange reaction is slow, consistent with previous observations for other Pt^{2+} complexes.[59] The absorbance of G4-OH$(Pt^{2+})_n$ at 250 nm is proportional to the number of Pt^{2+} ions (n = 0 to 60), which indicates that it is possible to control the G4-OH/Pt^{2+} ratio. Chemical reduction of an aqueous solution of G4-OH$(Pt^{2+})_n$ (n = 12, 40, or 60) yields intradendrimer Pt NPs [G4-OH(Pt_n)]. Spectra of these materials (**Fig. 1-21b**) display the monotonic increase in absorbance typical of the interband transition of Pt NPs.[60,61] The HRTEM image in **Fig. 1-21c** reveals the spherical shape (at this resolution) and high degree of monodispersity of the Pt clusters. Analysis of 100 randomly selected particles indicates their average diameter is 1.6 ± 0.2 nm, slightly larger than the theoretical value of 1.2 nm calculated by assuming that the Pt atoms are encompassed within the smallest sphere containing a 60-atom face-centered cubic (FCC) crystal. X-ray photoelectron spectroscopy (XPS) analysis provides elemental compositional information about the modified substrates. For example, the Pt($4f_{7/2}$) and Pt($4f_{5/2}$) peaks are present at 72.8 and 75.7 eV, respectively, prior to reduction, but after reduction they shift to 71.3 and 74.4 eV, respectively, consistent with a change in oxidation state from +2 to 0 by 1.5 eV (**Fig. 1-21d**).[62] Importantly, XPS data also indicate the presence of chlorine atoms prior to reduction, but not in the spectra of the G4-OH(Pt_{60})-modified surfaces. Martin et al. prepared Pt NCs (**Pt 98** in **Table 1-4**) through chemical reduction of H_2PtCl_6 with $LiBH_4$ in the micelles of hexa(ethylene glycol) mono-*n*-dodecyl ether (C12E6).[63] Although the 4.0 nm (±10%) **Pt 98A** NCs in **Fig. 1-22a** are not as stunning as a good Au sample, they have such a sufficiently low dispersity that superlattice formation can occur on the TEM grid. Also computed from the TEM image is the distribution of particle diameters, shown for **Pt 98A** in

Fig. 1-22b. Şen and Gökağaç prepared four Pt nanocatalysts for use in direct methanol fuel cells (DMFCs).[64] They studied the effects of various metal salts ($PtCl_4$ and H_2PtCl_6) and thiols (1-hexanethiol and tetra-octanethiol) on the size of the resulting Pt NCs. Obviously, the steric interaction of the terta-octanethiols induced larger-sized Pt NCs (**Fig. 1-23a**). In the analysis of the XPS spectrum of the Pt 4f energy level of catalyst II (**Fig. 1-23b**), it was assumed that the doublets are Gaussian shaped [(5/2-7/2) components of equal halfwidths with an intensity ratio of ca. 3:4 and a separation of ca. 3.35 eV]. While these approximations limit the accuracy with which precise band shape can be reproduced, the aim of spectral fitting is to identify and approximately quantify the Pt species present. Under these circumstances, the Pt 4f electron spectra of all catalysts provide a good fit when using two doublets with Pt $4f_{7/2}$ binding energies of 71.0–71.5 and 74.3–74.5 eV, respectively. The former is undoubtedly due to Pt(0), while the latter is most probably due to the presence of Pt(IV) species, such as PtO_2 or $Pt(OH)_4$. For $Pt(OH)_4$, the Pt $4f_{7/2}$ energy level appears at 74.4 eV;[65] for PtO_2, it is between 74.6 and 74.9 eV.[66] In addition to identifying the surface species, XPS enables quantification of the various oxidation states of a particular element present. The Pt(0)/Pt(IV) ratio is ca. 8:2 for catalyst II, which has the methanol oxidation reaction current at lower potentials. Cyclic voltammograms of catalyst II in 0.1 M $HClO_4$ at room temperature remained unchanged over a 3-month period, indicating the stability of the prepared catalysts. Typical hydrogen and oxygen adsorption and desorption features were observed on the Pt NPs. The addition of methanol to the electrolyte resulted in a dramatic change in the appearance of the voltammograms, due to the methanol oxidation reaction taking place on the surfaces of the Pt NPs (**Fig. 1-23c**). Mu et al. deposited Pt NCs onto the surface of carbon nanotubes (CNTs) for use in DMFCs.[67] In a comparison with chemical reductions mediated by

$NaBH_4$,[44,45] $LiBH_4$,[63] and $LiBEt_3H$,[64] they prepared Pt NCs through solvothermal reduction in EG at 160 °C for 3 h. After PPh_3-induced transfer of the Pt NCs from EG into toluene, the PPh_3-protected Pt NCs were adsorbed onto the surface of CNTs via the π–π interactions. After thermal treatment at 400 °C for 1 h, the Pd NCs sintered on the surface of the CNTs retained their small sizes, with average diameters of ca. 3 nm detected in TEM images (**Fig. 1-25a,c**). In addition, the composition of Pt could be detected from the TEM-assisted EDX spectrum (**Fig. 1-25b**).

Current needs for sustainable energy have popularized the development and use of fuel cell technology. Fuel cells provide a clean alternative to other types of energy. DMFCs are a subcategory of proton-exchange fuel cells where the methanol (CH_3OH) fuel is not reformed as in the indirect methanol fuel cell, but fed directly to the fuel cell operating at a temperature of ca. 90–120 °C. Because it is a relatively new technology, many aspects remain to be improved. The catalysts are the most vital components of fuel cells, so much research effort has been focused in recent years on the development new types of catalysts.[68] Several important types of nanocatalysts (Pt-Ru nanocomposites, Au nanocatalysts, and CNT-supported Pt-Fe) have been developed. Fuel cells are electrochemical devices that produce electricity from a continuous supply of chemical feedstock through specific electrode reactions and movements of charges between the electrodes.[69,70] In comparison with an internal combustion engine, the work of a fuel cell is considerably more efficient and has a less negative impact on the environment because it does not produce waste gases such as CO_2 and SO_2. All fuel cells work on the similar basic principle (**Fig. 1-26a**): H_2 (or another suitable fuel) is provided at the anode; as the H_2 molecules pass by the catalysts (mainly Pt) suspended on carbon-based supports on the polymer electrolyte membrane, they are oxidized to protons and electrons. Because only protons can permeate through the polymer electrolyte membrane (usually Nafion, a trademark of DuPont), electrons are forced though a different route to meet oxygen molecules and protons at the cathode side; therefore, producing electricity and water.[71] DMFCs face fewer problems related to the temperature and gas (H_2) fuel. They employ the same mechanism—the oxidation of methanol and reduction of O_2 across the polymer electrolyte membrane—to produce electricity, water, and CO_2. Whereas other fuel cells use the traditional compressed H_2 for fuel, DMFCs use methanol that is reduced directly at the anode to produce electrons, thus eliminating the problems of carrying the highly compressed gas.[72] Because the rate of electricity production is directly dependent on the turnover frequency (TOF, the maximum number of substrates that a catalyst can convert to product per catalytic site per unit of time), the performance of a catalyst can determine the overall efficiency of the whole fuel cell system. Currently, Pt NCs are considered to be among of the best catalysts for this application. Bimetallic Pt/Ru and Pt/Au NCs can also be used as anodic catalysts to improve the conversion of CO into CO_2, necessary because excess CO blocks the active sites on Pt NCs.[73] DMFCs rely upon the oxidation of methanol on a catalyst layer to form CO_2. Water is consumed at the anode and produced at the cathode. Positive ions (H^+) are transported across the proton exchange membrane—often made from Nafion—to the cathode, where they react with O_2 to produce water. Electrons are transported through an external circuit from the anode to the cathode, providing power to connected devices (**Fig. 1-26**).

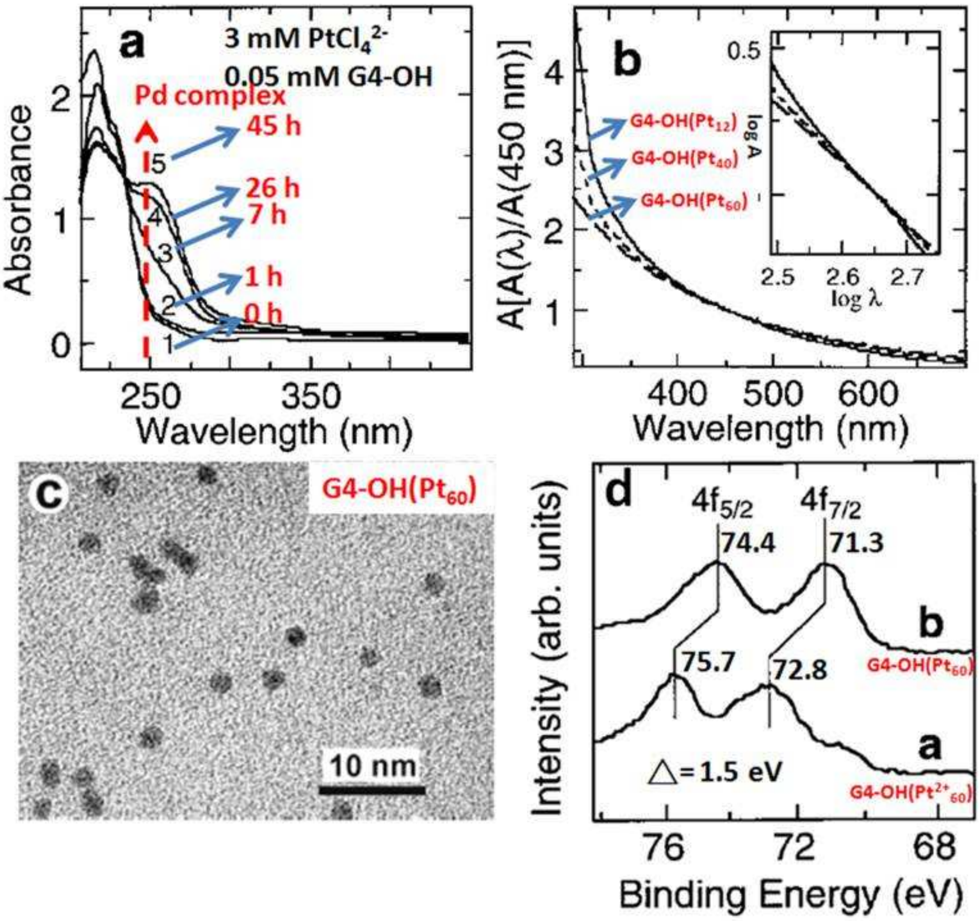

Figure 1-21. (a) Time-dependent UV–Vis spectra of a mixture of 3 mM $PtCl_4^{2-}$ and 0.05 mM G4-OH. (b) UV–Vis spectra of G4-OH(Pt_{12}), G4-OH(Pt_{40}), and G4-OH(Pt_{60}). (c) HRTEM image of G4-OH(Pt_{60}). (d) XPS spectra of G4-OH($Pt^{2+}{}_{60}$) and G4-OH(Pt_{60}).[45]

Table 1-4. Solution compositions for selected Pt NCs.[63]

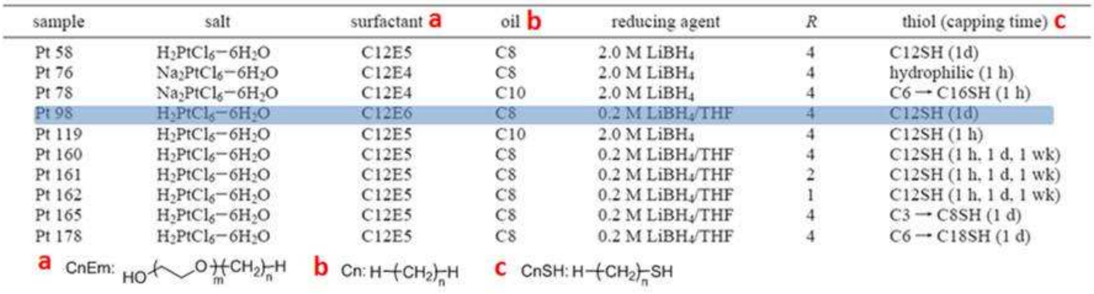

sample	salt	surfactant a	oil b	reducing agent	R	thiol (capping time) c
Pt 58	$H_2PtCl_6-6H_2O$	C12E5	C8	2.0 M $LiBH_4$	4	C12SH (1d)
Pt 76	$Na_2PtCl_6-6H_2O$	C12E4	C8	2.0 M $LiBH_4$	4	hydrophilic (1 h)
Pt 78	$Na_2PtCl_6-6H_2O$	C12E4	C10	2.0 M $LiBH_4$	4	C6 → C16SH (1 h)
Pt 98	$H_2PtCl_6-6H_2O$	C12E6	C8	0.2 M $LiBH_4$/THF	4	C12SH (1d)
Pt 119	$H_2PtCl_6-6H_2O$	C12E5	C10	2.0 M $LiBH_4$	4	C12SH (1 h)
Pt 160	$H_2PtCl_6-6H_2O$	C12E5	C8	0.2 M $LiBH_4$/THF	4	C12SH (1 h, 1 d, 1 wk)
Pt 161	$H_2PtCl_6-6H_2O$	C12E5	C8	0.2 M $LiBH_4$/THF	2	C12SH (1 h, 1 d, 1 wk)
Pt 162	$H_2PtCl_6-6H_2O$	C12E5	C8	0.2 M $LiBH_4$/THF	1	C12SH (1 h, 1 d, 1 wk)
Pt 165	$H_2PtCl_6-6H_2O$	C12E5	C8	0.2 M $LiBH_4$/THF	4	C3 → C8SH (1 d)
Pt 178	$H_2PtCl_6-6H_2O$	C12E5	C8	0.2 M $LiBH_4$/THF	4	C6 → C18SH (1 d)

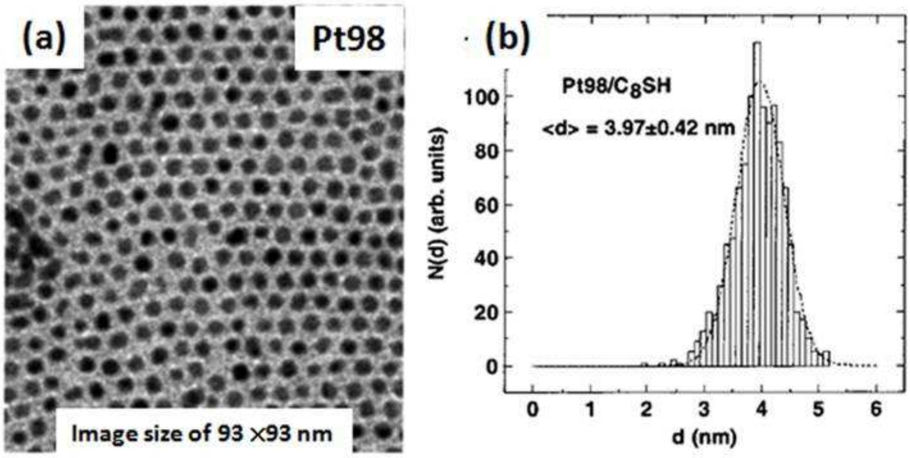

Figure 1-22. (a) TEM image and (b) histogram analysis of **Pt 98** NCs.[63]

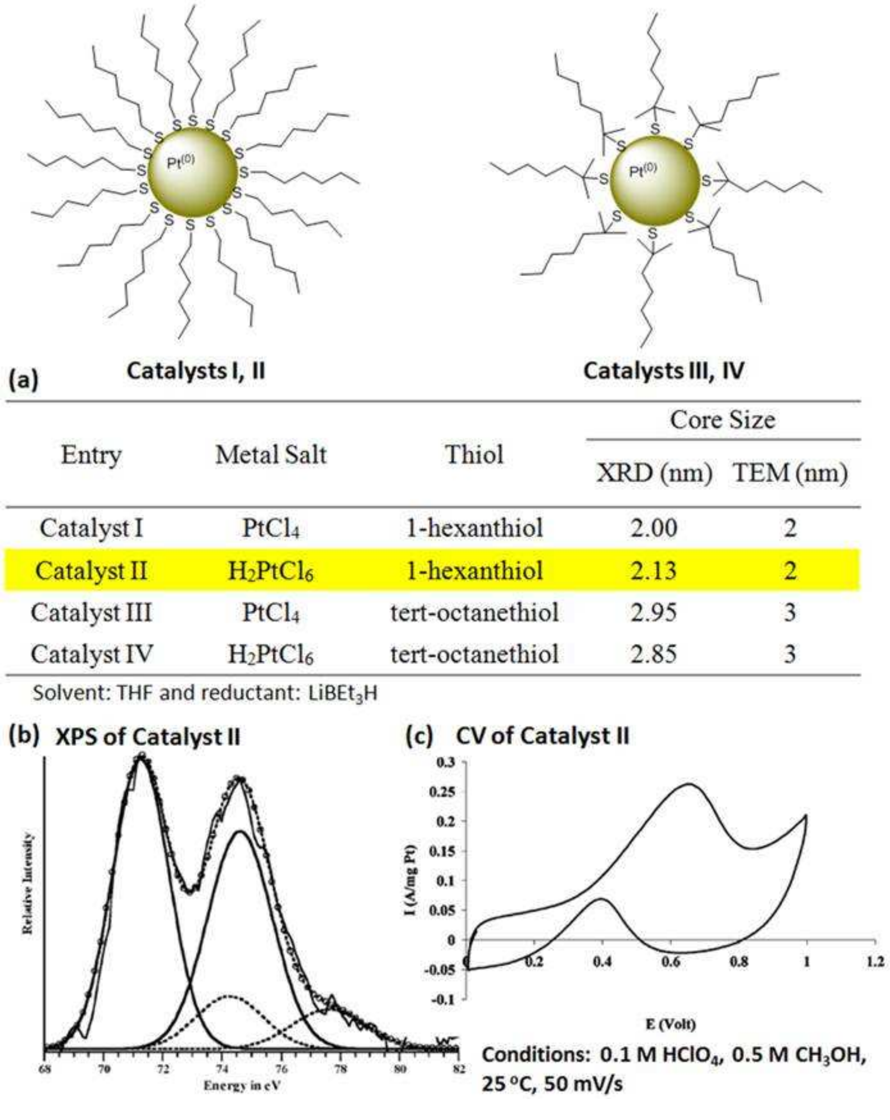

Entry	Metal Salt	Thiol	Core Size	
			XRD (nm)	TEM (nm)
Catalyst I	$PtCl_4$	1-hexanthiol	2.00	2
Catalyst II	H_2PtCl_6	1-hexanthiol	2.13	2
Catalyst III	$PtCl_4$	tert-octanethiol	2.95	3
Catalyst IV	H_2PtCl_6	tert-octanethiol	2.85	3

Solvent: THF and reductant: $LiBEt_3H$

Conditions: 0.1 M $HClO_4$, 0.5 M CH_3OH, 25 °C, 50 mV/s

Figure 1-23. (a) Compositions and sizes of catalysts I–IV. (b) XPS and (c) CV spectra of Catalyst II.[64]

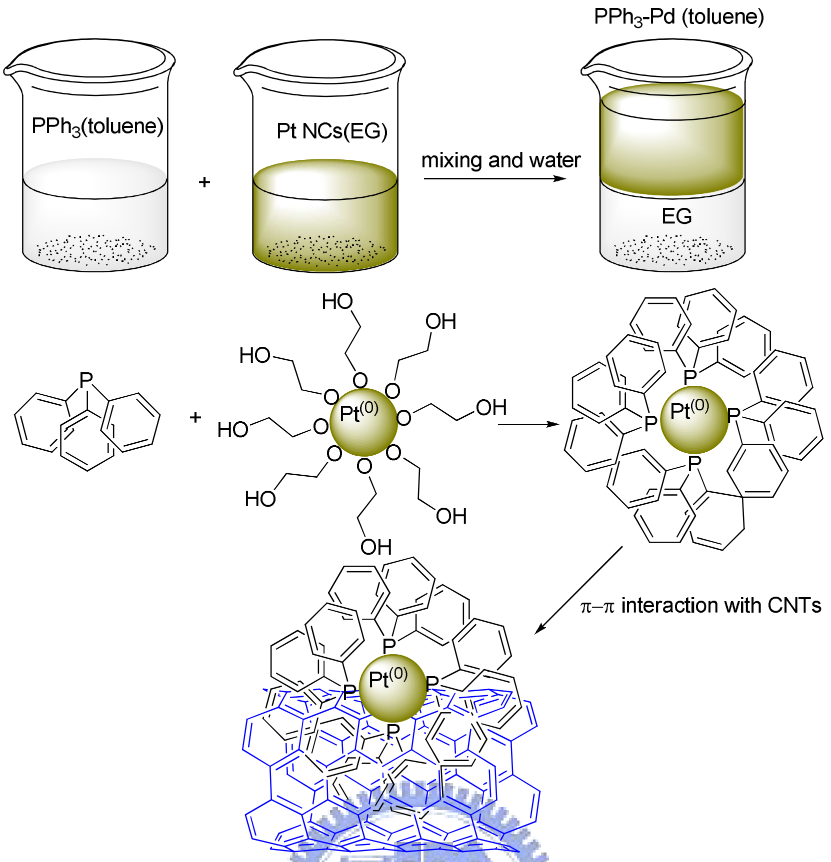

Figure 1-24. Schematic illustrations of the synthesis of Pt/CNTs nanocomposites.[67]

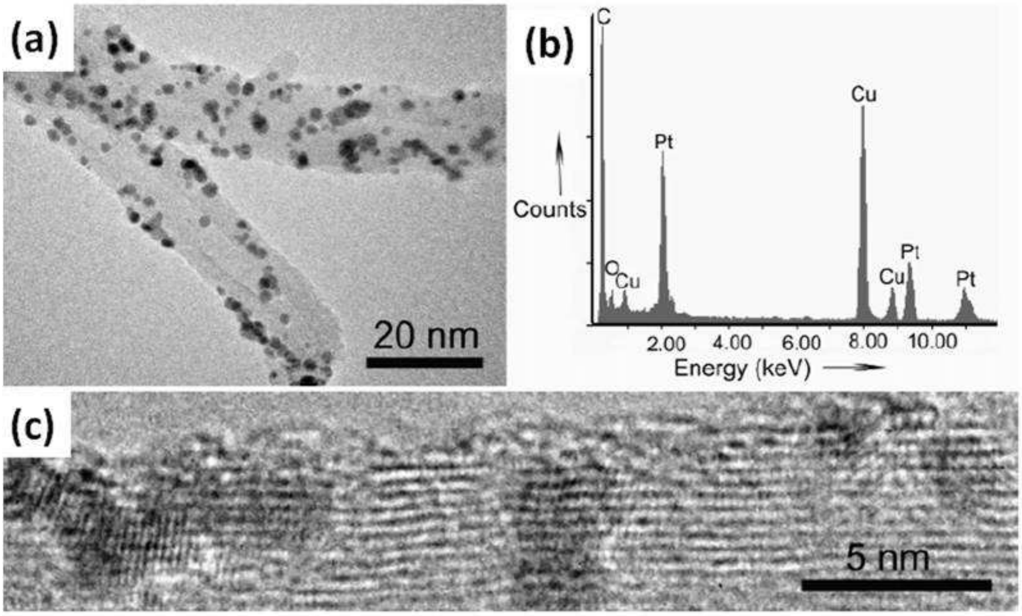

Figure 1-25. (a) TEM image of a Pt/CNT composite (24.0 wt%) after thermal treatment at 400 °C for 1 h. (b) EDS spectrum and (c) HRTEM image of the Pt/CNT composite in (a).[68]

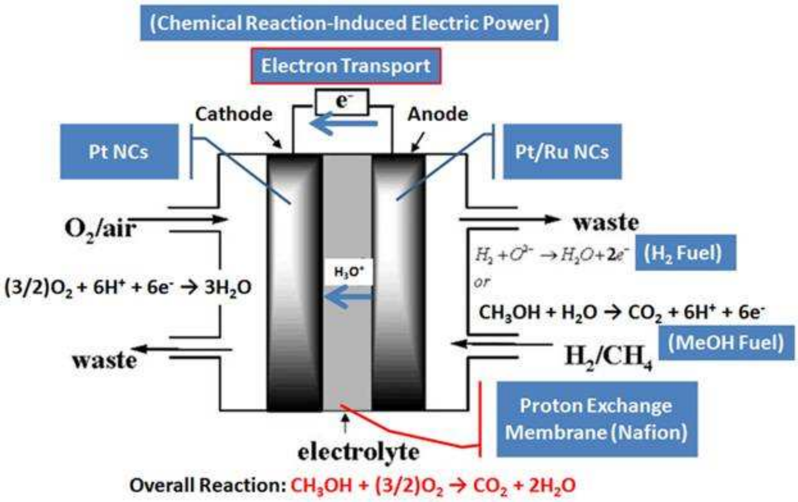

Figure 1-26. Schematic representation of the working principle of a fuel cell.[68]

1-2-2 Ionic Nanocrystals (Ionic NCs)

Unlike single-component metal NCs, ionic NCs comprise two components, packed into ordered structures within confined domains. Similar to metal atoms in metal NCs, the packing of cationic and anionic ions can be also observed in the high-angle regions of X-ray diffraction and in the lattice spacing distance of HRTEM images. According to their conductivity, ionic NCs can be divided into metal oxides (e.g., Fe_2O_3, ZnO, and TiO_2), and semiconductors (e.g., CdSe, CdS, and CdTe).

1-2-2.1 Metal Oxide Nanocrystals (Metal Oxide NCs)

Metal oxide NCs are mainly prepared through conventional sol–gel processing. The precursor metal alkoxide is hydrolyzed into a metal hydroxide, which is highly active for dehydration reactions with a metal alkoxide or metal hydroxide to give a network structure. In addition, the solvothermal decomposition of organometallic precursors has been developed to prepare highly crystalline metal oxide NCs. Solvothermal conditions afford high autogenous pressures inside the sealed autoclave, enabling low-boiling solvents to be heated to temperatures well above their boiling points. Thus, reactions can be carried out at elevated temperatures and the products obtained are generally crystalline compared with those obtained from other solution-based sol–gel processes.

Maghemite Nanocrystals

Maghemite (γ-Fe_2O_3) is a red-brown magnetic material that is isostructural with magnetite, but possesses cation-deficient sites. Various methods have been reported for the synthesis of iron oxide NPs, such as sonochemical synthesis, sol–gel reactions, and chemical reactions. Rockenberger et al. described the use of cupferron complexes as precursors to prepare γ-Fe_2O_3 NCs through thermal decomposition at 200 °C for 0.5 h. Cupferron, the ammonium salt of *N*-nitroso-*N*-phenylhydroxylamine, is a common reagent for the complexation of metal ions. Its formula is $NH_4^+[C_6H_5N(O^-)NO]$; the anion binds to metal cations through the two oxygen atoms, forming five-membered chelate rings.[74] **Figure 1-27** presents a low-resolution TEM image of γ-Fe_2O_3 NCs; the slow evaporation of a dispersion of these NCs in toluene onto the TEM grid led to the formation of an extended monolayer of particles. The covered area is larger than 2 μm^2 and extends beyond the bounds of the image in **Fig. 1-27**. Each particle is separated from its neighboring particles by a shell of surfactant. A relatively broad size distribution of 15% prevents the formation of the ordered superlattices observed with other systems.[75] The crystallinity of these particles is revealed by the HRTEM image in **Fig. 1-27** (top left). The observed lattice plane distances of 4.77 and 4.11 Å, as well as the angle of ca. 50° between the crossed fringes, indicate the presence of tetragonal γ-Fe_2O_3 with an ordered superlattice of cation vacancies.[76] The corresponding lattice planes are (113) and (201), respectively; the fast fourier transform (FFT) (top right) of the high-resolution image indicates that the particle was imaged along its [512h] zone axis. Similarly, Hyeon et al. prepared monodisperse γ-Fe_2O_3 NCs through thermal aging (300 °C) of a mixture of trimethyl-*N*-oxide and an Fe–oleic acid metal complex, which had been obtained through ligand exchange of iron pentacarbonyl with oleic acid at 100 °C.[77] Trimethylamine *N*-oxide, an oxidation product of trimethylamine (TMA), plays a similar role as that of cupferron in the oxidation to γ-Fe_2O_3 NCs, releasing TMA at high temperature.

Recently, γ-Fe_2O_3 NCs have been studied as a gas-sensitive materials because they can be fabricated without costly noble metal catalysts and they perform as good sensors.[78] Ray et al. prepared γ-Fe_2O_3 NCs through a sonication-assisted precipitation at 70 °C of an Fe^{2+} complex that had been obtained through the reduction of ferric nitrate nonohydrate [$Fe(NO_3)_3 \cdot 9H_2O$] with hydrazine monohydrate [$N_2H_4 \cdot H_2O$] (**Fig. 1-28a**). **Figure 1-28b** presents XRD patterns of the iron oxide powders prepared using a conventional precipitation route (without sonication) and a sonochemical route (using ultrasonic powers of 300 and 600 W). The powder synthesized under a high ultrasonic power rating (i.e., 600 W) displayed a pure γ-Fe_2O_3 NCs phase, whereas the powder synthesized under a low ultrasonic power rating (i.e., 300 W) was a mixed-phase powder (γ-Fe_2O_3 and α-Fe_2O_3). In the absence of sonication (conventional precipitation route), no crystalline phase could be identified. **Figure 1-28c** displays the curves obtained for the sensing of various concentrations (50–1000 ppm) of *n*-butane. The percent responses toward 1000, 750, 500 and 250 ppm *n*-butane were ca. 93, 88, 85 and 80%, respectively. **Figure 1-28d** reveals that the percentage response increased almost linearly as the *n*-butane concentration increased from 250 to 1000 ppm. This linear relationship may be attributed to the availability of a sufficient number of sensing sites on the film for *n*-butane sensing. A low gas concentration implies a lower surface coverage of gas molecules, resulting in a lower extent of surface reactions between the surface-adsorbed oxygen species and the gas molecules. An increase in the gas concentration increases the surface reaction because of the larger surface coverage. A further increase in the surface reaction will be gradual when saturation of the surface coverage of gas molecules is reached.

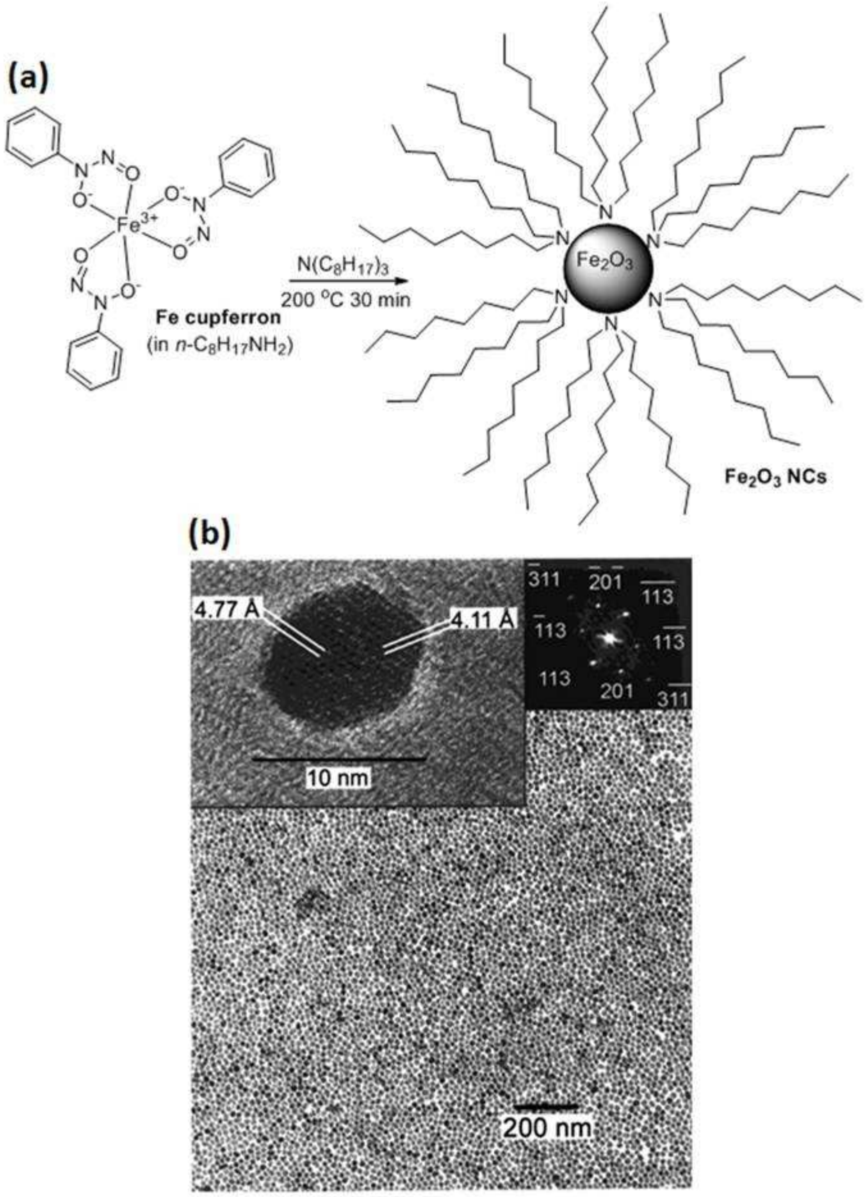

Figure 1-27. (a) Thermal decomposition of Fe cupferron into γ-Fe_2O_3 NCs. (b) TEM image of a monolayer of individual γ-Fe_2O_3 NCs (10.0 ± 1.5 nm) covering an area larger than 2 μm^2. Top left: HRTEM image of one of the NCs in this sample. The indicated lattice plane distances correspond to the (113) and (201) lattice planes of tetragonal γ-Fe_2O_3 with an ordered superlattice of the cation vacancies. Top right: FFT of the HRTEM image looking down the [512h] zone-axis.[74]

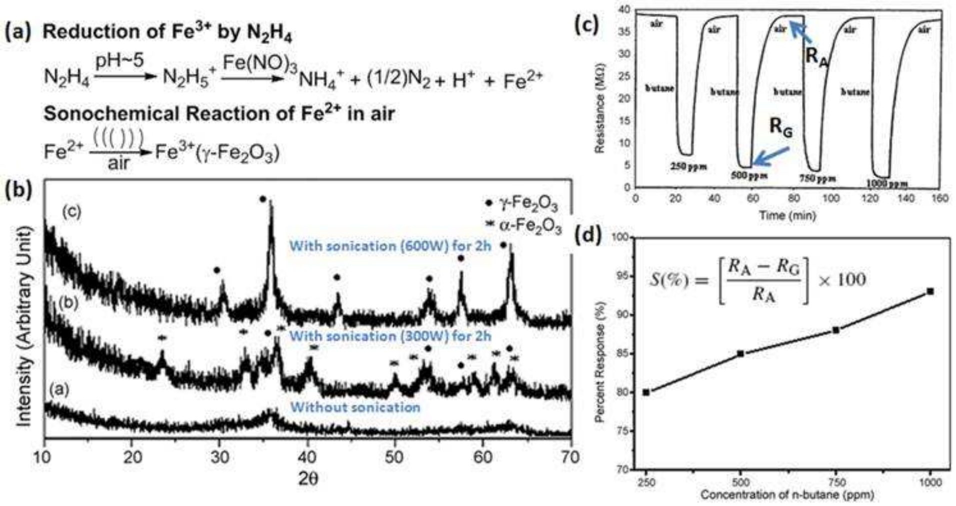

Figure 1-28. (a) Reaction scheme for the sonochemical reaction leading to Fe_2O_3 NCs. (b) XRD spectra of the as-synthesized Fe_2O_3 NCs. (c, d) Typical sensing curves for *n*-butane at concentrations ranging from 250 to 1000 ppm.[78]

Zinc Oxide Nanocrystals (ZnO NCs).

Hartlieb et al. prepared ZnO NCs having average diameters of 5 nm through conventional sol–gel processing of zinc nitrate hexahydrate [$Zn(NO_3)_2 \cdot 6H_2O$] with potassium hydroxide (KOH) in the presence of PVP as stabilizer (**Fig. 1-29a**).[79] Selected area electron diffraction by TEM of an aged sample revealed that the sample was crystalline ZnO, having the standard wurtzite structure (**Fig. 1-29b**). This structure was confirmed through XRD analysis (**Fig. 1-29c**). Diffraction rings corresponding to the (101) and (102) planes for wurtzite ZnO are absent in the selected area diffraction pattern. Careful examination of high-resolution images (e.g., **Fig. 1-29d**) reveals that the majority of the particles lie along either the <001> or <101> zone axis; therefore, it is likely that the effect seen in the electron diffraction pattern is due to the preferred orientation, potentially a result of the presence of facetted or platelike particles; this situation could mean that ripening occurs along specific crystallographic directions. Beek et al. prepared ZnO/ Poly[(3’,7’-dimethyloctyloxy)-p-phenylene vinylene] (MDMO-PPV) hybrid solar cells, using ZnO NCs to transfer the photoluminescence (PL) emission energy of

MDMO-PPV, to increase the efficiency of MDMO-PPV-based solar cells (**Fig. 1-30a**).[80] Because the extension of the electronic wave functions of semiconductor QDs is confined to the particle, their energy levels are size-dependent and UV–Vis spectroscopy can be used to determine the diameter of semiconductor NPs such as ZnO. **Figure 1-30b** displays the UV absorption spectrum of ZnO NPs in a mixture of chloroform and methanol. According to Meulenkamp,[81] the observed value of $\lambda_{1/2}$[33] of 360 nm corresponds to a particle diameter of 4.9 nm.[78] This finding indicates that quantum confinement—and its effect on the UV absorption onset—is only present in smaller particles. Therefore, the UV onset is not a suitable measure of the sizes of larger particles. In **Figure 1-30c**, the absorption spectrum of MDMO-PPV does not change, and the optical density at the maximum remains roughly the same because the MDMO-PPV concentration was constant and only the ZnO concentration was varied. Before addressing the effect of the ZnO concentration on the performance of the resulting photovoltaic (PV) devices, it is useful to observe how it affects charge formation. Because of the fast (sub-picosecond) forward electron transfer reaction, mixing ZnO and MDMO-PPV will result in quenching of the photoluminescence of the polymer. Indeed, the spectra (**Fig. 1-30d**) reveal that the PL of MDMO-PPV is quenched increasingly upon the addition of ZnO; at 35 vol% ZnO, 85% of the original MDMO-PPV PL intensity is lost. Because energy (exciton) transfer from the polymer to ZnO is highly endergonic, we attribute the fluorescence quenching to electron transfer, although a contribution from increased nonradiative decay (e.g., intersystem crossing) cannot be ruled out. From these results, we infer that a maximum of 85% of the absorbed photons leads to charge separation. Addition of more ZnO does not lead to a further quenching. The residual PL can be explained by assuming that phase separation between MDMOPPV and ZnO occurs on a length scale larger than the exciton diffusion length (ca. 10 nm for MDMO-PPV).

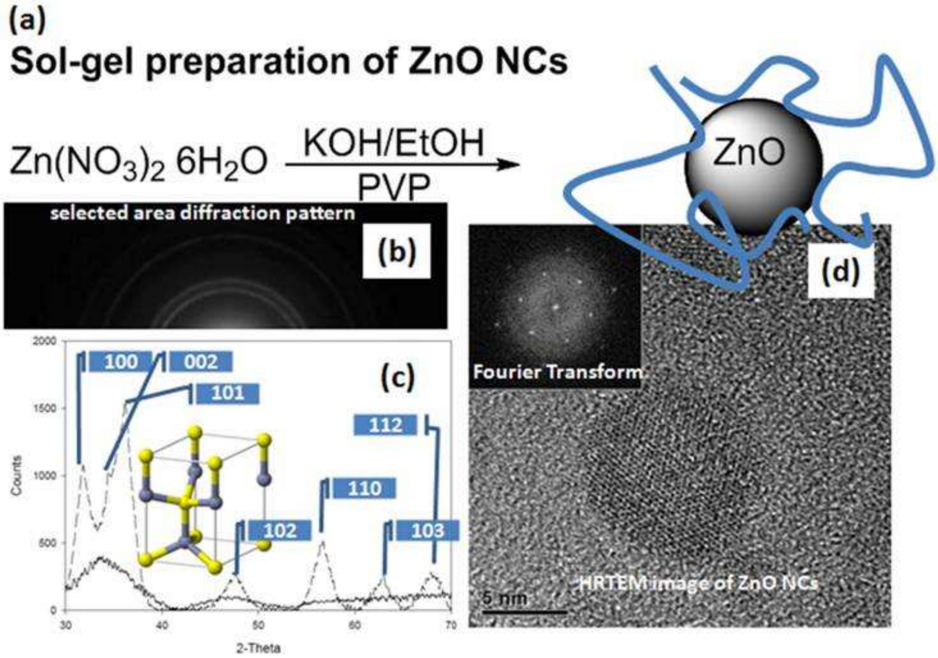

Figure 1-29. (a) Sol–gel preparation, (b) selected area diffraction pattern, (c) XRD spectrum, and (d) HRTEM images and Fourier transform of ZnO NCs.[79]

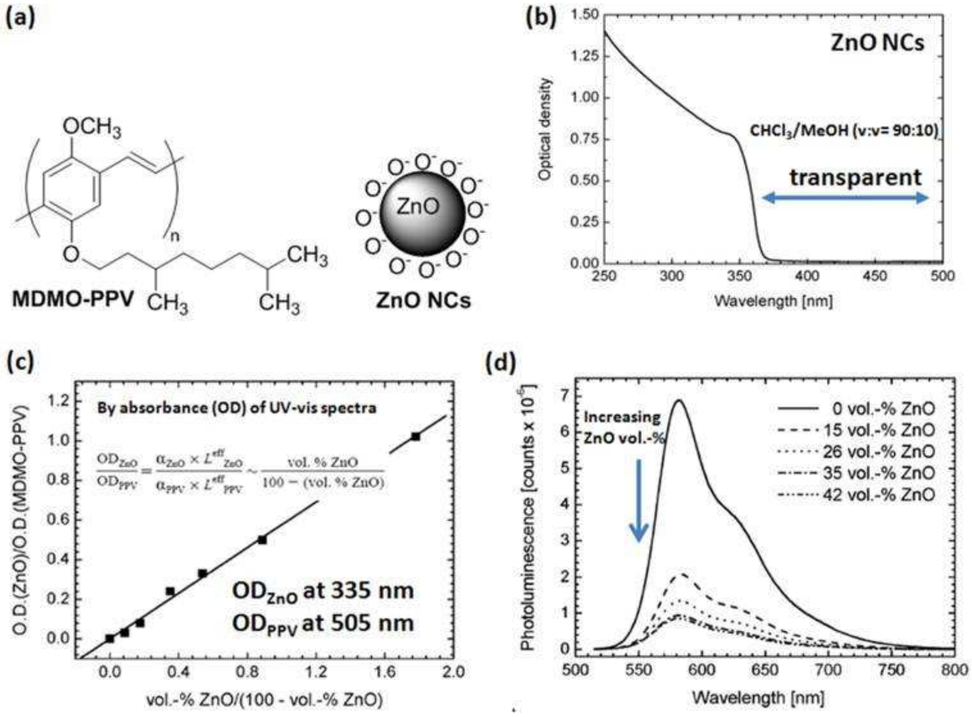

Figure 1-30. (a) Materials for a dye-sensitive solar cell. (b, c) UV–Vis spectra of (b) ZnO NCs and (c) ZnO/MDMO-PPV membranes. (d) PL spectrum of ZnO/MDMO-PPV membranes.[80]

Titanium Oxide Nanocrystals (TiO_2 NCs)

Recent developments in the synthesis of II–VI semiconductor clusters include the rapid thermal decomposition of molecular precursors in the presence of strong coordinating agents to create high-quality NCs.[82,83] To extend this strategy to oxides, Trentler et al. employed chemistry known to produce amorphous TiO networks at low temperatures. $TiCl_4$ reacts with titanium alkoxides or ethers with the resultant elimination of alkyl halides (**Fig. 1-31a**).[84] XRD analysis indicated that the powders obtained were anatase TiO_2 NCs; inspection of the diffraction line widths revealed that the crystalline domains were less than 10 nm in diameter (**Fig. 1-31b**).[84] Particle sizes monitored by TEM were in general agreement with those obtained through the XRD analyses, although it revealed a considerable distribution in size (**Fig. 1-31c**). Many particles exhibited irregular shapes, but their crystalline perfection was high (**Fig. 1-31d**). Redispersed NCs obtained from reactions performed at low concentration remained isolated or only very loosely aggregated depending on the method of TEM sample preparation; the precipitated products were somewhat more agglomerated. The degree of agglomeration was the only difference discerned between the precipitated products and the particles remaining in solution.

Titanium dioxide, particularly in its anatase form, is a photocatalyst under UV light. Recently, it has been found that TiO_2 spiked on the nitrogen-containing supporters or doped with metal oxides, such as tungsten trioxide, is a photocatalyst under visible light as well. The strong oxidative potential of the positive holes oxidizes water to create hydroxyl radicals; it can also oxidize O_2 and organic materials directly. Titanium dioxide is, therefore, added to paints, cements, windows and tiles to take advantage of its sterilizing, deodorizing and anti-fouling properties and its ability to function as a hydrolysis catalyst. When TiO_2 is exposed to UV light, it becomes increasingly hydrophilic because HO• free radicals are produced through the reactions of HO^- anions on the positively charged surfaces of UV-activated TiO_2 NCs; thus, these NCs can be used in anti-fogging coatings and self-cleaning windows (**Fig. 1-32**)[85]

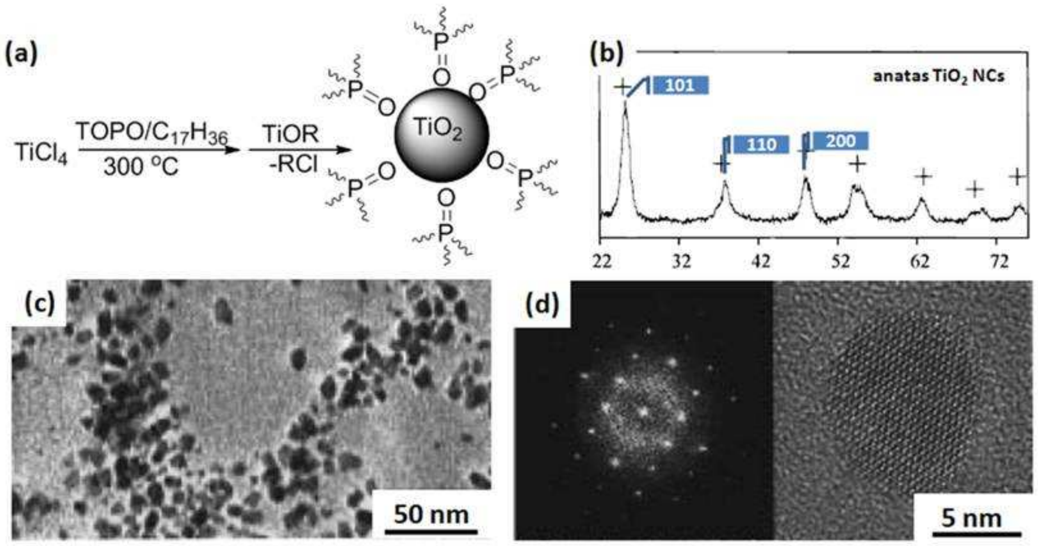

Figure 1-31. (a) Reaction scheme for the preparation of TiO networks. (b) XRD patterns, (c) TEM images, and (d) HRTEM images and FTIR spectra of anatase TiO_2 NCs having a diameter of 7.3 nm.[84]

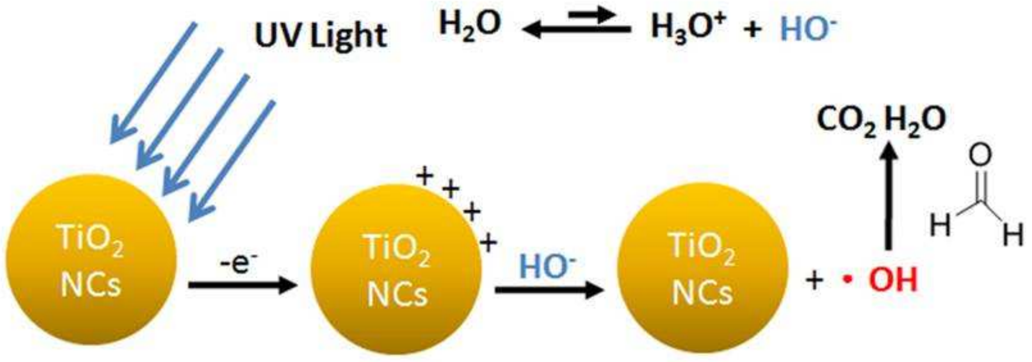

Figure 1-32. Reaction mechanism of TiO_2-induced photocatalysts.

1-2.2.2 Semiconductor Nanocrystals (Semiconductor NCs)

Semiconductor NCs are synthesized from precursor compounds dissolved in solutions (i.e., through traditional chemical processing). The synthesis of colloidal QDs is based on a three-component system comprising precursors, organic surfactants, and solvents. When heating a reaction medium to a sufficiently high temperature, the precursors chemically transform into monomers. Once the monomers reach a high enough supersaturation level, the NC growth begins with a nucleation process. The temperature during the growth process is one of the critical factors in determining the optimal conditions for the NC growth. It must be high enough to allow for rearrangement and annealing of atoms during the synthesis process, while being low enough to promote crystal growth. Another factor that must be stringently controlled during NC growth is the monomer concentration. The growth of NCs occurs in both “focusing” and “defocusing” regimes. At high monomer concentrations, the critical size (the size at which the NCs neither grow nor shrink) is relatively small, resulting in growth of almost every particle. In this regime, smaller particles grow faster than large ones (because larger crystals need more atoms to grow than small crystals), resulting in “focusing” of the size distribution to yield nearly monodisperse particles. The size focusing is optimal when the monomer concentration is maintained such that the average NC size present is always slightly larger than the critical size. When the monomer concentration is depleted during growth, the critical size becomes larger than the average size present, and the distribution “defocuses” as a result of Ostwald ripening. There are colloidal methods to produce many different semiconductors, including CdSe, CdS, InAs, and InP. These QDs can contain from as few as 100 to 100,000 atoms, with diameters ranging from 10 to 50 atoms.

Cadmium Chalcogenide Nanocrystals (CdS, CdSe, CdTe NCs)

Murray et al. reported that nearly monodisperse Cd chalcogenide NCs (CdE; E = S, Se, Te) can be synthesized through the injection of organometallic reagents, such as alkylcadmium species, into a hot coordinating solvent in the presence of silylchalcogenides and phosphinechalcogenides (**Fig. 1-33a**).[86] Me_2Cd is usually chosen as the Cd source and $(TMS)_2E$ (E = S, Se, Te), TOPSe, or TOPTe is selected as the chalcogen source, with TOPSe and TOPTe preferred because of their ease of preparation and stability. The dealkylsilylation Me_2Cd and $(TMS)_2E$ reagents occurs in a variety of solvents; these reactions provide a route toward the production of bulk materials. Trimethylphosphine telluride $[(TMP)_2Te]$ is a good source of Te NCs. Mixed phosphine/phosphine oxide solutions are good solvents for the high-temperature growth and annealing of CdSe crystallites. The coordinating solvent plays a crucial role in controlling the growth process, stabilizing the resulting colloidal dispersion, and electronically passivating the semiconductor surface. Injection of the reagents into the hot reaction pot results in a short burst of homogeneous nucleation. The depletion of reagents through nucleation and the sudden temperature drop associated with the introduction of room-temperature reagents prevents further nucleation. Gently reheating allows slow growth and annealing of the crystallites. Crystallite growth appears consistent with Ostwald ripening, where the higher surface free energy of small crystallites makes them less stable with respect to dissolution in the solvent than are the larger crystallites. The net result of this stability gradient within dispersion is slow diffusion of material from small particles to the surface of larger particles. I'Reiss has demonstrated how growth through this kind of transport can result in the production of highly monodisperse colloidal dispersions from systems that may initially be polydisperse. Capping groups present a significant steric barrier to the addition of material to the surface of a growing crystallite, slowing the growth kinetics. The TOP/TOPO solvent coordinates to the surface of the crystallites and permits slow steady growth at temperatures above 280 °C. Replacing the octyl chains with shorter groups reduces the temperature for controlled growth. Mixed alkylphosphine/alkylphosphine oxide solvents with butyl, ethyl, and methyl groups display uncontrolled growth at 230, 100, and 50 °C, respectively. Steady controlled growth results in highly monodisperse particles of consistent crystal structure and allows size selection by extracting samples periodically from the reaction vessel. **Fig. 1-33b** displays absorption spectra of 2–3-nm-diameter CdS, CdSe, and CdTe nanocrystallite samples. All three clearly exhibit the effects of quantum confinement, with the CdS, CdSe, and CdTe absorptions shifted dramatically from their bulk band gaps at 512, 716, and 827 nm, respectively. The spectrum of CdSe features three clearly resolved transitions, whereas the CdS and CdTe samples display fewer structural features. These CdS, CdSe, and CdTe crystallites all exhibit a predominantly wurtzite crystal structure having the same lattice spacing as that of the bulk materials (**Fig. 1-33c**). Bulk crystals of CdS and CdSe commonly exhibit the wurtzite structure when prepared at high temperature. Although the hexagonal modification of CdTe has been observed in thin films, to our knowledge it has not been observed in bulk crystals.

Peng et al. proposed the use of greener Cd sources, such as cadmium oxide (CdO), carbonate ($CdCO_3$), and acetate [$Cd(CH_3COO)_2$], in place of $(Me)_2Cd$. They found that the size distribution of the NCs improved when adding hexadecylamine, a long-chain phosphonic acid, or a carboxylic acid. Their method can be extended to prepare CdS NPs through the use of tri-*n*-octylphosphine sulfide (TOP-S) and hexyl or tetradecyl phosphonic acid in a mixture with TOPO–TOP.[87,88] Although their efforts focused mainly on the growth of CdSe NCs emitting in the orange–red window, their preliminary results implied that the method—and the concept—could be extended to the synthesis of CdSe NCs emitting other visible colors by varying the total concentration of the initial precursors, the types of precursors, the solvent system, the reaction temperature, and the growth time. **Figure 1-34b** displays the PL spectra of several CdSe NC samples featuring different emission colors. TEM imaging confirmed that the NCs synthesized using this approach had dot-like shapes (**Fig. 1-34c**, top-left panel); their size distribution was typically 5–10%. The crystal structure of the resulting NCs was quite sensitive to both the reaction temperature and the chain length of the amine. For the reactions that occurred below 230 °C and in a solvent containing dodecylamine (DDA), the XRD patterns of the resulting CdSe NCs were very much like that of zinc blende CdSe. At high temperatures (>270 °C), the addition of octyldecylamine (ODA) aided the formation of NCs that exhibited diffraction patterns similar to those of almost-perfect wurtzite CdSe NCs.[89]

Various kinds of organic dyes are used widely in modern biological analyses. With each passing year, more flexibility is required of these dyes, and traditional dyes often are unable to meet expectations. To this end, QDs have quickly filled the role, because they are superior to traditional organic dyes on several counts—especially for their brightness (high quantum yields) and stability (much less photodestruction); for single-particle tracking, however, the irregular blinking of QDs is a minor drawback. The use of QDs for highly sensitive cellular imaging has seen major advances over the past decade. Their improved photostability, for example, allows the acquisition of many consecutive focal-plane images that can be reconstructed into high-resolution 3D images. Another application that takes advantage of the extraordinary photostability of QD probes is the real-time tracking of molecules and cells over extended periods of time.[90] Dahan et al. used CdSe QDs to track individual glycine receptors (GlyRs) and analyze their lateral dynamics in the neuronal membrane of living cells for periods ranging from milliseconds to minutes.[90] The specific detection of endogeneous GlyR α1 subunits at the surface of spinal cultured neurons was achieved using a primary antibody (mAb2b), biotinylated antimouse Fab fragments, and streptavidin-coated QDs (**Fig. 1-35**). The

QD-GlyR complexes formed numerous clusters around the soma and dendrites (**Fig. 1-35A**), similar to observations from previous immunocytochemical studies performed using conventional fluorophores. GlyRs were also detected within synaptic and extrasynaptic domains (**Fig. 1-35B and C**).

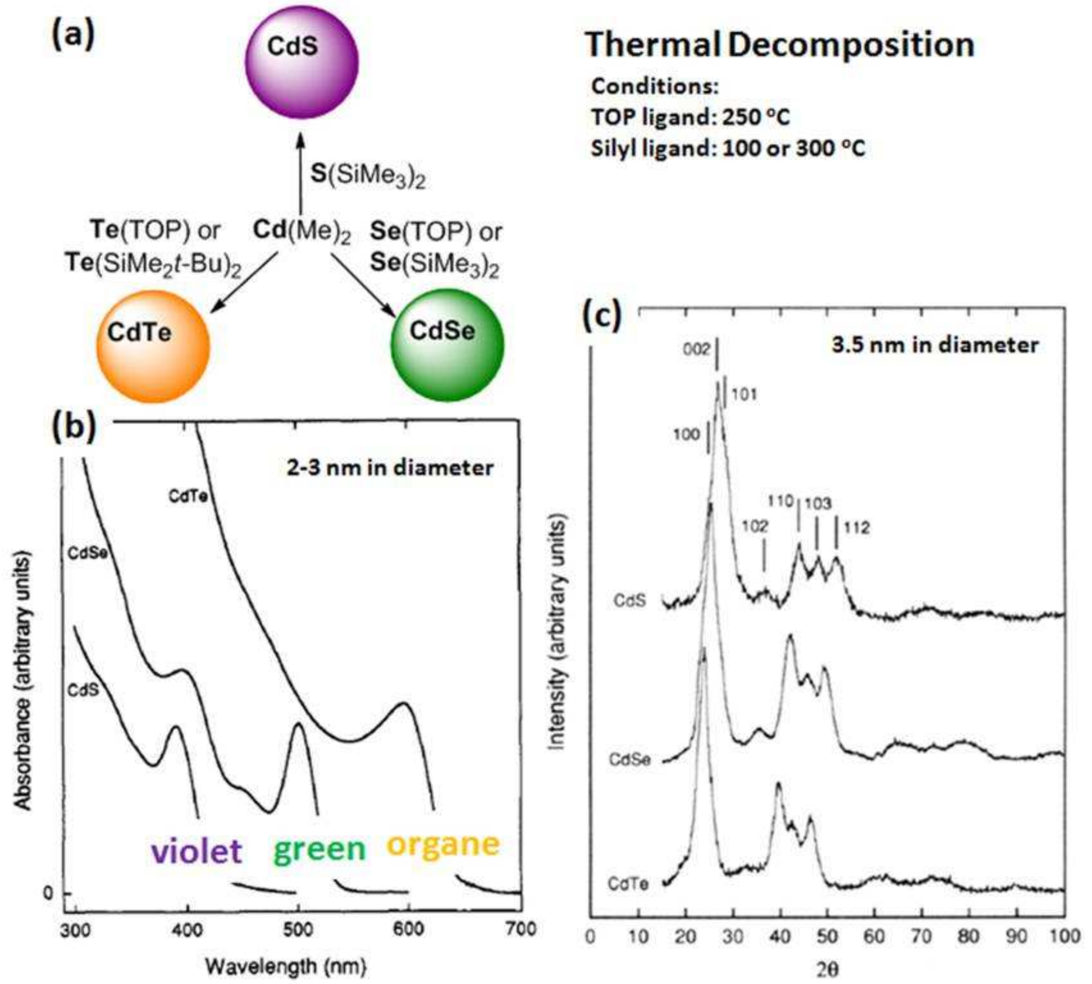

Figure 1-33. (a) Reaction scheme, (b) UV–Vis spectra, and (c) XRD analyses of CdS, CdSe, and CdTe NCs.[86]

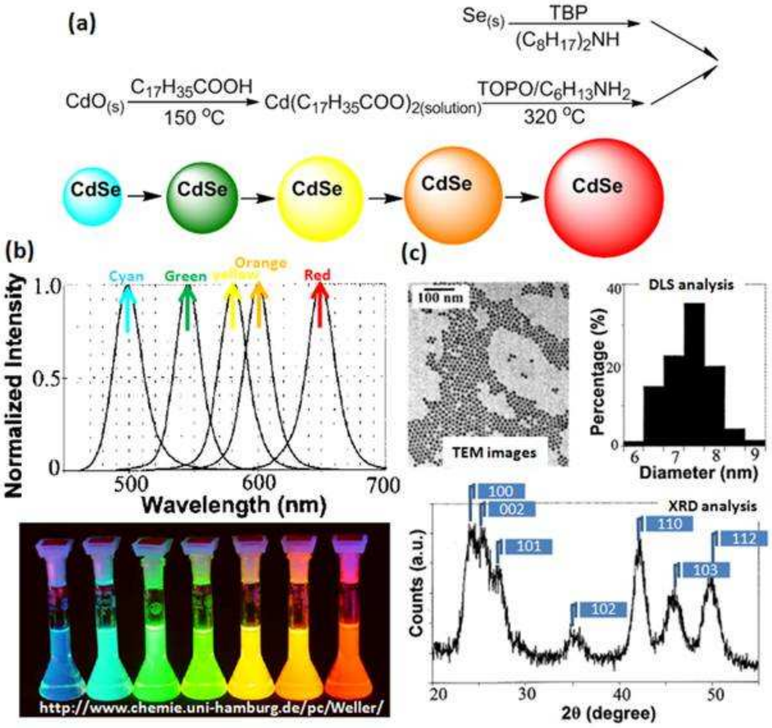

Figure 1-34. (a) Reaction scheme for the preparation of CdSe NCs. (b) PL spectra and photographs taken during the crystal growth for CdSe NCs. (c) TEM images, DLS analysis, and XRD spectrum of 7.5-nm-diameter CdSe NCs.[87]

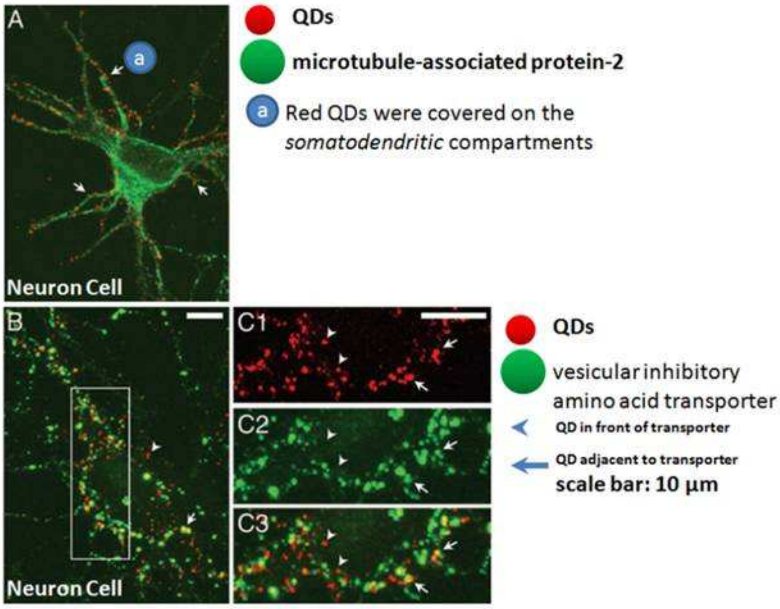

Figure 1-35. CdSe QDs (diameters: 5–10 nm) as markers for GlyR localization in neurons. (A) QD-GlyRs (red) detected over the somatodendritic compartment identified by microtubule-associated protein-2. (B, C) Relationship between the locations of QD-GlyRs (red) and inhibitory synaptic boutons labeled for a vesicular inhibitory amino acid transporter.[90]

1-3 Nanoparticles (NPs)

As above mentioned, NCs are composed of ordered packed metal atoms or ions. In contrast, zero-dimensional nanomaterials that lack ordered structures and compositions are classified as NPs. According to their composition, NPs can be further divided into inorganic, organic, inorganic/organic hybrid NPs. Some nanomaterials featuring unique chemical structures and molar masses are considered to be molecular NPs, e.g., inorganic C_{60} fullerene, organic cyclodextrins, and inorganic/organic hybrid polyhedral oligomeric silsesquioxane (POSS) derivatives. “Cluster NPs” include clays, pigments, and core/shell nanocomposites.

1-3.1 Inorganic Nanoparticles (Inorganic NPs)

Molecular C60 fullerene.

C_{60} is a molecule that consists of 60 carbon atoms, arranged as 12 pentagons and 20 hexagons. Its shape is the same as that of a soccer ball (**Fig. 1-36a**): the black pieces of leather are pentagons, the hexagons are white. The C60 molecule was discovered by Kroto et al.[91] The most striking property of the C60 molecule is its high symmetry. There are 120 symmetry operations, like rotations around an axis or reflections in a plane, which map the molecule onto itself. This makes C60 the molecule with the largest number of symmetry operations, the most symmetric molecule. Similar to metal atoms, highly symmetric C_{60} molecules can pack closely into crystals. The close-packing of spheres is the construction of an infinite regular arrangement (or lattice) of identical spheres that take up the greatest possible fraction of an infinite 3D space (i.e., they are packed as densely as possible). There are two regular lattices that achieve this highest average density: face-centered cubic (FCC) and hexagonal close-packed (HCP) (**Fig. 1-36b**). Both are based upon sheets of spheres arranged at the vertices of a triangular tiling; they differ in how the sheets are stacked upon one another. In both arrangements, each sphere has 12 neighbors. For every sphere there is one gap surrounded by six spheres (octahedral) and two smaller gaps surrounded by four spheres (tetrahedral). The morphology of C_{60} crystals can be either cubic (FCC) or hexagonal (HCP).[91] By evaporating solutions of C_{60} in dichloromethane at room temperature in the dark, Céolin et al. obtained small hexagonal needles (**Fig. 1-36c**).[92]

The strong tendency for C_{60} to crystallize usually results in its low miscibility with other organic systems, such as polymer blends. The chemical functionalization of fullerenes has provided access to a range of interesting new materials. These modified fullerenes, while retaining most of the properties of the pristine species, are more versatile in terms of their solubility, photochemistry, and electrochemistry.[93] Early clues to the reactivity of the fullerenes C_{60} and C_{70} came from cyclic voltammetry (CV) studies,[94] which revealed that they are mild oxidizing agents. This observation was in accord with the theoretically determined lowest unoccupied molecular orbitals (LUMOs) of C_{60}, but it did not provide a microscopic, structure–property relationship of the origin of the high electron affinity of the molecule. Close examination of a C_{60} “ball and stick” model revealed that there were a number of pyracyclene units in the cluster and, on the basis of pyracyclene being a 4nπ system,[95] it was hypothesized that each unit would provide a driving force for the capture of up to two electrons, either through direct electron transfer to give a 4n+2π electron dianion or in the form of a lone pair to give a “cyclopentadienide” monoadduct (**Fig. 1-37a**). When Suzuki surveyed the reactions of C_{60} with diazoalkanes, he observed, in the case of ethyl diazoacetate, that partitioning of the intermediate 1-pyrazoline to the 2-isomer and to a bridged molecule (cyclopropane) had occurred (**Fig. 1-37b**). Maggini and Scorrano used *N*-methylglycine to form a bridge (pyrrolidine) via a decarboxylation route; they obtained a relatively high yield (82%, based on C_{60} conversion) from a reaction mixture containing *N*-methylglycine, paraformaldehyde, and C60 in toluene under reflux for 2 h (**Fig. 1-37c**).[93]

C60 is used widely to capture and transport electrons in organic solar cells.[96] The electron accepting properties of fullerenes have also been utilized for photocurrent generation in porphyrene-C_{60}-based cluster films.[97] Kamat drop-casted a mixture of CdSe QDs and C_{60} on a conducting surface to demonstrate its photovoltaic performance.[98] The poor interaction between the two components resulted in a relatively low photocurrent. Thus, they adopted a new approach of capping the CdSe QDs with a molecular shell of the electron acceptor C_{60} to improve the capture of photogenerated electrons in QDs (**Fig. 1-38a**).[99] **Figure 1-38b,c** provides a comparison of the absorption and emission spectra of C_{60}, CdSe, and CdSe-nC_{60} cluster films cast on a conducting glass electrode. The absorption of CdSe exhibits the characteristic excitonic peak at 563 nm; the nC_{60} clusters exhibit a broad absorption in the visible region. The absorption spectrum of CdSe-nC_{60} composite clusters reveals an additive effect, with photoresponse at wavelengths of less than 600 nm along with an excitonic peak at 552 nm. The emission spectrum (**Fig. 1-38c**) exhibits the characteristic emission band of CdSe QDs with a maximum at 580 nm. More than 95% of the CdSe emission is quenched because the excited CdSe QDs interact with nC_{60} in the cluster, similar to the role of ZnO NCs in their application to solar cells (**Fig. 1-30d**). Although both energy and electron transfer mechanisms can dictate the luminescence quenching, the electron accepting properties of C_{60} favor the electron transfer pathway. **Figure 1-38d** displays the reproducibility and stability of the photocurrent response of these films. The Na_2S electrolyte scavenges the holes from CdSe, thus enabling the regeneration of the CdSe in the film. The CdSe-nC_{60} composite clusters exhibit an incident-photon-to-photocurrent generation efficiency (IPCE) of ~4%, significantly greater than those of CdSe or nC_{60} films. The IPCE response of CdSe-nC_{60} is not a simple additive effect arising from individual components, but reflects the synergy arising from the excited interaction between CdSe and nC_{60}. **Figure 1-38e** illustrates the photoinduced electron transfer between CdSe and C_{60} followed by electron transport through the C_{60} network to the collecting surface of the OTE, which had previously been coated with SnO_2 NPs. Because the conduction band of SnO_2 is at 0 V vs NHE, it facilitates the capture of electrons from C_{60} quite efficiently.

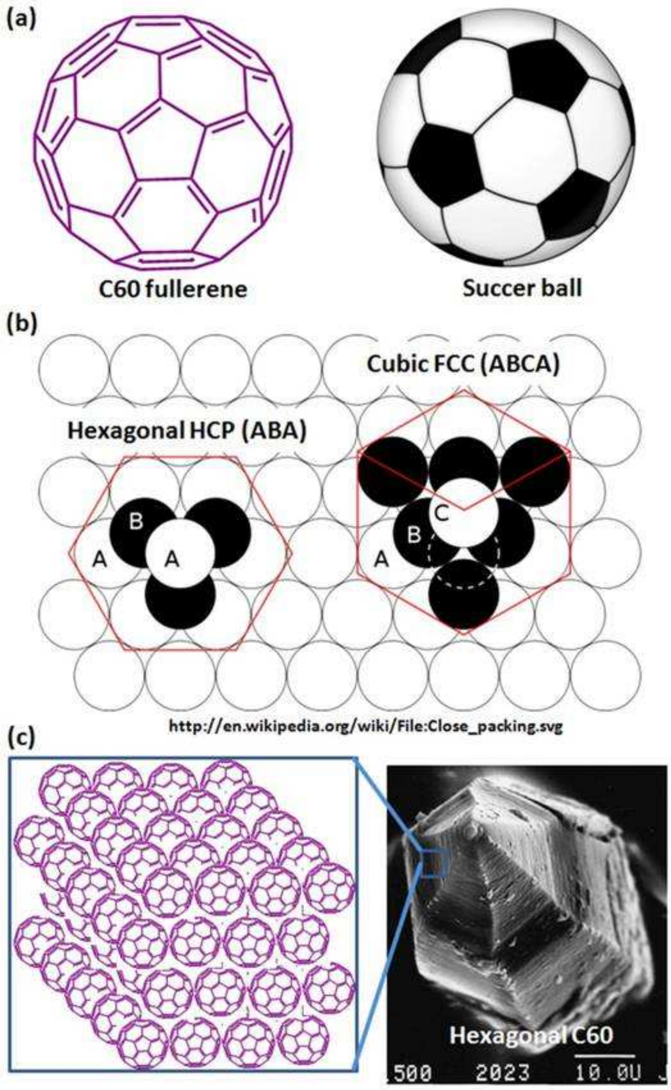

http://en.wikipedia.org/wiki/File:Close_packing.svg

Figure 1-36. (a) Comparison of the shapes of C_{60} and a soccer ball. (b) Closed packing of hard spheres, including HCP and FCC. (c) Hexagonal needle featuring the HCP of C_{60} molecules.[92]

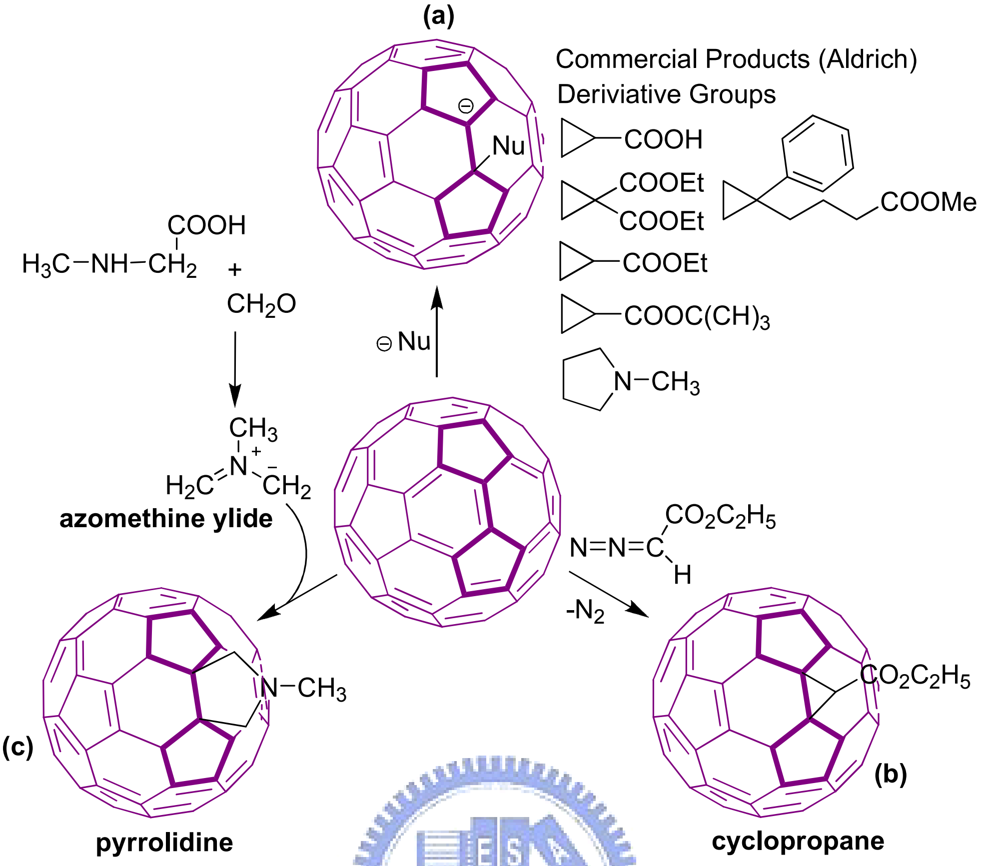

Figure 1-37. (a) Active site of cyclopentadienide monoadduct for nucleophilic attack. (b) Cyclopropane bridge formed from the reaction of C_{60} with a diazoalkanes. (c) Pyrrolidine bridge formed from the reaction of C_{60} with *N*-methylglycine.[93,95]

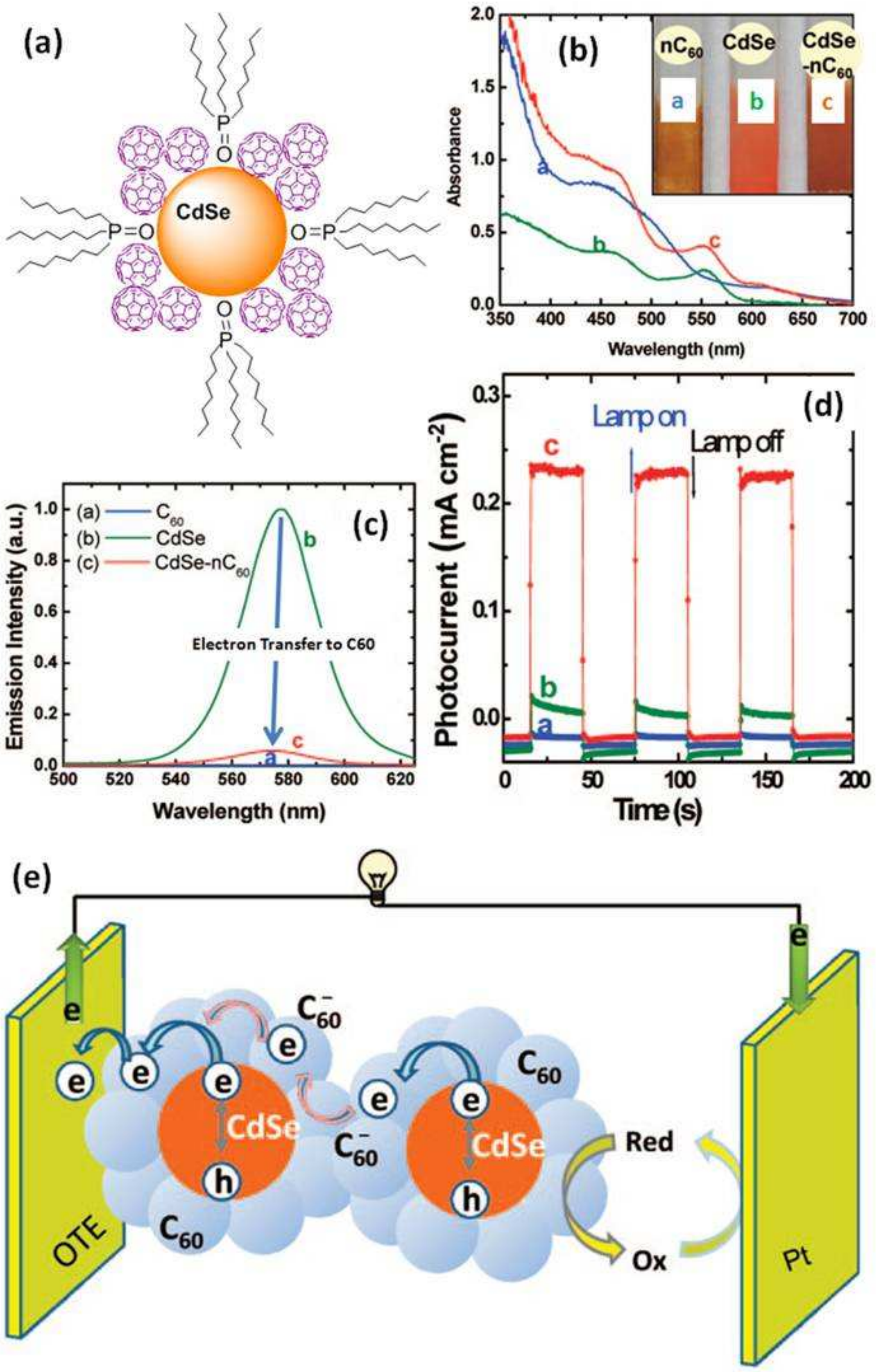

Figure 1-38. (a) Chemical structure of a CdSe-nC_{60} nanocomposite. (b) UV–Vis spectra, (c) PL spectra, and (d) the photocurrent response of electrodes to the ON-OFF cycles of illumination of C60, CdSe, and CdSe-nC_{60}. (e) Photocurrent generation at CdSe-nC_{60} composite clusters.[99]

Clay Cluster.

Montmorillonite, which has the chemical composition $(Na,Ca)_{0.33}(Al,Mg)_2(Si_4O_{10})(OH)_2 \cdot nH_2O$, is a very soft phyllosilicate mineral having the structure of a tetrahedral silicate group (SiO_4^{4-}) that typically forms in microscopic crystals, forming a clay. Montmorillonite, a member of the smectite family, is a 2:1 clay, meaning that it has two tetrahedral sheets sandwiching a central octahedral sheet (**Fig. 1-39a**). The particles are plate-shaped with an average diameter of ca. 1 μm and an average thickness of ca. 1 nm. Similar to other clays, montmorillonite swells upon the addition of water; notably, some montmorillonites expand considerably more than other clays as a result of water penetrating the interlayer molecular spaces and concomitant adsorption. The degree of expansion is due largely to the type of exchangeable cation contained in the sample. The presence of Na^+ as the predominant exchangeable cation can result in the clay (Na-montmorillonite) swelling to several times its original volume.

Clays are useful reinforcing materials because individual platelets are exposed through exfoliation; these platelets offer a large surface area for chemical bonding. The synthesis of a composite material through the addition of large amounts of clay to a polymer is problematic, however, because dispersion or aggregation effects lead to poor mechanical or optical properties. Haraguchi et al. used gel formation in an aqueous medium to create a composite of hydrophobic poly(2-methoxyethyl acrylate) and hydrophilic hectorite clay.[100] Hectorite is a soft, greasy clay mineral that forms near Hector, California (in San Bernardino County). The mineral is rare in that it is found primarily in one mine; its chemical composition is $Na_{0.4}Mg_{2.7}Li_{0.3}Si_4O_{10}(OH)_2$. Hectorite is mostly used in the manufacturing of cosmetics, but has uses in chemical and other industrial applications. During polymerization, the clay platelets become excluded from the polymer particles and instead formed a shell around them (**Fig. 1-39b**). Once dried, the clay shells comprised a 3D network, which Haraguchi et al. characterized structurally using TEM imaging (**Fig. 1-39d**). A surprising feature of the composites was their ability to undergo huge elongations when subjected to stress (e.g., ca. 1000 and 1900% expansions for 23 and 11 wt% clay-PEMA, respectively). After an initial irreversible necking deformation, subsequently applied large strains were reversible, with good shape recovery observed on release. The composites were also transparent (**Fig. 1-39c**), with greater than 90% light transmission, independent of clay concentration (up to 30 wt%). Unlike many clay composites, these materials did not reswell upon exposure to water, nor did they dissolve in organic solvents that could solubilize the pure polymer.

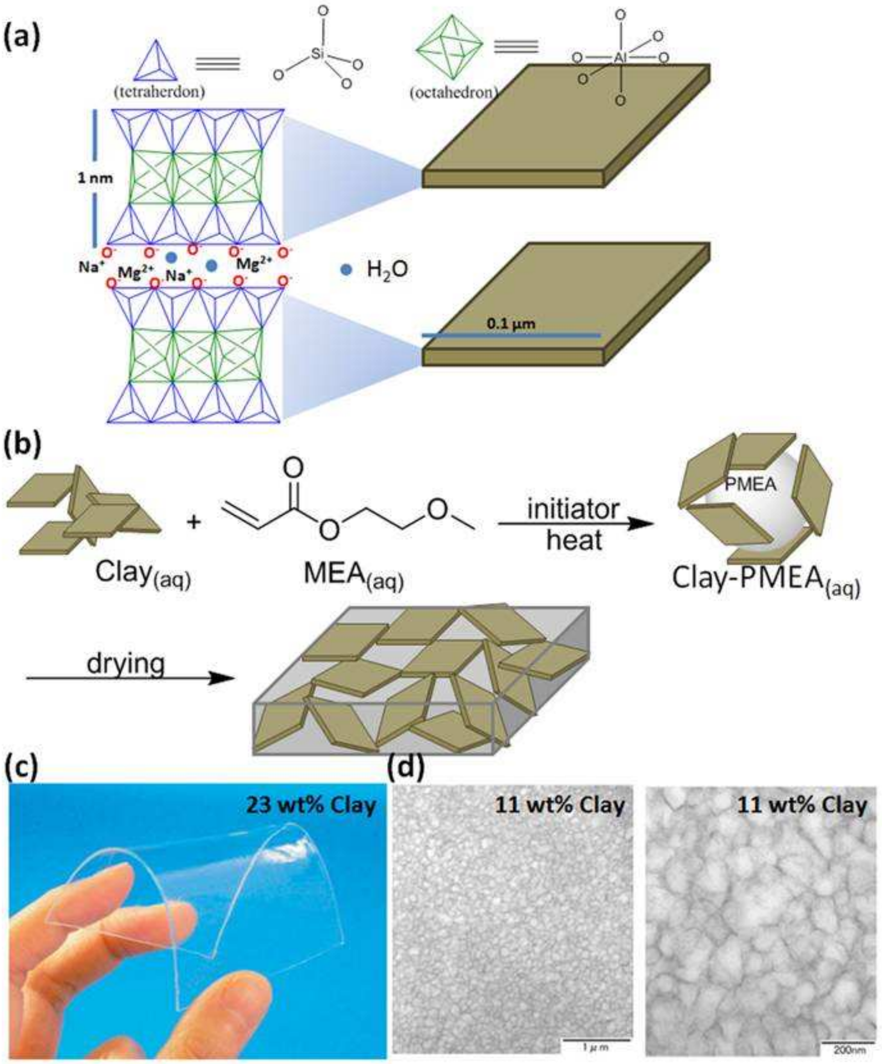

Figure 1-39. (a) Chemical structure of Montmorillonite clay. (b) synthesis of hectorite clay-PMEA. (c) Photograph of a transparent film containing 23 wt% clay. (d) TEM images of 11 wt% clay/PMEA nanocomposites.[100]

Silica Clusters (SiO_2 NPs)

Silicon dioxide (SiO_2), also known as silica (from the Latin *silex*), is an oxide of silicon that has been known for its hardness since antiquity. Silica is most commonly found in nature as sand and quartz, as well as in the cell walls of diatoms. It is a principal component of most types of glass and substances such as concrete. SiO_2 has a number of distinct crystalline and amorphous forms. With the exception of stishovite and fibrous silica, all of the crystalline forms feature tetrahedral SiO_4 units linked together through shared vertices in different arrangements. Nevertheless, the random connection of silicon and oxygen atoms results in amorphous SiO_2 in most cases.

In 1968, Stöber et al.[101] developed a method to synthesize colloidal silica microspheres (the so-called SFB method). The procedure consists in hydrolyzing a silicon alkoxide $Si(OR)_4$, with R being an alkyl group having the general formula C_mH_{2m+1}. Subsequently, the hydrolyzed species are condensed, forming siloxane groups (SiOSi). When reaction proceeds in a basic medium (pH 7–11), electrostatic repulsion causes monomer addition to already condensed species. This way, aggregation is avoided and non-soluble particles are obtained as opposed to a sol–gel. For common silica microspheres, the precursor alkoxide is usually tetraethyl orthosilicate (TEOS) and the hydrolyzing agent is doubly distilled water (DDW). Ammonia (NH_3) is used to catalyze the reaction and to obtain a basic medium. Finally, absolute ethanol is commonly the solvent in which the reaction occurs. The rate of hydrolysis is strongly related to quality and average diameter of the spherical particles (**Fig. 1-40a**). This rate is proportional to the ratio $[NH_3]^{0.9}:[H_2O]^{1.5}$ and is also temperature-dependent.[102] For this reason, to obtain particles of various diameters, the TEOS and NH_3 concentrations are usually kept constant while the concentration of H_2O is varied. Using this method, silica spheres having diameters ranging from 200 to 700 nm can be obtained with a narrow size distribution (ca. 3–4%).

Materials that present a 3D periodic modulation of the dielectric constant have attracted much attention from theorists and experimentalists over the last decade. These structures, known as photonic bandgap materials, have interesting technological applications in photonics and electronics[103] because of their photonic crystal properties in the near infrared–visible–ultraviolet (NIR–Vis–UV) region of the electromagnetic spectrum. With a periodic change in refraction index across the order structure between SiO_2 spheres and air gaps, light of a particular wavelength is absorbed to result in the complementary color (**Fig. 1-40b**). This challenge has prompted many research groups to prepare periodic dielectrics having a lattice parameter of less than 1 μm.[104] Recently, solid colloidal crystals made of submicrometer SiO_2 spheres packed in an FCC structure were found to display the properties of a photonic crystal.[105] The sample of photonic crystals was prepared using the method developed by Park and Xia.[106] The cell (**Fig. 1-40c**) used in the assembly of mesoscale particles was constructed from two glass substrates and a square frame of photoresist and tightened with binder clips. A small hole (diameter: ca. 3 mm) was generated in the top glass substrate by etching in an aqueous HF solution; a glass tube (diameter: ca. 6 mm) was attached to this hole using an epoxy adhesive. These devices can be easily tuned through the sphere diameter, covering the whole visible and NIR region of the spectrum. Between the as-grown samples and those treated at 1050 °C, there was a change of 111 nm in the characteristic wavelength, i.e., a change of 11% in the Bragg reflected wavelength. For samples made of spheres having diameters of less than 300 nm, the diffraction effects occur in the visible range. Thus, the 11% shift caused by the sintering process described here would lead to a color change that is readily observable by the naked eye. As an example, **Figure 1-40d** displays three photographs corresponding to one as-grown and two treated (sintered at 950 and 1050 °C, respectively) pieces of a sample made from spheres having diameters of 260 nm. These photographs were taken while illuminating the samples with white light at $\theta = 0°$ (normal incidence) and using an optical microscope operated in reflection mode; optical transmission spectra recorded at $\theta = 0°$ are also displayed. We observe that, depending on the extent of thermal treatment, different ranges of wavelengths are reflected. In this example, the reflected light shifted from 628 nm (as-grown sample) to 561 nm (sintered at 1050 °C). These results demonstrate that the optical properties of SiO_2 FCC colloidal photonic crystals can be easily and accurately controlled over a wide range by means of both the sphere size and extent of thermal treatment (**Fig. 1-40e**).

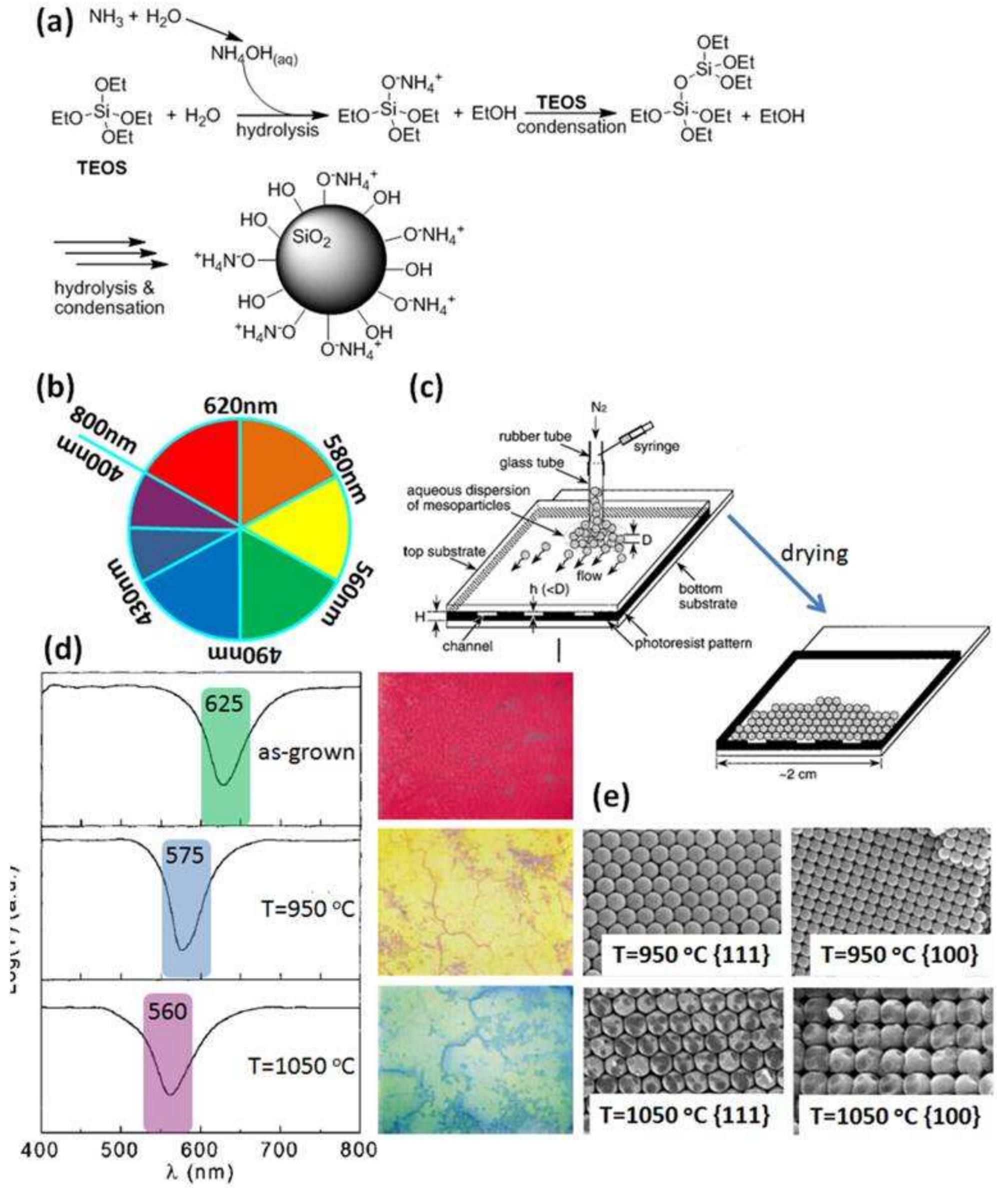

Figure 1-40. (a) Sol–gel preparation of SiO_2 inorganic NPs. (b) relationship between UV absorbance (wavelength) and complementary color and (c) formation of SiO_2 photonic crystals. (d) UV absorbance and optical color and (e) SEM images of SiO_2 photonic crystals.[105]

1-3.2 Organic Nanoparticles (Organic NPs)

In many organic macromers having molecular masses of up to 1000 g/mol, the compositional atoms can construct organic molecular NPs. In this section, we mention the cyclodextrins and dendrimers as examples. In addition, amphiphilic small molecules or macromolecules can also form the organic aggregate NPs having diameters of several nanometers.

Molecular Cyclodextrin.

Cyclodextrins (CDs, sometimes called cycloamyloses) are a family of cyclic oligosaccharides, composed of five or more α-D-glucopyranoside units linked 1→4, as in amylose (a fragment of starch). The most common CDs, the cone-shaped α-, β-, and γ-CDs, contain rings of six, seven, and eight α-D-glucopyranoside units, respectively (**Fig. 1-41a**). Cyclodextrins are non-reducing cyclic glucose oligosaccharides resulting from the cyclomaltodextrin glucanotransferase-catalyzed degradation of starch. Their structures have been reviewed.[107] The glucose residues have the $^4C_1$ (chair) conformation. The α-, β-, and γ-CDs have similar structures (i.e., bond lengths and orientations), apart from the structural necessities of accommodating a different number of glucose residues. They are bottomless bowl (truncated cone)-shaped molecules stiffened by hydrogen bonding between the C_3-OH and C_2-OH groups around the outer rim (**Fig. 1-41b**; hydrogen bond strengths: α-CD < β-CD < γ-CD). The flexible C_6-OH hydroxyl groups are also capable of forming linking hydrogen bonds around the bottom rim, but these interactions are destabilized by dipolar effects (i.e., easily dissociated in aqueous solution and not normally found in CD crystals). The mode of hydrogen bonding is all C_3-OH (donor) and C_2-OH (acceptor) in α-CD, but flips between this and all C_3-OH (acceptor) and C_2-OH (donor) in the β- and γ-CD.[107] The cavities have different diameters depending on the number of glucose units (empty diameters between the anomeric oxygen atoms are given in **Fig. 1-41**). The side rim depth is the same for all three CDs (ca. 0.8 nm). Cyclodextrin rings are amphiphilic with the wider rim displaying the C_2- and C_3-OH groups and the narrower rim displaying the C_6-OH groups on flexible arms. All of these hydrophilic groups exist on the outside of the molecular cavity; in contrast, the inner surface is hydrophobic, lined with the ether-like anomeric oxygen atoms and the C_3-H and C_5-H hydrogen atoms. In aqueous solution, this hydrophobic cavity contains approximately three (α-DC), seven (β-DC), or nine (γ-DC) poorly held (but low-entropy) and readily displaceable water molecules. This water in the cavities has low density (i.e., the cavities are sufficiently large to accommodate several more molecules). Thus, the otherwise hydrophilic CD molecules bind suitably sized nonpolar aliphatic and aromatic compounds, such as aroma compounds and lipophilic drugs, in 1:1, 2:1, and 1:2 stoichiometries, depending on the molecules involved (e.g., two molecules of γ-CD bind well to a single molecule of C_{60}).[108] The binding is driven by the enthalpic and entropic gains: the reduction of free energy at the hydrophobic–aqueous interface and the release of water molecules from the cavity to the bulk phase. Such binding also allows CDs to be used to increase the water solubility of normally hydrophobic compounds or to minimize undesirable properties, such as odor or taste, in certain food additives. Cyclodextrin complexes are now widely used in the pharmaceutical, food, cosmetics, and toiletry fields. γ-Cyclodextrin is most flexible and easily hydrolyzed by α-amylases, whereas α-CD is most rigid and is hydrolyzed only very poorly. The CDs, by themselves, are natural, non-toxic additives. The OH groups may be derivatized to modify the specificity and other physical and chemical properties of the CDs. The C_6-OH groups are most easily derivatized. The low solubility of β-CD, relative compared to those of the α- and γ-CDs,[109] is similar to the poor solubility of scyllo-inositol; i.e., it appears to be the result of a stronger crystal structure (as with cellulose) arising from better-placed intramolecular hydrogen bonds, together with a similarly better fit with the structure of water and, consequently, a low entropy of hydration.

β-Cyclodextrin has been the starting molecule for most amphiphilic CDs made to date; mono- and per-substitution of one face are most convenient, i.e., modification of one or all of the C_6-OH groups or all of the C_2,C_3-OH groups (**Fig. 1-41c**).[110] Selective mono-functionalization of β-CD normally proceeds via the C_6-O-tosyl (OTs) derivative from which the azide and amine are accessible. Persubstitution of the primary C_6-OH face can be performed via the perhalide derivatives, which are amenable to nucleophilic reactions; per-C_6-O-*tert*-butyldimethylsilylation (OTBDMS) can be used for protection during modifications to the secondary-C_2,C_3-OH face. CDs form supramolecular inclusion complexes with small-molecule chromophore compounds that fit into their 0.5–0.8-nm-diameter cavities;[111] in this way, the fluorescence intensity, biocompatibility, and photostability of the guest chromophore compounds can be enhanced. For example, Wu et al. synthesized a photosensitive cyclodextrin (CDSP) by covalently attaching spiropyran moieties onto β-CD. Rhodamine B (RhB) was used as a model fluorophore to form a supramolecular complex with the CDSP to realize photoreversible fluorescence modulation (**Fig. 1-42a**).[112] The guest RhB molecules are readily replaced by other chromophore compounds. In addition, the self-quenching of RhB can be decreased through supramolecular complexation (e.g., sample II in **Fig. 1-42b**). The strategy provides a facile means of reversible fluorescence modulation, controlled by light, for a wide range of chromophores—an essential process for applications such as reversible bioimaging (**Fig. 1-42b**). At the same time, the chromophore complexes have the necessary biocompatibility and hydrophilicity for applications in the field of biotechnology because of the presence of the oligosaccharide CD.

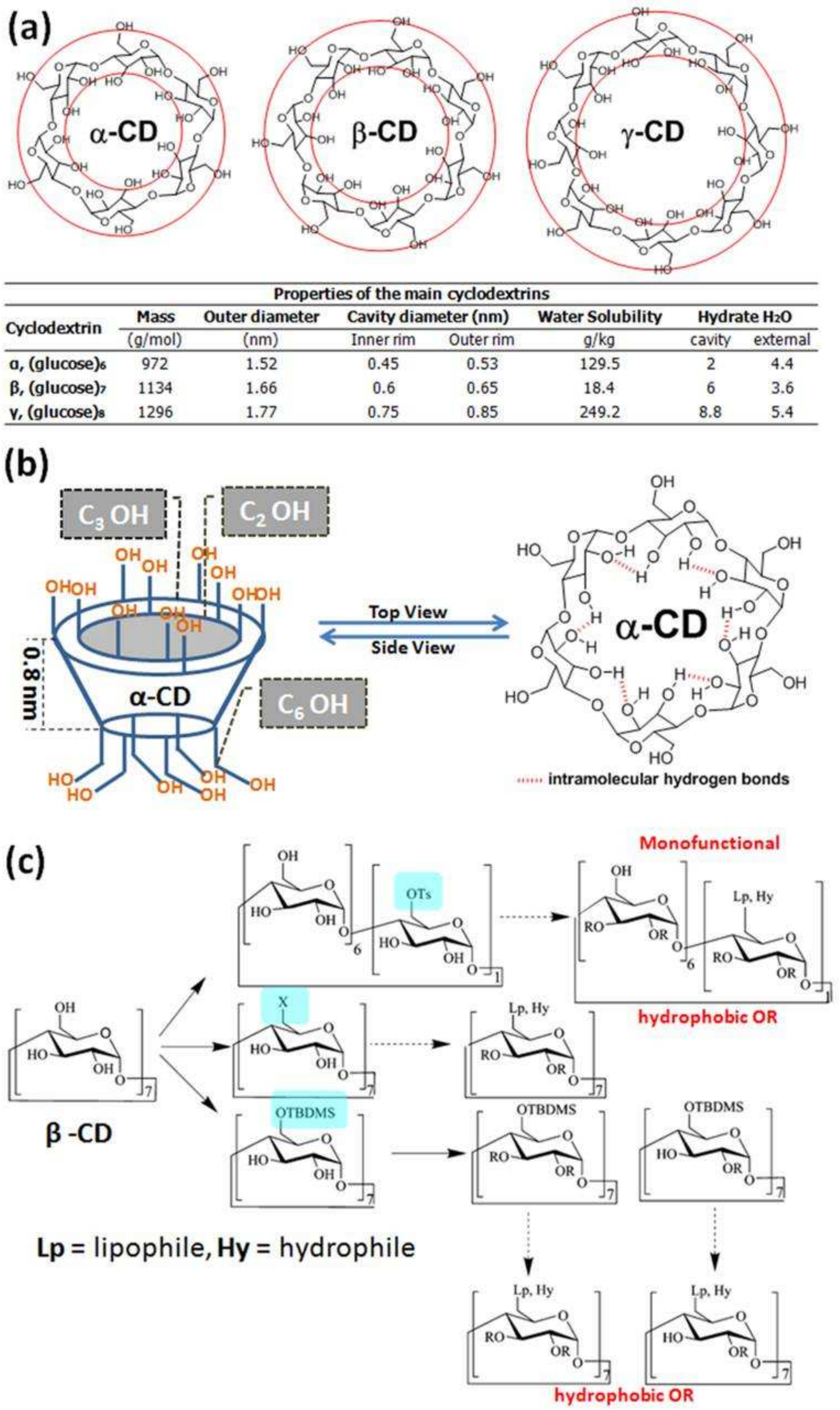

Properties of the main cyclodextrins

Cyclodextrin	Mass (g/mol)	Outer diameter (nm)	Cavity diameter (nm) Inner rim	Cavity diameter (nm) Outer rim	Water Solubility g/kg	Hydrate H2O cavity	Hydrate H2O external
α, (glucose)6	972	1.52	0.45	0.53	129.5	2	4.4
β, (glucose)7	1134	1.66	0.6	0.65	18.4	6	3.6
γ, (glucose)8	1296	1.77	0.75	0.85	249.2	8.8	5.4

Figure 1-41. (a) Chemical structures and properties of α-, β-, and γ-CD. (b) Top and side views of α-CD, highlighting the strong intramolecular hydrogen bond between C_2-OH and C_3-OH.[107] (c) Common synthetic paths to amphiphilic β-CD.[110]

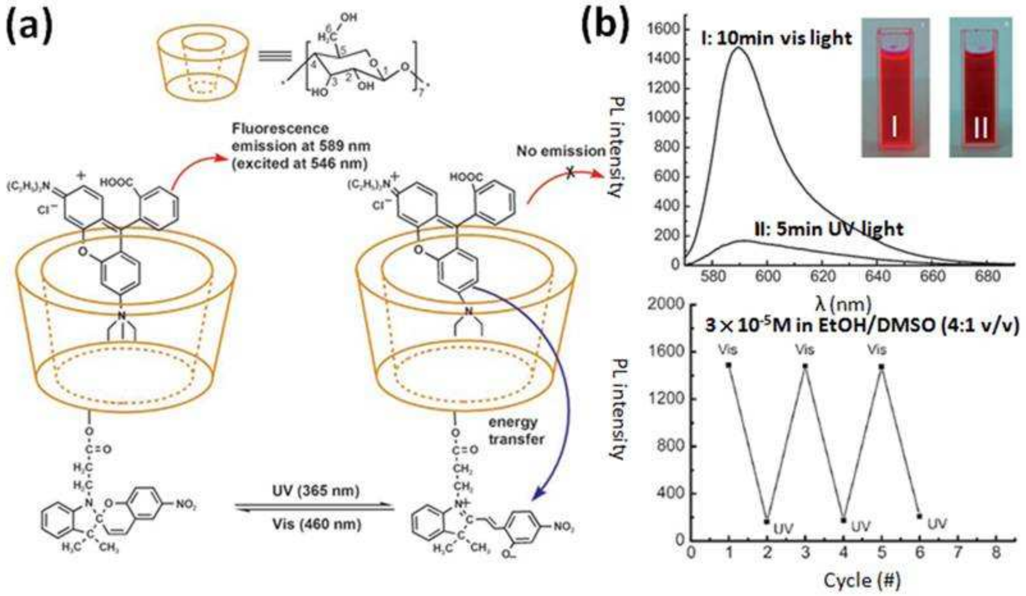

Figure 1-42. (a) Supramolecular complex formed from photosensitive β-CD and RhB and their photoreversible fluorescence modulation. (b) PL spectra (λ_{ex} = 546 nm) of complex under (I) visible light for 10 min and (II) UV light (λ = 365 nm) for 5 min, and the recycling test.[112]

Molecular Dendrimer.

The huge number of papers describing dendritic architectures, such as spherical dendrimers (**Fig. 1-43a**) and cone-shaped dendronized (**Fig. 1-43b**), hyperbranched, and brush polymers, has generated a vast array of inconsistent terms and definitions, which makes it difficult to provide a clear and concise summary of the topic. Dendrimers are repeatedly branched molecules that are characterized by their structural perfection in terms of both symmetry and polydispersity. Dendritic molecules can be roughly divided into the low-molecular weight and the high-molecular weight species. The first category includes dendrimers and dendrons; the second encompasses dendronized polymers, hyperbranched polymers, and brush polymers (also called bottle-brushes).

The properties of dendrimers are dominated by the nature of the functional groups on the molecular surface. Dendritic encapsulation of functional molecules mimics the structures of the active sites in biomaterials; i.e., dendritic scaffolds exhibit separate internal and external functions.[113] For example, it is possible to design a water-soluble dendrimer possessing hydrophilic end groups (e.g., carboxyl groups) that features internal hydrophobicity; such systems can carry hydrophobic drugs in their interior voids. Redox-active NPs have recently been synthesized using redox molecules placed between the NP core and the dendritic wedges; despite their isolation, some of the redox molecules (COOH in this case) remained uncoupled and, thus, remained reactive. Another property of dendrimers is that their volume increases when they gain positive charges. If this property could be harnessed, dendrimers could be used as drug delivery systems (DDS) that can provide medication to an affected part inside a patient's body directly. Lang et al. reported the successful preparation of supported Pt NCs using dendrimer-encapsulated Pt NCs as metal precursors.[114] Polyamidoamine (PAMAM) dendrimers were first used to templates and to stabilize the Pt NCs prepared in solution. These dendrimer-encapsulated NPs were then deposited onto a commercial high-surface-area silica support and thermally activated to remove the organic dendrimer. The resulting materials were active oxidation and hydrogenation catalysts. **Figure 1-4ab** presents the effects of the catalyst preparation and activation processes on the activity of the catalysts toward the hydrogenation of toluene and the oxidation of CO. Silica-supported samples were prepared using a conventional method (Pt/SiO_2; via insipient wetness impregnation of H_2PtCl_6 onto the same silica support) and through dendrimer-encapsulated NPs at Pt-to-dendrimer ratios of 100:1 (Pt_{100}/SiO_2) and 50:1 (Pt_{50}/SiO_2). The performance of the CO oxidation catalyst highlights the potential advantages of using the dendrimer route. Pt_{100}/SiO_2 exhibited slightly higher activity (**Fig. 1-44b**) than that of the conventional catalyst Pt/SiO_2, presumably because of the higher dispersion of Pt_{100}/SiO_2. Once the total activity is corrected for the number of available Pt atoms (Pt_{50}/SiO_2 and Pt_{100}/SiO_2), however, there are no significant differences in the values of the 60 °C CO oxidation TOFs (i.e., 1.3, 1.3, and 1.4 s^{-1} for Pt/SiO_2, Pt_{50}/SiO_2, and Pt_{100}/SiO_2). This result demonstrates that dendrimer-deposited nanocrystals are appropriate models for traditionally prepared catalysts (H_2PtCl_6) and indicates that the small amount of chlorine left on the Pt/SiO_2 catalyst does not substantially affect CO oxidation catalysis. Pt_{50}/SiO_2 was more active for CO oxidation than were the other two catalysts. At all of the temperatures studied, the values of the TOFs for the reactions catalyzed by Pt_{50}/SiO_2 were two to three times greater than those for Pt_{100}/SiO_2 and Pt/SiO_2.

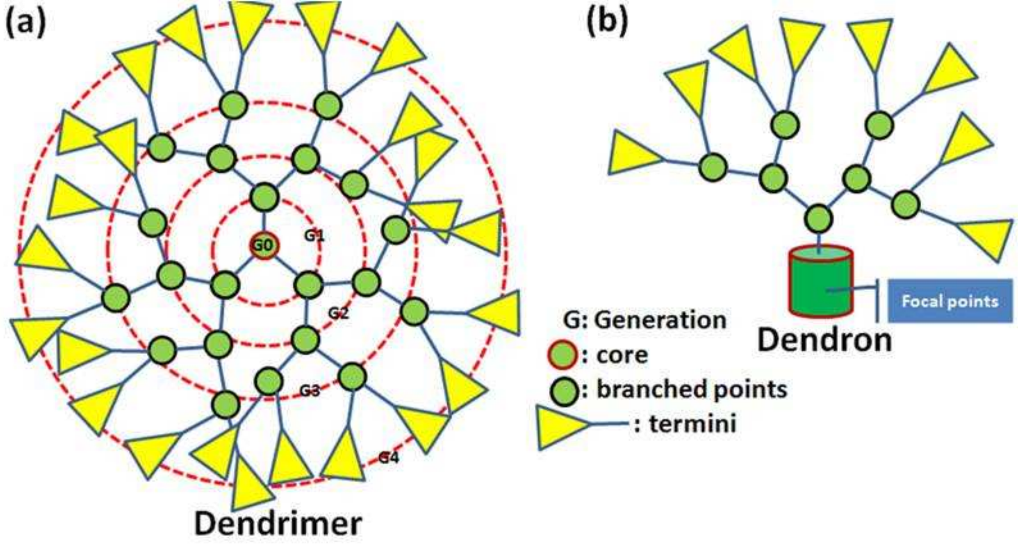

Figure 1-43. Schematic representation of (a) a spherical dendrimer and (b) a cone-shaped dendron.

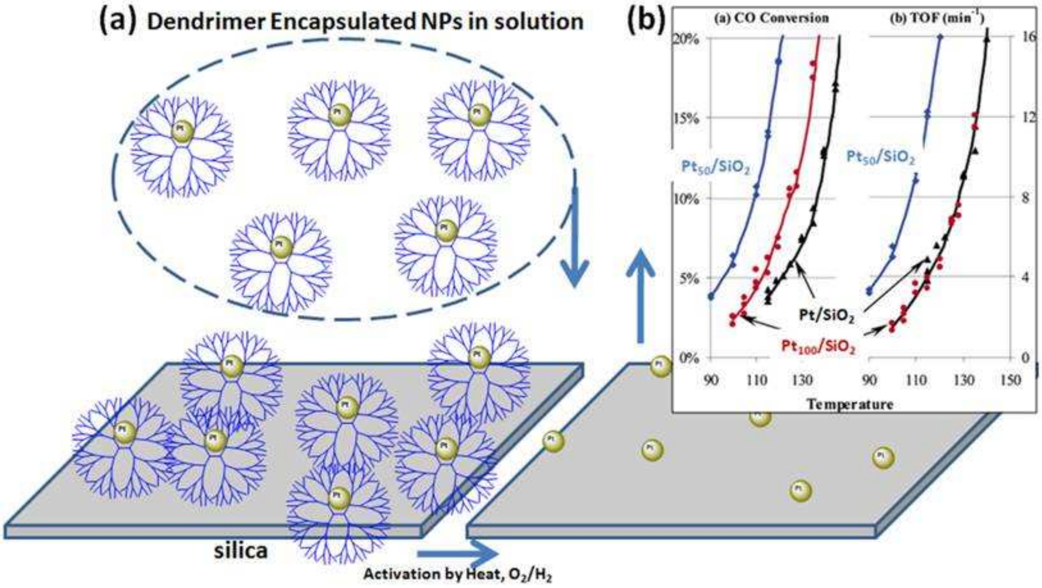

Figure 1-44. (a) Schematic representation of the preparation of dendrimer-derived supported Pt NCs catalysts. (b) Performance of CO oxidation catalysts after oxidation at 300 °C (20% O_2/He, 4 h) and reduction at 300 °C (20% H_2/He, 2 h).[114]

Amphiphilic Small molecules Aggregates

Some small molecules (surfactants) are composed of polar groups (heads) and nonpolar chains (tails). In polar solvents, they tend to form the micelles with polar groups surrounding on the surface of nonpolar microdomains. Only when the amphiphile possesses hydrophobic chains in a fluid state (neither crystalline nor chiral compounds) is the following structural guideline for self-assembly applicable for predicting an aggregate morphology. Israelachivili proposed an optimal surface area per polar head group, which depends on the packing parameter, $p = V/(a_0 l_c)$, where v is the volume of the hydrophobic chain, a_0 is the polar head surface area at the critical micellar concentration (cmc), and l_c is the chain length (**Fig. 1-45**).[115] For $p < 1/3$, the amphiphilic small molecules have a tendency to aggregate into spherical micelles; for $1/3 < p < 1/2$, cylindrical micelles will be favored; for $1/2 < p < 1$, bilayers displaying a spontaneous curvature (vesicles) are produced; for $p =$ ca. 1, planar bilayers are favored; and for $p > 1$, micellar aggregates with a reverse curvature will be formed.[116] For example, Yamaguchi et al. reported a novel method to form a hybrid membrane (porous SiO_2/AAO) composed of silica-surfactant nanocomposites and a porous alumina membrane (AAO), with which size-selective transport of molecules across the membrane becomes possible.[117] Nanoporous silica having diameters of less than 10 nm are frequently observed when using amphiphilic small molecules as removable agents; in contrast, the corresponding bulk materials become brittle upon increasing their porosity. Thus, Yamaguchi et al. used a 200-nm-diameter AAO membrane (**Fig. 1-46a**) as a support for porous SiO_2. When they introduced a precursor solution, containing cetyltrimethylammonium bromide (CTAB) surfactant and TEOS as the silica source, into the alumina pores, the porous SiO_2/AAO nanocomposite assembled at the pore walls to form surfactant-templated silica nanochannels, the direction of which was oriented predominantly along the columnar alumina pores. As a result, the alumina membrane including the silica–surfactant nanocomposite was capable of performing nanometer-scale size-exclusive separation of molecules.

The local structure of this porous SiO_2/AAO nanocomposite was investigated using TEM imaging. **Figure 1-46b** reveals that all of the alumina pores were filled with the porous SiO_2/AAO nanocomposite. At the alumina wall, a few layers of ordered structures of silica mesopores were observed, with the structural order slightly distorted in the interior region. In the region featuring the ordered mesopore structure, the pore-to-pore distance was ca. 5 nm. Considering the wall thickness of ca. 1 nm in the surfactant-templated mesoporous silica materials,[118-120] this value suggests a pore diameter of ca. 3 nm, which agrees with the values estimated from N_2 adsorption/desorption isotherms. The side-view TEM image of the porous alumina membrane incorporating the silica–surfactant nanocomposite reveals mesoporous silica nanochannels running predominantly parallel to the wall of the columnar alumina pores (**Fig. 1-46b**). Molecular transport across the membrane was examined (**Fig. 1-46c**) using a series of molecules of various molecular sizes that are usually employed to evaluate the molecular-weight cutoffs and pore sizes of ultrafiltration membranes. In the absence of the silica–surfactant nanocomposite in the alumina membrane, all of the molecules were transported through the 200-nm-diameter AAO membrane (**Fig. 1-46c**). In contrast, the alumina membrane incorporating the porous SiO_2/AAO nanocomposite displayed selective size-dependent molecular transport: relatively small molecules, such as rhodamine B (molecular size: ca. 1.0 nm) and vitamin B12 (ca. 2.4 nm), were transported, but large molecules, such as myoglobin (ca. 4.0 nm) and bovine serum albumin (ca. 7.2 nm), were not (**Fig. 1-46c**). Transport through the membrane was completely absent for molecules having sizes larger than the channel diameter (3.4 ± 0.2 nm). These experimental results suggest that large molecules could not permeate the porous surfactant-templated silica nanochannels within the columnar alumina pores, allowing them to function as a nanometer-scale size-exclusion system as a result of the channel diameter.

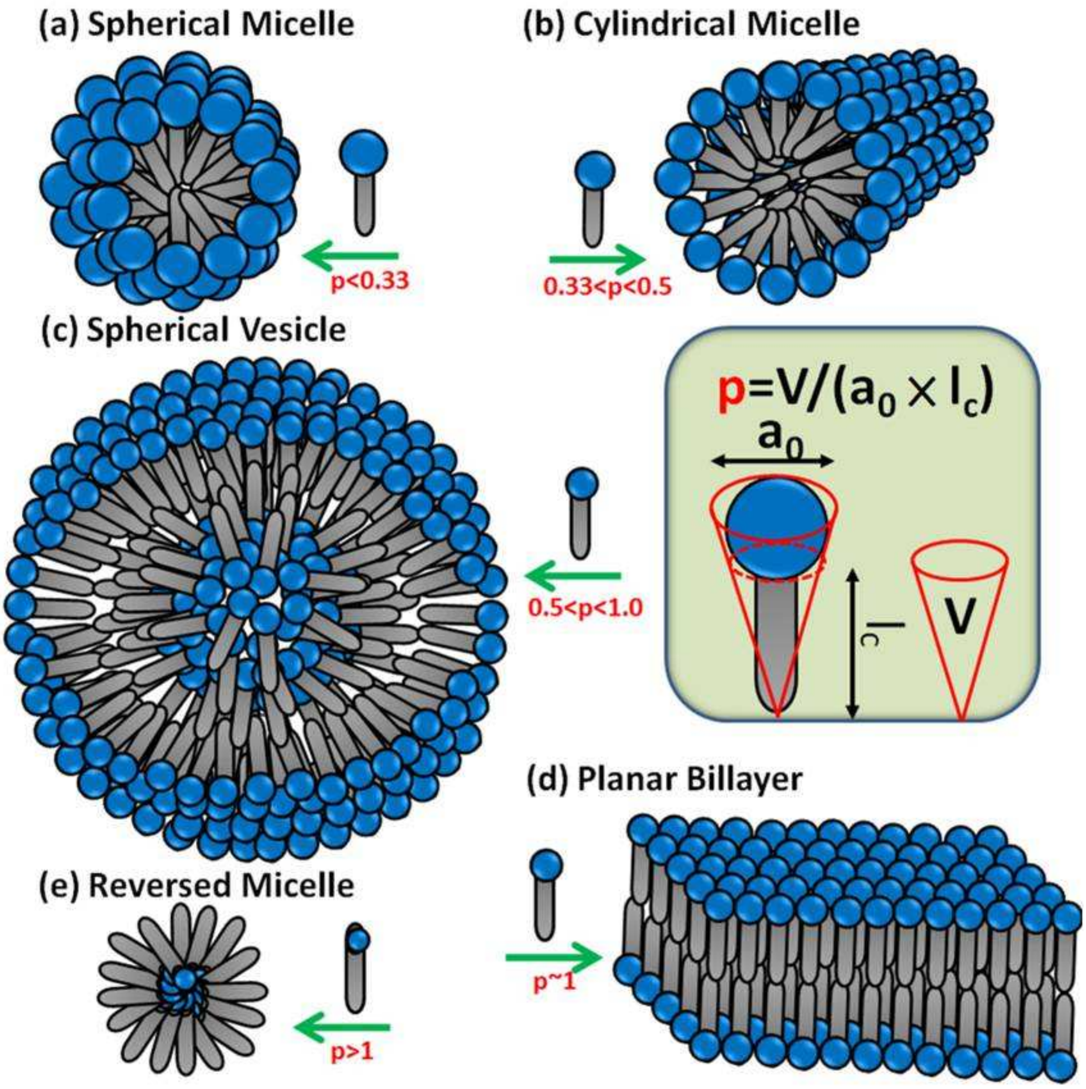

Figure 1-45. Various self-assembled morphologies depending on the critical packing parameter (p) of the amphiphilic small molecule: (a) spherical micelles ($p < 0.33$), (b) cylindrical micelles ($0.33 < p < 0.5$), (c) spherical vesicles ($0.5 < p < 1$), (d) planar bilayers (p = ca. 1), and (e) reversed micelles ($p > 1$).[115]

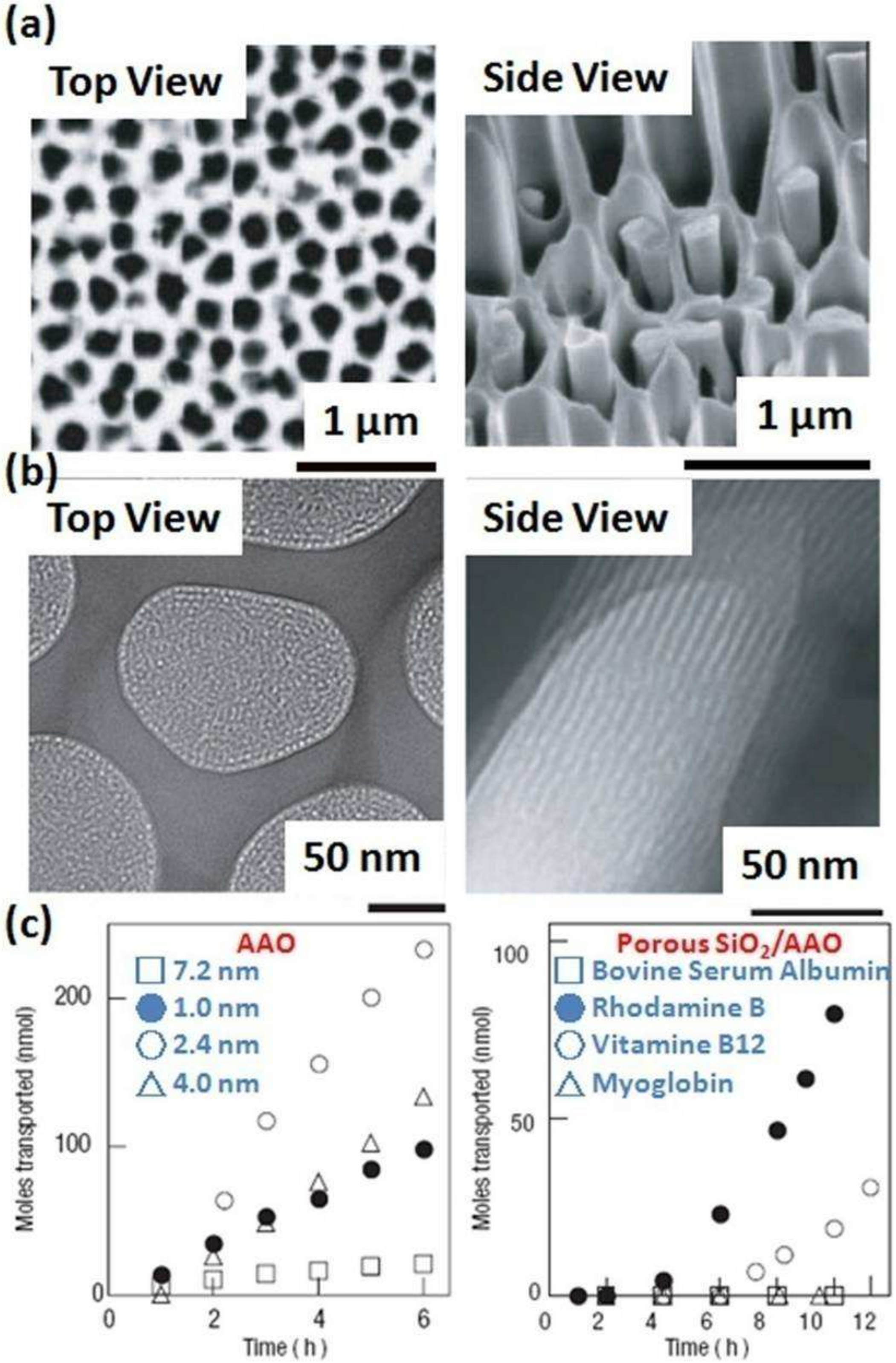

Figure 1-46. (a) SEM images of an alumina oxide (AAO) membrane (white height). (b) TEM images of porous SiO_2 in the AAO membrane (white cave), (c) Mass transport of bovine serum albumin, rhodamine B, vitamin B12, and myoglobin through the AAO and porous SiO_2/AOO composite membranes.[117]

Amphiphilic Block Copolymers Aggregates

A copolymer is a polymer (a string of covalently bonded monomeric species) derived from two (or more) monomeric species, as opposed to a homopolymer, in which only one monomer is used. Block copolymers consist of two or more linear homopolymers of different chemical compositions, joined end-to-end (**Fig. 1-47a**). Amphiphilic block copolymers play a role similar to that of amphiphilic small molecules in aggregate organic NPs, wherein only one block can be dissolved in the selective solvent (**Fig. 1-47b**). After thermal annealing, the two blocks can separate thermodynamically into ordered microstructures exhibiting phase separation in the condensed phase (**Fig. 1-47c**). The thermodynamic properties of block copolymers are discussed in detail later. Herein, we treat amphiphilic block copolymers as amphiphilic small molecules. In general, different micellar morphologies are observed in TEM images depending on the relative block lengths, playing roles similar to the parameters a_0 and l_c of the critical packing parameter (p) in **Fig. 1-45**.[121,122] **Figure 1-48** displays typical examples of these structures, including spheres, rods, lamellae, vesicles, and large compound micelles, the latter featuring reverse micelle-like aggregates contained in up to micrometer-size spheres featuring hydrophilic surfaces. Jeong et al. prepared a PEO-PLLA-PEO triblock copolymer by forming a urethane linkage through the reaction of hexamethyl diisocyanate (HMDI) and the hydroxyl groups on PLLA-b-PEO diblock copolymers (**Fig. 1-49a**).[123] Biodegradable polymers used for drug delivery to date have mostly been prepared in the form of injectable microspheres or implant systems, which require complicated fabrication processes and organic solvents.[124] Aqueous solutions of these PEO-PLLA-PEO triblock copolymers exhibit temperature-dependent reversible gel–sol transitions. The hydrogel can be loaded with bioactive molecules in an aqueous phase at an elevated temperature (ca. 45 °C), where they form a sol (**Fig.**

1-49b). In this form, the polymer is injectable. On subcutaneous injection and subsequent rapid cooling to body temperature, the loaded copolymer forms a gel that can act as a sustained-release matrix for drugs (**Fig. 1-49c**). The system is designed mainly for delivery of high molecular mass (Mn) protein drugs that have a low diffusion coefficients. An in vitro release study was conducted using a fluorescein isothiocyanate (FITC)-labeled dextran (Mn 20,000) as a model drug. The system can also be used for the sustained release of low-Mr hydrophobic drugs. The sol–gel transition temperature is affected by the presence of a drug. These polymers and the bioactive agents are dissolved in water at a temperature (45 °C) above body temperature. The FITC-labeled dextran was mixed with the polymer solution at 45 °C, followed by lowering the temperature to 37 °C. Afterwards, the solutes released from the formed gel were monitored using fluorescence spectroscopy. **Figure 1-49c** displays the release of the FITC-labeled dextran from the gel as a function of time. The release rate can be controlled in terms of the initial loading, the values of Mr and the hydrophobicity of the drug, and the concentration of polymer; for example, upon increasing the polymer concentration, the release rate decreased (**Fig. 1-49c**). As dextran is highly water soluble; at day 12, 70% was released from the 23 wt% gel and 40% from the 35 wt% gel. These numbers suggest that the release of a hydrophobic drug or protein drug from the gel will occur over a period of one month.

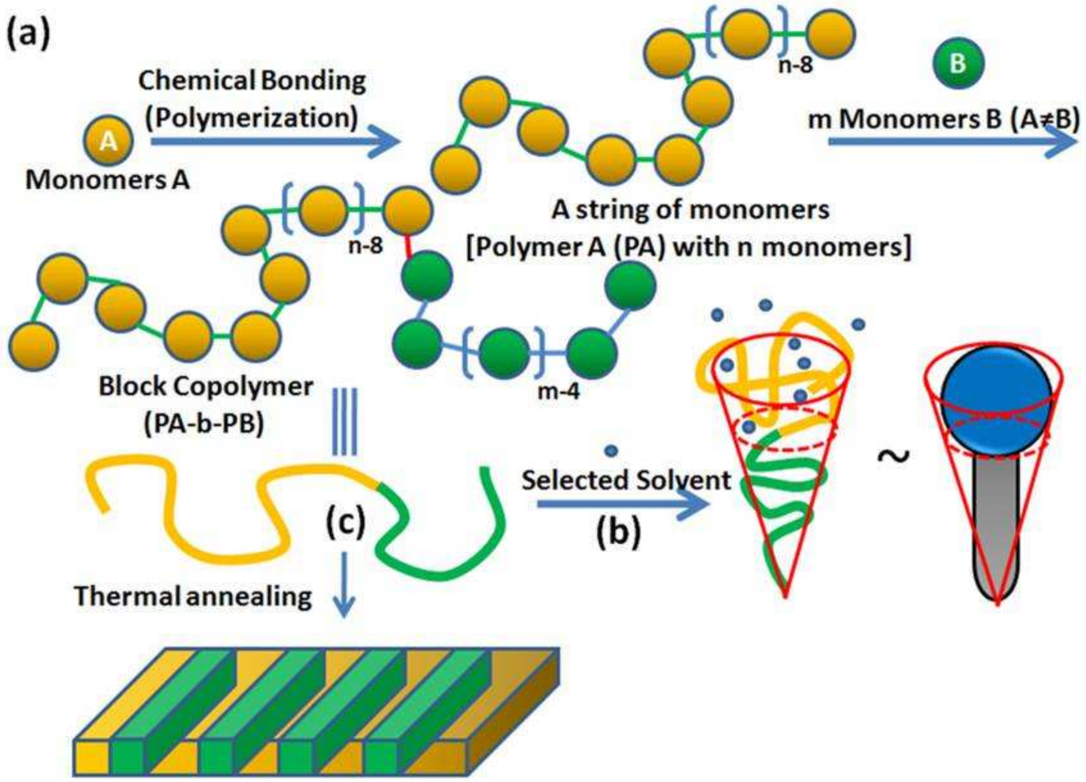

Figure 1-47. (a) Polymerization of a homopolymer PA and a block copolymer PA-*b*-PB. (b, c) Self-assembly of the block copolymer (b) in solution and (c) in the condensed phase.

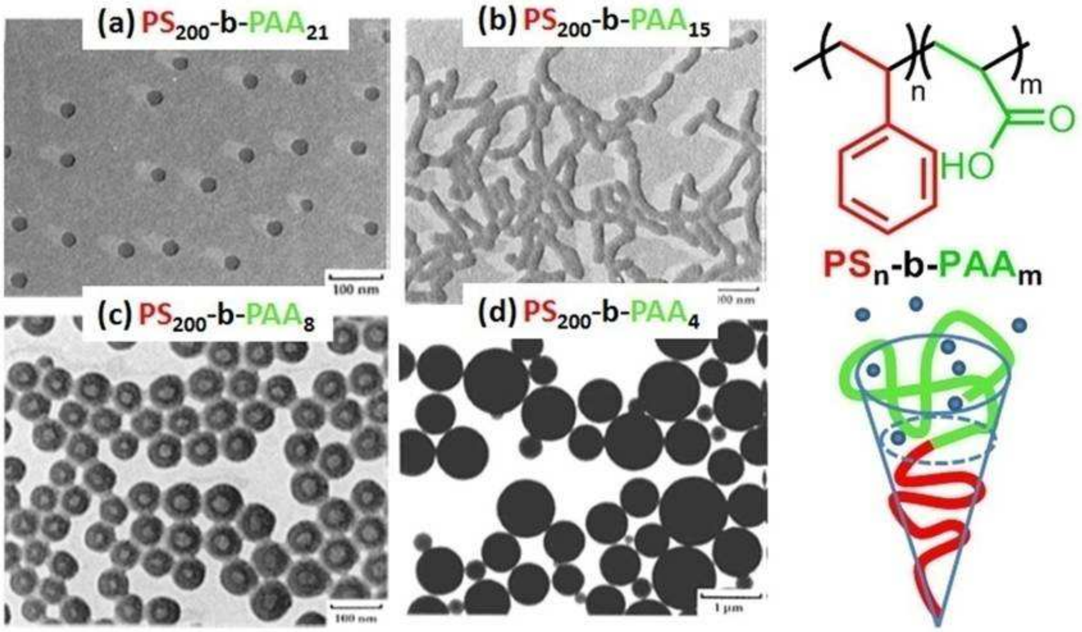

Figure 1-48. Multiple morphologies of the crew-cut aggregates formed in water from PS_n-*b*-PAA_m block copolymers (n > m) featuring PAA block lengths (m) of (a) 21, (b) 15, (c) 8, and (d) 4.[121]

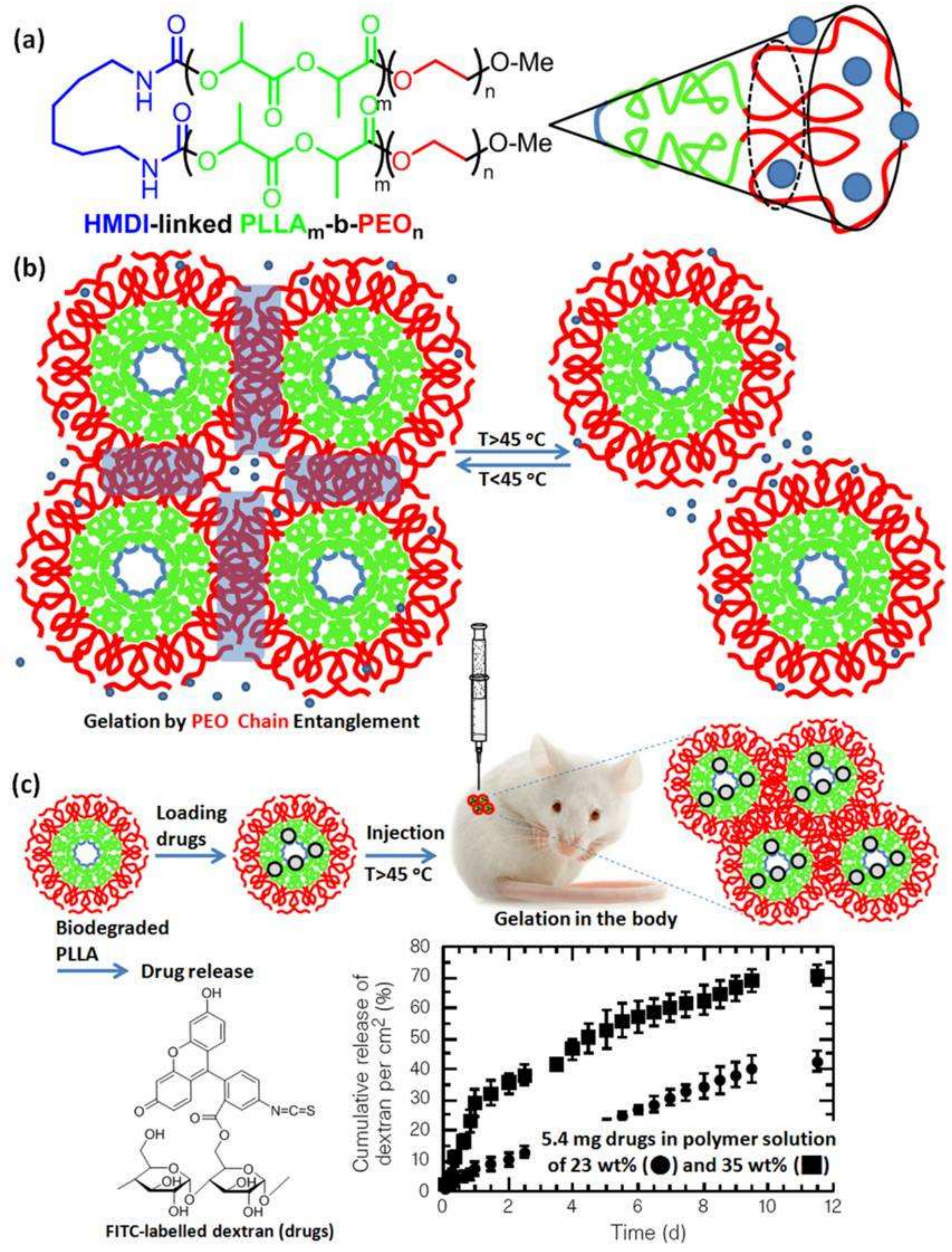

Figure 1-49. (a) Chemical structure and aggregate model of HMDI-linked PLLA-*b*-PEO. (b) Reversible sol–gel transitions at temperatures higher and lower than 45 °C. (c) Results of a drug delivery test using an FITC-labeled dextran.[123]

1-3.3 Inorganic/Organic Hybrid NPs

As mentioned above, many organic stabilizers are needed to disperse NCs and inorganic NPs in organic solvents via physical and chemical absorption on their surface. Although such inorganic and organic complex compounds could be also regarded as inorganic/organic hybrid NPs, we suggest that molecules composed of organic and inorganic atoms or aggregates of organic NPs and other inorganic nanomaterials are more suitable for the name "inorganic/organic hybrid NPs."

Molecular Polyhedral Oligomeric Silsesquioxanes (POSS)

Silsesquioxanes are products of sol–gel reactions between monofunctional trichloro- and trialkoxyl-silanes nanostructures; they have the chemical structure $(RSiO_{1.5})_n$, where R is a hydrogen atom or an organic functional group, such as an alkyl, alkylene, acrylate, hydroxyl, or epoxide unit, and n is the number of repeating units. **Figure 1-50** indicates that silsesquioxanes may be formed in random, ladder, cage, and partial-cage structures.[125] The siloxane plane having the chemical structure $Si_4O_4R_4(OH)_4$ is the building block in the ladder polysilsesquioxanes and the cage-type polyhedral oligomeric silsesquioxane (POSS) derivatives. Interestingly, POSS molecules can be regarded as cyclic polysilsesquioxane oligomers; for example, the combination of four, five, and six siloxane planes gives T8, T10, and T12 POSS derivatives (T = number of $RSiO_{1.5}$ units; **Fig. 1-50b,c**). Schmid et al. prepared the incomplete T7-POSS through a sol–gel reaction in a water/acetone mixture (**Fig. 1-51a**).[126] This incomplete T7-POSS structure can be used as a precursor for the synthesis of various monofunctionalized T8-POSS derivatives, which have attracted a great deal of attention. The common products of cubic T8 POSS, composed of six identical siloxane planes, are easily obtained in the form of crystalline powders; e.g., the norbornyl cyclopentyl-POSS (**Fig. 1-51b,c**),[127] the 1.2-nm-diameter spheres of which can pack into ordered crystals exhibiting (101), (110), and (012) diffraction planes corresponding to *d*-spacings of 1.08, 0.8, and 0.73 nm, respectively. In addition to monofunctional POSS, octafunctional POSS can be also obtained through the direct sol–gel reactions or subsequent modification. As an example of the direct method, Tamaki et al. prepared octa(aminophenyl)silsesquioxane (OAPS) through the sol–gel reaction of phenyltrichlorosilane to give octaphenylsilsesquioxane (OPS), nitration with fuming nitric acid to give octa(nitrophenyl)silsesquioxane (ONPS), and reduction with formic acid, triethylamine, and a Pt catalyst (**Fig. 1-52**).[128] They then used OAPS to prepare a crosslinked POSS-based polyimide exhibiting high thermal stability (T_d > 500 °C for 5 wt% loss; char yield > 75%).[129] Another approach to generating functionalized cubic silsesquioxane macromonomers—one that offers access to nanocomposites—relies primarily on introducing functionality through hydrosilylation using $(HSiO1.5)_8$[130] or $(HMe_2SiOSiO_{1.5})_8$ nanoplatforms.[130-132] This approach has been employed successfully to introduce functional groups, including methacrylates,[133] mesogenic groups,[134] epoxies,[135,136] and alcohols,[137] to POSS derivatives. These hydrosilylated products are usually amorphous liquid glasses having glass transition temperatures below 25 °C. Our group has prepared three amorphous octafunctional POSS derivatives—octakis[dimethyl(phenethyl)siloxy]silsesquioxane (OS-POSS), octakis[dimethyl(4-acetoxyphenethyl)siloxy]silsesquioxane (OA-POSS), and octakis[dimethyl(4-hydroxyphenethyl)siloxy]silsesquioxane (OP-POSS)—through hydrosilylation of $(HMe_2SiOSiO_{1.5})_8$ with styrene and 4-acetoxystyrene and subsequent hydrazinolysis of the latter, respectively (**Fig. 1-53a**).[138] The DSC thermograms (**Fig. 1-53c**) of OS-POSS, OA-POSS, and OP-POSS reveal glass transition temperatures of –51.8, –14.2, and 18.7 °C, respectively; in addition, they display monodisperse molar mass distributions in their MALDI-TOF mass spectra

(**Fig. 1-53b**). The increase in the glass transition temperatures can be attributed to the increased strength of the intermolecular interactions; i.e., weak hydrophobic forces for OS-POSS, medium-strength dipole–dipole interactions for OA-POSS, and strong hydrogen bonds for OP-POSS. In comparison with monofunctional crystalline POSS derivatives, the presence of mixtures of isomeric linkages [β(-Si-CH_2-CH_2-R) and α(-Si-CH(CH_3)-R)] is responsible for the amorphous forms of the octafunctional POSS derivatives prepared through hydrosilylation and their liquid glass characteristics.

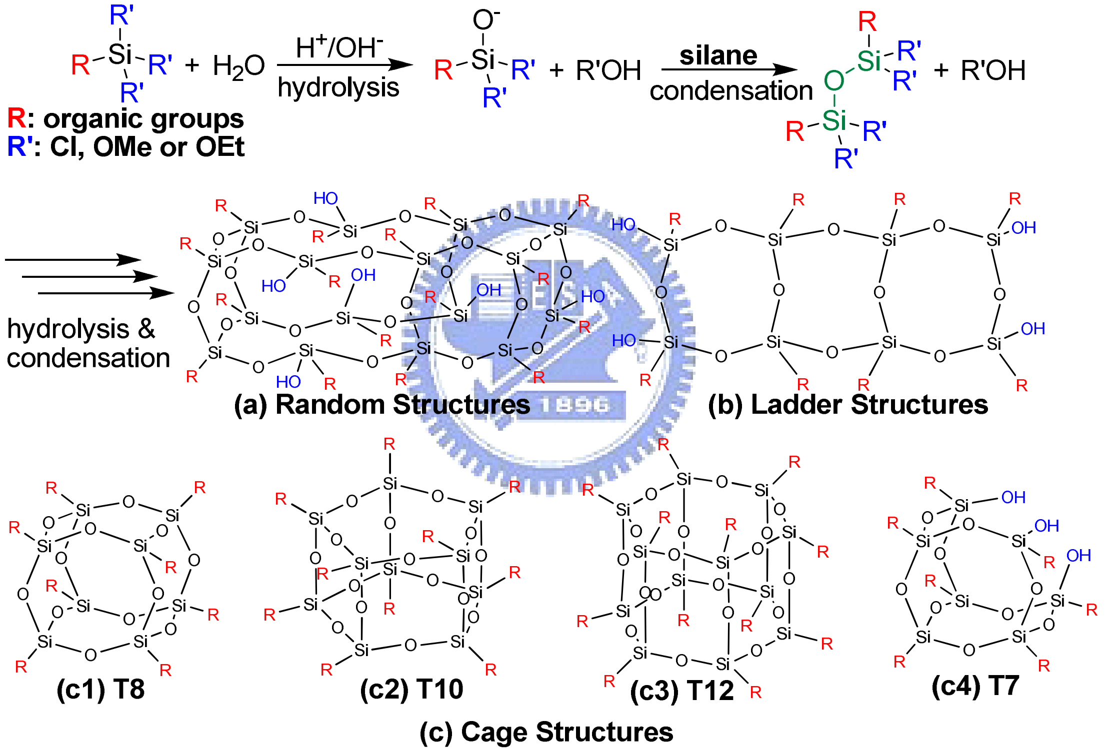

Figure 1-50. Preparation and chemical structures of silsesquioxanes ($RSiO_{1.5}$)$_n$: (a) random networks, (b) ladder chains, and (c) the cage NPs T8 (n = 8), T10 (n = 10), T12 (n = 12), and T7 (n = 7).[125]

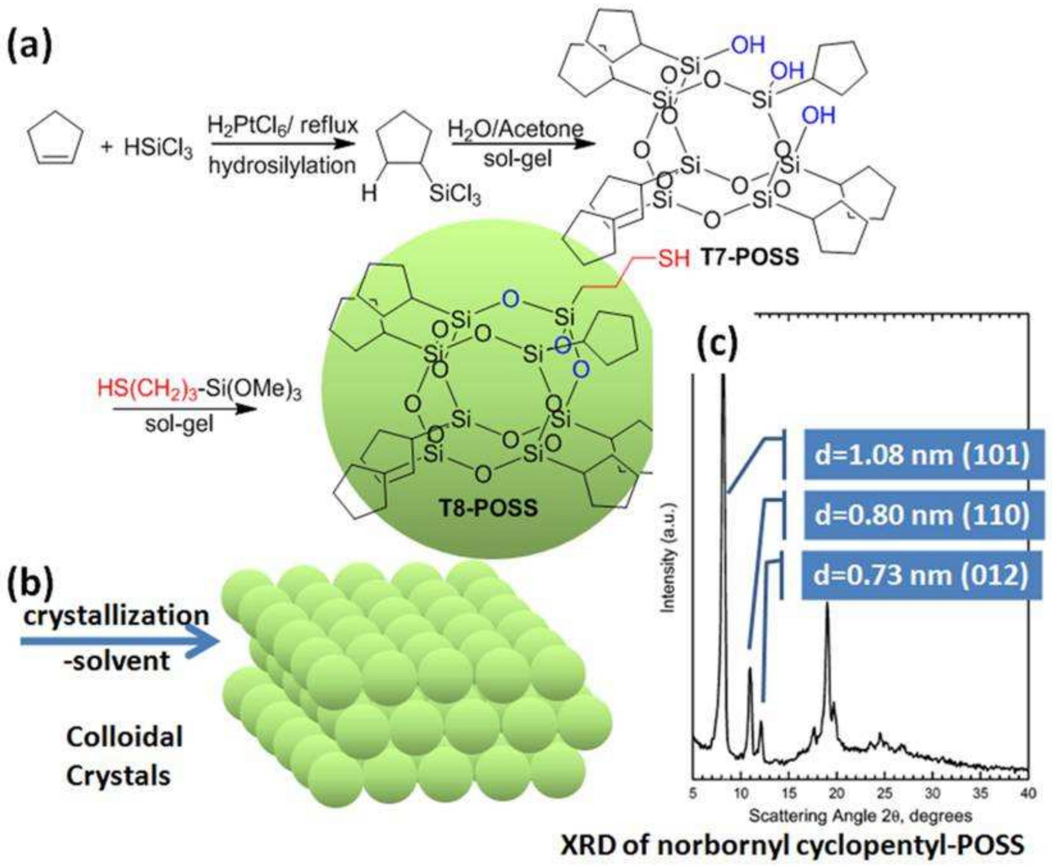

Figure 1-51. (a) Preparation of 3-mercaptopropyl cyclopentyl-POSS via hydrosilylation and sol–gel reactions.[126] (b) Crystallization of POSS colloids during the removal of solvent. (c) XRD spectrum of norbornyl cyclopentyl-POSS.[127]

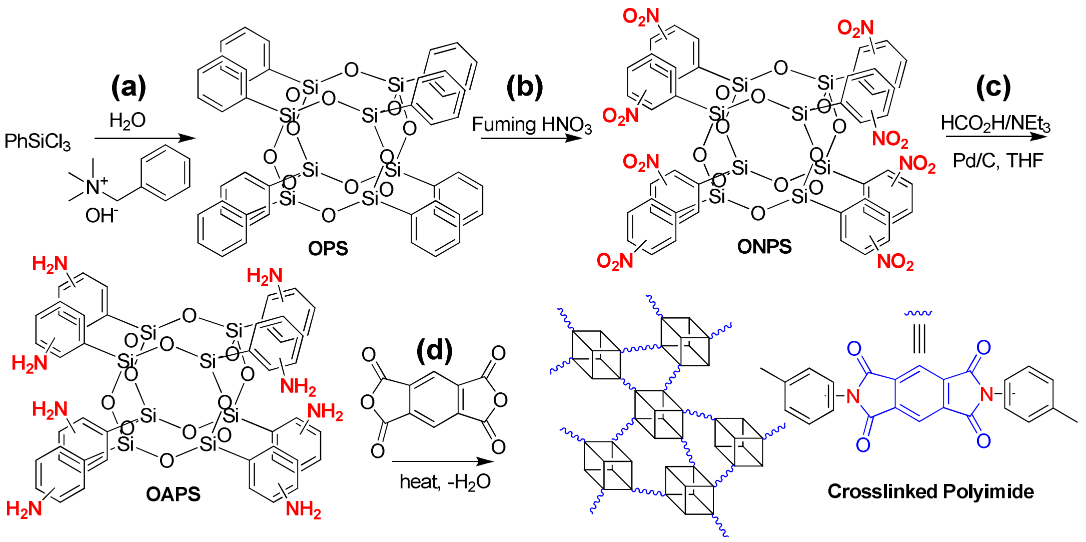

Figure 1-52. Preparation of a crosslinked POSS-based polyimide: (a) sol–gel reaction, (b) nitration with HNO_3,[128] (c) reduction with HCO_2H,[128] and (d) imidization with dicarboxylic anhydride.[129]

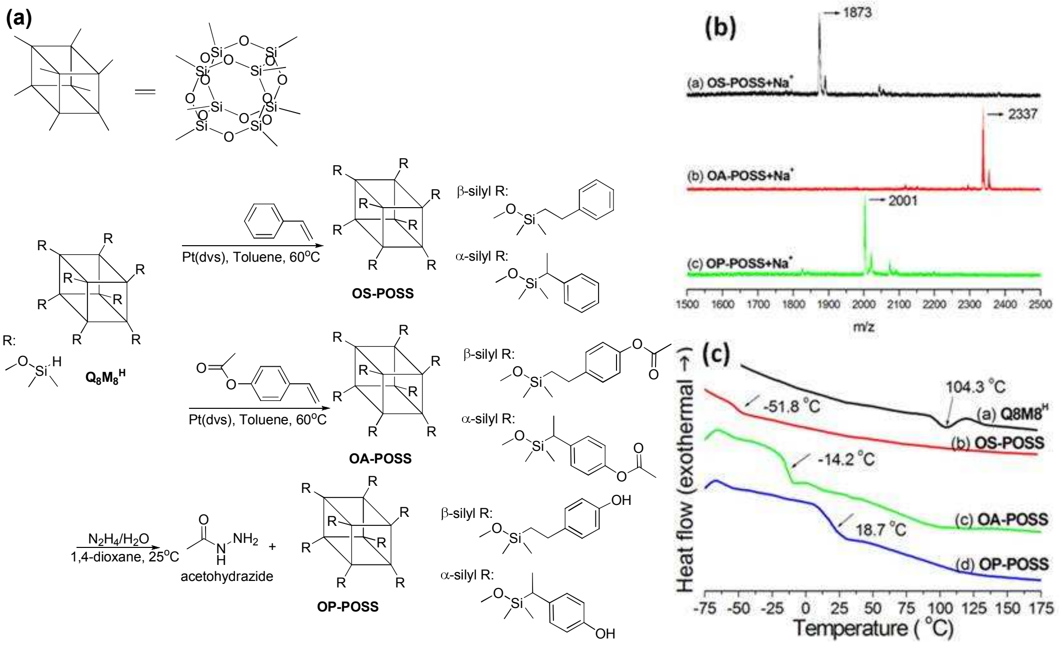

Figure 1-53. (a) Preparation, (b) MALDI-TOF mass spectra, and (c) DSC thermograms of OS-POSS, OA-POSS, and OP-POSS.[138]

Gold Nanocrystals-incorporated Block Copolymer Micelles

As mentioned above, amphiphilic block copolymers can self-assemble into nanosized hydrophobic domains in water. In addition, heavy metal NCs, such as Au or Ag NCs, can function as excellent contrast agents for TEM imaging of microtomed biological samples. Because direct contact of Au or Ag NCs with living cells can damage their growth and reproduction, biocompatible and amphiphilic block copolymers can play an important role in the protection of Au or Ag NCs in water for their use as metal NC-labeled agents. Azzam and Eisenberg prepared a poly(ethylene oxide)-*b*-poly(ε-caprolactone) derivative (PEO-*b*-PCL-TE) in which the PCL-end group presented a thioctate ester.[139] The successful preparation of Au NC-incorporated micelles (**Fig. 1-54**) was confirmed through the TEM image observation of dark Au NCs located in the gray regions of PEO-*b*-PCL micelles in water.

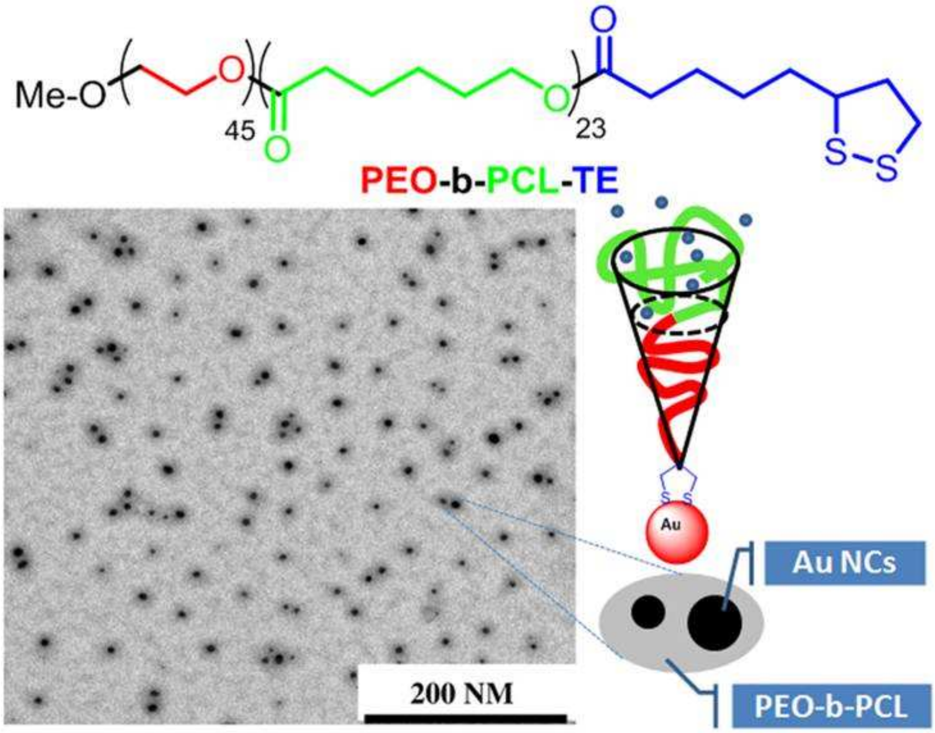

Figure 1-54. (a) Preparation of PEO-*b*-PCL-TE micelles for the incorporation of Au NCs and (b) TEM images of Au NCs-incorporated PEO-*b*-PCL-TE micelles.[139]

1-4 Block Copolymers

1-4.1 Character of Diblock Copolymers

A polymer is a large molecule (macromolecule) composed of repeating structural units (monomers) typically connected via covalent chemical bonds. While the word “polymer” in popular usage suggests “plastic,” the term actually refers to a large class of natural and synthetic materials having a variety of properties and purposes. Well-known examples of polymers include plastics and proteins. A simple example is polyethylene (PE), which possesses a repeating unit structure of $-CH_2CH_2-$. Common plastic bags used to carry trash are made of high-molecular-weight (long chains) PE; ultrathin bags are formed through thermal extending and compressing of PE thin films. In contrast, the brittle crystals of small molecules usually break, rather than extend, under a loading stress. The ability to extend PE films is attributed to the deformation of entangled PE chains, rather than the stretching of C–C bonds (**Fig. 1-55a**). Thus, a polymer's bulk mechanical properties are strongly dependent on the size of the polymer chain. Similarly, the shear thickening behavior of polymer solutions is frequently observed as a result of the strong tendency to recover deformed chain entanglement under a shear stress—a very important factor in the application of polymer coatings. For example, we can obtain a flat surface of paint when brushed on a wall.

In general, polymeric mixtures of polymers A and B are far less miscible than mixtures of small molecule materials A and B ($\Delta_{mix}G$~0).[140] This effect is a result of the fact that the driving force for mixing is usually entropics ($\Delta_{mix}S$), not entropy ($\Delta_{mix}H$~0) for weak intermolecular interaction between polymers A and B in **Fig. 1-55b**. In other words, miscible polymers usually form a solution with solvents not because their interaction with each other is more favorable than their self-interaction, but because of an increase in entropy and hence free energy associated with increasing the amount of volume available to each component. This increase in entropy scales ($\Delta_{mix}S = -R\left[\frac{x_A}{M_A}\ln x_A + x_B \ln x_B\right] > 0$) is attributed to mix the number of long chain polymers A and solvent molecules B. The square root of the mean-square end-to-end distance ($\left\langle r^2 \right\rangle^{0.5}$) of a linear polymer chain averaged over all conformations of the chain. For a freely jointed chain consisting of N segments each of length L, it is given by: $\left\langle r^2 \right\rangle^{0.5} = N^{0.5}L$. For example, a 280,000 g/mol PE chain composed of 10,000 repeating units (N=10,000; L=0.255 nm) can form a spherical coil with the end-to-end distance of 25.5 nm in solution. Thus, diblock copolymers with average molecular masses from 20,000 to 300,000 g/mol can form various ordered nanostructures (dimensions of 10~100 nm) with the interface dispersed of linking groups between two immiscible blocks. These phase behavior of diblock copolymers is driven by thermodynamic disfavor between two immiscibe two blocks. Similar to amphiphilic small molecules, a variety of architectures can be produced by manipulating the ratio of the volumes of the two blocks and the degree of immiscibility between them (**Fig. 1-56**).[141] An enormous amount of work has been published using diblock copolymers of the AB type. In bulk, four different ordered structures can be obtained (alternating lamellae, cylinders, body-centered cubic arrays of spheres and gyroid) depending on the copolymer composition and architecture.

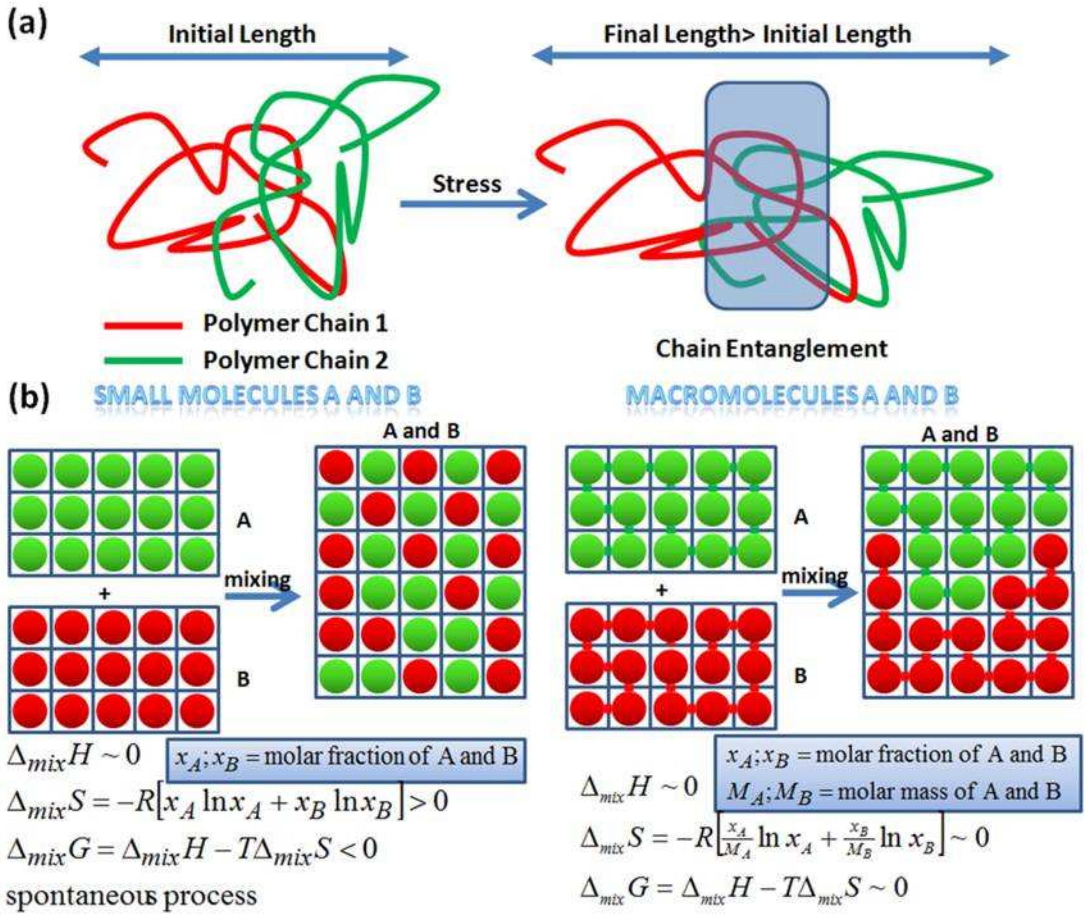

Figure 1-55. (a) Deformation of polymer chains and (b) depictions and descriptions of the miscible and immiscible modes of small molecules and macromolecules, respectively.

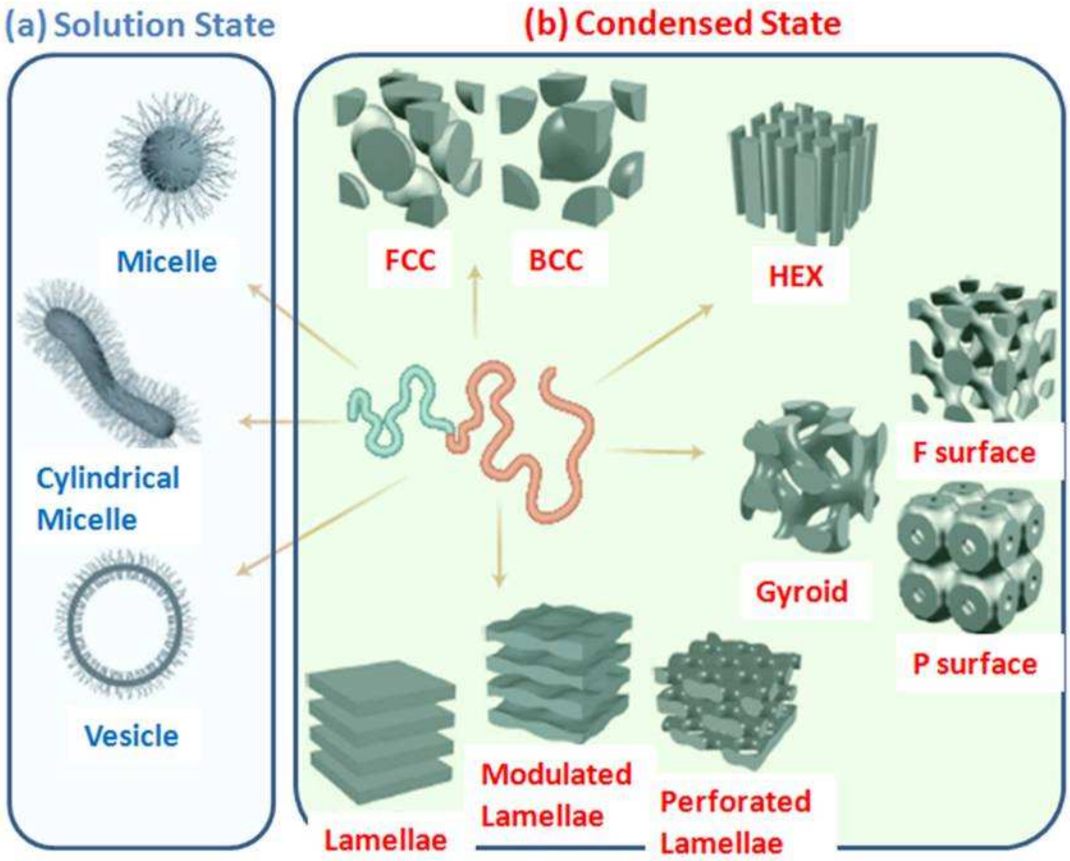

Figure 1-56. Self-assembling morphologies of block copolymers (a) in solution (spherical micelles, cylindrical micelles, and bilayer vesicles) and (b) in condensed phases [spherical separation (FCC and BCC), hexagonal cylinder arrays (Hex), bicontinuous gyroid phases (F and P surface), and lamellar alternate bilayers (normal, modulated, and perforated)].[141]

1-4.2 Synthesis of Diblock Copolymers

Conventional Polymerization

According to their mechanisms, polymerization reaction can be classified broadly into condensations and additions. A condensation polymer is prepared through coupling of the difunctional groups of monomers. For example, a high-performance polyimide, such as Kapton, can be obtained through amidation between a diamine and dicarboxylic anhydride, followed by thermal imidation. Kapton, a polyimide film developed by DuPont, can remain stable over a wide range of temperatures (from –273 to +400 °C); it is used in, among other things, flexible printed circuits (flexible electronics). High-molecular-weight polymers are obtained in step polymerizations only near the very end of the reaction (>98% conversion) (**Fig. 1-57a**). Thus, in step polymerizations, both the polymer size and the amount of polymer are dependent on the conversion. Conventional addition polymerizations require radical precursors (initiators) to initiate the polymerization.[142] For example, benzoyl peroxide (BPO) can be decomposed into two benzoyloxyl radicals at temperatures up to 90 °C. The addition of benzoyloxyl radicals to styrene (St) monomers quickly forms a carbon-centered radical for subsequent propagation; the rate of initiation is given by $R_i = k_i[\mathrm{BPO}]$. By integrating this equation, we obtain the decomposition time of half of the radical precursors ($t_{1/2}$), given by $\ln 2/k_i$. A rate constant (k_i) of $1.0 \times 10^{-4}\ \mathrm{s}^{-1}$ at 90 °C for BPO in ethylbenzene suggests that half of the BPO is decomposed in ca. 2 h. Because propagation is relatively rapid, the polymer chains grow quickly to high molecular mass as soon as the propagating radicals are produced (**Fig. 1-57b**). The propagating radicals react with St monomers to produce other propagating radicals with similar chemical structures; the rate of propagation is given by $R_P = k_P[\mathrm{PS}\cdot][\mathrm{St}]$. At high conversion (i.e., low [St]), the radical combination (termination) of propagating radicals can compete with propagation, resulting in high-molecular-mass polymers that do not feature active propagating radicals.

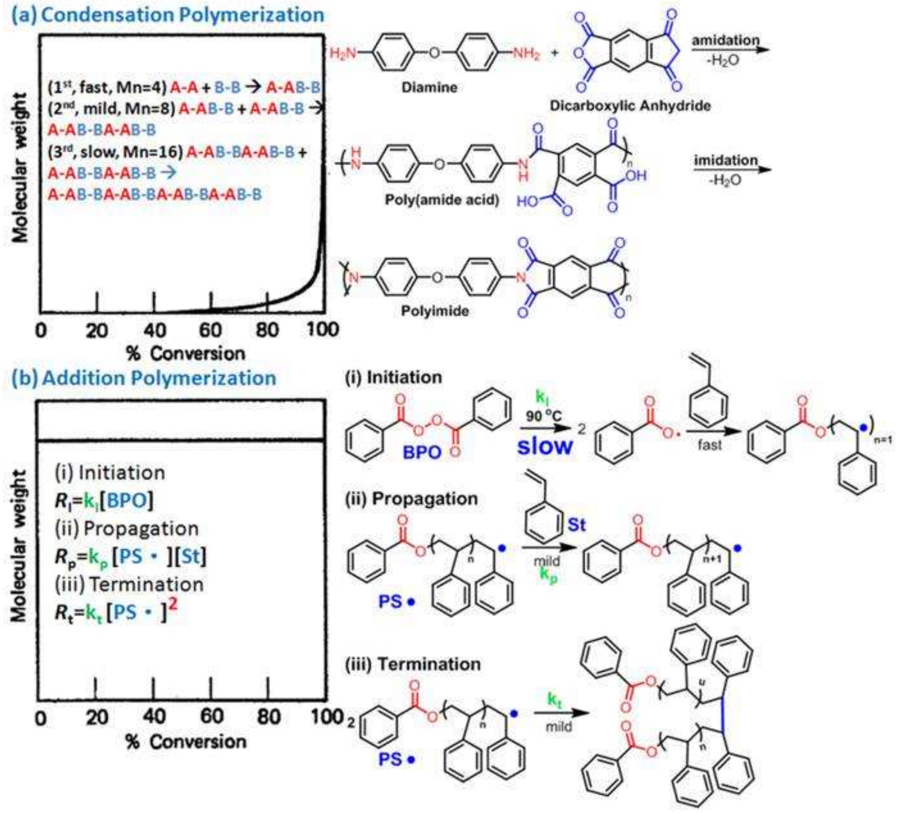

Figure 1-57. Molecular weight/conversion profiles and reaction mechanisms of (a) the condensation polymerization of polyimide and (b) the radical polymerization of polystyrene.

Living/ Controllable Addition Polymerization

Although free radical polymerization processes are generally tolerant of protic and aqueous solvents and certain functional monomers, their main disadvantage is that they produce polydisperse polymers with little control over the molecular lengths because of the long-term initiation and automatic termination events. Recent advances in free radical polymerization have led to the development of synthetic methods that eliminate or suppress undesired initiation and termination.[143] Three most important methods include (i) nitroxide-mediated polymerization (NMRP),[144,145] (ii) atom transfer radical polymerization (ATRP),[146] and (iii) reversible addition/fragmentation chain transfer polymerization (RAFT).[147] These methods are based on chemical equilibria lowering the concentrations of propagating radicals. Thus, the first-order rate of propagation becomes small, requiring a much longer time (ca. 24 h) to attain a high monomer conversion relative to that of the conventional addition polymerization. The second-order rate of termination, however, decreases, thereby reducing the probability of termination (pseudo-living character). In ATRP and NMRP, the initiating species containing haloalkane and *N*-alkoxyamine with similar chemical structures to monomers can be used in polymerization through propagation only (so-called “monomer insertion”). For example, polystyrene (PS) and poly(methyl methacrylate) (PMMA) can be prepared through NMRP and ATRP (**Fig. 1-58**). The chemical equilibrium between *N*-alkoxyamines, propagating radicals, and TEMPO can reduce the concentration of propagating radicals and, thereby, inhibit radical termination. The chemical equilibrium between the haloalkane, Cu^{I} complex, propagating radicals, and Cu^{II} complex plays a similar role in the ATRP of PMMA. Because all monomers are inserted from the *N*-alkoxyamine in NMRP or from the haloalkane in ATRP, the number-average molecular weights ($\overline{M}_n$) of the synthetic polymers depend strongly on the conversion (α), given by $\overline{M}_n = [M]_0(1-\alpha)/[\mathrm{N-alkoxyamine\ or\ haloalkane}]$, where $[M]_0$ is the initial monomer concentration. In the absence of decomposition of the radical precursors (initiation), the chemical equilibria in NMRP and ATRP result in constant and dilute concentrations of propagating radicals. Thus, the rate of propagation for the NMPR of PS can be rewritten as $R_p = k_{app}[St]$, where k_{app} is the apparent rate constant resulting from the combination of k_p and $[PS\bullet]$. Thus, a linear correlation between $\ln([M]_0/[M])$ and time is obtained through integration of the first-order propagation.

In comparison with the conventional addition polymerizations, the initiation and termination steps are insignificant in both NMRP and ATRP. Thus, the functional end groups, such as *N*-alkoxyamines and haloalkanes for NMRP and ATRP, allow the insertion of a second type of monomer (living behavior). In addition, the narrow distribution of polymer chains ($\overline{M}_w/\overline{M}_n < 1.5$) can result from rapid chemical equilibrium between propagating radicals and dormant species, such as Cu^{I} complexes and TEMPO. Living/controllable polymerization is a popular method for synthesizing diblock copolymers because the polymer can be prepared in stages, with each stage containing a different monomer. Additional advantages include a predetermined molar mass and control over the constitution of the end-groups.

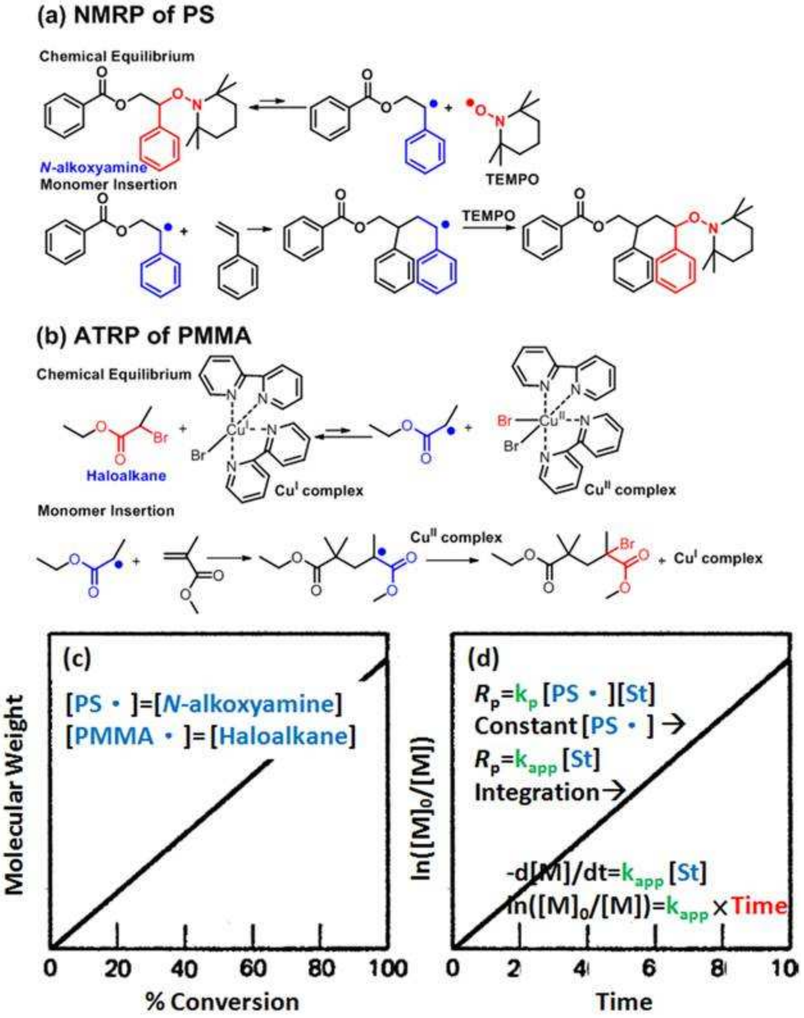

Figure 1-58. Reaction mechanisms of (a) the NMRP of PS and (b) the ATRP of PMMA. (c, d) Linear correlations, for both NMRP and ATRP, between (c) the molecular weight and the conversion and (d) the value of $\ln([M]_0/[M])$ and the time.[144,146]

1-5 References

1. Schmid, G. Clusters and Colloids, In *Theory to Applications*, VCH, Weinheim, **1994**.
2. *The Chemistry of Nanomaterials*, Eds. Rao, C. N. R.; Muller, A.; Cheetham, A. K., Wiley-VCH, Weinheim, Vols. 1 & 2, **2004**.
3. *Nanomaterials Chemistry: Recent Developments*, Eds. Rao, C. N. R.; Muller, A.; Cheetham, A. K., Wiley-VCH, Weinheim, **2007**.
4. Rao, C. N. R.; Govindaraj, A. *Nanotubes and Nanowires*, RSC Series on Nanoscience, London, **2005**.
5. Rao, C. N. R.; Govindaraj, A.; Vivekchand, S. R. C. *Ann. Rep. Prog. Chem.*, Royal Society of Chemistry, London, **2006**, 102, 20.
6. Rao, C. N. R.; Thomas, P. J.; Kulkarni, G. U. *Nanocrystals: Synthesis, Properties and Applications*, Springer Series on Material Science, 95, **2007**.
7. Rao, C. N. R.; Vivekchand, S. R. C.; Biswasa, K.; Govindaraja, A. *Dalton Trans.* **2007**, 3728.
8. Fahlman, B. D. *Materials Chemistry*, Springer, Mount Pleasant, MI, **2007**, 1, 282.
9. Faraday, M. *Philos. Trans. R. Soc. London* **1857**, *147*, 145.
10. Frens, G. *Nature* **1973**, *241*, 20.
11. Wilcoxon, J. P.; Williamson, R. L.; Baughman, R. *J. Chem. Phys.* **1993**, *98*, 9933.
12. Brust, M.; Walker, M.; Bethell, D.; Schiffrin, D. J.; Whyman, R. *J. Chem. Soc., Chem. Commun.* **1994**, 801.
13. *Colloidal gold: Principles, methods, and applications*, Ed. Hayat M. A., Academic Press, San Diego, **1989**, Vol. 3.
14. Hiramatsu, H.; Osterloh, F. E. *Chem. Mater.* **2004**, *16*, 2509.

15. Clarke, T. G.; Hampson, N. A.; Lee, J. B.; Morley, J. R.; Scanlon, B. *Tetrahedron Lett.* **1968**, *54*, 5685.

16. Capdevielle, P.; Lavigne, A.; Sparfel, D.; Baranne-Lafont, J.; Cuong, N. K.; Maumy, M. *Tetrahedron Lett.* **1990**, *31*, 3305.

17. Lim, Y. T.; Kim, J. K.; Shin, Y. B.; Chung, B. H. *Adv. Funct. Mater.* **2006**, *16*, 1015.

18. Roduner E. *Chem. Soc. Rev.* **2006**, *35*, 583

19. Ishida, T.; Haruta, M. *Angew. Chem. Int. Ed.* **2007**, *46*, 7154.

20. Prati, L.; Rossi, M. *J. Catal.* **1998**, *176*, 552.

21. Biella, S.; Prati, L.; Rossi, M. *J. Catal.* **2002**, *206*, 242.

22. Corma, A.; Serna, P. *Science* **2006**, *313*, 332.

23. Shi, F.; Deng, Y. *J. Catal.* **2002**, *211*, 518;

24. Shi, F.; Zhang, Q.; Ma, Y.; He, Y.; Deng, Y. *J. Am. Chem. Soc.* **2005**, *127*, 4182.

25. Burato, C.; Centomo, P.; Pace, G.; Favaro, M.; Prati, L.; Corain, B.; *J. Mol. Catal. A* **2005**, *238*, 26.

26. Hughes, M. D.; Xu, Y.-J.; Jenkins, P.; McMorn, P.; Landon, P.; Enache, D. I.; Carley, A. F.; Attard, G. A.; Hutchings, G. J.; King, F.; Stitt, E. H.; Johnston, P.; Griffin, K.; Kiely, C. J. *Nature* **2005**, *437*, 1132.

27. He, S.; Yao, J.; Jiang, P.; Shi, D.; Zhang, H.; Xie, S.; Pang, S.; Gao, H. *Langmuir* **2001**, *17*, 1571.

28. Silvert, P.-Y.; Herrera-Urbina, R.; Duvauchelle, N.; Vijayakrishnan, V.; Elhsissen, K. T. *J. Mater. Chem.* **1996**, *6*, 573.

29. Silvert, P.-Y.; Herrera-Urbina, R.; Tekaia-Elhsissen, K. *J. Mater. Chem.* **1997**, *7*, 293.

30. Faraday, M. *Philos. Trans. R. Soc. London* **1857**, *147*, 145.

31. Frens, G. *Nature* **1973**, *241*, 20.

32. Wilcoxon, J. P.; Williamson, R. L.; Baughman, R. *J. Chem. Phys.* **1993**, *98*, 9933.

33. Brust, M.; Walker, M.; Bethell, D.; Schiffrin, D. J.; Whyman, R. *J. Chem. Soc., Chem. Commun.* **1994**, 801.

34. *Colloidal gold: Principles, methods, and applications*, Ed. Hayat M. A. San Diego: Acdemic Press, **1989**, vol 3.

35. Hiramatsu, H.; Osterloh, F. E. *Chemistry of Materials*, **2004**, *16*, 2509.

36. Wang, H.-T.; Nafday, O. A.; Haaheim, J. R.; Tevaarwerk, E.; Amro, N. A.; Sanedrin, R. G.; Chang, C.-Y.; Ren, F.; Pearton, S. J. *Appl. Phys. Lett.* **2008**, *93*, 143105.

37. Li, Y.; Wu Y.; Ong, B. S. *J. Am. Chem. Soc.* **2005**, *127*, 3266.

38. Lok, C.-N.; Ho, C.-M.; Chen, R.; He, Q.-Y.; Yu, W.-Y.; Sun, H.; Tam, P. K.-H.; Chiu, J.-F.; Che, C.-M. *J. Biol. Inorg. Chem.* **2007**, *12*, 527.

39. Chen, W.; Liu, Y.; Courtney H. S.; Bettenga, M.; Agrawai, C. M.; Bumgardner J. D.; Ong, J. L. *Biomaterials* **2006**, *27*, 5512.

40. Vik, H.; Andersen, K. J.; Julshamn, K.; Todnem, K. *Lancet* **1985**, *1*, 872.

41. Hidalgo, E.; Dominguez, C. *Toxicol. Lett.* **1998**, *98*, 169.

42. Quiros, I.; Yamada, M.; Kubo, K.; Mizutani, J.; Kurihara, M.; Nishihara, H. *Langmuir* **2002**, *18*, 1413.

43. Li, Y.; EI-Sayed, M. A. *J. Phys. Chem. B* **2001**, *105*, 8938.

44. Zhao, M.; Crooks, R. M. *Angew. Chem., Int. Ed. Engl.* **1999**, *38*, 364.

45. Zhao, M.; C rooks, R. M. *Adv. Mater.* **1999**, *11*, 217.

46. Chechik, V.; Crooks, R. M. *J. Am. Chem. Soc.* **2000**, *122*, 1243.

47. Crooks, R. M.; Zhao, M.; Sun, L.; Chechik, V.; Yeung, L. K. *Acc. Chem. Res.* **2001**, *34*, 181.

48. Kim S.-W.; Park, J.; Jang, Y.; Chung, Y.; Hwang, S.; Kim, Hyeon, T.; Kim, Y. W. *Nano Lett.* **2003**, *3*, 1289.
49. Wu, L.; Li, Z.-W.; Zhang, F.; He, Y.-M.; Fan, Q.-H. *Adv. Synth. Catal.* **2008**, *350*, 846.
50. Budarin, V. L.; Clark, J. H.; Luque, R.; Macquarrie, D. J.; White, R. J. *Green Chem.* **2008**, *10*, 382.
51. Barau, A.; Budarin, V.; Caragheorgheopol, A.; Luque, R.; Macquarrie, D. J.; Prelle, A.; Teodorescu, V. S.; Zaharescu, M. *Catal. Lett.* **2008**, *124*, 204.
52. Wei, G.; Zhang, W.; Wen, F.; Wang, Y.; Zhang, M. *J. Phys. Chem. C* **2008**, *112*, 10827.
53. Miyaura, N.; Yamada, K.; Suzuki, A. *Tetrahedron Lett.* **1979**, 3437.
54. Miyaura, N.; Suzuki, A. *J. Chem. Soc, Chem. Commun.*, **1979**, 866.
55. Heck, R. F. *Org. React.* **1982**. *27*, 345.
56. Kobayashi, H.; Yamauchi, M.; Kitagawa, H.; Kubota, Y.; Kato, K.; Takata, M. *J. Am. Chem. Soc.* **2008**, *130*, 1828.
57. Kobayashi, H.; Yamauchi, M.; Kitagawa, H.; Kubota, Y.; Kato, K.; Takata, M. *J. Am. Chem. Soc.* **2008**, *130*, 1818.
58. Gerloch, M.; Constable, E. C. *Transition Metal Chemistry: The Valence Shell in d-Block Chemistry*, VCH, Weinheim **1994**.
59. Fanizzi, F.; Intini, F. P.; Maresca, L.; Natile, G. *J. Chem. Soc., Dalton Trans.* **1990**, 199.
60. Kreibig, U.; Vollmer, M. *Optical Properties of Metal Clusters*, Springer, Berlin **1995**.
61. Furlong, D. N.; Launikonis, A.; Sasse, W. H. F. *J. Chem. Soc., Faraday Trans. 1* **1984**, *80*, 571.
62. Wagner, C. D.; Riggs, W. M.; Davis, L. E.; Moulder, J. F. *Handbook of X-Ray*

Photoelectron Spectroscopy, Perkin-Elmer, Eden Prairie, **1979**.

63. Martin, J. E.; Wilcoxon, J. P.; Odinek, J.; Provencio, P. *J. Phys. Chem. B* **2002**, *106*, 971.
64. Şen, F.; Gökağaç, G. *J. Phys. Chem. C* **2007**, *111*, 1467.
65. Goodenough, J. B.; Hamnett, A.; Kennedy, B. J.; Manoharan, R.; Weeks, S. A. *J. Electroanal. Chem.* **1988**, *240*, 133.
66. Watanabe, M.; Uchida, M.; Motoo, S. *J. Electroanal. Chem.* **1987**, *229*, 395.
67. Mu, Y.; Liang, H.; Hu, J.; Jiang, Li, Wan, L. *J. Phys. Chem. B* **2005**, *109*, 22212.
68. Xu, K.; Pierce, D. T.; Li, A.; Zhao, J. X. *Synth. React. Inorg., Met.-Org., Nano-Met. Chem.* **2008**, *38*, 394.
69. Thomas, C. E.; James, B. D.; Lomax, F. D.; Kuhn, I. F. *Int. J. Hydrogen Energy* **1998**, *26*, 551.
70. Giorgi, R.; Ascarerlli, P.; Turtu, S.; Contini, V. *Appl. Surf. Sci.* **2001**, *178*, 149.
71. Thomas, S.; Zalbowitz, M. *Fuel Cells—Green Power*, Los Alamos National Laboratory, New Mexico, Report No. LA-UR-99-3231, **1999**.
72. Prater, K. B. *J. Power Sources* **1994**, *51*, 129.
73. Tremiliosi-Filho, G.; Kim, H.; Chrzanowski, W.; Wieckowski, A.; Grzybowska, B.; Kulesza, P. *J. Electroanal. Chem.* **1999**, *467*, 143.
74. Rockenberger, J.; Scher, E. C.; Alivisatos, A. P. *J. Am. Chem. Soc.* **1999**, *121*, 11595.
75. Murray, C. B.; Kagan, C. R.; Bawendi, M. G. *Science* **1995**, *270*, 1335.
76. Shmakov, A. N.; Kryukova, G. N.; Tsybulya, S. V.; Chuvilin, A. L.; Solovyeva, L. P. *J. Appl. Crystallogr.* **1995**, *28*, 141.
77. Hyeon, T.; Lee, S. S.; Park, J.; Chung, Y.; Na, H. B. *J. Am. Chem. Soc.* **2001**, *123*, 12798.
78. Liao, M.; Chen, D. *J. Mater. Chem.* **2002**, *12*, 3654.

79. Hartlieb, K. J.; Raston, C. L.; Saunders, M. *Chem. Mater.* **2007**, *19*, 5453.

80. Beek, W. J. E.; Wienk, M. M.; Kemerink, M.; Yang, X.; Janssen, R. A. *J. Phys. Chem. B* **2005**, *109*, 9505.

81. Meulenkamp, E. A. *J. Phys. Chem. B.* **1998**, *102*, 5566.

82. Murray, C. B.; Norris, D. J.; Bawendi, M. G. *J. Am. Chem. Soc.* **1993**, *115*, 8706.

83. Katari, J. E. B.; Colvin, V. L.; Alivisatos, A. P. *J. Phys. Chem.* **1994**, *98*, 4109.

84. Trentler, T. J.; Denler, T. E.; Bertone, J. F.; Agrawal, A.; Colvin, V. L. *J. Am. Chem. Soc.* **1999**, *121*, 1613. Size determinations were made by applying the Debye–Scherrer formula to the (101) reflection. See: Cullity, B. D. *Elements of X-ray Diffraction*, 2nd ed., Addison-Wesley, Reading, MA, **1978**.

85. Jones, B. J.; Vergne, M. J.; Bunk, D. M.; Locascio, L. E.; Hayes, M. A. *Anal. Chem.* **2007**, *79*, 1327.

86. Murray, C. B.; Norris, D. J.; Bawendi, M. G. *J. Am. Chem. Soc.* **1993**, *115*, 8706.

87. Qu, L.; Peng, X. *J. Am. Chem. Soc.* **2002**, *124*, 2049.

88. Peng, Z. A.; Peng, X. *J. Am. Chem. Soc.* **2001**, *123*, 183

89. Qu, L.; Peng, Z. A.; Peng, X. *Nano Lett.* **2001**, *1*, 333.

90. Dahan, M.; Levi, S.; Luccardini, C.; Rostaing, P.; Riveau, B.; Triller, A. *Science* **2003**, *302*, 442.

91. Kroto, H. W.; Heath, J. R.; O'Brien, S. C.; Curl, R. F.; Smalley, R. E. *Nature* **1985**, *318*, 162.

92. Céolin, R.; Tamarit, J. Ll.; López, D. O.; Barrio, M.; Agafonov, V.; Allouchi, H.; Mousssa, F.; Szwarc, H. *Chem. Phy. Lett.* **1999**, *314*, 21.

93. Maggini, M.; Scorrano, G.; Prato, M. *J. Am. Chem. Soc.* **1993**, *115*, 9798.

94. Dubois, D.; Kadish, K. M.; Flanagan, S.; Wilson, L. J. *J. Am. Chem. Soc.* **1991**, *113*, 7773.

95. Trost, B. M.; Bright, G. M.; Frihart, C.; Brittelli, D. *J. Am. Chem. Soc.* **1971**, *93*,

737.

96. Tada, K.; Onoda, M. *Adv. Funct. Mater.* **2004**, *14*, 139.

97. Hasobe, T.; Imahori, H.; Kamat, P. V.; Fukuzumi, S. *J. Am. Chem. Soc.* **2005**, *127*, 1216.

98. Biebersdorf, A.; Dietmuller, R.; Susha, A. S.; Rogach, A. L.; Poznyak, S. K.; Talapin, D. V.; Weller, H.; Klar, T. A.; Feldmann, J. *Nano Lett.* **2006**, *6*, 1559.

99. Brown, P.; Kamat, P. V. *J. Am. Chem. Soc.* **2008**, *130*, 8890.

100. Haraguchi, K.; Ebato, M.; Takehisa, T. *Adv. Mater.* **2006**, *18*, 2250.

101. Stöber, W.; Fink, A.; Bohn, E. *J. Colloid Interface Sci.* **1968**, *26*, 62.

102. Harris, M. T., Brunson, R. R.; Byers, C. H. *J. Non-Cryst. Solids* **1990**, *121*, 397.

103. Joannopoulos, J. D.; Villeneuve, P. R.; Fan, S. *Nature* **1997**, *386*, 143.

104. Lin, H. B.; Tonucci, R. J.; Campillo, A. J. *Appl. Phys. Lett.* **1996**, *68*, 2927.

105. Míguez, H.; Meseguer, F.; López, C.; Blanco, A.; Moya, J. S.; Requena, J.; Mifsud, A.; Fornés, V. *Adv. Mater.* **1998**, *10*, 480.

106. Park, S. H.; Xia, Y. *Langmuir* **1999**, *15*, 266.

107. Saenger, W.; Jacob, J.; Gessler, K.; Steiner, T.; Hoffmann, D.; Sanbe, H.; Koizumi, K.; Smith S. M.; Takaha, T. *Chem. Rev.* **1998**, *98*, 1787.

108. Buvári-Barcza, Á.; Rohonczy, J.; Rozlosnik, N.; Gilányi, T.; Szabó, B.; Lovas, G.; Braun, T.; Samu, J.; Barcza, L. *J. Chem. Soc., Perkin Trans*. **2001**, *2*, 191.

109. Sabadini, E.; Cosgrovea, T.; do Carmo Egídio, F. *Carbohydr. Res.* **2006**, *341***,** 270.

110. Sallas, F.; Darcy, R. *Eur. J. Org. Chem.* **2008**, 957.

111. Harada, A.; Hashidzume, A.; Takashima, Y. *Adv. Polym. Sci.* **2006**, *201*, 1.

112. Wu, S.; Lua, Y.; Zeng, F.; Chen, J.; Chen, Y.; Tong, Z. *Angew. Chem. Int. Ed.* **2007**, *46*, 7015.

113. Hecht, S.; Fréchet, J. M. J. *Angew. Chem. Int. Ed.* **2001**, *40*, 74.

114. Lang, H.; May, R. A.; Iversen, B. L.; Chandler, B. D. *J. Am. Chem. Soc.* **2003**, *125*, 14832.

115. Israelachivili, J. N. *Intermolecular and Surface Forces*; Academic Press: New York, **1985**.

116. Shimizu, T.; Masuda, M.; Minamikawa, H. *Chem. Rev.* **2005**, *105*, 1401.

117. Yamaguchi, A.; Uejo, F.; Yoda, T.; Uchida, T.; Tanamura, Y.; Yamashita, T.; Teramae, N. *Nat. Mater.* **2004**, *3*, 337; Ogawa, M. A. *Chem. Commun.* **1996**, 1149.

118. Kresge, C. T.; Leonowicz, M. E.; Roth, W. J.; Vartuli, J. C.; Beck, J. S. *Nature* **1992**, *359*, 710.

119. Beck, J. S.; Vartuli, J. C.; Roth, W. J.; Leonowicz, M. E.; Kresge, C. T.; Schmitt, K. D.; Chu, C. T. W.; Olson, D. H.; Sheppard, E. W. *J. Am. Chem. Soc.* **1992**, *114*, 10834.

120. Tanamura, Y.; Uchida, T.; Teramae, N.; Kikuchi, M.; Kusaba, K.; Onodera, Y. *Nano Lett.* **2001**, *1*, 387.

121. Zhang, L.; Eisenberg, A. *Science* **1995**, *268*, 1728.

122. Zhang, L.; Eisenberg, A. *J. Am. Chem. Soc.* **1996**, *118*, 3168.

123. Jeong, B.; Bae, Y. H.; Lee, D. S.; Kim, S. W. *Nature*, **1997**, *388*, 860.

124. Youxin, L.; Kissel, T. *J. Controlled Release* **1993**, *27*, 247.

125. Baney, R. H.; Itoh, M.; Sakakibara, A.; Suzuki, T. *Chem. Rev.* **1995**, *95*, 1409.

126. Schmid, G.; Pugin, R.; Malm, J.-O.; Bovin, J.-O. *Eur. J. Inorg. Chem.* **1998**, 813.

127. Waddon, A. J.; Coughlin, E. B. *Chem. Mater.* **2003**, *15*, 4555.

128. Yamaki, R.; Tanaka, Y.; Asuncion, M. Z.; Choi, J.; Laine, R. M. *J. Am. Chem. Soc.* **2001**, *123*, 12416.

129. Tamaki, R.; Choi, J.; Laine, R. M. *Chem. Mater.* **2003**, *15*, 793.

130. Agaskar, P. A. *Inorg. Chem.* **1991**, *30*, 2707.

131. Hasegawa, I.; Sakka, S.; Sugahara, Y.; Kuroda, K.; Kato, C. *J. Chem. Soc., Chem. Commun.* **1989**, 208.

132. Hasegawa, I.; Motojima, S. *J. Organomet. Chem.* **1992**, *441*, 373.

133. Sellinger, A.; Laine, R. M. *Macromolecules* **1996**, *29*, 2327.

134. Sellinger, A.; Laine, R. M.; Chu, V.; Viney, C. *J. Polym. Sci., Part A: Polym. Chem.* **1994**, *32*, 3069.

135. Sellinger, A.; Laine, R. M. *Chem. Mater.* **1996**, *8*, 1592.

136. Laine, R. M.; Choi, J.; Lee, I. *Adv. Mater*. **2001**, *13*, 800.

137. Zhang, C.; Laine, R. M. *J. Am. Chem. Soc.* **2000**, *122*, 6979.

138. Sheen, Y.-C.; Lu, C.-H.; Huang, C.-F.; Kuo, S.-W.; Chang, F.-C. *Polymer* **2008**, *49*, 4017.

139. Azzam, T.; Eisenberg, A. *Langmuir* **2007**, *23*, 2126.

140. Coleman, M. M.; Painter P. C. *Prog. Polym. Sci.* **1995**, *20*, 1.

141. Bucknall, D. G.; Anderson, H. L. *Science* **2003**, *302*, 1904.

142. Odian, G. *Principles of Polymerization*, 4th Edn.; Wiley: NY, **2004**.

143. Greszta, D.; Mardare, D.; Matyjaszewski, K. *Macromolecules* **1994**, *27*, 638.

144. Hawker, C. J.; Bosman, A. W.; Harth, E. *Chem. Rev.* **2001**, *101*, 3661.

145. Sciannamea, V.; Jerome, R.; Detrembleur, C. *Chem. Rev.* **2008**, *108*, 1104.

146. Matyjaszewski, K.; Xia, J. *Chem. Rev.* **2001**, *101*, 2921.

147. Moad, G.; Rizzardo, E.; Thang, S. H. *Polymer*, **2008**, *49*, 1079.

Chapter 2

Synthesis and Characterization of Poly(ε-caprolactone-*b*-4-vinyl pyridine): Initiation, Polymerization, Solution Morphology, and Gold Metalation

Abstract

We have synthesized a difunctional initiator—the hydroxyl-4-oxo-*N*-alkoxyamine **HOA**—by first mixing benzoyl peroxide (BPO) and 4-hydroxyl 2,2,6,6-tetramethylpiperdinooxy (4-OH-TEMPO) in styrene at temperatures below 25 °C to give the 4-oxo-*N*-alkoxyamine (**OA**) and then hydrolyzing the benzoate ester on **OA** with NaOH. This low-temperature preparation of **OA** reveals that benzyloxyl radicals can be generated from the BPO through redox reaction with 4-OH-TEMPO as well as through thermal decomposition. The *N*-oxoammonium cation (i.e., the oxidative state of 4-OH-TEMPO), which formed as a side product, mediated the alcohol oxidation to give **OA**. We prepared three PCL-*b*-P4VP diblock copolymers (**BC1**–**3**) from **HOA** through two-step polymerizations: (i) diethyl aluminum alkoxide-induced ring-opening polymerization of ε-caprolactone at 25 °C followed by (ii) nitroxide-mediated radical polymerization of 4-vinylpyridine at 125 °C. With the combination of biodegradable hydrophobic PCL blocks and polymeric blocks of P4VP ligands, we used the immiscible PCL-*b*-P4VP copolymers to transport $AuCl_4^-$ anions from aqueous phases to organic phases and to stabilize Au nanoparticles in the PCL-*b*-P4VP micelles **Au-BC1**–**3** after reduction with $NaBH_4$.

2-1 Introduction

Diblock copolymers comprising two dissimilar blocks can form two separate and thermodynamically stable microstructures in the bulk state. The hydrophilic side groups of amphiphilic diblock copolymers are highly permeable to water[1–6] or can be selectively removed to create nanopores for water passage.[7,8] When placed in a solvent that solvates only one of the components well, diblock copolymers self-assemble into core/shell micellar microstructures in which the insoluble block comprises the core, thereby avoiding contact with the solvent.[9] In their pioneering research, Eisenberg and coworkers observed that micelles formed from linear diblock copolymers in several morphologies, including spheres, rods, vesicles, and large compound micelles.[10–12] Depending on the molecular masses of the two blocks, the sizes of micelles can range from 10 to 1000 nm, providing a large contact area for two-phase extraction of metal ions: one block to capture metal ions from water in the insoluble cores and the other to stabilize the micelles in organic solvent. Metal-binding polymers are usually amphiphilic because of the need for highly polar interactions (e.g., ionic bonds) between the metal ions and the polymer. Therefore, hydrophobic nonmetallic PCL block is necessary to form the shells of diblock-copolymer micelles in organic solvent while P4VP block captured metal ions from aqueous phase or protecting metal nanoparticles after reduction for two-phase extraction of metal ions. Biodegradable and biocompatible polymers are better choices for use as shell components, i.e., to minimize the use of chemicals and the impact on the environment.[1] For example, poly(ε-caprolactone-*block*-4-vinylpyridine) (PCL-*b*-P4VP) is such a diblock copolymer that forms core/shell micelle structures in toluene.[13]

Gold nanoparticles (Au NPs)[14] have recently found many applications in industrial chemistry, such as in low-temperature CO oxidation,[15,16] hydrocarbon hydrogenation,[17–19] low-temperature hydrocarbon oxidation,[20,21] and NO reduction.[22] Most Au NPs are prepared through the chemical reduction of tetrachloroaurate ($AuCl_4^-$) using reducing agents such as sodium borohydride,[23] hydrazine,[24] or lithium borohydride.[25] The protonated pyridyl nitrogen atoms of P4VP blocks form ionic bonds with $AuCl_4^-$ ions and they also coordinate to the Au NPs formed after reduction of these ions.[24–27] Thus, PCL-*b*-P4VP copolymer micelles can be prepared to capture $AuCl_4^-$ ions from water and to recycle Au NPs into organic solvents.

PCL-*b*-P4VP copolymers can be synthesized through ring-opening polymerization (ROP) of ε-caprolactone (ε-CL) followed by free radical polymerization (FRP) of 4-vinylpyridine (4-VP). After ligand exchange of the hydroxyl groups with either stannous(II) octoate [$Sn(Oct)_2$] or aluminum tris(isopropoxide) [$Al(iOPr)_3$], the stannous alkoxide group (SnOR) can catalyze the bulk ROP of ε-CL at 110 °C or the aluminum alkoxide group (Al-OR) can initiate ROP of ε-CL at 25 °C in toluene or tetrahydrofuran.[28,29] Living free radical polymerizations (LFRPs) exhibiting low degrees of radical termination are necessary for polymerization of the second P4VP block from the PCL-macroinitiator.[30] In such LFRPs as atom transfer radical polymerization (ATRP), nitroxide-mediated radical polymerization (NMRP), and reversible addition fragmentation (RAFT), the propagating radicals $P^\bullet$ react reversibly with inert persistent species T [e.g., a Cu(I) complex for ATRP, a stable nitroxide free radical (e.g., TEMPO or 4-OH-TEMPO in this study) for NMRP, or a dithioate for RAFT] to form reversible dormant products (P-T), significantly increasing the selectivity (r_p/r_t = ca. $1/[P^\bullet]$) of propagation (r_p = ca. $[P^\bullet]$) to termination (r_t = ca. $[P^\bullet]^2$), where r_p, r_t, and $[P^\bullet]$ are the rates of propagation and termination and the concentration of the propagation radical, respectively.[31–33] Because the strong metal ligands of the P4VP block react with copper cations to form metal complexes during ATRP, purification of the resulting polymers can be very time-consuming and repetitious. Using the RAFT technique, the dithioate reagents can bond with the metal ions. Thus, it is not easy to incorporate dithioate groups onto the chain end of PCL for preparation of PCL-*b*-P4VP block copolymers. The use of styrenic monomers, a unimolecular initiator, and bulk polymerization are the three major limitations of the TEMPO-mediated NMRP because of the high dissociation energy of the C–O bonds on the *N*-alkoxyamine groups, the high reactivity of TEMPO, and the ready transfer of the free radicals to the solvent. In the absence of a metal catalyst, NMRP remains the preferable route toward PCL-*b*-P4VP copolymers.[34] Moreover, Hawker et al. succeeded in the preparation of poly(ε-caprolactone-*block*-styrene) through the ROP of ε-CL and the NMRP of styrene when using hydroxyl-functionalized *N*-alkoxyamines (the same structure as **HA** in this study) as difunctional initiators.[35]

During the propagation step of TEMPO-mediated NMRPs using a starting material of benzoyl peroxides (BPOs) at 120 °C, a vinyl monomer is inserted into the C–O bond of the *N*-alkoxyamine end-group (**Scheme 2-1b**), which arises as the product of the radical addition between a carbon-centered radical and TEMPO (**Scheme 2-1a**). Such *N*-alkoxyamine products are stable at temperatures below 50 °C and, thus, they can be isolated for use as unimolecular initiators for one-step polymerizations at 120 °C.[36] In contrast, the in situ preparation of *N*-alkoxyamine intermediates—by mixing a radical source (e.g., BPO or AIBN) and a stable nitroxide free radical (e.g., TEMPO or 4-OH TEMPO)—allows them to be used as bimolecular initiators for two-step polymerizations (e.g., one performed at 80 °C for 2 h and the other at 120 °C for 24 h; **Scheme 2-1**). In 1993, it was determined that the optimal TEMPO addition for living polystyrene polymerization was 1.3 equivalents relative to BPO (rather than the two-fold ratio expected theoretically), implying that side reactions occurred for the bimolecular initiator.[37,38] The decomposition temperature

(T_d, i.e., the temperature at which half of the concentration is consumed within 1 h) of the BPO is 92 °C in toluene. Thus, the reaction temperature for the preparation of *N*-alkoxyamines using BPO and TEMPO in styrene has been established to be 80 °C. A 42% yield of *N*-alkoxyamine products was obtained after column chromatographic purification at this reaction temperature.[36] Gravert and Janda found, however, that this product was formed in 34% yield at 50 °C.[39] Moad et al.[40,41] and Veregin et al.[42] studied the mechanism of the reaction between BPO and TEMPO in styrene at 60 °C. In addition to the thermolysis of BPO, they found that TEMPO can react with BPO to give the benzoxyloxyl radical, benzoate anion, and *N*-oxoammonium cation through one-electron transfer. Unfortunately, this redox reaction has been studied only rarely, even though NMRP has been applied widely to polymer synthesis since 1993.[37] Many reports mention that high-temperature decomposition of BPO results in radical-induced side reactions and, thus, low yields (<50%) of *N*-alkoxyamine products. We suspected that TEMPO-induced BPO decomposition could be a major reason for this behavior because an equimolar amount of TEMPO is required to prepare the benzoyoxyl radicals in this reaction pathway. For this purpose, it was necessary to clarify the mechanism of the reaction occurring between BPO and TEMPO in the styrene medium prior to NMRP. Braslau et al. demonstrated many alternative methods for generating carbon-centered radicals at temperatures below 50 °C for preparing high-yield *N*-alkoxyamine products as unimolecular initiators for NMRP; these methods included PbO_2-mediated oxidation of benzyl hydrazine, Cu^{II}-mediated oxidation of lithium enolates, and hydrogen or halide abstraction with non-carbon-centered radicals formed through photolysis or low-temperature thermolysis.[43] Nevertheless, most polymer chemists still select the BPO-TEMPO initiation system to prepare *N*-alkoxyamine unimolecular initiators because of its low-cost raw materials and simplicity. In addition, the benzoic ester products of

N-alkoxyamines can be used in many wide-ranging applications after alkaline hydrolysis. Use of the commercially available 4-hydroxyl-TEMPO is another option because the additional hydroxyl unit on the nitroxyl moiety is another group that can be converted into a variety of functionalities through chemical modification. Yin et al. attempted to prepare 4-OH-TEMPO-based *N*-alkoxyamines, but found that major products of the 4-hydroxyl-*N*-alkoxyamines were oxidized to 4-oxo-*N*-alkoxyamines, resulting in 8.6 and 18.5% yields for the 4-hydroxyl- and 4-oxo-*N*-alkoxyamines, respectively.[44] Thus, Hawker et al. protected the hydroxyl unit of 4-hydroxyl-TEMPO in the form of its benzoate ester to prepare diol *N*-alkoxyamines for the radical crossover study.[45] Taken together, all of these reports suggest that the reaction mechanism between BPO and TEMPO is worth studying, especially for living free radical polymerizations.

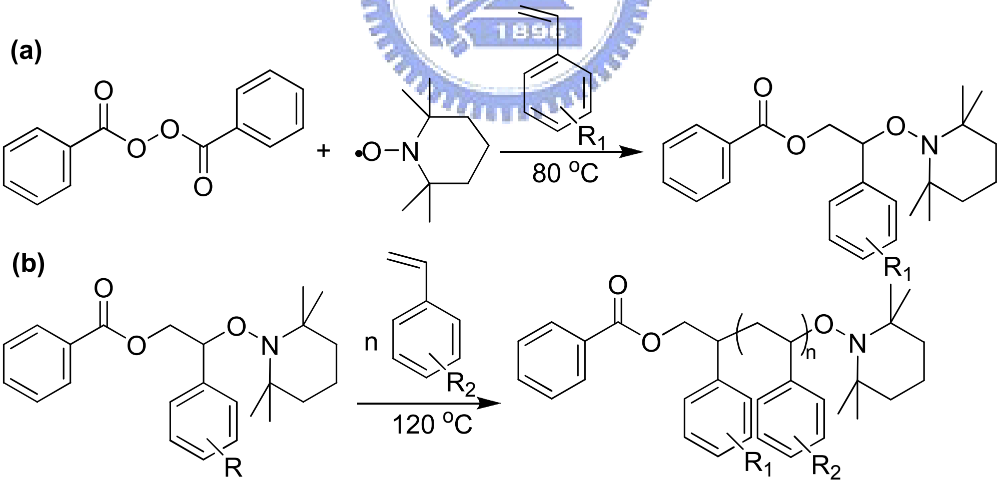

Scheme 2-1. Synthetic route toward NMRP through BPO-TEMPO bimolecular initiation: (a) *N*-alkoxyamine initiator formation; (b) styrene monomer insertion.

In this study, we synthesized the hydroxyl-functionalized *N*-alkoxyamine **HOA** for use in PCL-*b*-P4VP diblock copolymerizations employing sequential ROP and NMRP procedures in one batch. When preparing the *N*-alkoxyamines **A** and **OA**, heating was unnecessary, but the reaction rates were suppressed upon immersing the flask in an ice bath. The color of the solution changed from reddish brown to pale green initially for the reactions proceeding at temperatures below 25 °C. The comprehensive reaction mechanism was deduced after structural identification of the *N*-alkoxyamine products and their side products. With the stable nitroxide free radical of 4-OH-TEMPO, the product of **HOA** was used to initiate the ROP of ε-CL in toluene at 25 °C after the reaction with triethylaluminum ($AlEt_3$). The PCL-*b*-P4VP copolymers were obtained through bulk NMRP of 4-VP from PCL macroinitiators at 125 °C. Using ^1H NMR spectroscopic and GPC analyses, the living behavior of the ROP was confirmed by the linear relationship between the monomer conversion and the polymer molecular mass because all of the monomers were inserted from the aluminum alkoxide (Al-OR) bonds. Two HOA-to-$AlEt_3$ molar ratios (r = 1:1.2 or 1:0.6) were investigated for a kinetic study for the ROP of ε-CL in toluene (v = 30 or 60 mL). When r and v were 1.5 and 30 mL, respectively, the 99.5% conversion of the ε-CL monomers was achieved and then the solution batch was allowed to proceed via the NMRP of 4-VP at 125 °C after vacuum distillation of toluene. The similar trends in the GPC traces obtained using RI and UV dual detectors provided evidence for the NMRP of 4VP from the PCL-macroinitiator, i.e., because only the P4VP blocks absorb UV light. DSC thermograms revealed two glass transition temperatures—i.e., distinct thermal chain motions in the separation microdomains of the PCL and P4VP blocks—confirming that immiscible PCL-*b*-P4VP diblock copolymers had formed. After staining the P4VP cores with RuO_4 vapor, TEM images revealed micellar structures for the PCL-*b*-P4VP copolymers in a selective solvent for the PCL block [90% toluene/10% dichloromethane (DCM), v/v]. Although the two blocks of the PCL-*b*-P4VP copolymers are intrinsically insoluble in water, the P4VP block can capture $AuCl_4^-$ from the water–DCM interface in the form of an ionic pair

($NH^+\cdots AuCl_4^-$). Upon reduction with aqueous $NaBH_4$ solution, Au NPs were formed in the P4VP block core. As a result, the organic phase became yellow after two-phase extraction, but turned red after reduction. After the addition of excess toluene, we used UV–Vis spectroscopy, DLS, and TEM to analyze the Au NPs formed through PCL-*b*-P4VP copolymer-mediated reduction in the solvent selective for the PCL block.

2-2 Experimental Section

2-2.1 Materials.

ε-Caprolactone (ε-CL, 99.5%, ACROS), 4-vinylpyridine (4-VP, 99.5%, ACROS), and toluene (HPLC grade, TEDIA) were dried over calcium hydride (CaH_2, 95%, ACROS) for 24 h and then distilled under reduced pressure. The following chemicals and solvents were used as received: benzoyl peroxide (BPO, >97%, Fluka), styrene (St, 99%, ACROS), 2,2,6,6-tetramethylpiperidinooxy (TEMPO, 98%, ACROS), 4-hydroxy-2,2,6,6-tetramethylpiperidinooxy (4-OH-TEMPO, 98%, ACROS), triethylaluminum ($AlEt_3$, 0.9 M in hexane, Fluka), glacial acetic acid (HPLC grade, TEDIA), cyclopentanol (**a**, 99%, Alfa Aesar), hydrogen tetrachloroaurate(III) trihydrate ($HAuCl_4$·3H2O, 99.9%, ACROS), sodium borohydride ($NaBH_4$, 99.5%, ACROS), cyclohexanol (**b**, 99%, Alfa Aesar), cycloheptanol (**c**, 95%, Alfa Aesar), 1-pentanol (**d**, 98%, ACROS), 2-octanol (**e**, 97%, ACROS), tetrahydrofuran (THF, HPLC grade, TEDIA), methanol (MeOH, HPLC grade, TEDIA), and diethyl ether (Et_2O, HPLC grade, TEDIA). Reactions were performed in glassware under a static atmosphere of argon.

2-2.2 Measurement.

^{1}H and ^{13}C NMR spectra were recorded using a Varian Unityinova 500 NMR spectrometer. Elemental analyses were performed using a Heraeus CHN-O Rapid apparatus (Heraeus VarioEL). MS/MS measurements were performed using an ESI quadrupole time-of-flight instrument (Q-TOF; Micromass) operated in positive ion mode. GC-MS analyses were performed using a Trio 2000 quadrupole mass spectrometer (Micromass, Manchester, UK) equipped with a Fisons Instruments 8060 gas chromatograph and a fused silica capillary column (length: 30 m; inner diameter: 0.5 mm; film thickness: 0.25 μm) from Supelco. EI-MS analyses were performed through continuous quadrupole scanning at an ionization energy of 70 eV. UV–Vis spectra were measured using a UV-1601 spectrophotometer (Shimadzu, Japan). Melting points were measured on a Fargo MP-2D apparatus. The weight-average (M_w), number-average (M_n), and maximum (M_v) molecular weights and the polydispersity index (M_w/M_n) were determined through gel permeation chromatography (GPC) using a Waters 510 HPLC, equipped with a 410 differential refractometer, a refractive index (RI) detector, and three Ultrastyragel columns (100, 500, and 103) connected in series in order of increasing pore size, with DMF as eluent at a flow rate of 0.6 mL/min. DLS measurements were performed on a Brookhaven photon correlation spectrometer with BI9000 AT digital correlation. The instrument was equipped with a compass 315M-150 laser (Coherent Technologies), which was operated at a wavelength of 532 nm. Dust-free vials were used for sample preparation at a concentration of 1 mg/mL in a mixture of 10% DCM/90% toluene (v/v); measurements were made at 25 °C at an angle of 90°. The CONTIN algorithm was used to analyze the data. A DuPont DSC-9000 calorimeter, operated at a scan rate of 20 °C/min over the range from –100 to +180 °C, was used to record the DSC thermograms of samples (ca. 5–10 mg) sealed in aluminum pans. The temperature and energy were calibrated with indium. The glass transition temperature was obtained as the midpoint of the specific heat increment. A TA Instruments thermogravimetric analyzer, operated at a scan rate of 20 °C over temperatures ranging from 30 to 800 °C under a nitrogen purge of 40 mL/min, was used to record TGA thermograms of samples on a platinum holder. A Hitachi H-7500 transmission electron microscope (100 kV) was used to record TEM images of the diblock copolymer micelles after staining with RuO_4 vapor. A drop of dilute solution (1 mg/mL) was placed onto a carbon-coated copper grid. After 3 min, the excess solution was blotted away using a strip of filter paper. The samples were air-dried at room temperature and then stained with RuO_4 vapor.

2-2.3 UV–Vis Calibration of TEMPO Concentration.

The concentration of TEMPO in a reaction mixture can be determined using the Beer–Lambert law ($A = \varepsilon bc$) by monitoring the characteristic UV–Vis signal of TEMPO at 469.5 nm (**Figure 2-1**). In this equation, A is the absorbance at 469.5 nm in the UV–Vis spectrum, ε (L/mol/cm) is the molar absorptivity of TEMPO in THF, c (mol/L) is the concentration of TEMPO, and b (cm) is the path length of the sample holder. The constant εb was calculated to be 10.59 L/mol from the slope of the linear curve fitting the absorbance to the concentration (**Figure 2-2**). Therefore, the concentration of TEMPO at a given time interval can be deduced from the expression $A/(\varepsilon b)$. To ensure that all data were located on the calibration curve, the reaction mixtures were diluted with THF prior to analysis. The TEMPO calibration curve correlating the absorbance at 469.5 nm to the concentration, $y = 0.00596 + 0.01059x$ ($R^2 = 0.9995$), was determined from UV–Vis spectroscopic analysis of the standard solutions of TEMPO in THF.

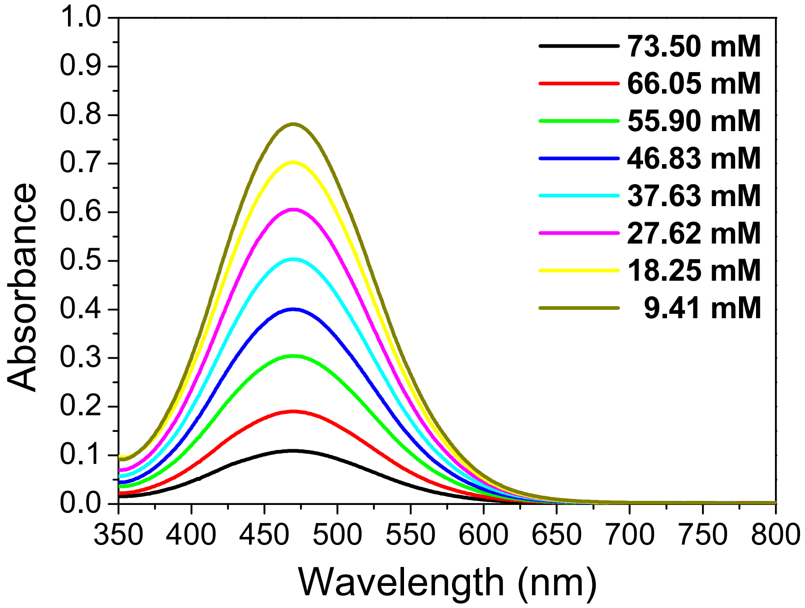

Figure 2-1. UV–Vis spectra of TEMPO in THF at various concentrations.

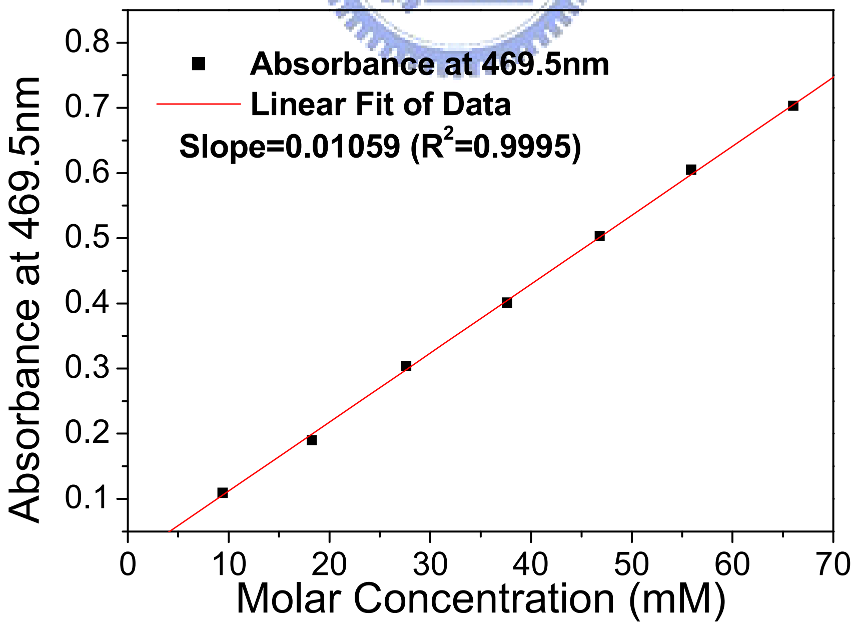

Figure 2-2. TEMPO calibration curve, correlating the absorbance at 469.5 nm to the concentration in THF.

2-2.4 Syntheses of *N*-Alkoxyamines.

A solution of BPO (15.0 g, 61.9 mmol) and TEMPO (5.0 g, 32 mmol) or 4-hydroxy TEMPO (5.5 g, 32 mmol) in styrene (50 mL) was cooled to 5 °C in an ice bath and then naturally warmed to room temperature after a removal of the bath. The reddish-brown solution gradually faded, turning into a pale green solution over several hours. The excess styrene was removed through vacuum distillation and the residual solid was partitioned between diethyl ether and 1 N aqueous NaOH. The product in the organic phase was dried (anhydrous $MgSO_4$) and the solvent was evaporated to give a light-yellow powder. White crystals of *N*-alkoxyamine products—the *N*-alkoxyamine **A** (5.2 g, 43%) and 4-oxo-*N*-alkoxyamine **OA** (4.3 g, 37%)—were obtained after recrystallization from MeOH. Melting points: **A**, 74.5 °C; **OA**, 111.0 °C. Mass spectra (ESI, *m/z*): **A**, 382.1 [MH^+]; **OA**, 396.2 [MH^+]. Elem. Anal. for **A** ($C_{24}H_{31}NO_3$): Calcd: C, 75.56; H, 8.19; N, 3.67; Found: C, 75.66; H, 8.23; N, 3.46; for **OA** ($C_{24}H_{29}NO_4$): Calcd: C, 72.89; H, 7.39; N, 3.54; Found: C, 72.84; H, 7.45; N, 3.31. ^1H and ^{13}C NMR spectra of **A** and **OA** are presented in **Figure 2-3**. FTIR spectra of **A** and **OA** are presented in **Figure 2-4**.

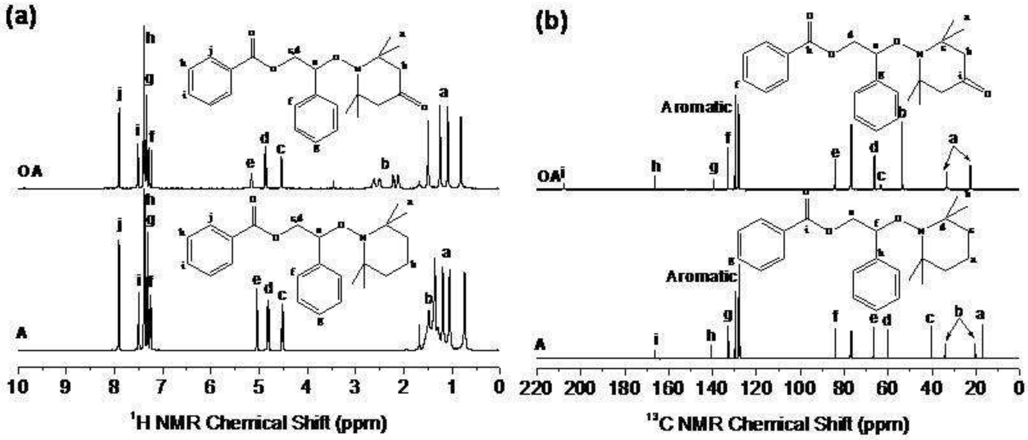

Figure 2-3. (a) ^1H and (b) ^{13}C NMR spectra of the *N*-alkoxyamine **A** and the 4-oxo-*N*-alkoxyamine **OA** formed from the reaction between BPO and TEMPO or 4-OH-TEMPO in styrene at temperatures below 25 °C.

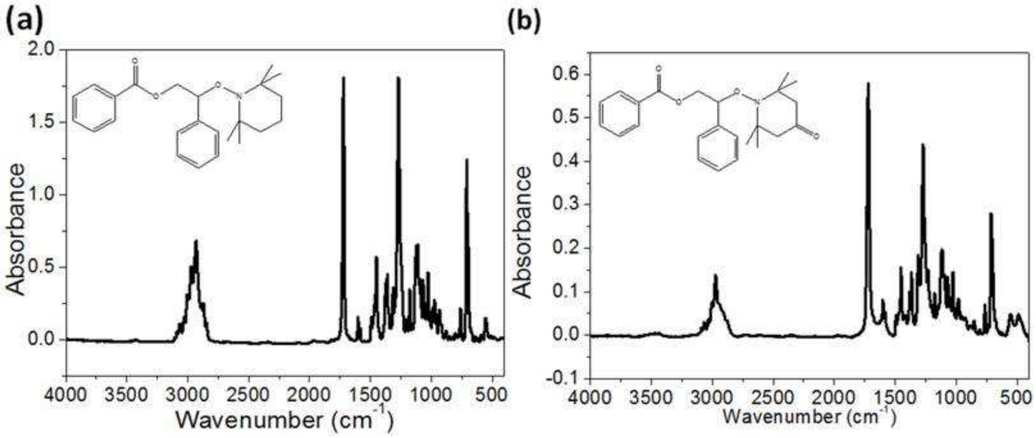

Figure 2-4. FTIR spectra of (a) the *N*-alkoxyamine **A** and (b) the 4-oxo-*N*-alkoxyamine **OA**.

2-2.5 Synthesis of Hydroxyl-*N*-alkoxyamines.

10 N Aqueous NaOH (10 mL) was added dropwise to a solution of the *N*-alkoxyamine adduct **A** (5.0 g, 13.1 mmol) or **OA** (5.0 g, 12.6 mmol) in a mixture of THF (10 mL) and MeOH (30 mL). After several hours, the solvent was removed through rotary evaporation and the product was washed with excess diethyl ether. After rotary evaporation, **HA** (3.3 g, 90 %) was obtained as a light-yellow liquid or **HOA** (3.2 g, 87 %) was obtained as a white solid (m.p. 69.2 °C). Mass spectra (ESI, *m*/*z*): **HA**, 278 [MH$^+$]; **HOA**, 292 [MH$^+$]; Elem. Anal. for **HA** ($C_{17}H_{27}NO_2$): Calcd: C, 73.61; H, 9.81; N, 5.05; Found: C, 73.79; H, 9.57; N, 4.95; for **HOA** ($C_{17}H_{25}NO_3$): Calcd: C, 70.07; H, 8.65; N, 4.81, Found: C, 69.96; H, 8.76; N, 5.43. The ^{1}H and ^{13}C NMR spectra of **HA** and **HOA** are presented in **Figure 2-5**; their FTIR spectra appear in **Figure 2-6**, respectively.

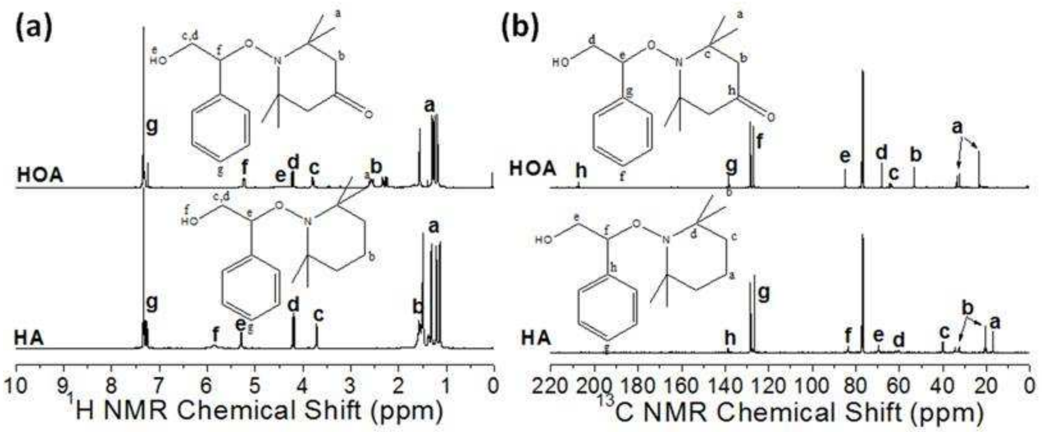

Figure 2-5. (a) ^{1}H and (b) ^{13}C NMR spectra of **HA** and **HOA.**

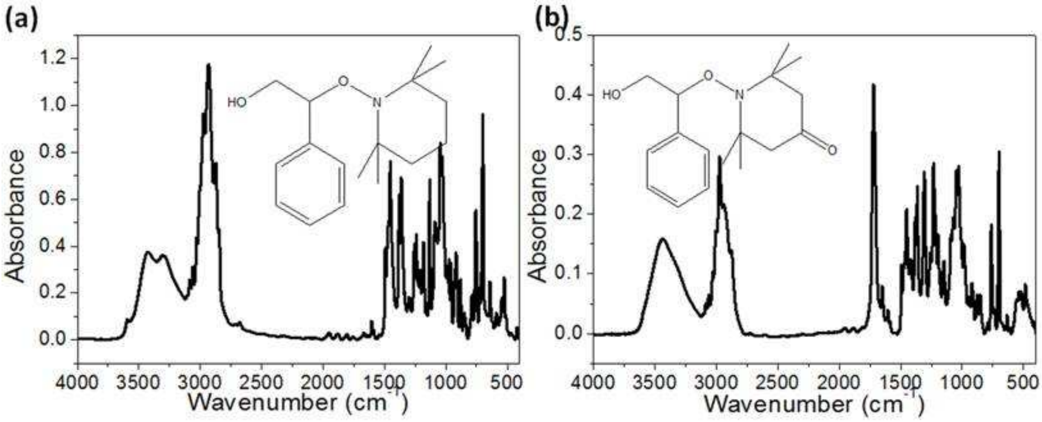

Figure 2-6. FTIR spectra of (a) hydroxyl the *N*-alkoxyamine **HA** and (b) hydroxyl the 4-oxo-*N*-alkoxyamine **HOA**.

2-2.6 Synthesis of *N*-Alkoxyamine-Functionalized Poly(ε-caprolactone).

A solution of $AlEt_3$ (ca. 0.9 mol/L in hexane, 0.42 mL) was added to a solution of hydroxyl-4-oxo-*N*-alkoxyamines (**HOA**, 27.8 mg, 0.25 mmol) in dry toluene (5 mL) under an argon atmosphere. The mixture was stirred at room temperature for 30 min, and then the resultant ethane was removed under reduced pressure. After adding dry toluene (25 mL), the flask was cooled in an ice bath and then ε-CL (5 mL) was quickly injected into the reaction mixture. The polymerization was performed at 25 °C for a given time and then stopped through the addition of glacial acetic acid (0.2 mL). After evaporation of the toluene through vacuum distillation, the PCL macroinitiator was used directly for the polymerization of 4-VP.

2-2.7 Synthesis of Poly(ε-caprolactone)-*block*-poly(4-vinylpyridine) Copolymers.

The dried PCL macroinitiator was charged with one, two, or four equivalents of the 4-VP monomer, based on the content of ε-CL. The vessel was immersed in an oil bath maintained at a temperature of 125 °C. When the stirrer bar stopped stirring in the highly viscous solution, the polymerization was quenched through immersion of the flask in an ice bath. The resultant diblock copolymers **BC1–3** were purified twice through dissolution in chloroform and precipitation from hexane.

2-2.8 Preparation of Micelle Solutions.

The diblock copolymer was dissolved DCM, a good solvent for both blocks, at a concentration of 10 mg/mL. Next, a poor solvent for one of the blocks was added to the polymer solution very slowly (up to 90%, v/v) to obtain a desired concentration of 1 mg/mL. Stirring of the solution was continued for 1 hrs (**Figure 2-12** and **Figure 2-14a**) and 24 hrs (**Figure 2-14b**) prior to characterization.

2-2.9 Synthesis of PCL-*b*-P4VP Copolymer-Mediated Au NPs.

Equimolar amounts of the pyridine units of the PCL-*b*-P4VP copolymers **BC1–3** in DCM (10 mL) were added to an $AuCl_4^-$ solution (30 mM, 10 mL) under stirring with a magnetic bar stirring. After 1 h, aqueous $NaBH_4$ solution (300 mM, 10 mL) was added and then the mixture was stirred for another 1 h. The PCL-*b*-P4VP copolymer-protected Au NPs **Au-BC1–3** were stabilized after adding toluene and separating the organic phase.

2-3 Results and Discussion

2-3.1 *N*-Alkoxyamines.

In comparison with bimolecular initiation, unimolecular initiation of NMRP provides improved control over the molecular mass distribution with narrow polydispersity ($M_w/M_n < 1.5$). Therefore, we prepared *N*-alkoxyamine unimolecular initiators for the synthesis of PCL-*b*-P4VP diblock copolymers using benzoyl peroxide (BPO) and 2,2,6,6-tetramethylpiperdinooxy (TEMPO) in the styrene medium. We observed, however, abnormal release of heat, resulting in the temperature increasing up to 50 °C, after mixing BPO with TEMPO in the styrene medium at 25 °C. Thus, this exothermic reaction should be suppressed by cooling, rather than heating. Because of the low solubility of BPO in styrene at temperatures below 20 °C, we controlled this reaction by dissolving BPO slowly during natural warming at temperatures between 5 and 25 °C. Remarkably, the color of the solution turned from reddish brown to pale green (**Figure 2-7b**), indicating consumption of TEMPO (note that reddish brown is the intrinsic color of stable nitroxide free radicals). Monitoring of TEMPO content at regular intervals using UV–Vis spectroscopy (**Figure 2-7a**), we observed that the nitroxide absorbance at 469.5 nm decreased as the solution's color faded. We determined the conversion of TEMPO quantitatively through calibration with the UV–Vis spectra of pure TEMPO in THF; we found that the conversion of TEMPO reached 60% after 2 h at temperatures from 5 to 25 °C and 90% after another 5 h at 25 °C (**Figure 2-7b**). We suspected that BPO would also participate in this reaction to produce benzoate anions as side products. Indeed, after using 1 N aqueous NaOH solution to extract the benzoate anions from an ethyl ether solution, we obtained the *N*-alkoxyamine products (**A** and **OA**) after recrystallization from MeOH. The NMR spectra (**Figure 2-3**) of the *N*-alkoxyamines **A** and **OA** were identical to those described previously,[33,35,39,44] confirming the release of the benzoyloxyl radicals from BPO and radical addition with styrene and TEMPO. The protons labeled H_c, H_d, and H_e from styrene in the *N*-alkoxyamine (**A**) and 4-oxo-*N*-alkoxyamine (**OA**) products appeared as three AB quartets of benzylic protons at 4.50–5.20 ppm in **Figure 2-3a**, providing direct evidence for the radical addition having occurred at such low temperatures (<25 °C). In comparison with the results of a previous study,[44] only the 4-oxo-*N*-alkoxyamines **OA** was obtained when using 4-OH-TEMPO. Because crystals of **OA** are insoluble in MeOH, it is easy to purify these compounds through precipitation. Upon recrystallization from the filtrate, we obtained a mixture of *N*-hydroxy-4-oxo-2,2,6,6-tetramethylpiperidine (*N*-hydroxylamine) and 2,6-dimethyl-6-nitrosohept- 2-en-4-one (nitroso compound), which we identified using ^{1}H NMR and FTIR spectroscopy and mass spectrometry (**Figure 2-8**).

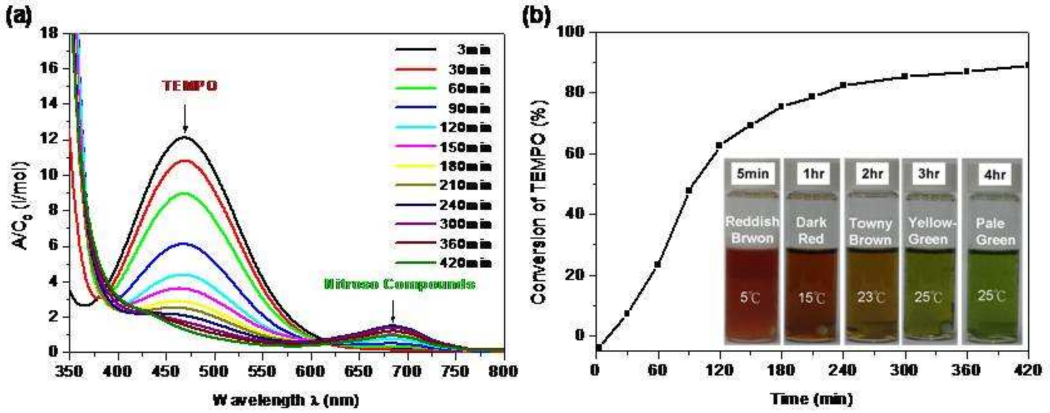

Figure 2-7. (a) UV–Vis spectra and (b) TEMPO conversion of the reaction mixture containing BPO, TEMPO, and styrene at various time intervals during ambient warming from 0 to 25 °C (A: UV–Vis absorbance; C_0: initial concentration of TEMPO in solution; UV-Vis quantification at 469.5 nm).

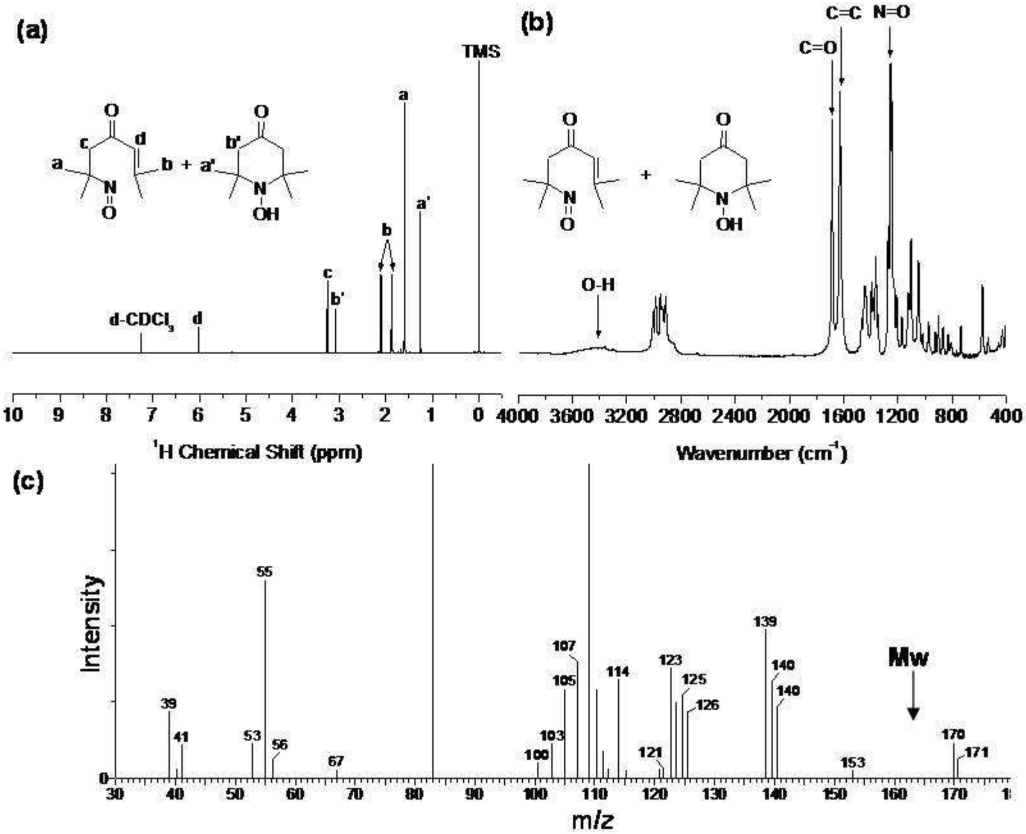

Figure 2-8. Structural identification of a mixture of *N*-hydroxy-4-oxo-2,2,6,6-tetramethylpiperidine and 2,6-dimethyl-6-nitrosohept-2-en-4-one using (a) ^{1}H NMR and (b) FTIR spectroscopy and (c) mass spectrometry.

2-3.2 Nitroxide-Induced Alcohol Oxidation.

In addition to NMRP, cyclic nitroxide free radicals (e.g., TEMPO and 4-OH-TEMPO) can also be used as catalysts for the oxidation of alcohols, for example, in the oxidation of alcohols using *m*-chloroperbenzoic acid (*m*-CPBA).[46,47] Cella et al. observed 4-oxo-TEMPO and 4-oxo-*N*-ammonium cations as side products when they used 4-OH-TEMPO in the nitroxide-catalyzed oxidation of alcohols with *m*-CPBA.[46] In the mechanism of nitroxide-catalyzed alcohol oxidation,[48] one electron is transferred from TEMPO or 4-OH-TEMPO to *m*-CPBA, resulting in *N*-oxoammonium cations, which behave as efficient oxidants (not *m*-CPBA) to produce *N*-hydroxyamines and the corresponding aldehyde or ketone. The activated *m*-CPBA, with its additional electron, should decompose into the *m*-chlorobenzoyloxyl radical and hydroxide. Excess *m*-CPBA can also react with *N*-hydroxyamines to regenerate *N*-oxoammonium cations and, therefore, the relatively low amounts of TEMPO and 4-OH-TEMPO behave catalytically. We suggested that the reaction between BPO and TEMPO proceeds through a similar one-electron transfer and heterogeneous decomposition to give benzoyloxyl radicals, the benzoate anion, and *N*-oxoammonium cations (**Scheme 2-2a**). Thus, *N*-alkoxyamine products can be obtained at temperatures below 25 °C through radical addition of the benzoyloxyl radical with styrene and TEMPO (**Scheme 2-2b**). The side products of the *N*-oxoammonium cations are well-known strong organic oxidants[48] (**Scheme 2-2c**), and these unstable (ring strain) cations could undergo intermolecular rearrangement with benzoate anions to give a nitroso compound (**Scheme 2-2d**).[49] In the presence of the stable nitroxide free radical 4-OH-TEMPO, we attribute the formation of the 4-oxo-*N*-alkoxyamine **OA** to oxidation with the *N*-oxoammonium cation. Therefore, the 4-oxo-*N*-oxoammonium cation can be converted to *N*-hydroxy-4-oxo-2,2,6,6- tetramethylpiperidine through alcohol oxidation or to 2,6-dimethyl-6-nitrosohept-2-en-4-one through ring-opening rearrangement with benzoate anions (**Figure 2-8**). According to Langhals' study, the pale green color observed in the photograph in **Figure 2-7b** corresponds to the UV–Vis absorbance of 2,6-dimethyl-6-nitrosohept-2-ene (nitroso compound) at 685 nm.[49]

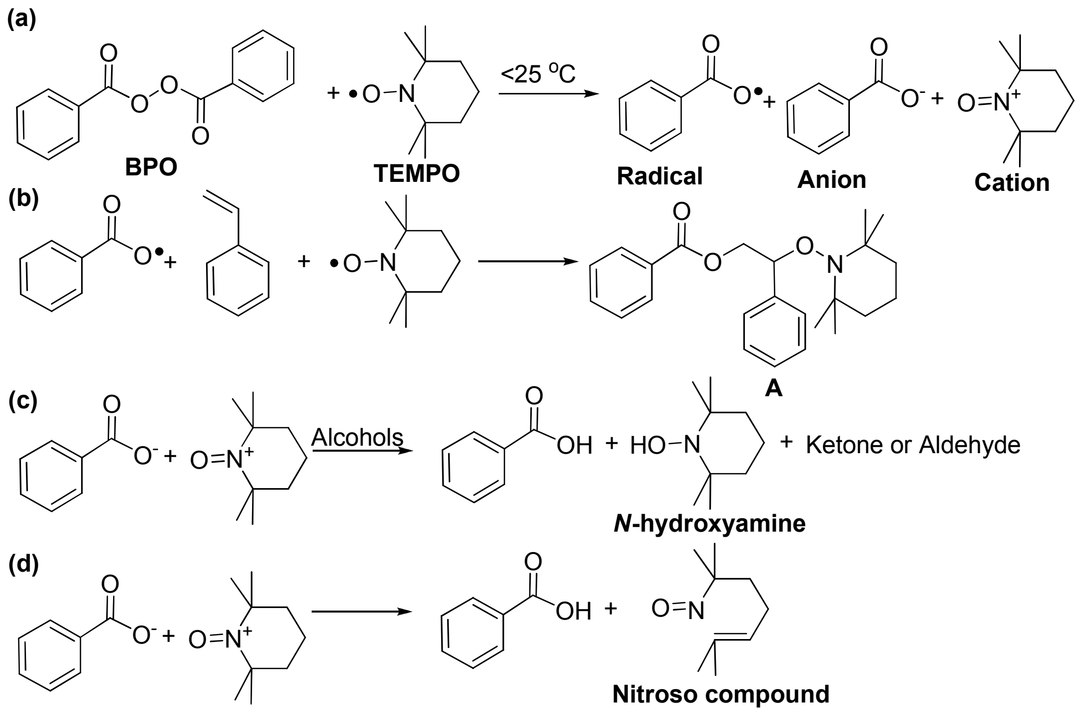

Scheme 2-2. Low-temperature reaction mechanism: (a) redox-induced decomposition of BPO; (b) radical addition; (c) alcohol oxidation; (d) ring-opening rearrangement.

2-3.3 Temperature Effect.

In the study reported by Yin et al.,[44] 4-hydroxyl- and 4-oxo-*N*-alkoxyamine products were obtained in 8.6 and 18.5% yields after heating BPO and 4-OH-TEMPO in styrene at 80 °C. In contrast, we obtained only the 4-oxo-*N*-alkoxyamine in 37% yield at temperatures below 25 °C. When we added five equivalents of an alcohol to a solution containing BPO, TEMPO, and styrene, we found that the conversion of the alcohol—determined using ^{1}H NMR spectroscopy (**Table 2-1**)—was less than 20%, i.e., equal to the TEMPO content (**Figure 2-9**). In this reaction, the conversion of the alcohol through oxidation depends on the concentration of *N*-oxoammonium cations.[48] In the presence of excess BPO, we suspect that *N*-oxoammonium cations were generated through a redox reaction between BPO and TEMPO, although BPO is not a sufficiently strong oxidant to regenerate *N*-oxoammonium cations from *N*-hydroxylamines. Therefore, the *N*-oxoammonium cations could not oxidize all of the 4-hydroxyl-*N*-alkoxyamines, resulting in a mixture of 4-hydroxyl-*N*-alkoxyamine and 4-oxo-*N*-alkoxyamine products when some of the BPO decomposed thermally at 80 °C. Our proposed reaction mechanism suggests that some nitroxyl radicals are converted into *N*-oxoammonium cations during the bimolecular initiation for NMRP. Thus, unimolecular initiation is a better choice for preparing PCL-*b*-P4VP diblock copolymers so as to avoid inactive polymer chains.[13] During NMRP, the high mobility of the nitroxyl moiety is a very important factor of the rapid combination reaction between propagating free radical and nitroxyl radicals for the well-controlled living polymerization. Therefore, a more efficient ROP of ε-CL is initiated from the OH groups on the carbon-centered fragments, rather than the nitroxyl moieties. We selected the low-cost and commercially available 4-OH-TEMPO to prepare the hydroxyl-4-oxo-N-alkoxyamine **HOA** for use as a difunctional initiator in the synthesis of PCL-*b*-P4VP because all of the OH groups of 4-OH-TEMPO are oxidized and the products **OA** and **HOA** are very easily obtained.

Table 2-1. Oxidation Conversion of Alcohols to Ketones or Aldehydes, Determined From Integral Area Ratio of Their Characteristic Peaks in ^{1}H NMR Spectra.

Entry	Alcohol	Ketone/Aldehyde	Assigned Peak in ^{1}H NMR Spectrum		Conversion[a] (%)
			$C\underline{H}OH$ (ppm)	$C\underline{H}_2C{=}O$ (ppm)	
a	Cyclopentanol	Cyclopentanone	4.41	2.22	10.9
b	Cyclohexanol	Cyclohexanone	3.68	2.39	13.7
c	Cycloheptanol	Cycloheptanone	3.94	2.57	16.8
d	1-Pentanol	1-Pentanal	3.73	2.48	9.6
e	2-Octanol	2-Octanone	3.89	2.48	18.7

[a]: Addition of five equivalents of alcohol with respect to the TEMPO content.

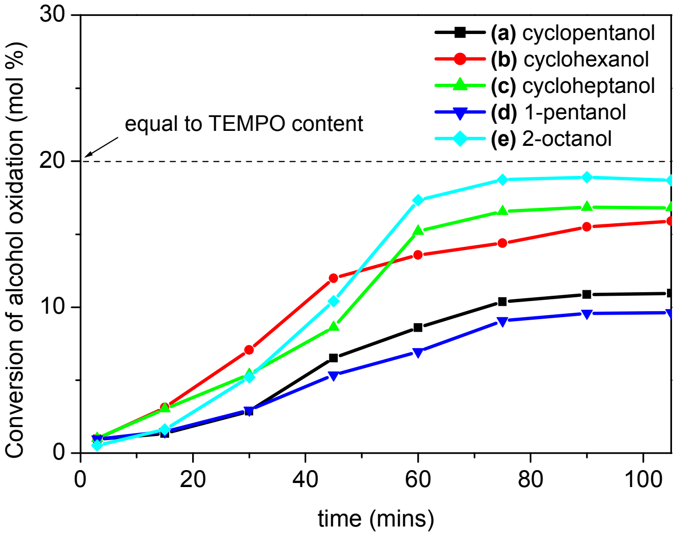

Figure 2-9. ^{1}H NMR monitoring the alcohol conversion in the reaction mixture: (a) cyclopentanol, (b) cyclohexanol, (c) cycloheptanol, (d) 1-pentanol, and (e) 2-octanol.

2-3.4 PCL Macroinitiators.

After hydrolysis of the benzoate ester on the 4-oxo-*N*-alkoxyamine **OA**, the dual (or double-headed) product, the hydroxyl-4-oxo-*N*-alkoxyamine **HOA**, contains a single primary alcohol, which is used as the initiating center for the living ROP of cyclic lactones, and a secondary benzylic group, which is an efficient initiator for the nitroxide-mediated “living” free radical polymerization of vinyl monomers. **Scheme 2-3c** depicts the ROP of ε-CL after the hydroxyl-4-oxo-*N*-alkoxyamine **HOA** had reacted with $AlEt_3$. Three types of aluminum alkoxides— $AlEt_2OR$, $AlEt(OR)_2$, and $Al(OR)_3$—may be formed in this step; living chain propagation succeeds through ester exchange with the ε-CL monomers. Because excess $AlEt_3$ can coordinate with the C=O groups on the ε-CL monomers to promote ester exchange (**Scheme 2-4**),[50] at a high ratio (r = 1.5) of $AlEt_3$ to **HOA**, most of the products were in the form $AlEt_2OR$, the propagation rate of which is the highest because of the low degree of steric hindrance for the approach of the next ε-CL monomer. The GPC trace for the product of ε-CL polymerization (**Figure 2-10a**) displays a shift in the molar mass distribution to higher molecular mass upon increasing the degree of monomer conversion. The presence of trace amounts of $AlEt(OR)_2$ and $Al(OR)_3$, with their low propagation rates, may have resulted in PCL chains of lower molecular mass (i.e., the chromatographic tail). The ^1H NMR spectrum (**Figure 2-10b**) of the product of PCL polymerization (a dilute solution in $CDCl_3$ containing a trace of acetic acid) exhibits two signals at 4.24 and 4.14 ppm for protons on the carbon atoms adjacent to oxygen atoms, corresponding to cyclic monomers and linear polymers, respectively, indicating that complete conversion (>99.5%) occurred after 3 h. Therefore, we expected that upon increasing the conversion, the number-average molecular mass (M_n in **Figure 2-10a**) would deviate from the theoretical values (M_w), which we calculated from ^1H NMR spectra (**Figure 2-10b**), as indicated in **Figure 2-10c**. In contrast, the maximum intensity (M_v) of the molecular mass distribution would agree with M_w; this trend provides evidence for a living PCL polymerization in which most of the ε-CL monomers are inserted from reactions with $AlEt_2OR$ species. Thus, the presence of $AlEt(OR)_2$- or $Al(OR)_3$-initiated low-molecular-mass PCL chains result in the deviation of the GPC-obtained values of M_n from the ^1H NMR spectroscopy-derived values of M_w at high monomer conversions. At a lower $AlEt_3$ content ($r = 1.2$), fewer monomers become activated and PCL polymerization requires more time (ca. 8 h) to reach completion. In contrast, when r is equal to 0.6, the $AlEt(OR)_2$- and $Al(OR)_3$-initiated PCLs form gels at ca. 20% conversion because they exist in the form of two- or three-arm high-molecular-mass star polymers prior to cleavage of the Al-OR bonds with glacial AcOH. By adding two equivalents of toluene ($r = 0.6$; $v = 60$), the reaction rates are depressed as a result of a dilution effect and the ultimate conversion also stops at 20%, as indicated in **Figure 2-10d**.

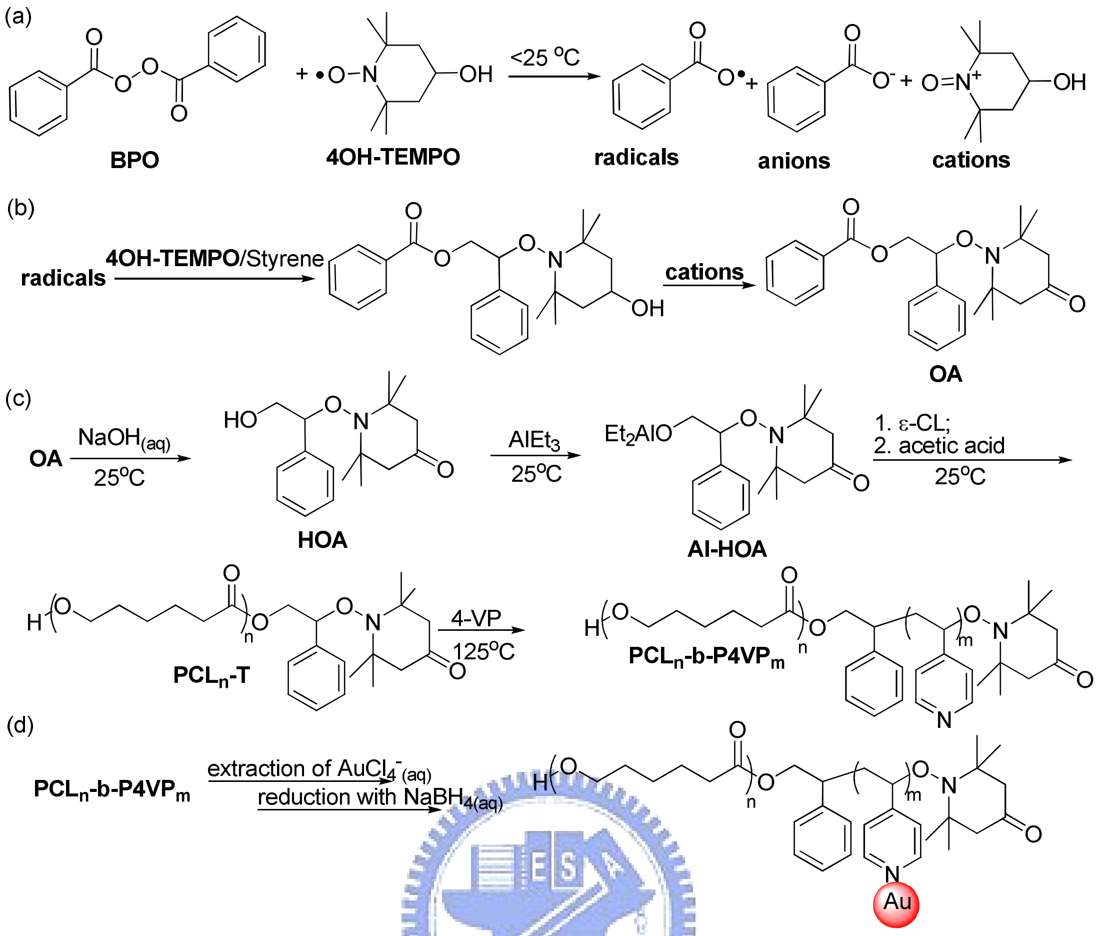

Scheme 2-3. Synthetic route toward PCL-b-P4VP block copolymer-mediate Au NPs: (a) redox-induced decomposition of BPO; (b) radical addition and alcohol oxidation; (c) synthesis of PCL-b-P4VP; (d) incorporation of Au NPs.

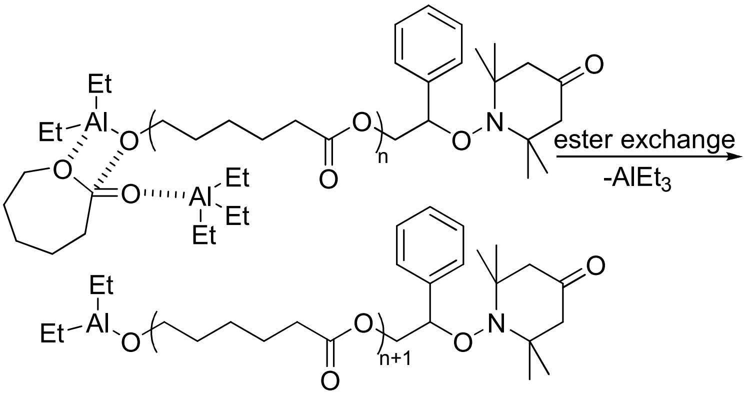

Scheme 2-4. Diethyl aluminum alkoxide-induced ROP of ε-CL in the presence of $AlEt_3$.

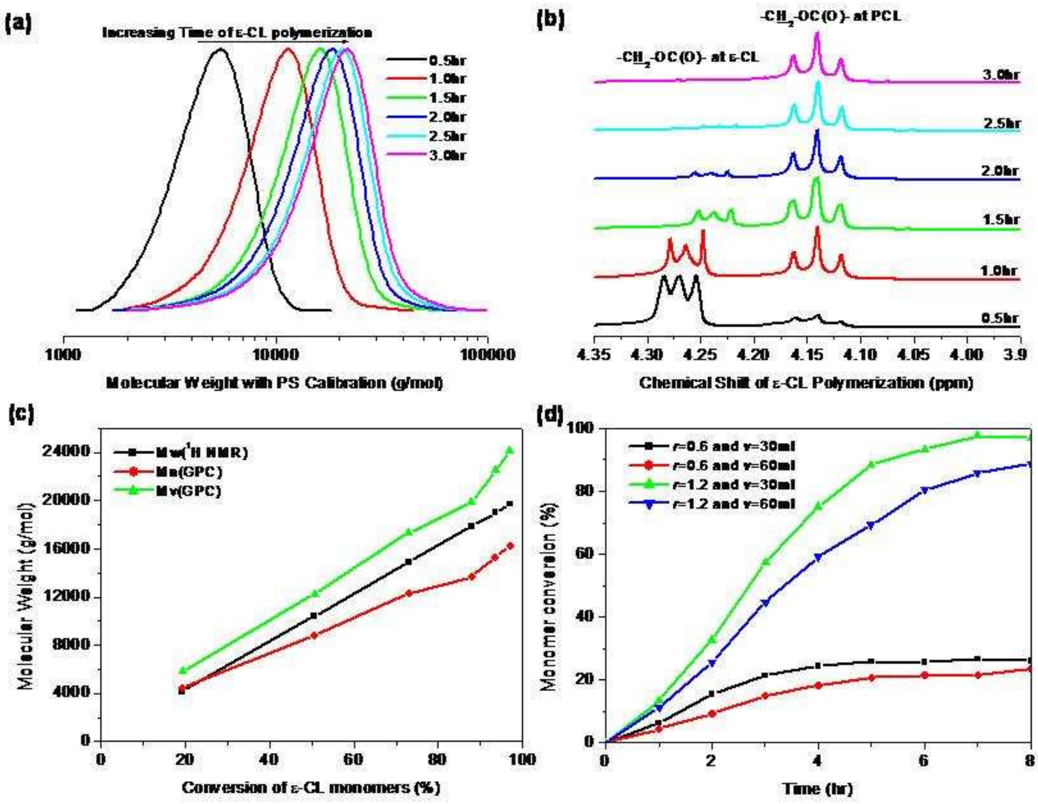

Figure 2-10. Aluminum alkoxide-initiated ROP of ε-CL leading to PCL (5g, 20,000 g/mol): (a) GPC traces, (b) ^{1}H NMR spectra, and (c) molecular mass comparison of polymerization (r = 1.5; v = 30 mL); (d) monomer conversions at values of r of 0.6 or 1.2 and values of v of 30 or 60 mL.

2-3.5 PCL-*b*-P4VP Copolymer.

Under conditions where r and v are 1.5 and 30 mL, respectively, the high conversion of PCL polymerization (>99.5%) for 20,000 g/mol PCL allows the bulk NMRP immediately at 125 °C (without precipitation with MeOH) after deactivation of aluminum alkoxide with glacial AcOH, followed by vacuum distillation of toluene and replacement with the 4-VP monomer in **Scheme 2-3c**. After another 20 h, the solution becomes a gel (immobilizing the magnetic stirrer), which is a direct indication of diblock copolymer formation. **Table 2** lists the compositions of the as-synthesized PCL-*b*-P4VP diblock copolymers (**BC1–3**) and their thermal properties. For homopolymerization of poly(4-vinypyridine) by NMRP, the conversion of the monomers was ca. 50%.[34] Even when adding one, two, or four equivalents of 4-VP monomers by weight, the conversions of the three bulk NMRPs were relatively low (23, 20, and 15% for **BC1–3**, respectively) because the *N*-alkoxyamine end groups are restricted in the P4VP domain, which is segregated from the PCL block because of their immiscibility. **Figure 2-11a** indicates that the RI signals (unbroken lines) in the GPC traces shifted to higher molecular mass after the addition of more 4-VP monomer, especially in the high-molecular-mass region. The arene-sensitive UV signals (dashed lines) of the three PCL-*b*-P4VP diblock copolymers are coincident with those of the density-sensitive RI detector, indicating that all of the 4-VP monomers had been inserted from the *N*-alkoxyamine end groups of the PCL-macroinitiator. Upon increasing the molecular mass, deviation of the UV- and RI-derived signals resulted from more 4-VP units being present in the high-molecular-mass PCL-*b*-P4VP diblock copolymers (e.g., in **BC3**). This behavior for the living P4VP polymerization is fully consistent with the insertion of the 4-vinylpyridine monomer units from the *N*-alkoxyamine end groups of the PCL-macroinitiators. ^{1}H NMR spectra confirmed the diblock copolymer composition; **Table 2-2** presents the integral areas of the signals at 4.14 and 6.39 ppm for the two protons on the PCL and P4VP repeat units, respectively.

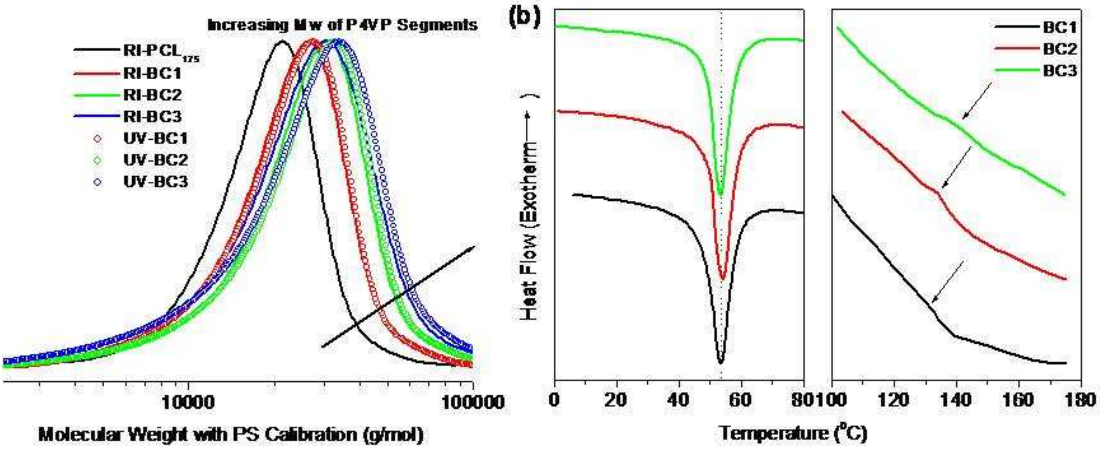

Figure 2-11. (a) GPC traces (RI and UV dual detection) of the **PCL** and the **BC1–3** and (b) DSC thermograms of the **BC1–3**: PCL melting transition (left) and P4VP glass transition (right).

Table 2-2. Compositions, molecular mass distributions, and thermal properties of PCL-macroinitiator **PCL** and PCL-*b*-P4VP diblock copolymers **BC1–3** and **Au-BC1-3**

Composition				Molecular Mass Distribution				Thermal Properties				
PCL$_n$-b-P4VP$_m$				M_w^{c}	M_n^{d}	M_v^{d}	PDI^d	T_d^{e} 5wt. % loss	Char Yield^e at 700 °C	T_g^{f} PCL	T_g^{f} P4VP	T_m^{f} PCL
Entry	n^a	m	n/m^b	g/mol	g/mol	g/mol		°C	wt.%	°C	°C	°C
PCL	175	0	—	20000	16700	20200	1.21	299	0.5	–58	—	54
BC 1	175	44	3.99	24900	19000	24600	1.29	291	0.3	–57	140	53
BC 2	175	75	2.16	28800	21700	28600	1.32	289	2.16	–59	134	54
BC 3	175	117	1.50	32600	21300	29700	1.40	296	2.65	–54	132	55
Au-BC 1	—	—	—	—	—	—	—	253	16.08	—	—	—
Au-BC 2	—	—	—	—	—	—	—	213	15.18	—	—	—
Au-BC 3	—	—	—	—	—	—	—	223	15.79	—	—	—

[a]: Obtained from kinetic studies of ^{1}H NMR spectra, where n and m are the number of repeat units for the PCL and P4VP blocks, respectively.

[b]: Obtained from integration of the signals at 4.14 and 6.39 ppm in the ^{1}H NMR spectra for the PCL and P4VP blocks, respectively.

[c]: Calculated using the expression n × $M_{\varepsilon\text{-CL}}$ (114.1 g/mol) + m × $M_{4\text{-VP}}$ (105.1 g/mol) + $M_{\text{initiator}}$ (291.4 g/mol).

[d]: Obtained from GPC trace (eluent: DMF; 0.6 mL/min; PS-standard calibration): M_n, number-average molecular mass; M_v, molecular mass with the highest RI-intensity; PDI, molecular mass distribution.

[e]: Obtained from TGA thermograms recorded at a heating rate of 20 °C/min.

[f]: Obtained from second-run DSC thermograms recorded at a heating rate of 20 °C/min.

Chemical dissimilarity between two blocks (i.e., melting point of PCL block and glass transition of P4VP block are observed in **Figure 2-11b**) often confers an amphiphilic character to be used as polymeric surfactants. When dispersed in a selective solvent, which is compatible with PCL block but not with the other, asymmetric thermodynamic interactions lead to the formation of nanodomains with dimensions comparable to the molecular dimensions.[51] Although NMRP cannot control the molecular weight distribution as well as anionic polymerization ($M_w/M_n < 1.10$), TEM images revealed that the three PCL-*b*-P4VP diblock copolymers **BC1**–**3** possessed regular star-micellar structures with smooth and distinct boundaries—i.e., spheres for **BC1** and **BC2**; spheres and rods with hemispherical caps for **BC3**—in the good solvent (toluene) for only the PCL block. Bedejacq et al also found that the polystyrene-b-poly(acrylic acid) diblock copolymers ($M_w/M_n > 2$) can form the well-ordered microdomain structures in the bulk state.[52] DLS analysis of the PCL-*b*-P4VP diblock copolymers **BC1–3** in toluene/DCM (**Figure 2-12**) exhibited average micellar sizes (D_h) of 36, 58, and 87 nm, respectively, and polydispersity indices of 0.266, 0.094, and 0.179, respectively. TEM images of the RuO_4-stained PCL-*b*-P4VP diblock copolymers **BC1**–**3** revealed average core sizes (D_c) of 18, 29, and 41 nm due to the increase of P4VP block length. This observation indicates that the propagation of P4VP blocks initiate from the PCL macroinitiators to give the PCL-b-P4VP copolymers without P4VP homopolymers. Thus, the PCL-b-P4VP copolymer can form the smooth boundary of micelles through self-assembling P4VP chains in the core region (**Figure 2-13**). Both PCL and P4VP blocks are soluble in dichloromethane (DCM, green dots), showing DCM-swelled polymeric chains. When adding toluene (brown dots), the P4VP blocks are excluded from the solvent mixture due to the thermodynamic disfavor with toluene. When the length of PCL is very long, the repulsive interactions among intercoronal chains exceed the interfacial energies and dominate the equilibrium structure. As adding more toluene, the P4VP blocks are quickly segregated into the separated phase (transient micelles) to reduce the interface area with toluene but the stable micelles with thermodynamic stable state need time to balance three interactions: stretching between aggregated P4VP chains, repulsion between DCM-swelled PCL chains, and interface tension between P4VP and PCL domains.[53,13] When the volume fractions of P4VP domains are larger than 0.3, the solution morphology of PCL-b-P4VP shifts from spheres to rods in toluene/DCM (90/10 v/v). As the length of the P4VPis increased, the core chain stretching becomes relatively significant and can be suppressed by connecting spheres to form smooth rods with hemisphereical caps.[54] Meanwhile, the repulsion between PCL chains and the interface tension can be also decreased. In addition, the increase of PCL shell thickness from 18 to 29, and to 46 nm for **BC1**, **BC2**, and **BC3** results from stretching PCL corona chains. As a result, the coexistence of spherical and rod-like structures of **BC3** with low total interfacial energies is favored, rather than spherical micelles such as **BC1** and **BC2**. It is believed that rod-like micelles are formed by collision of the spherical micelles followed by fusion. Thus, the coexistence of spherical and rod-like micelles can be attributed to at least two factors. First, a lack of communication between spherical micelles results in long-lived metastable structures. Second, polydispersity, an inevitable consequence of synthetic techniques, may contribute as well.[51,55,56] In comparison with TEM images in **Figure 2-14**, the more rod-like morphology for a long term of stirring indicates that a lack of communication between spherical micelles mainly results in the coexistence microstructures in **Figure 2-12c**.

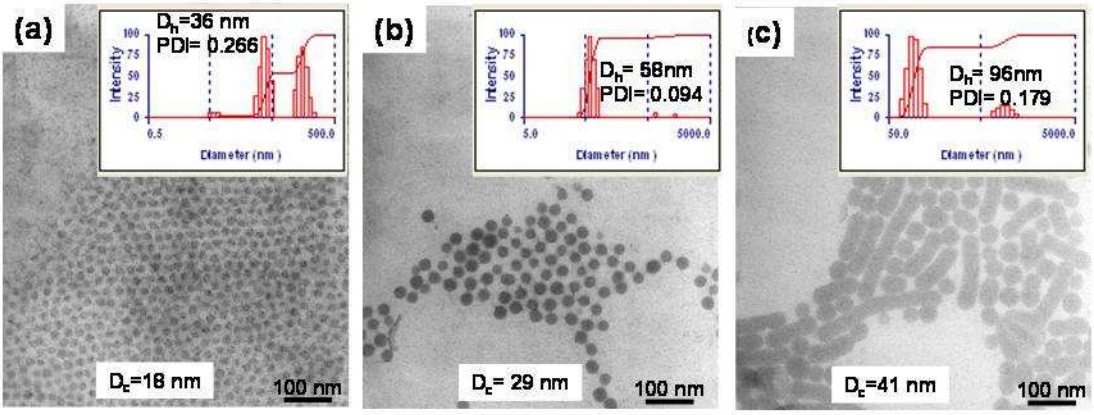

Figure 2-12. TEM images and inserted DLS graphs of PCL-*b*-P4VP diblock copolymer micelles (1 mg/mL) in a solvent of 10% DCM and 90% toluene (v/v) under stirring for 1h: (a) **BC1**, (b) **BC2**, and (c) **BC3**.

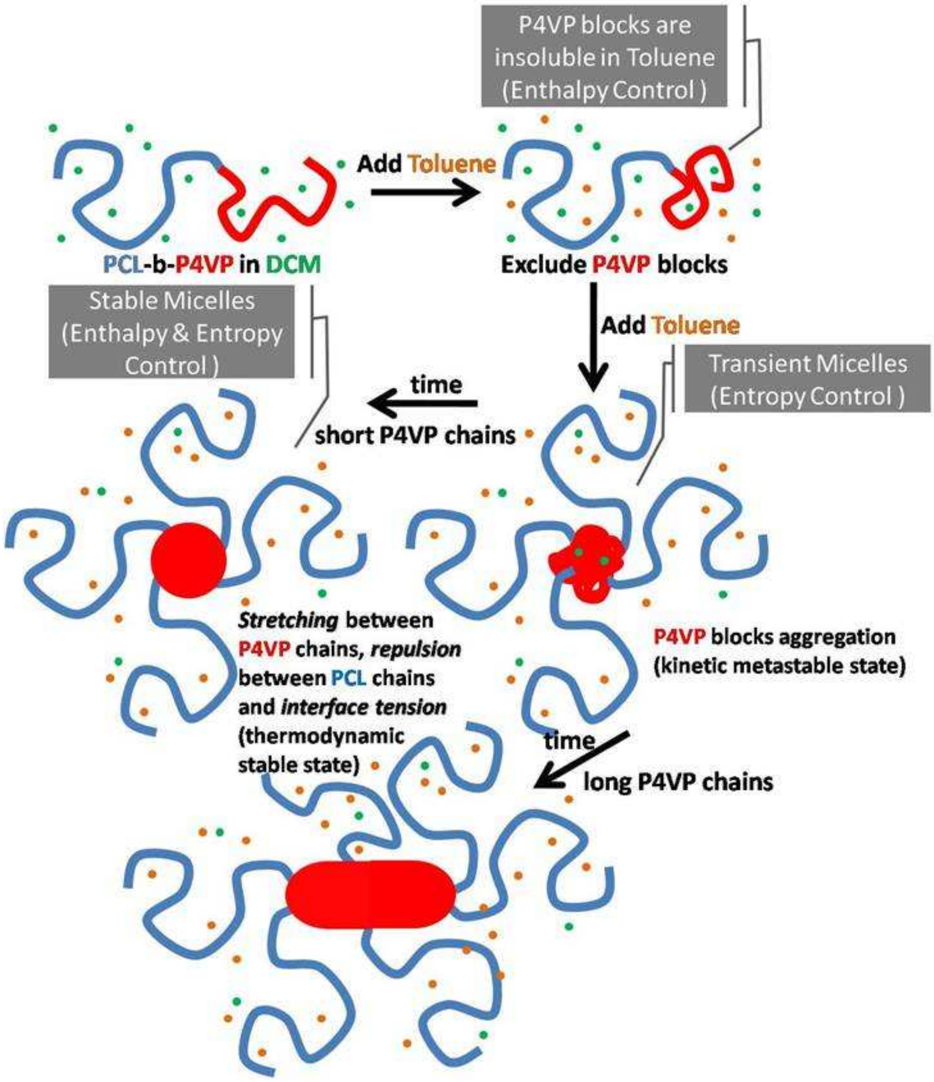

Figure 2-13. Schematic self-assembly mode of PCL-*b*-P4VP copolymers in toluene/DCM (90/10 v/v).

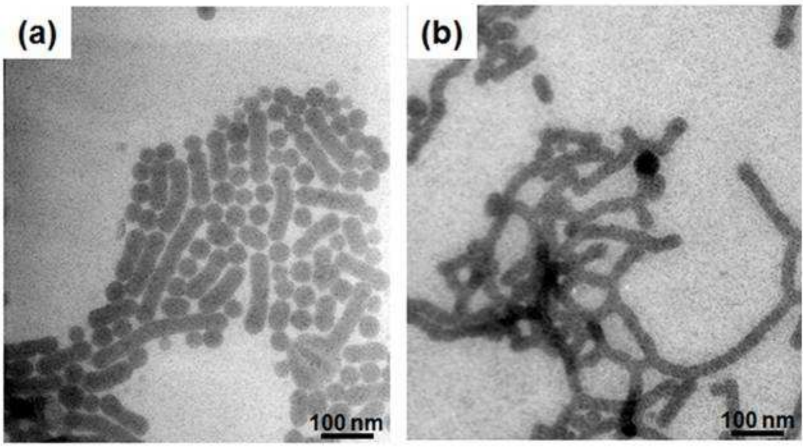

Figure 2-14. TEM images of **BC3** micelles (1 mg/mL) in toluene/DCM (90/10 v/v) under stirring for (a) 1hr and (b) 24 hr.

2-3.6 PCL-*b*-P4VP Copolymer-Protected Au NPs.

To remove heavy metal ions from wastewater through simple filtration separation, coagulation of metal-binding polymers is required. In this case, the hydrophobic PCL block plays an important role during the two-phase extraction because the metallated P4VP block with an ionic bond of $NH^+\cdots AuCl_4^-$ becomes amphiphilic,[57] which would emulsify partial copolymers possessing short-chain PCL blocks, resulting in turbid aqueous solutions (see, for example, the upper layer of the inserted graphs after extraction of $HAuCl_4$ in **Figure 2-15**). For the organic phase, we can also recycle metal ions in the form of NPs through chemical reduction. As indicated in **Scheme 2-3d** and **Figure 2-15**, an equimolar amount of $AuCl_4^-$ anions (with respect to pyridine units) can be added to transfer from water to DCM through ionic interactions with the protonated pyridyl groups (i.e., $NH^+\cdots AuCl_4^-$). The miscible of P4VP block in DCM was deteriorated due to the excess amounts of $HAuCl_4$ at which the accommodation of coordination reached maximum allowance and thus led to the occurrence of solubility limit.[24] Therefore, the organic phase [see, for example, the bottom layer of the inserted graphs after extraction of $HAuCl_4$ in **Figure 2-15b**] became slightly turbid and yellowish because the $NH^+\cdots AuCl_4^-$ ion pairs transported some water molecules, which provided a medium to react with $NaBH_4$ in the aqueous solution and remove the byproduct $HCl_{(aq)}$ (deprotonation of 4VP units) from the organic phase after reduction. Protonation of P4VP blocks might result in swelling of the micelle cores (fully protonated P4VP is soluble in water) due to increase in osmotic pressure.[57-59] After adding excess toluene, the diblock copolymer micelles could store the Au NPs in their cores, resulting in a transparent reddish solution. **Figure 2-16** displays UV–Vis spectra of Au NPs in the cores of the PCL-*b*-P4VP micelles **Au-BC1–3**; we observe typical surface plasmon behavior for the Au NPs, with maximum intensity at 533 nm. The signal maximum did not shift to higher wavelength (red shift) for the larger Au NPs, but the signal did broaden. The broad UV–Vis signal for **Au-BC3** corresponds to the larger size of Au NPs (ca. 12 nm) in comparison with those (ca. 7 nm) for **Au-BC1** or **Au-BC2**, as determined from the TEM images displayed in **Figure 2-17**.

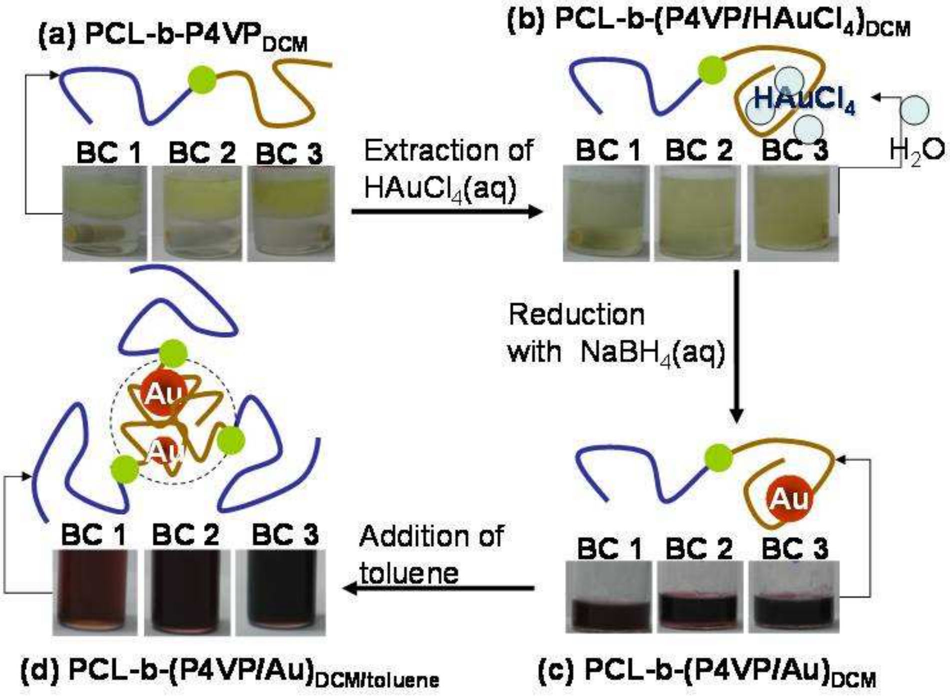

Figure 2-15. Schematic route toward the preparation of PCL-*b*-P4VP-protected Au NPs (**Au-BC1–3**): (a to b) two-phase extraction of $HAuCl_4$ via ion pairs $NH^+\cdots AuCl_4^-$; (b to c) reduction with aqueous $NaBH_4$ solution; and (c to d) stabilization of Au NPs in the micellar cores upon the addition of excess toluene.

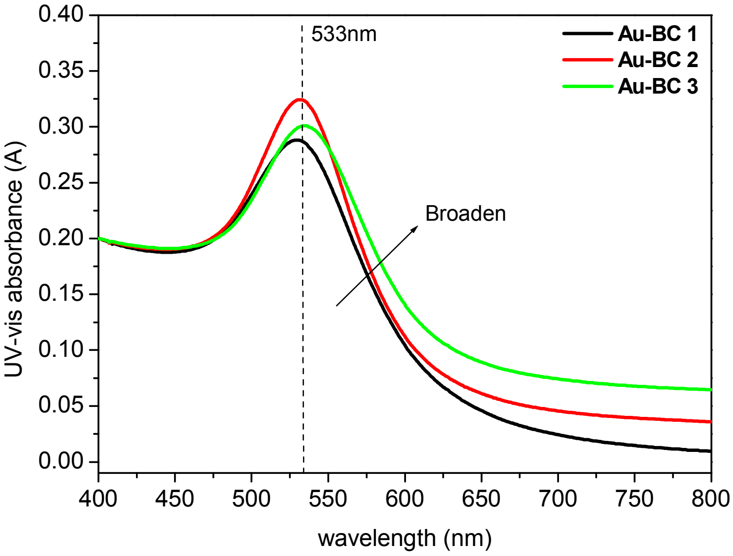

Figure 2-16. UV–Vis spectra of Au NPs located in the micellar cores of three PCL-*b*-P4VP copolymers (**Au-BC1–3**).

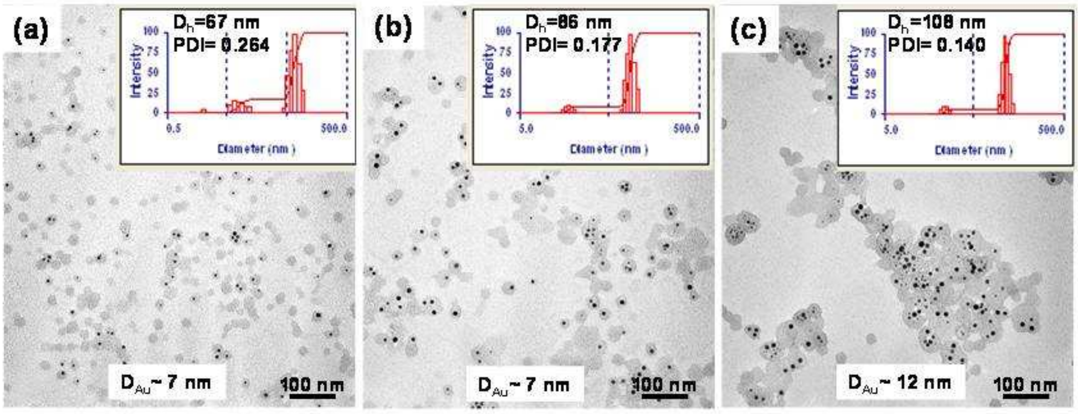

Figure 2-17. TEM images and inserted DLS graphs of Au NPs located in the micellar cores of three PCL-*b*-P4VP copolymers: (a) **Au-BC1**, (b) **Au-BC2**, and (c) **Au-BC3**.

At the equimolar ratio of HAuCl4 to 4-VP units, the more Au NPs can be incorporated to the longer P4VP chains of **BC3** resulting in the morphologic transform from rod-like **BC3** to spherical **Au-BC3** (**Figure 2-12c** and **2-17c**). Not surprisingly, metalation suppress regular aggregation of the PCL-b-P4VP micelles due to the complexation of the P4VP blocks with spherical Au NPs.[24] DLS analysis of the Au NPs in the cores of the PCL-*b*-P4VP micelles **Au-BC1–3** in toluene/DCM (**Figure 2-17**) revealed average micellar sizes (D_h) of 67, 86, and 108 nm, respectively, and polydispersity indices of 0.264, 0.177, and 0.140, respectively. From a comparison with the sizes of the PCL-*b*-P4VP micelles **BC1–3** in **Figure 2-12**, we attribute the increases in the micelle sizes of 31, 28, and 21 nm for **Au-BC1–3**, respectively, to the incorporation of the 7–12-nm-diameter Au NPs in the P4VP cores. In addition, the absence of large Au aggregates (>50 nm in diameter) in the TEM images reveals that the P4VP blocks not only captured the $AuCl_4^-$ anions in form of $NH^+ \cdots AuCl_4^-$ complexes but also stabilized the Au NPs through the formation of metal complexes. We quantitatively calculated the capacities of the Au NPs relative to PCL-*b*-P4VP block copolymers **BC1–3** to be 0.19, 0.15, and 0.16 g/g for **Au-BC1–3**, respectively, deduced from the char yield at 700 °C (**Table 2-2** and **Figure 2-18**).

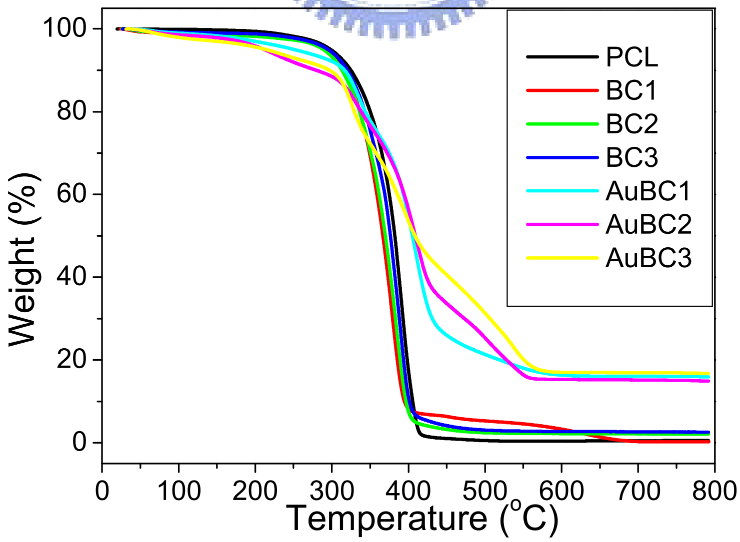

Figure 2-18. TGA thermograms of **PCL**, **BC1-3**, and **Au-BC1-3**.

2-4 Conclusions.

Benzoyloxyl radicals can be produced through TEMPO-induced BPO decomposition at temperatures below 25 °C. Thus, the preparation of *N*-alkoxyamine unimolecular initiators for nitroxide-mediated radical polymerizations becomes easier because radical side reactions seldom occur at such low temperatures. As a result, the ability to control polymer properties through the synthesis of diblock copolymers and complex macromolecular architectures becomes cheaper and simpler for the preparation of *N*-alkoxyamine products. Active byproducts of the *N*-oxoammonium cations would undergo alcohol oxidization to produce *N*-hydroxylamines or ring-opening rearrangement to form nitroso compounds. Thus, during this process, we observed a color change for the solution from reddish brown (nitroxide absorbance) to pale green (nitroso absorbance). When using the cheaper 4-OH-TEMPO, we prepared only 4-oxo-*N*-alkoxyamine products through a process involving redox reaction, radical addition, and alcohol oxidation. After hydrolysis of the benzoate ester, the hydroxyl-4-oxo-*N*-alkoxyamine can be used as a difunctional initiator for the preparation of PCL-*b*-P4VP diblock copolymers through (i) ring-opening polymerization of ε-CL after reaction with $AlEt_3$ and (ii) bulk nitroxide-mediated radical polymerization of 4-VP. When using 1.5 equivalents of $AlEt_3$, diethyl aluminum alkoxide initiation and the presence of more active monomers can lead to the conversion of ε-CL monomer reaching 99.5% after 3 h in toluene at 25 °C; as a result, the preparation of PCL-*b*-P4VP can be performed at 125 °C after replacing the toluene solvent with 4-VP monomers. The immiscible PCL-*b*-P4VP diblock copolymers display not only two distinct glass transitions in the DSC thermograms but also unique micellar structures, such as spheres or rods, in the TEM images. Using this combination of ROP and NMRP, we prepared three PCL-*b*-P4VP copolymers having polydispersities of 1.29–1.40 that retained the desired characteristics of a uniform P4VP core size in a mixed solvent of 10% DCM and 90% toluene (v/v). The relative block length plays an important role in affecting the resulting supramolecular architecture. Depending on the diblock ratio n/m, the **BC1** and **BC2** diblock copolymers initially formed spheres (n/m = 3.99, 2.16) and then shifted to a mixture of spheres and rods (n/m = 1.50). For the extraction of $HAuCl_4$ from aqueous solution, $AuCl_4^-$ anions were transferred into DCM in the form of ionic pairs ($NH^+ \cdots AuCl_4^-$), which then were stabilized in the form of Au NPs through reduction with aqueous $NaBH_4$ solution.

2-5 References.

1. Shannon, M. A.; Bohn, P. W.; Elimelech, M.; Georgiadis, J. G.; Mariñas, B. J.; Mayes, A. M. *Nature* **2008**, *452*, 301.
2. Rahman M. A. ; Ahsan S. ; Kaneco S. ; Katsumata H. ; Suzuki T. ; Ohta K. *J. Environ. Manage.* **2005**, *74*, 107.
3. Akthakul, A.; Salinaro, R. F.; Mayes, A. M. *Macromolecules* **2004**, *37*, 7663.
4. Zhou, M.; Kidd, T. J.; Noble, R. D.; Gin, D. L. *Adv. Mater.* **2005**, *17*, 1850.
5. Asatekin, A.; Menniti, A.; Kang, S.; Elimelech, M.; Morgenroth, E.; Mayes, A. M. *J. Membr. Sci.* **2006**, *285*, 81.
6. Revanur, R.; McCloskey, B.; Breitenkamp, K.; Freeman, B. D.; Emrick, T. *Macromolecules* **2007**, *40*, 3624.
7. Yang, S. Y.; Ryu, I.; Kim, H. Y.; Kim, J. K.; Jang, S. K.; Russell, T. P. *Adv. Mater.* **2006**, *18*, 709.
8. Phillip, W. A.; Rzayev, J.; Hillmyer, M. A.; Cussler, E. L. *J. Membr. Sci.* **2006**, *286*, 144.
9. Förster, S.; Plantenberg, T. *Angew. Chem. Int. Ed.* **2002**, *41*, 688.
10. Zhang, L.; Eisenberg, A. *Science* **1995**, *268*, 1728.

11. Zhang, L.; Eisenberg, A. *J. Am. Chem. Soc.* **1996**, *118*, 3168.
12. Zhang, L.; Yu, K.; Eisenberg, A. *Science* **1996**, *272*, 1777.
13. Chan, S. C.; Kuo, S. W.; Lu, C. H.; Lee, H. F., Chang, F. C. *Polymer* **2007**, *48*, 5059.
14. Konya, Z.; Puntes, V. F.; Kiricsi, I.; Zhu, J.; Ager, J. W., III; Ko, M. K.; Frei, H.; Alivisatos, P.; Somorjai, G. A. *Chem. Mater.* **2003**, *15*, 1242.
15. Lin, S. D.; Bollinger, M.; Vannice, M. A. *Catal. Lett.* **1993**, *17*, 245.
16. Lee, S. J.; Gavriilidis, A. *J. Catal.* **2002**, *206*, 305.
17. Okumura, M.; Akita, T.; Haruta, M. *Catal. Today* **2002**, *74*, 265.
18. Sárkány, A.; Horváth, A.; Bech, A. *Appl. Catal. A* **2002**, *229*, 117.
19. Milone, C.; Tropeano, M. L.; Gulino, G.; Neri, G.; Ingoglia, R.; Galvagno, S. *Chem. Commun.* **2002**, 868.
20. Blick, K.; Mitrelias, T. D.; Hargreaves, J. S. J.; Hutechings, G. J.; Joyner, R. W.; Kiely, C. J.; Wagner, F. E. *Catal. Lett.* **1998**, *50*, 211.
21. Grisel, R. J. H.; Kooyman, P. J.; Nieuwenhuys, B. E. *J. Catal.* **2000**, *191*, 430.
22. Salama, T. M.; Ohnishi, R.; Shido, T.; Ichikawa, M. *J. Catal.* **1996**, *162*, 169.
23. Brust, M.; Walker, M.; Bethell, D.; Schiffrin, D. J.; Whyman, R. *J. Chem. Soc., Chem. Commun.* **1994**, 801.
24. Ho, R. M.; Lin, T.; Jhong, M. R.; Chung, T. M.; Ko, B. T.; Chen, Y. C. *Macromolecules* **2005**, *38*, 8607.
25. Azzam, T.; Eisenberg, A. *Langmuir* **2007**, *23*, 2126.
26. Mössmer, S.; Spatz, J. P.; Möller, M. *Macromolecules* **2000**, *33*, 4791.
27. Hou, G.; Zhu, L.; Chen, D.; Jiang, M. *Macromolecules* **2007**, *40*, 2134.
28. Albertsson, A. C.; Varma I. K. *Adv. Polym. Sci.* **2002**, *157*, 1.
29. Stridsberg, K. M.; Ryner, M.; Albertsson, A.-C. *Adv. Polym. Sci.* **2002**, *157*, 41.
30. Greszta, D.; Mardare, D.; Matyjaszewski, K. *Macromolecules* **1994**, *27*, 638.

31. Matyjaszewski, K.; Xia, J. *Chem. Rev.* **2001**, *101*, 2921.

32. Hawker, C. J.; Bosman, A. W.; Harth, E. *Chem. Rev.* **2001**, *101*, 3661.

33. Sciannamea, V.; Jerome, R.; Detrembleur, C. *Chem. Rev.* **2008**, *108*, 1104.

34. Fischer, A.; Brembilla, A.; Lochon, P. *Macromolecules* **1999**, *32*, 6069.

35. Hawker, C. J.; Hedrick, J. L.; Malmström, E. E.; Trollsås, M.; Mecerreyes, D.; Moineau, G.; Dubois, Ph.; Jérôme, R. *Macromolecules* **1998**, *31*, 213.

36. Hawker, C. J. *J. Am. Chem. Soc.* **1994**, *116*, 11185.

37. Georges, M. K.; Veregin, R. P. N.; Kazmaier, P. M.; Hamer, G. K. *Macromolecules* **1993**, *26*, 2987.

38. Moad, G.; Rizzardo, E.; Solomon, D. H. *Macromolecules* **1982**, *15*, 909.

39. Gravert D. J.; Janda, K. D. *Tetrahedron Lett.* **1998**, *39*, 1513.

40. Moad, G.; Rizzardo, E.; Solomon, D. H. *Tetrahedron Lett.* **1981**, *22*, 1165.

41. Moad, G.; Rizzardo, E.; Solomon, D. H. *J. Macromol. Sci. Chem.* **1982**, *A17*, 51.

42. Veregin, R. P. N.; Georges, M. K.; Kazmaier, P. M.; Hamer, G.. K. *Macromolecules* **1993**, *26*, 5316.

43. Braslau, R.; Burrill, L. C., II; Siano, M.; Naik, N.; Howden, R. K.; Mahal, L. K. *Macromolecules* **1997**, *30*, 6445.

44. Yin, M.; Wang, Y.; Bauer, I.; Habicher, W. D.; Voit, B. *Des. Monomers Polym.* **2005**, *8*, 211.

45. Hawker, C. J.; Barclay, G. G.; Dao, J. *J. Am. Chem. Soc.* **1996**, *118*, 11467.

46. Cella, J. A.; Kelley, J. A.; Kenehan, E. F. *J. Org. Chem.* **1975**, *40*, 1860.

47. Rychnovsky, S. D.; Vaidyanathan, R. *J. Org. Chem.* **1999**, *64*, 310.

48. Sheldon, R. A.; Arends, I. W. C. E.; ten Brink, G.-J.; Dijksman, A. *Acc. Chem. Res.* **2002**, *35*, 774.

49. Fritz-Langhals, E. *Org. Process Res. Dev.* **2005**, *9*, 577.

50. Dubois, Ph.; Ropson, N.; Jerome, R.; Teyssie, Ph. *Macromolecules* **1996**, *29*, 1965.
51. Won, Y. Y., Bates, F. S. (2006). Nonionic block compolymer wormlike micelles. In R Zana & E.W. Kaler (Eds.), Giant Micelles. USA: Surfactant Sciences Series, Taylor & Franics-CRC press.
52. Benejacq, D.; Ponsinet, V.; Joanicot, M.; Loo, Y.-L.; Register, R. A. *Macromolecules* **2002**, *35*, 6645.
53. Zhang, L.; Eisenberg, A. *J. Am. Chem. Soc.* **1996**, *118*, 3168.
54. Burke S. E.; Eisenberg, A. *Langmuir* **2001**, *17*, 6705.
55. Lynd, N. A.; Hillmyer, M. A. *Macromolecules*, **2005**, *38*, 8803.
56. Listak, J.; Jakubowski, W.; Mueller, L.; Plichta, A.; Matyjaszewski, K.; Bockstaller, M. R. *Macromolecules* **2008**, 41, 5919.
57. Sidorov, S. N.; Bronstein, L. M.; Kabachii, Y. A.; Valetsky, P. M.; Soo, P. L.; Maysinger, D.; Eisenberg, A. *Langmuir* **2004**, *20*, 3543.
58. Kostarelos, K.; Luckham, P. F.; Tadros, T. F. J. Chem. Soc. Faraday Trans, **1998**, *94*, 2159.
59. Groenewegen, W.; Egelhaaf, S. U.; Lapp, A.; van der Maarel. J. R. C. *Macromolecules* **2000**, *33*, 3283.

Chapter 3

Syntheses and Characterizations of Star Polymers and Star Block Copolymers from Polyhedral Oligomeric Silesesquioxane Core through Nitroxide-mediated Radical Polymerization

Abstract

We introduced *N*-alkoxyamine groups onto eight corners of a POSS cube through hydrosilylation between allyl *N*-alkoxyamine and Q_8M_8 POSS. The quantitative hydrosilylation (~100% conversion) can be used to prepare the well-defined eight-functional unimolecular initator for nitroxide-mediated free radical polymerization of polystyrene (POSS(PS)$_8$), polystyrene-*block*-poly(4-vinylpyridine) (POSS(PS-*b*-P4VP)$_8$), and polystyrene-*block*-poly(vinylphenol) (POSS(PS-*b*-PVPh)$_8$). The GPC and ^{1}H NMR results reveal living and controllable free radical polymerization.

3-1 Introduction

The synthesis of novel materials with improved properties and performance is a continually expanding frontier at the interface of chemistry and materials science. In this pursuit, the ability to control molecular structure on atomic and macroscopic dimensions is a key parameter in designing materials with preprogrammed activity.[1] Recently, a novel class of hybrid polymers based on polyhedral oligomeric silesesquioxanes (POSS) has been developed.[2-8] POSS compounds embody a truly hybrid (inorganic-organic) architecture, which contains an inner inorganic framework made up of silicone and oxygen $(SiO_{1.5})_x$, covered externally by organic substituents. These substituents can be totally hydrocarbon in nature or they can incorporate with a range of polar structures and functional groups. POSS nanostructured chemicals, with sizes of from 1 to 3 nm in diameter, can be thought of as the smallest possible particles of silica (namely molecular silicas).[9-11] Applying POSS monomers or initiators to living and controlled polymerizations is desirable to develop novel materials of varying composition, topology, and well-defined molecular weights. The synthesis of star homopolymers or star-block copolymers using the cubic POSS as a nanosized multifunctional initiator is particularly interesting. In this communication, we report the nitroxide-mediated radical polymerization (NMRP) of styrene, 4-vinylpyridine, and 4-acetoxystyrene monomers. Using this approach we have synthesized star polymers and star-block copolymers from an octa-*N*-alkoxyamine-functionalized POSS core (OT-POSS) as shown in **Scheme 3-1**.

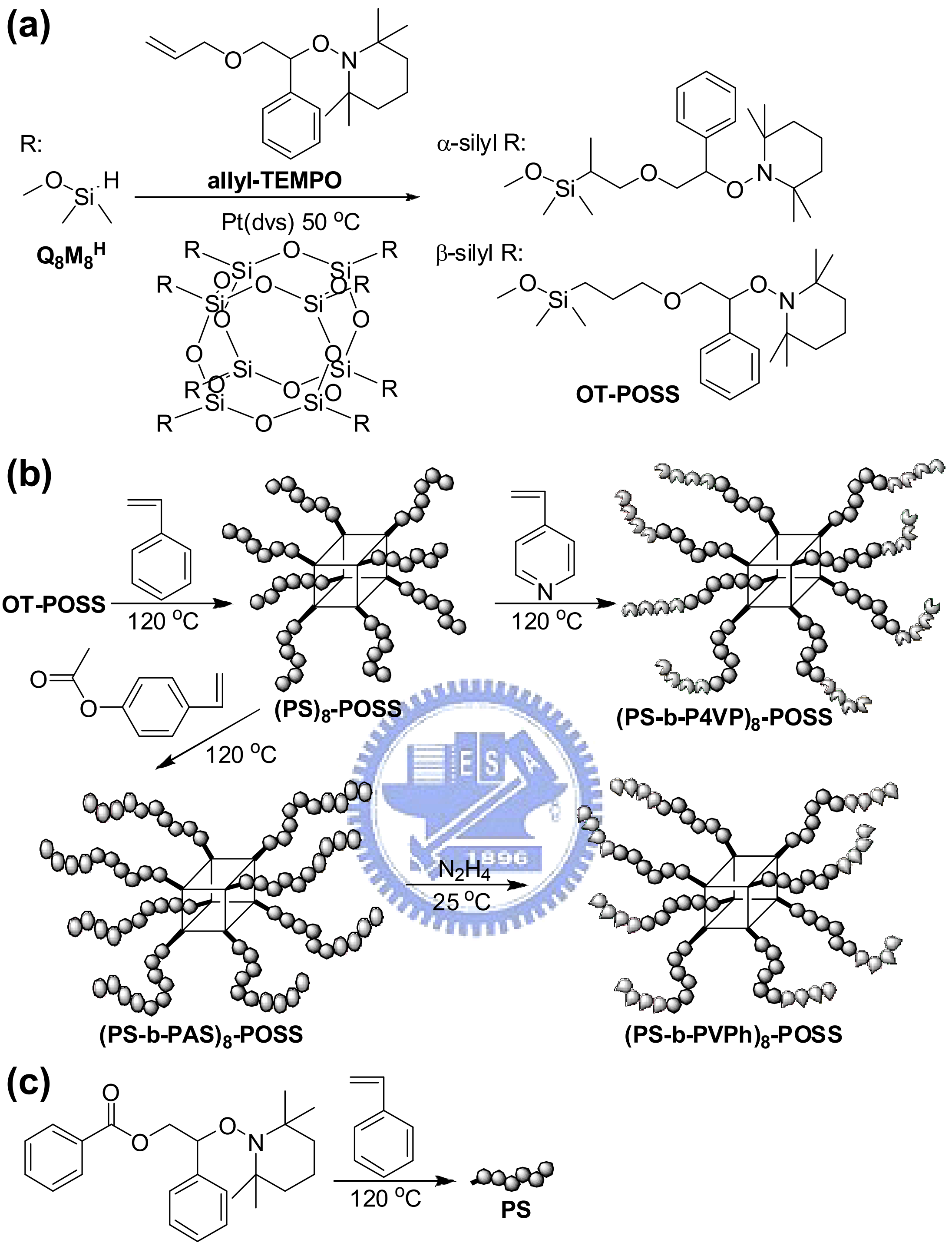

Scheme 3-1. (a) synthesis of OT-POSS initiator (b) synthesis of $(PS)_8$-POSS, (PS-b-P4VP)$_8$-POSS, and (PS-b-PVPh)$_8$-POSS (c) synthesis of linear PS.

3-2 Experimental Session

3-2.1 Materials.

Styrene (St, 99.5%, ACROS), 4-vinylpyridine (4-VP, 99.5%, ACROS), and 4-acetoxystyrene (4-AS, 99.5%, ACROS) were dried over calcium hydride (CaH_2, 95%, ACROS) for 24 h and then distilled under reduced pressure. The following chemicals and solvents were used as received: benzoyl peroxide (BPO, >97%, Fluka), styrene (St, 99%, ACROS), 2,2,6,6-tetramethylpiperidinooxy (TEMPO, 98%, ACROS), allylbromide (allyl-Br, 98%, ACROS), octakis(dimethylsiloxy)silsesquioxane (Q8M8H POSS, >95%, Hybrid Plastics), hydrazine monohydrate (N_2H_4, 98%, Aldrich), potassium hydride (KH, 40% in oil, ACROS) and platinum(0)-1,3-divinyl-1,1,3,3-tetramethyldisiloxane complex solution (2% [Pt(dvs)] in xylene, Aldrich). Reactions were performed in glassware under a static atmosphere of argon.

3-2.2 Synthesis of 1-(2-(allyloxy)-1-phenylethoxy)-2,2,6,6-tetramethylpiperidine (allyl-TEMPO)

According to the Chapter 2, the hydroxyl-functional *N*-alkoxyamine was prepared by reaction between benzoyl peroxide and TEMPO at temperatures below 25 °C for 24 hrs followed by hydrolysis with sodium hydroxide (**Scheme 3-2**). A solution of BPO (15.0 g, 61.9 mmol) and TEMPO (5.0 g, 32 mmol) in styrene (50 mL) was cooled to 5 °C in an ice bath and then naturally warmed to room temperature after a removal of the bath. The reddish-brown solution gradually faded, turning into a pale green solution over several hours. The excess styrene was removed through vacuum distillation and the residual solid was partitioned between diethyl ether and 1 N aqueous NaOH. The product in the organic phase was dried (anhydrous $MgSO_4$) and the solvent was evaporated to give a light-yellow powder. A white crystals of

N-alkoxyamine product—the *N*-alkoxyamine **Ester-TEMPO** (5.2 g, 43%)—was obtained after recrystallization from MeOH. Melting points: 74.5 °C. Mass spectra (ESI, *m*/*z*): 382.1 [MH^+]. Elem. Anal. for $C_{24}H_{31}NO_3$: Calcd: C, 75.56; H, 8.19; N, 3.67; Found: C, 75.66; H, 8.23; N, 3.46. IR (neat) 3100-2850, 1720, and 1200 cm^{-1}; ^1H NMR ($CDCl_3$) δ 0.75, 1.07, 1.21, 1.37 (each br s, 12H, $C\underline{H_3}$), 1.38-1.52 (m, 6H, $C\underline{H_2}$); 4.53 (ABq, J= 6 Hz, 1H, $C\underline{H}H$), 4.83 (ABq, J= 6 Hz, 1H, $CH\underline{H}$), 5.06 (ABq, J= 3 Hz, 1 H, $C\underline{H}$), 7.25-7.56 (m, 8 H, $Ar\underline{H}$) and 7.91 (B of ABq, J= 6 Hz, 2H, $Ar\underline{H}$); ^{13}C NMR ($CDCl_3$) δ 17.09, 20.31, 34.00, 40.36, 60.01, 66.68, 83.90, 127.54, 127.97, 128.18, 129.48, 130.14, 132.72, 140.61, and 166.20.

10 N Aqueous NaOH (10 mL) was added dropwise to a solution of the *N*-alkoxyamine adduct **Ester-TEMPO** (5.0 g, 13.1 mmol) in a mixture of THF (10 mL) and MeOH (30 mL). After several hours, the solvent was removed through rotary evaporation and the product was washed with excess diethyl ether. After rotary evaporation, **HO-TEMPO** (3.3 g, 90 %) was obtained as a light-yellow liquid. Mass spectra (ESI, *m*/*z*): 278 [MH^+]; Elem. Anal. for $C_{17}H_{27}NO_2$: Calcd: C, 73.61; H, 9.81; N, 5.05; Found: C, 73.79; H, 9.57; N, 4.95. ^1H NMR ($CDCl_3$) δ 1.14, 1.21, 1.33, 1.50 (each br s, 12H, $C\underline{H_3}$), 1.38-1.72 (m, 6H, $C\underline{H_2}$); 3.71 (br d, J= 9 Hz, 1H, $C\underline{H}H$), 4.21 (d of d, J= 2 and 6 Hz, 1H, $CH\underline{H}$), 5.29 (d of d, J= 2 and 3 Hz, 1H, $C\underline{H}$), 5.88 (br s, $O\underline{H}$), and 7.25-7.56 (m, 5 H, $Ar\underline{H}$); ^{13}C NMR ($CDCl_3$) δ 17.15, 20.41, 20.73, 32.76, 34.61, 40.23, 40.41, 60.38, 61.69, 69.73, 83.59, 126.20, 127.89, 128.34, and 138.92.

The synthesis of allyl-TEMPO was as the followings (**Scheme 3-3**). 5N *N*-alkoxyamine adduct **HO-TEMPO** (3.42 ml in anhydrous THF, 17.1 mmol) was added dropwise to an anhydrous THF solution of 10N potassium hydride KH (8.56 ml, 85.6 mmol, washed by hexane extraction). After stirring for 1hr, the upper clear solution was transferred to a new round bottle and 5N allyl bromide (4.14 ml in anhydrous THF, 34.2 mmol) was added dropwise. For another 24 hrs, the product was purified by column chromatography. After rotary evaporation, **allyl-TEMPO** (4.5 g, 83 %) was obtained as a light-yellow liquid. Mass spectra (ESI, *m*/*z*): 318 [MH$^+$]; Elem. Anal. for $C_{20}H_{31}NO_2$: Calcd: C, 75.67; H, 9.84; N, 4.41; Found: C, 75.45; H, 8.99; N, 4.43. ^{1}H NMR ($CDCl_3$) δ 0.64, 1.03, 1.19, 1.35 (each br s, 12H, $C\underline{H}_3$), 1.38-1.72 (m, 6H, $C\underline{H}_2$); 3.65 (ABq, J= 10 Hz, 6.5H, $C\underline{H}H$), 3.90 (m, 2H, $C\underline{H}_2$), 3.96 (ABq, J= 10 and 5 Hz, 1H, $CH\underline{H}$), 4.83 (ABq, J= 6.5 and 5 Hz, 1H, $C\underline{H}$), 5.12 (m, 1H, $C\underline{H}$), 5.79 (m, $C\underline{H}_2$), and 7.25-7.56 (m, 5 H, $Ar\underline{H}$); ^{13}C NMR ($CDCl_3$) δ 17.16, 20.34, 40.49, 72.05, 72.88, 85.37,116.39, 127.22, 127.79, 127.83, 134.89, and 141.95.

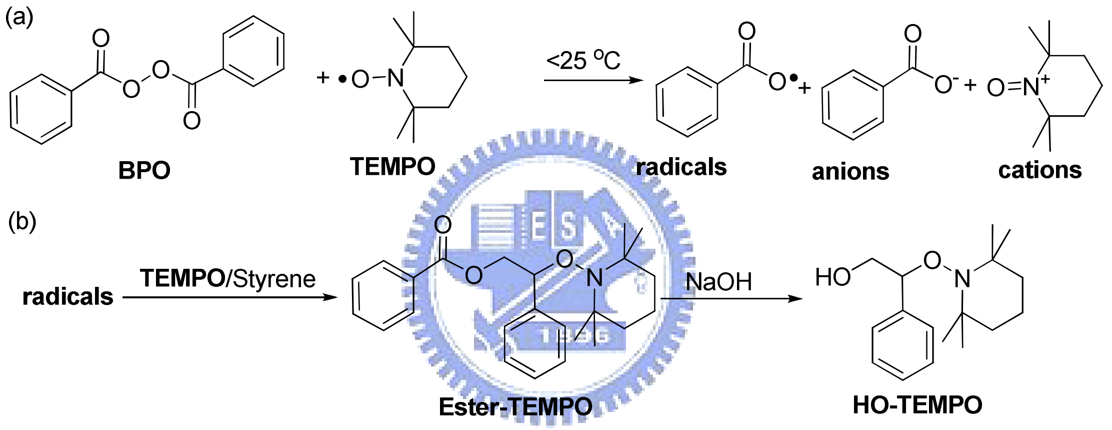

Scheme 3-2. (a) low-temperature reaction between BPO and TEMPO; (b) synthesis of the Ester-TEMPO and HO-TEMPO.

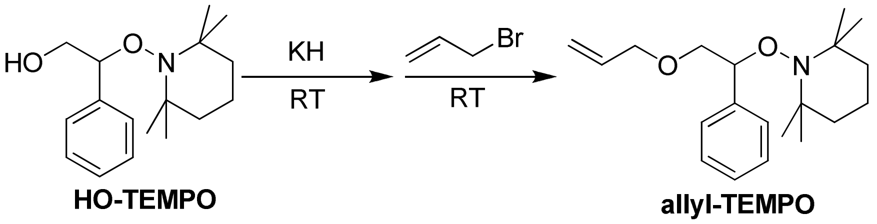

Scheme 3-3. Preparation of allyl-TEMPO.

3-2.3 Synthesis of octa-*N*-alkoxyamine-functionalized POSS initiator (OT-POSS).

Scheme 3-1a depicts the hydrosilylation approach used to prepare OT-POSS. A solution of $Q_8M_8^H$ POSS (3.00 g, 2.95 mmol) and allyl-TEMPO (9.38 g, 29.50 mmol) in toluene (30 mL) in a 100-mL Schlenk flask equipped with a reflux condenser and a magnetic stirrer was heated at 60 °C under argon and then Pt(dvs) (0.2 mL, 0.4 mmol) was added via syringe. The reaction, which was monitored by measuring the decrease in intensity of the FTIR spectral signal at 2134 cm^{-1} for the Si–H bonds, was complete after 4 h. The yellowish, transparent reaction mixture became clear after removal of the Pt(dvs) catalyst through flash chromatography (neutral Al2O3; toluene). The solvent was evaporated under reduced pressure and then the residual allyl-TEMPO was removed by precipitation into acetonitrile, selective solvent for POSS deriviatives, to yield OT-POSS (5.46 g, 52%). OT-POSS is a viscous liquid at 25 °C. Both are soluble in common organic solvents, such as tetrahydrofuran, chloroform, and acetone.

3-2.4 Synthesis of eight-arm star polystyrene from a POSS core [POSS-$(PS)_8$]

The dried OT-POSS macroinitiator was charged with one hundred equivalents of the styrene monomer, based on the content of *N*-alkoxyamine groups. The vessel was immersed in an oil bath maintained at a temperature of 125 °C. The kinetic study of PS polymerization was performed by dropping solution into excess dimethylforamide (DMF) for the determination of molecular mass by GPC analyses and excess *d*-chloroform (CD_3Cl) for the determination of monomer conversion by ^1H NMR spectra. The resultant star polystyrene [POSS-$(PS)_8$] were purified twice through dissolution in tetrahydrofurane and precipitation from methanol. The macroinitiator of low molar-mass POSS-$(PS)_8$ are obtained by 3h polymerization for the preparation of star-blok copolymers. The target of theoretical $\overline{M}_n$ = 36162 g/mol to POSS-$(PS)_8$ with 39 styrene units per polystyrene chain are obtained.

3-2.5 Synthesis of eight-arm stra-block polystyrene-block-poly(4-vinylpyridine) and polystyrene-block-poly(4-acetoxystyrene) from a POSS core [POSS-(PS-b-P4VP)$_8$ and POSS-(PS-b-PAS)$_8$]

The dried POSS-(PS)$_8$ macroinitiator was charged with one equivalent of the 4-VP or 4-AS monomer, based on the content of styrene units. The vessel was immersed in an oil bath maintained at a temperature of 125 °C. When the stirrer bar stopped stirring after 3h, the polymerization was quenched through immersion of the flask in an ice bath. The resultant star-block copolymers POSS-(PS-b-P4VP)$_8$ and POSS-(PS-b-PAS)$_8$ were purified twice through dissolution in chloroform and precipitation from hexane. The targets of theoretical $\overline{M}_n$ = 52984 and 67302 g/mol to POSS-(PS-b-P4VP)$_8$ with 20 4-vinylpyridine units and POSS-(PS-b-PAS)$_8$ with 24 4-acetoxystyrene units per polystyrene chain are obtained.

3-2.6 Hydrolysis of POSS-(PS)$_8$ using HF

The hydrolysis on the siloxane cage of POSS-(PS)$_8$ are performed by mixing 50 wt% HF in aqueous solution (25 mol, 1 mL) and 10 wt% POSS-(PS)$_8$ in THF solution (0.028 mmol, 10 mL). After stirring for 24 h, the resultant polymers were purified twice through dissolution in tetrahydrofurane and precipitation from methanol.

3-2.7 Hydrazinolysis of POSS-(PS-b-PAS)$_8$ to give POSS-(PS-b-PVPh)$_8$

Scheme 3-1b depicts the acetoxyl hydrazinolysis of POSS-(PS-b-PAS)$_8$ with hydrazine monohydrate used to prepare POSS-(PS-b-PVPh)$_8$. POSS-(PS-b-PAS)$_8$ (1.00 g, 0.015 mmol) was dissolved in 1,4-dioxane and then hydrazine monohydrate (0.2 g, 4 mmol) was added. The acetoxyl hydrazinolysis, which was monitored by measuring the decrease in intensity of the FTIR spectral signal for the C=O bond at 1762 cm^{-1}, was complete after 2 h. The resultant polymers were purified twice through dissolution in dichloromethane and precipitation from ethyl ether.

3-3 Results and Discussion

3-3.1 Octa-*N*-alkoxyamine functionalized POSS (OT-POSS)

The synthesis of an OT-POSS initiator is the first step in the preparation of well-defined hybrid polymers using hydrosilylation (**Scheme 3-1a**). In the hydrosilylated addition of octakis(dimethylsiloxy)silsesquioxane ($Q_8M_8^H$ POSS) with 1-(2-(allyloxy)-1-phenylethoxy)-2,2,6,6-tetramethylpiperidine (allyl-TEMPO), Karstedt's agent (a platinum divinylsiloxane complex) was used as a catalyst.[12] For the reaction temperature at 50 °C, the *N*-alkoxyamine groups are stable so as to chemically modify POSS cages.[13] Herein, the preparation of allyl-TEMPO is shown in the supporting information. Monitoring the hydrosilylation by FTIR reveals that the hydrosilylation conversion increases up to 100% according to the silane stretching mode (Si—H, at 2134 cm^{-1}) when the feeding molar ratio of $Q_8M_8^H$ to allyl-TEMPO is 1 : 10 (**Figure 3-1a**). The quantitative hydrosilylation with 100% conversion plays an important role in the preparation of the well-defined POSS-based initiator. The grafting degree of 7.97 on the purified OT-POSS cube determined from ^{1}H NMR [signals (*a*+*a'*) and *j*] matches well with the theoretically predicted octakis-functional chemical structure (**Figure 3-1b**). The isomerism of hydrosilylation results in β [$RSiCH_2CH_2R'$] and α [$RSiCH(CH_3)R'$] linkages, where R is the POSS core and R′ is the organic functional group. The molar ratio of β to α linkage is 1.11 : 1 according to the integration of the signals for $-C\underline{H_2}\underline{O}-$ (signals *f* and *f'*).

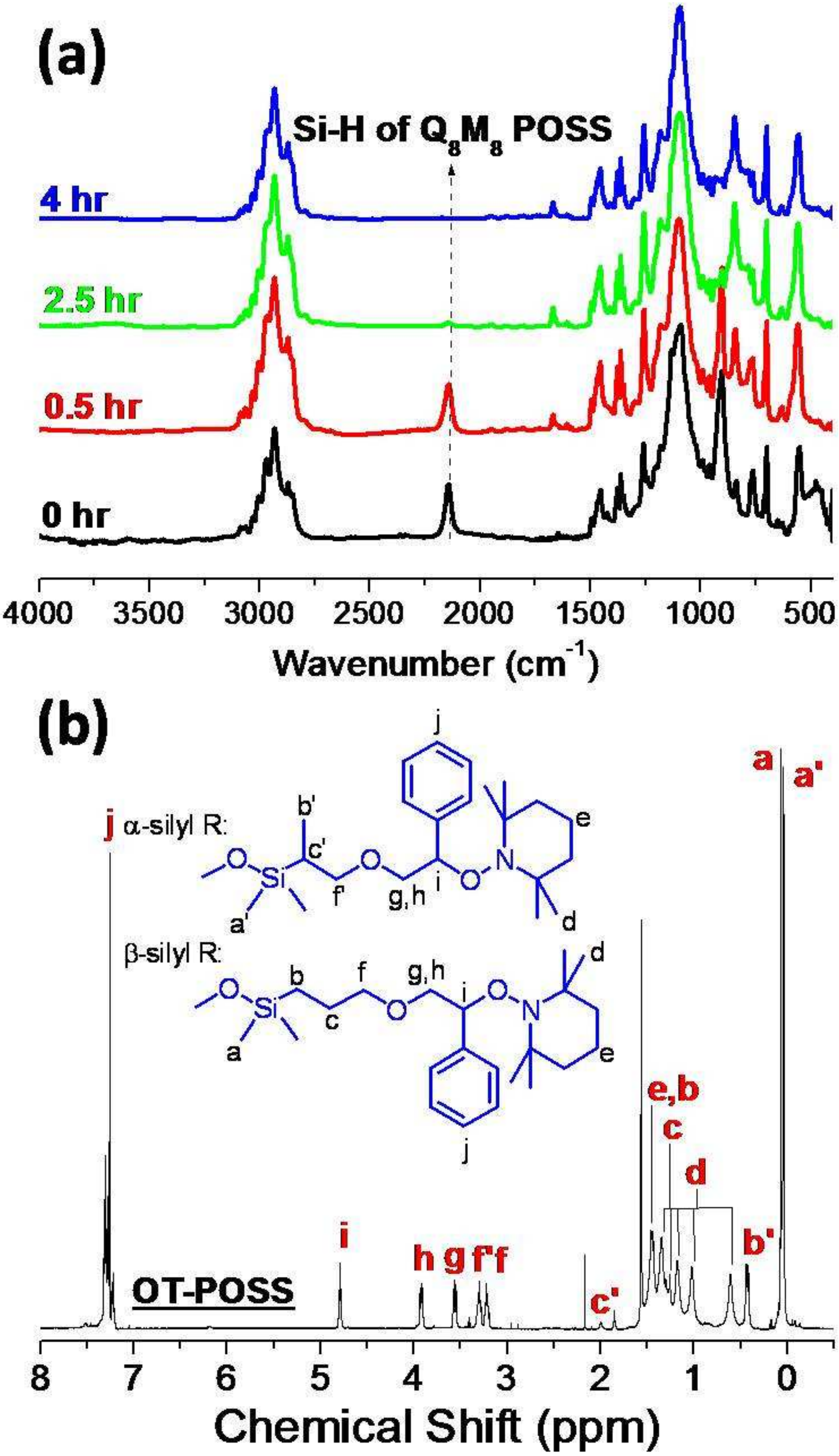

Figure 3-1. (a) FTIR monitoring of hydrosilylation and (b) ^{1}H NMR spectra of purified OT-POSS.

3-3.2 Synthesis of eight-arm star polystyrene from a POSS core [POSS-(PS)$_8$]

The synthesis of star polystyrene [(PS)$_8$-POSS] from OT-POSS is the second step in the preparation of well-defined hybrid polymers using NMRP (**Scheme 3-1b**). The NMRP polymerization without requiring metal catalyst and the initiation step from an unimolecular initiator are two major advantages over other living/controlled free radical polymerizations to simplify the purification and the polymerization.[14,15] In the NMRP of styrene, heating the mixture of OT-POSS (11.4 mM for target M$_n$= 80,000 g/mol) and styrene at 120 °C gives monomer conversion at 80% after 17h and star polystyrene with degree of polymerization (DP$_n$) = 77 for each arm based on the vinyl protons of styrene monomers (**Figure 3-2a**). In addition, the observed linear relationship between ln(M$_0$/M) and reaction time indicates a first order reaction for controllable polymerization. In comparison with styrene conversion of 85 % for linear polystyrene (PS, **Scheme 3-1c**) from the monofunctional *N*-alkoxyamine initiator (1.4 mM for target M$_n$= 10,000 g/mol), the similar high conversions indicate that NMRP propagation from a POSS cube can suppress the steric effect of divergent polymerization for a star polymer, which would result in gelation at the relatively low conversion.[16] The theoretical molecular weight of 67,700 g/mol for (PS)$_8$-POSS was determined from ^{1}H NMR (DP$_n$ theoretical = 77 for each arm at 17hrs). In comparison with the results from ^{1}H NMR and SEC, the shift of SEC distribution to high molar mass matches well with the increase of the monomer conversion (**Figure 3-2b**). However, molecular weight determined from SEC is slightly lower than the theoretically predicted value (Mn SEC = 60,600 g/mol vs Mn theoretical 67,700), and low polydispersities (Mw/Mn = 1.12) are observed. The discrepancy between the observed SEC molecular weights and the theoretical values can be attributed to hydrodynamic difference between star PS sample and linear PS standards in DMF mobile phase.

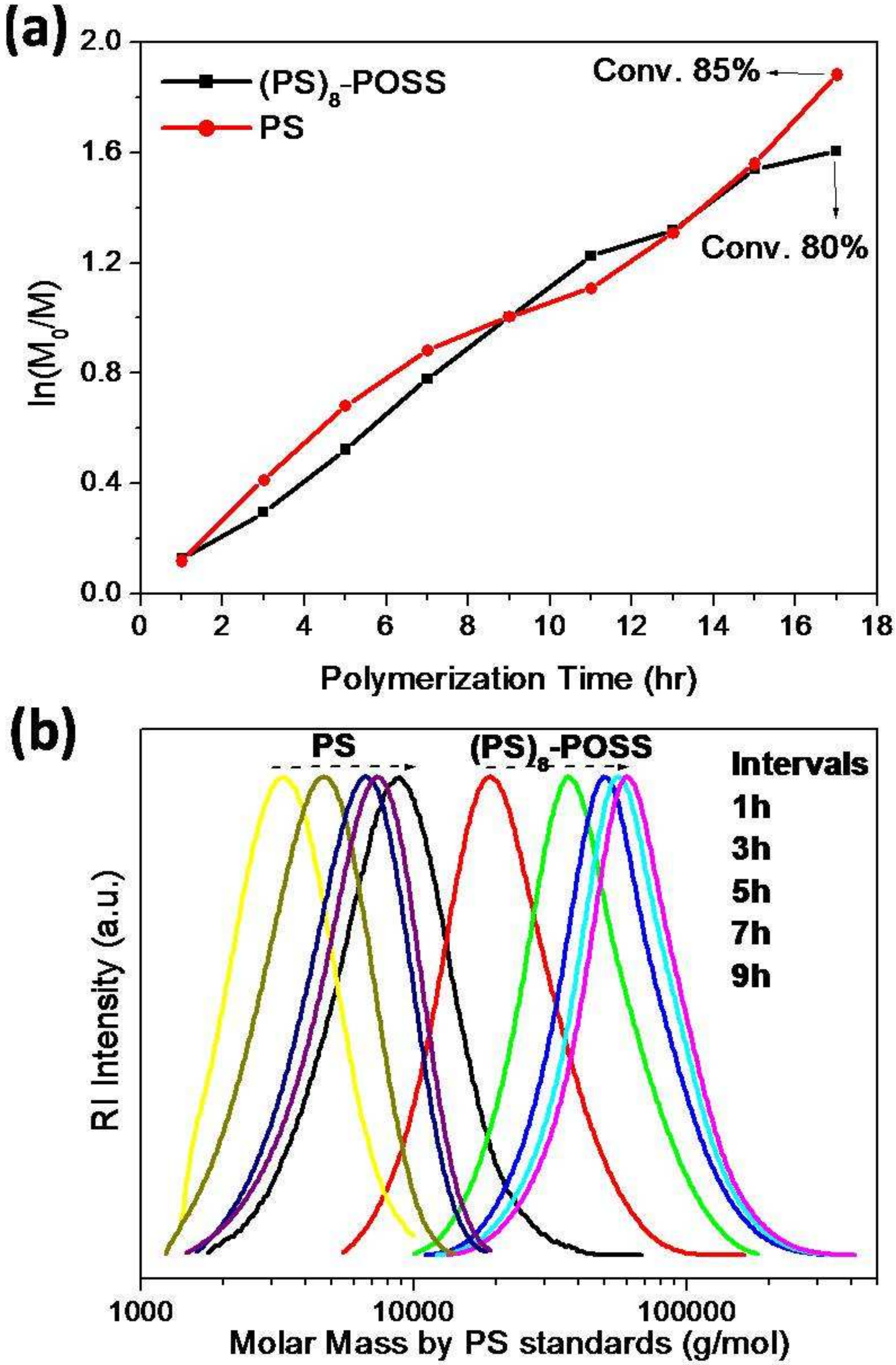

Figure 3-2. (a) Comparative conversion of linear and star-like polystyrene using ^{1}H NMR spectra and (b) SEC trace of polymerization for linear and star-like polystyrene.

3-3.3 Synthesis of eight-arm stra-block polystyrene-block-poly(4-vinylpyridine) and polystyrene-block-poly(4-acetoxystyrene) from a POSS core [POSS-(PS-b-P4VP)$_8$ and POSS-(PS-b-PAS)$_8$]

The synthesis of star-block copolymer from (PS)$_8$-POSS is the third step in the preparation of well-defined hybrid polymers using NMRP (**Scheme 3-1b**). The pseudo-living NMRP polymerization can preserve the reactive chain ends containing *N*-alkoxyamine to incorporate other monomers. To obtained low molar mass of the (PS)$_8$-POSS macroinitiator, the polymerization was paused at 5 hrs by quenching in the ice bath and the conversion of styrene monomers was around 41%. Analyses of the purified (PS)$_8$-POSS by ^{1}H NMR revealed that the repeating units of PS per arm reached 39 (about 4,060 g/mol) based on the protons of $-Si(CH_3)_3$ from the OT-POSS and that of PS benzene ring (**Figure 3-3a**). In the NMRP of 4-vinylpyridine or 4-acetoxystyrene, the residual styrene in the (PS)$_8$-POSS was removed by vacuum distillation at 25 °C and followed by adding 3-fold weights of 4-vinylpyridine or 4-acetoxystyrene to dissolve (PS)$_8$-POSS and heated at 120 °C for 3 hrs. Analyses of the purified (PS-b-P4VP)$_8$-POSS and (PS-b-P4VP)$_8$-POSS by ^{1}H NMR revealed that the repeating units of P4VP and PAS per arm reached 20 (about 2,100 g/mol) and 24 (about 3,890 g/mol) by comparing protons from the styryl, pyridyl, and methyl protons (**Figure 3-3a**). The shift of SEC distribution from 21,400 g/mol (PS)$_8$-POSS to 56,300 g/mol (PS-b-P4VP)$_8$-POSS or 53,900 g/mol (PS-b-PAS)$_8$-POSS demonstrated the versatility of “living” free radical polymerizations of second monomers such as 4-vinypyridine and 4-acetoxystyrene from the (PS)$_8$-POSS macroinitiator (**Figure 3-3b**).

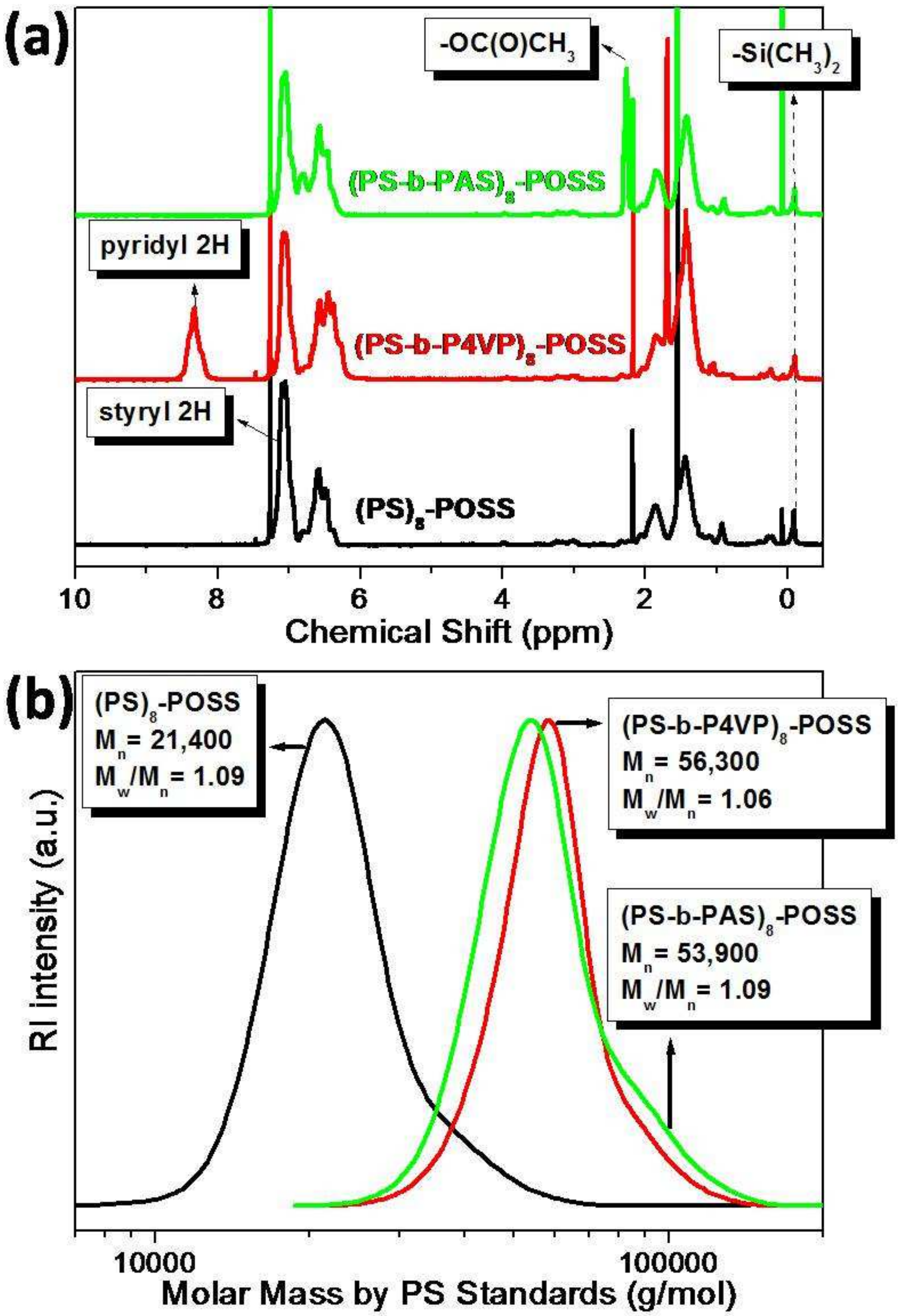

Figure 3-3. (a) 1H NMR spectra and (b) SEC trace of star－block $(PS)_8$-POSS, (PS-b-P4VP)$_8$-POSS and (PS-b-PAS)$_8$-POSS.

3-3.4 Hydrolysis of POSS-(PS)$_8$ and Hydrazinolysis of POSS-(PS-b-PAS)$_8$

The large discrepancy of (PS)$_8$-POSS between the SEC molecular weight (21,400 g/mol) and the ^{1}H NMR-predicted value (36,000 g/mol) can be attributed to chemical confinement (smaller hydrodynamic volume) of eight PS chains onto a POSS cube. To clarify this discrepancy, the POSS cage was decomposed by the HF treatment.[17] Resultant mass distribution of the (PS)$_8$-POSS after HF treatment became two narrower peaks (**Figure 3-4a**). In addition to the unreacted (PS)$_8$-POSS, the new and lower molar-mass peak can be attributed to the PS arms (4,200 g/mol), which is closed to the ^{1}H NMR predicted value of 4,060 g/mol. The FTIR spectra of (PS)$_8$-POSS before and after HF treatment clearly show the decomposition of POSS cages based on the decreasing intensity of the Si-O-Si bond at 1096 cm^{-1} (**Figure 3-4b**). Subsequent deprotection of the acetoxy groups of the PAS block with hydrazine monohydrate led to the (PS-b-PVPh)$_8$-POSS star-block copolymer. The mass distribution of (PS-b-PAS)$_8$-POSS after N_2H_4 treatment became another new peak (**Figure 3-4a**). This broader molar-mass distribution can be attributed to the chromatographic tailing from the hydrogen bonding of eight PVPh arms. FTIR spectra of (PS-b-PAS)$_8$-POSS before and after N_2H_4 treatment can apparently indicate the deprotection of acetoxy groups at 1768 cm-1 and the formation of phenols at 3362 cm^{-1} (**Figure 3-4b**). (PS-b-PVPh)$_8$-POSS containing a strongly hydrogen-donating poly(vinylphenol) block onto a relatively hydrophobic polystyrene core. In contrast, star — block (PS-b-P4VP)$_8$-POSS possess a strongly hydrogen-accepting poly(4-vinylpyridine) block is attached to a relatively hydrophobic polystyrene core. The hydrogen-bonding blends of star-block copolymers appeal our interest in the further study.

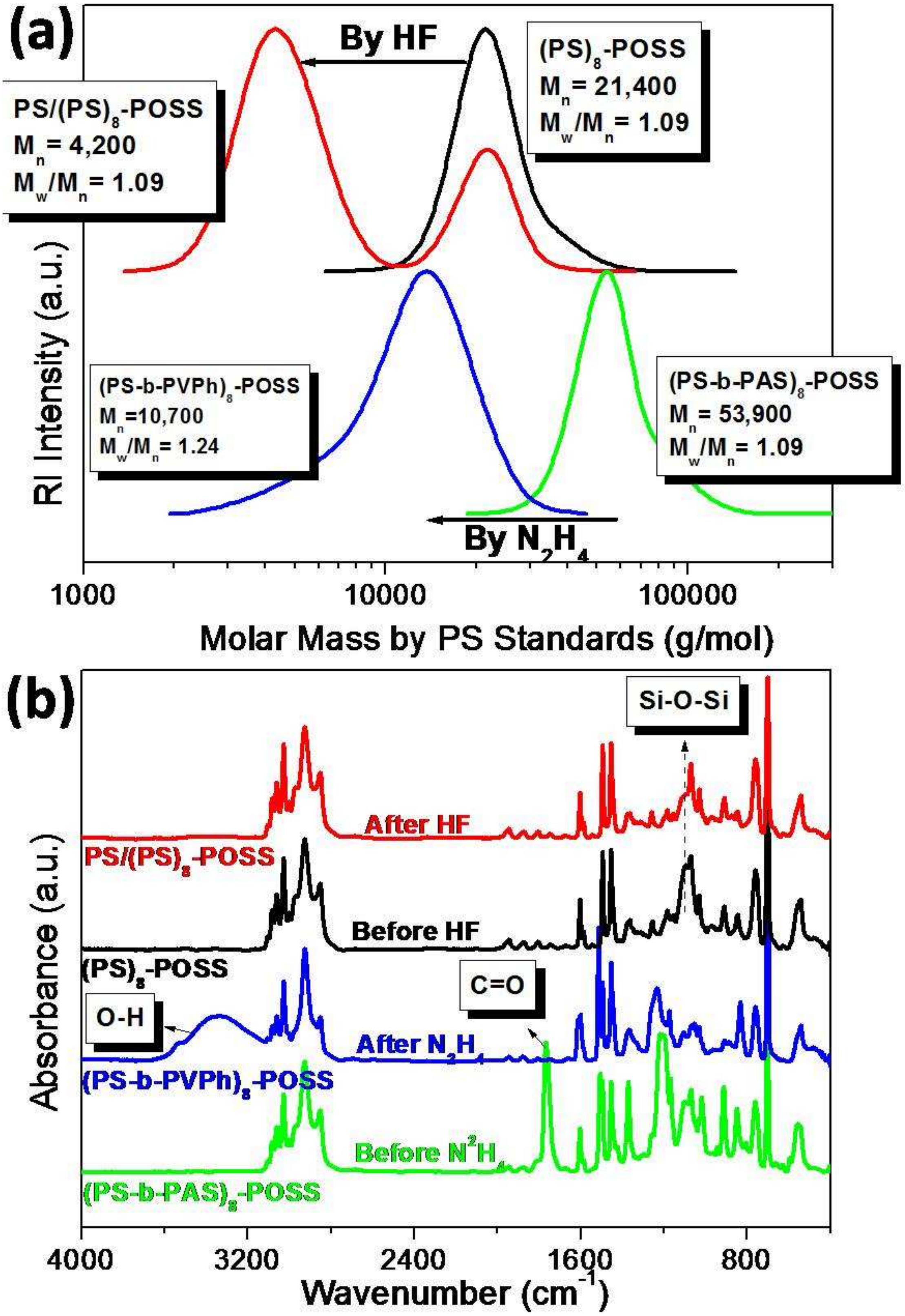

Figure 3-4. (a) SEC traces and (b) FTIR spectra of HF treatment of $(PS)_8$-POSS and N_2H_4 treatment of $(PS\text{-}b\text{-}PAS)_8$-POSS.

3-4 Conclusions

We have synthesized novel hybrid polymers from a POSS-based initiator using NMRP. From this approach, star homopolymer and star—block copolymers have been prepared. The characteristic of living free radical polymerization from a POSS-based initiator or macroinitiator was investigated by ^{1}H NMR spectra and SEC analyses.

3-5 References

1. MacLachlan, M. J.; Manners, I.; Ozin, G. A. *Adv. Mater.* **2000**, *12*, 675.
2. Pyun, J.; Matyjaszewski, K. *Macromolecules* **2000**, *33*, 217.
3. Miyamoto, K.; Hosaka, N.; Otsuka, H.; Takahara, A. *Chem. Lett.* **2006**, *35*, 1098.
4. Pyun, J.; Matyjaszewski, K. *Chem. Mater.* **2001**, *13*, 3436.
5. Huang, C.-F.; Kuo, S.-W.; Lin, F.-J.; Huang, W.-J.; Wang, C.-F.; Chen, W.-Y.; Chang F.-C. *Macromolecules* **2006**, *39*, 300.
6. Koh, K.; Sugiyama, S.; Morinaga, T.; Ohno, K.; Tsujii, Y.; Fukuda, T.; Yamahiro, M.; Iijima, T.; Oikawa, H.; Watanabe, K.; Miyashita, T. *Macromolecules* **2005**, *38*, 1264.
7. Ríos-Dominguez, H.; Ruiz-Treviño, F. A.; Contreras-Reyes, R.; González-Montiel, A. *J. Membrane Sci.* **2006**, *271*, 94.
8. Ohno, K.; Sugiyama, S.; Koh, K.; Tsujii, Y.; Fukuda, T.; Yamahiro, M.; Oikawa, H.; Yamaoto, Y.; Ootake N.; Watanabe, K. *Macromolecules* **2004**, *37*, 8517.
9. Shockey, E. G.; Bolf A. G.; Jones, P. F.; Schwab J. J.; Chaffee, K. P.; Haddad, T. S.; Lichtenhan, J. D. *Appl. Organometal. Chem.* **1999**, *13*, 311.
10. Provatas, A.; Matisons, J. G. *Trends Polym. Sci.* **1997**, *5*, 327.
11. Li, G.; Wang, L.; Ni, H.; Pittman, Jr. C. U. J. *Inorg. Organomet. P.* **2002**, *11*, 123.
12. Y. C. Sheen, C. H. Lu, C. F. Huang, S. W. Kuo, F. C. Chang, *Polymer* 2008, **49**, 4017.

13. Gravert, D. J.; Janda, K. D. *Tetrahedron Lett.* **1998**, *39*, 1513.

14. Hawker, C. J.; Bosman, A. W.; Harth, E. *Chem. Rev.* **2001**, *101*, 3661.

15. Sciannamea, V.; Jerome, R.; Detrembleur, C. *Chem. Rev.* **2008**, *108*, 1104.

16. Huang, C.-F.; Lee, H.-F.; Kuo, S.-W.; Xu, H.; Chang, F.-C. *Polymer* **2004**, *45*, 2261.

17. Costa, R. O. R.; Vasconcelos, W. L. *Macromolecules* **2001**, *34*, 5398.

Chapter 4

Self-Assembled Fernlike Microstructures of POSS/Gold Nanoparticle Hybrids

Abstract

We have used a thiol-functionalized polyhedral oligomeric silsesquioxane (SH-POSS) as a protective group for the preparation of POSS-protected gold nanoparticles (POSS–Au NPs). The organic/inorganic hybrid SH-POSS NPs exhibited an interesting platelike morphology arising from steric hindrance between the isobutyl groups of SH-POSS. An XRD study of the SH-POSS crystal revealed the relatively large interstice (1.64-nm-lattice constant a > 1.3-nm-diameter SH-POSS) on the basal plane of the unit cell, which resulted in a platelike morphology having lateral dimensions on the order of a few micrometers and thicknesses of a few hundred nanometers. In addition to behaving as a stabilizer for the preparation of Au NPs, an excess of SH-POSS colloids led to the formation of a crystalline template that incorporated the POSS–Au hybrid NPs on its surface, providing a unique fernlike microstructure. After removal of the POSS template (through sublimation and decomposition to a silica char) at 350 °C in air for 1 h, nanosized Au islands having diameters of 50–100 nm and thicknesses of 2–20 nm were sintered onto the substrate. As a result, SH-POSS is an excellent protective group for the preparation of Au NPs of high stability in the powder state. In addition, we suspect that SH-POSS crystals could be used to disperse Au NPs onto substrates for a wide range of applications (e.g., Au catalysts).

4-1 Introduction

Self-assembly of nanoparticles (NPs)—i.e., the controlled organization of NPs into ordered or hierarchical structures—allows coupling of their size- and shape-dependent properties to obtain potentially useful materials for optoelectronics, sensing and imaging, and biomedical applications.[1–4] A broad range of targeted self-assembled structures can be produced by organizing NPs exhibiting compositional heterogeneity;[5–8] they can be realized either by synthesizing NPs from several different materials or by selectively attaching organic molecules to different sites of the NPs.[9–11] Compositional heterogeneity makes NPs conceptually similar to amphiphilic molecules (e.g., surfactants or block copolymers) and allows the thermodynamic approach of self-assembly to be used to form "colloidal molecules" in energetically favorable structures possessing unique properties.[12–22] Ordered monolayers of NPs over large surface areas are sensitive to the presence of defects on the substrate's surface, which can destroy the assembly. In contrast, large ordered arrays of NPs can be obtained through judicious choice of the types of chemical interactions between the particles and the substrate.[23,24] In this paper, we report the preparation of ordered fernlike 3D microstructures of assembled POSS–Au hybrid NPs on to a large-scale crystalline POSS template. Alkyl-functionalized polyhedral oligomeric silsesquioxane (alkyl POSS) derivatives are well-known organic/inorganic hybrid NPs comprising 0.5-nm-diameter siloxane cages and eight alkyl chains.[25] Thus, alkyl POSS molecules can be regarded as colloids (a dispersed phase and a dispersion medium) in solution. Interestingly, platelike morphologies of POSS crystals, with lateral dimensions on the order of a few micrometers and thicknesses of a few hundred nanometers, have been described several times previously.[26–29] Therefore, in this study we employed a thiol-functionalized POSS as (i) a protective group to stabilize Au NPs in solution and (ii) a novel template for the incorporation of Au NPs into thin films.

Thiol compounds are often used to form monolayers on the surfaces of Au NPs via the formation of dynamic S–Au covalent bonds.[30] The concentration of the Au NPs is usually maintained at less than 5 wt% to prevent irreversible aggregation. Thus, the self-assembly of Au NPs in condensed phases is difficult because of the strong tendency to form a concentrated droplet, rather than a large-scale thin film, during evaporation of the solvent. Schmid et al. used 3-mercaptopropylcyclopentyl-POSS to quantitatively exchange the PPh_3 ligands in $(PPh_3)_{12}Au_{55}Cl_6$ in an attempt to obtain POSS–Au NPs stabilized through Au–S bonds; instead, they obtained amorphous structures.[31] Naka et al.[32,33] and Rotello et al.[34,35] have prepared POSS–Au hybrid NPs that were stabilized through electrostatic interactions with the HCl salts of octa(3-aminopropyl)octasilsesquioxane or through hydrogen bonding recognition processes with diaminopyridine-monofunctionalized octasilsesquioxane. Such strong intermolecular interactions (i.e., electrostatic and hydrogen bonding interactions) would suppress the thin-film character of POSS during crystallization. In an attempt to exploit the "crystalline template" of alkyl POSS colloids to self-assemble Au NPs, we turned our attention toward the use of a thiol-monofunctionalized 3-mercaptopropylisobutyl-POSS (herein denoted "SH-POSS"; **Figure 4-1a**). We synthesized SH-POSS-protected Au NPs (POSS–Au) using the method developed by Brust et al., in which $HAuCl_4$ was transferred into the toluene phase with tetraoctylammonium bromide (TOAB) and then reduced with sodium borohydride ($NaBH_4$) in the presence of SH-POSS.[36,37] Thus, interesting large-scale POSS–Au hybrid microstructures[36,38]—featuring 2~4-nm-diameter Au NPs surrounded by 1.3-nm-diameter POSS colloids—could be constructed from a crystalline POSS template (an excess of SH-POSS).[33–35] In addition, at temperatures above 250 °C, most alkyl POSS derivatives can be sublimed, with the residual alkyl POSS (ca. 7.5 wt%) decomposing and oxidizing into a silica char (a network of POSS cages).[39,40] Therefore, we obtained Au-island films through subsequent sintering of well-dispersed Au NPs on the large fernlike microstructures in air at 350 °C.

In this study, we first investigated the characteristic of SH-POSS crystals using power X-ray diffraction analysis; we found that steric hindrance of the alkyl groups on the POSS cages dominated the formation of fernlike or dendritic crystals and provided relatively large interstices on the crystal surface, similar to those observed for NH_4Cl, NH_4Br, and CsCl crystals because of large interstices resulting from ionic repulsion between halide anions.[41] We suspected that it would be reasonable to self-assemble POSS-surrounded Au NPs onto the relatively large interstices on the surface of excess SH-POSS crystals because of the strong tendency for POSS units to aggregate. This novel template—the SH-POSS crystal—can form on several substrates, including water, silicon wafers, and glass slides. Because of its easy and reproducible sample preparation process, the fernlike microstructures of the POSS–Au hybrids can be analyzed using many microscopic techniques, including transmission electron microscopy (TEM), scanning electron microscopy (SEM), atomic force microscopy (AFM), and optical microscopy (OM).

4-2 Experimental Section

4-2.1 Materials.

3-Mercaptopropyl isobutyl-POSS (SH-POSS) was purchased from Hybrid Plastics, Inc. 1-Dodecanethiol (SH-C12, >98%, Sigma–Aldrich), tetraoctylammonium bromide (TOAB, 98%, ACROS), hydrogen tetrachloroauate(III) trihydrate ($HAuCl_4$, ACS grade, ACROS), sodium borohydride ($NaBH_4$, >96%, Fluka), and HPLC-grade solvents were used as received.

4-2.2 Preparation of Au NPs.

The molar feeding ratio (n/m) of $HAuCl_4$ to thiol compounds was the only controlling factor under the reaction conditions. SH-POSS and SH-C12 were selected to compare the effects of the protecting groups on the self-assembly of the Au NPs. A solution of $HAuCl_4$ (0.12 g) in water (100 mL, 6.03 mmol/L) was mixed with a solution of TOAB in toluene (6.03 mmol/L, 100 mL). The two-phase mixture was stirred vigorously until all the $AuCl_4^-$

ions were transferred into the organic layer; SH-POSS or SH-C12 was then added to the organic phase. Freshly prepared aqueous $NaBH_4$ (301.5 mmol/L, 100 mL) was slowly added with vigorous stirring. After further stirring for 3 h, the organic phase was separated, the toluene was evaporated using a rotary evaporator, and the residue was mixed with ethanol (400 mL) to remove excess TOAB. The mixture was maintained at –18 °C for 4 h and then the dark brown precipitate was filtered off and washed twice with ethanol. The Au NPs of C12–Au (n/m = 1) and POSS–Au1 (n/m = 1) were obtained in yields of 53.75 and 36.31 wt%.

4-2.3 Analytical Procedures.

For the TEM images, three drops of a toluene solution (40.9 μL; 10 mg/mL of POSS–Au1; 50 mg/mL of SH-POSS) were placed onto a water surface having a diameter of 5 cm. After air-drying at 25 °C for 30 min, the aggregates were transferred to a carbon-coated Cu TEM grid. For the AFM, SEM, and OM analyses, one drop of dilute toluene solutions (13.7μL, 10 mg/mL of POSS–Au1 and 50 mg/mL of SH-POSS) was placed onto a wafer and then they were air-dried at 25 °C.

4-2.4 Measurements.

A TA Instruments thermogravimetric analyzer (TGA), operated at a scan rate of 20 °C over temperatures ranging from 30 to 800 °C under a nitrogen purge of 40 mL/min, was used to record TGA thermograms of samples on a platinum holder. A Hitachi H-7500 transmission electron microscope (100 kV) was used to record TEM images of dilute solutions and aggregated **POSS-Au1**, **SH-POSS**, and **C12-Au**. The XRD patterns were collected using a D8 Advance powder X-ray diffractometer (Cu K , 40 kV/40 mA; Bruker, Germany). Transmission electron microscopy (TEM) with electron diffraction analysis and energy dispersive X-ray spectra are performed by Philips Tecnai G2 F20 at 200 kV. The atomic force microscopy (AFM) employed in this study is a Digital Instruments Veeco Dimension 5000 Scanning Probe Microscope (Veeco Metrology Group). The AFM tapping mode with a 5-10 nm radius silicon tip was used to scan the cranial suture and cranial bone surface. The displacement resolution of AFM is about 0.1 nm.

4-3 Results and Discussion

4-3.1 POSS Crystals on Au NPs

Although it is difficult to evaluate the exact size of an alkyl POSS derivative because of the flexibility of the alkyl chain, the total diagonal length of alkyl POSS can be considered as a measure of its size. SH-POSS can be regarded as a 1.3-nm-diameter organic/inorganic hybrid colloid ($d_{SH\text{-}POSS}$) because it possesses 0.4-nm-long isobutyl chains on its 0.53-nm-diameter inorganic siloxane cage.[21,32,42] Once the critical particle concentration is reached, a sharp transition from dispersed colloids to a condensed crystalline-like behavior is observed. The transition from the colloid liquid (dispersed state) to the colloidal crystalline phase (condensed state) is first order in nature, similar to the phase transitions from liquid to solid observed in molecular systems.[43] Thus, the crystallography of the condensed POSS state can be also studied through X-ray diffraction analyses (XRD). **Figure 4-1b** reveals that the powder XRD (wavelength: 1.5418 Å) patterns of the SH-POSS crystals displayed four major diffraction angles (2θ) and *d*-spacing distances (d_{hkl})—8.03° (11.00 Å), 10.78° (8.20 Å), 11.92° (7.42 Å), and 18.73° (4.69 Å)—that corresponded to the (*hkl*) diffraction planes (101), (110), (102), and (113) for a hexagonal POSS crystal with the following lattice parameters: $\gamma = 120°$; $\alpha = \beta = 90°$. According to the hexagonal unit cell, the lattice parameters ($a = b = 16.4$ Å; $c = 17.4$ Å) were calculated using **Eq. (4-1)** and **Table 4-1**. When the crystalline model of the 1.3-nm-diameter SH-POSS spheres was made (**Figure 4-1b**), we observed relatively large interstices (lattice parameter a of 16.4 Å > SH-POSS diameter of 1.3 nm) on the basal plane of a SH-POSS unit cell. For hexagonal close packing (HCP) of hard spheres having a diameter d_s, **Eq. (4-2)** suggests that the z-pitch distance (d_z) of the ABA repeating layers in the axial direction is $0.816 \times d_S$. Herein, the lattice parameters a and c for HCP are equal to the diameter of the hard spheres (d_s) and twice the z-pitch distance ($2d_z$) for the two repeating layers, respectively. Thus, the dimensional ratio c/a for HCP is calculated to be 1.63 in **Figure 4-2a**.

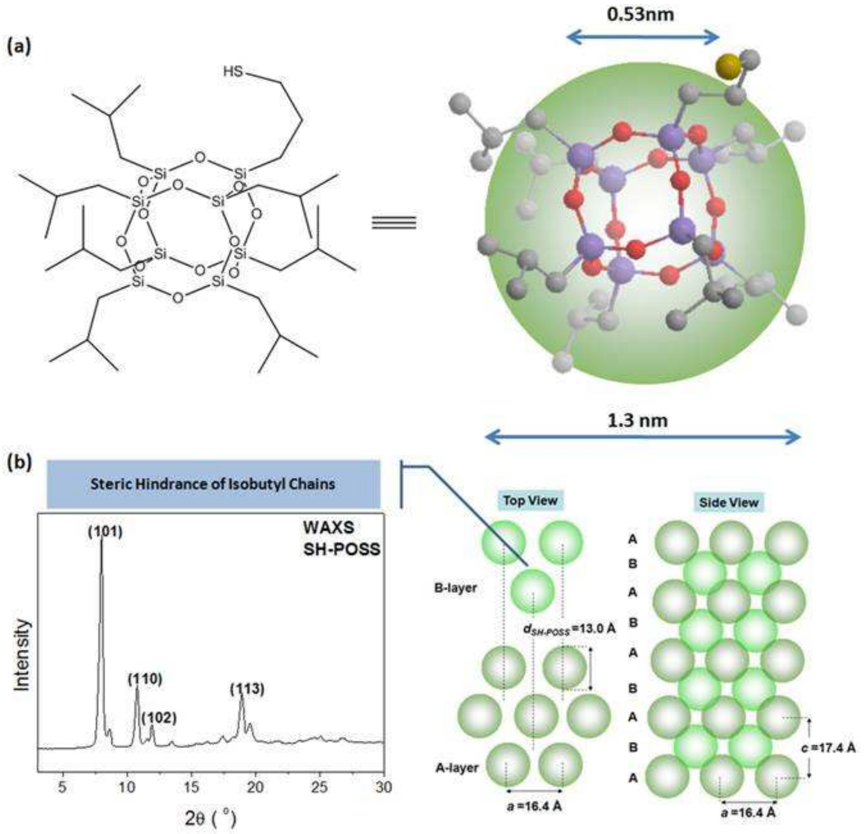

Figure 4-1. (a) Chemical structure and 3D model of SH-POSS; (b) WAXS spectrum and cartoon representation of the molecular packing in a SH-POSS crystal.

Table 4-1. Crystal parameters of **SH-POSS** powders

line	2θ	d_{hkl}	plane (hkl)			a	C
	(°)	(Å)	h k l	$4/3(h^2+h^k+k^2)$	l^2	(Å)	(Å)
1	8.03	11.00	1 0 1	1.33	1		17.387
2	10.78	8.20	1 1 0	4.00	0	16.394	---
3	11.92	7.42	1 0 2	1.33	4		17.392
4	18.73	4.73	1 1 3	4.00	9		17.385

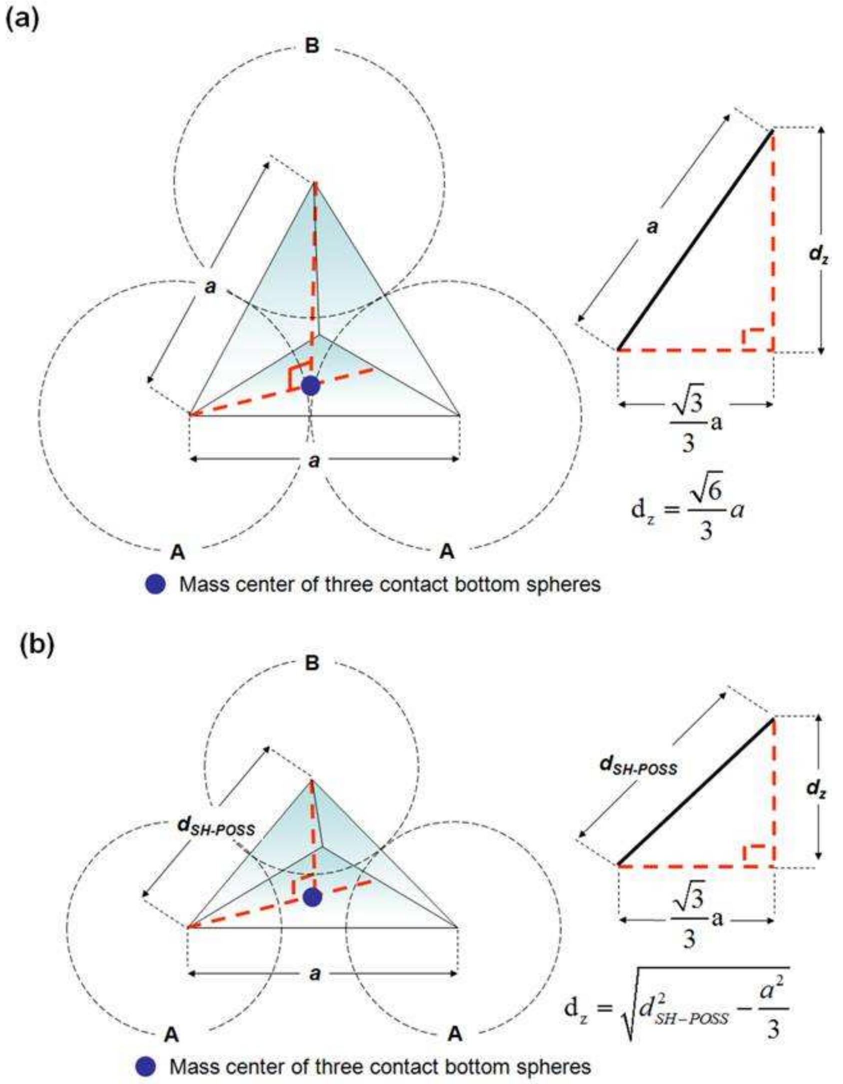

Figure 4-2. Calculated layer-to-layer thicknesses d_z for (a) ABA two-repeating HCP system and (b) **SH-POSS** system for only *z*-directional close packing.

Assuming non-overlapping packing in the axial direction (*z* direction), **Eq. (4-3)** suggests that the theoretical *z*-pitch distance (d_z^*) of an SH-POSS crystal is 8.91 Å, a value larger than the experimental (**Figure 4-1b** and **4-2b**) *z*-pitch distance ($d_{z,SHPOSS}$) of 8.7 Å (i.e., lattice parameter *c*/2). Unlike the HCP of hard spheres, we speculate that the substrate-supported SH-POSS colloids can approach one another to pack into the basal plane with a relatively large interstice of a crystal. Because of repulsion between the sterically demanding isobutyl groups on the POSS cages, the intermolecular distance is slightly larger than the diameter of the SH-POSS colloid. The free SH-POSS colloid in solution can then pack onto the surface interstices of the first layer. For non-supported free SH-POSS colloids, the soft organic shell of SH-POSS colloids can overlap slightly with the low-level SH-POSS colloids, forming a three-dimensional crystal. Thus, the dimension *c*/*a* of SH-POSS crystal is calculated to be 1.06 for platelike unit cells (i.e., less than the value of 1.63 for the HCP of hard spheres). In addition, the difference in the intermolecular distances between the basal plane and the axial direction results in major crystal growth in two approximately orthogonal directions parallel to the substrate, leading to the ordered aggregation of platelike unit cells into fernlike or dendritic crystals having lateral dimensions on the order of a few micrometers and thicknesses of a few hundred nanometers.[26–29]

Steric interactions of the alkyl chains on the POSS cages appear to dominate the low dimensional ratio *c*/*a* (1.06 < 1.63) of the unit cell of a SH-POSS crystal. For bulky molecules without alkyl chains, C_{60}[44,45] molecules and octahydro-POSS [$(HSiO_{1.5})_8$, 424.74 g/mol],[46] possess lattice dimensional ratios (*c*/*a*) of 1.62 and 1.68, respectively, in their hexagonal unit cells—values quite close to the idea dimensional ratio (1.63) expected for the HCP of hard spheres. Fernlike and dendritic crystals of inorganic salts, such as NH_4Cl, NH_4Br, and CsCl, are commonly observed.[41] In these cases, repulsion of hydrated halide anions induces loose packing on the basal plane of a unit cell, allowing cations to insert into the kink sites (interstices) after dehydration. Thus, we infer that the formation of fernlike or dendritic SH-POSS crystals was dominated by steric hindrance between the solvated isobutyl chains on the POSS cages.

$$\frac{1}{d_{hkl}^2} = \frac{4}{3}\left(\frac{h^2 + hk + k^2}{a^2}\right) + \frac{l^2}{c^2} \tag{4-1}$$

$$d_z = \sqrt{d_s^2 - d_s^2/3} \tag{4-2}$$

$$d_z^* = \sqrt{d_s^2 - a^2/3} \tag{4-3}$$

4-3.2 Character of POSS–Au Hybrids

Because bulky SH-POSS colloids can pack loosely into crystals on various substrates, we expected them to be excellent protective agents for the dispersion of Au NPs after becoming anchored onto their surfaces through Au–S bonds. We synthesized the SH-POSS-protected Au NPs (POSS–Au) through the reduction of $HAuCl_4$ in the presence of SH-POSS. Because $HAuCl_4$ is water-soluble, a phase-transfer agent (TOAB) was required to transfer it into the toluene phase. TOAB also transfers the reducing agent ($NaBH_4$) into toluene. Using this approach, we obtained POSS–Au1 and POSS–Au2 at $HAuCl_4$-to-SH-POSS feeding molar ratios (n:m) of 1:1 and 1:0.5, respectively. 1-Dodecanethiol (C12-SH)-protected Au NPs (C12-Au; n:m = 1:1) were also prepared as a control (**Table 4-2**). We used many techniques to analyze our POSS–Au and C12-Au hybrid NPs—OM, SEM, TEM, AFM, Fourier transform infrared (FTIR) spectroscopy, ESCA, small-angle X-ray scattering (SAXS), wide-angle X-ray scattering (WAXS), dynamic light scattering (DLS), and thermogravimetric analysis (TGA). Because Au atoms scatter electrons efficiently as a result of their high mass number, the sizes of the Au cores are easily measured using TEM (i.e., high the contrast between the Au NPs and thiol compounds). To disperse the POSS–Au or C12–Au NPs, we prepared dilute samples for TEM imaging by (i) placing a drop of dilute solution (1 mg/mL) onto a carbon-coated copper grid, (ii) blotting away the excess solution using a strip of filter paper, and (ii) air-drying at 25 °C for 3 min. Thus, through statistical analysis using the Gatan image process, we obtained Au core sizes for C12–Au, POSS–Au1, and POSS–Au2 of 2.0 ± 0.7, 1.8 ± 0.9, and 2.8 ± 0.9 nm (**Figure 4-3**), respectively. These values suggest that SH-POSS plays the same role as that of the well-known C12-SH for the dispersion of Au NPs in toluene.[31]

Table 4-2. Compositions and element analysis results of thiol-protected gold nanoparticles.

Entry	State	Yield[a]	Thiol	n/m[c]				
	(25 °C)	(%)		Input	Output			
					TGA[d]	ICP-MS[e]	SEM-EDX	XPS
C12-Au	Liquid	53.8	1-Dodecanthiol	1	2.61	---	---	---
POSS-Au1	Solid	36.3	SH-POSS	1	2.76	2.42	3.25	2.47
POSS-Au2	Liquid	N.A.[b]	SH-POSS	2	---	6.02	6.75	---

[a] determined by weights [b] a mixture of gold nanoparticles with tetraoctylammonium bromide [c] feeding molar ratio (n/m) of gold salts to thiol compounds [d] determined by the char yield at 700 °C [e] determined by atomic fraction of gold and silicon after digestion.

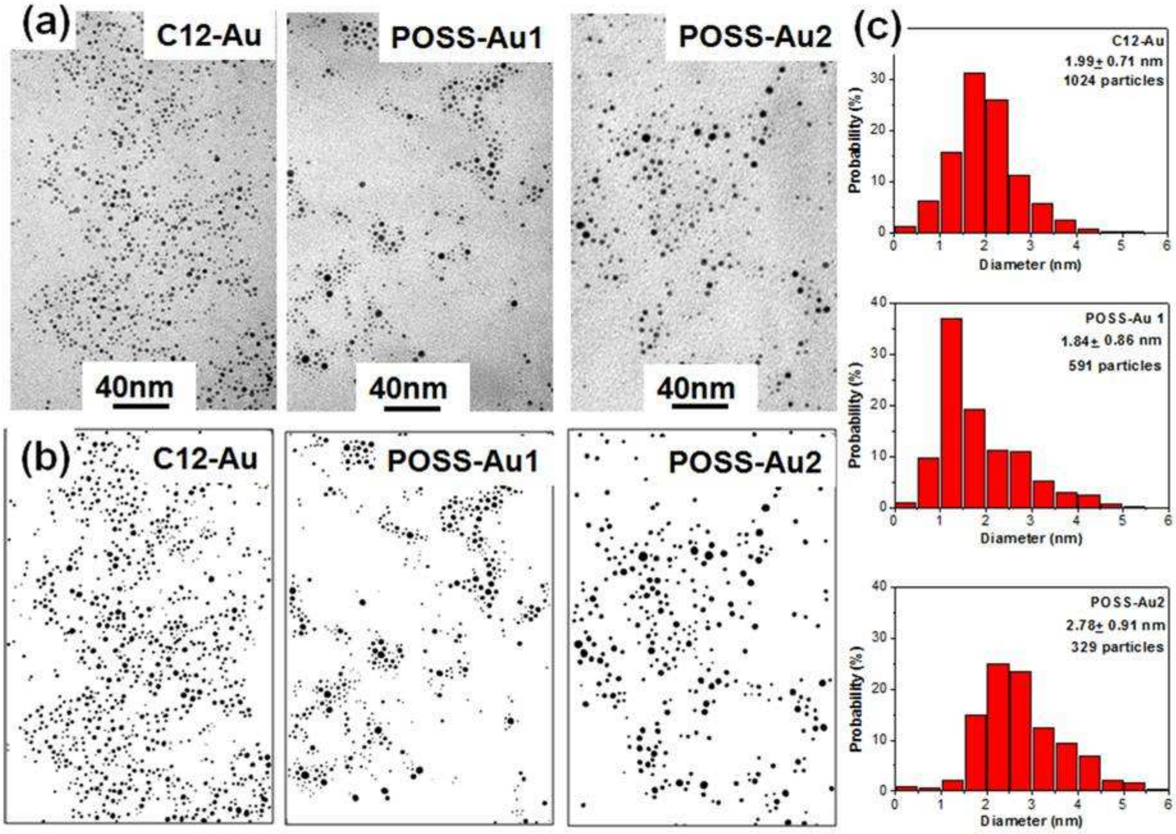

Figure 4-3. (a) TEM images (×200k, top), (b) schematic particle distributions, and (c) probability size distributions of dilute C12-Au, POSS-Au1, and POSS-Au2.

In addition to the dispersed state, we also studied the condensed states of POSS–Au and C12–Au.[43] After evaporation of the toluene, we extracted TOAB and excess $NaBH_4$ into methanol to obtain a pure powder for POSS–Au1 and a sticky material for C12–Au. Based on their char yields at 700 °C, TGA revealed n/m ratios for POSS–Au1 and C12-Au of 2.76 and 2.61 (**Figure 4-4**), respectively. Thus, in the preparation of Au NPs using the water/toluene two-phase method,[36,37] the loss of SH-POSS and C12-SH resulted in higher experimental n/m ratios for both POSS–Au1 and C12–Au. With its low content of SH-POSS, we could not purify POSS–Au2 because the amorphous SH-POSS units became redispersed in methanol. Theoretically, if most SH-POSS colloids are bound onto the spherical surfaces of Au NPs, crystallization of SH-POSS colloids would be suppressed, as was the case for POSS–Au2 (see the FTIR in **Figure 4-5**). In contrast, POSS–Au1 was a powderlike crystal (see the inserted graphs in **Figure 4-6b**). Thus, we needed to determine the packing mode of the SH-POSS colloids on the spherical surface of Au NPs (**Figure 4-6a**). The number of SH-POSS colloids absorbed on the surface of each Au NP can be calculated in terms of the n/m ratio, based on the bulk Au density of 19.3 g/cm^3 and the packing mode of a SH-POSS crystal. Because of the large interstices on the basal plane of a SH-POSS unit cell, we supposed that the SH-POSS colloids would pack into a bilayer shell on the surfaces of the Au cores, thereby reducing thermodynamically disfavored contact between the Au cores and toluene (**Figure 4-6a**). The SH-POSS colloids in the first layer are chemically absorbed onto the Au cores through Au–S bonds; in contrast, those in the second layer can be classified as physically absorbed through POSS–POSS recognition.[35] As a result, the theoretical n/m ratios of POSS–Au1 were 14.48 and 4.24 for the monolayer and bilayer, respectively, of 1.3-nm-diameter SH-POSS spheres surrounding 1.84-nm-diameter Au cores. To determine the mode of assembly of the SH-POSS bilayer on the Au core, we performed an SAXS study on the POSS–Au1 powder (**Figure 4-6b**). The broad band at a scattering vector (*q*) of 1.41 nm^{-1} corresponds to a spacing distance of 4.45 nm, indicating the center-to-center distance between two Au cores (**Figure 4-6a**). Thus, the surface-to-surface distance of 2.60 nm can be assigned to the aggregation of the protective POSS bilayer encapsulating 1.84-nm-diameter

Au NPs.[19] In addition, DLS analysis of POSS–Au1 revealed an average size (D_h) of 7.9 nm, slightly larger than the predicted size (6.23 nm) because of reversible absorption of toluene-solvated SH-POSS colloids onto the surfaces of the Au NPs (**Figure 4-7**). We also performed WAXS (**Figure 4-6b**) analyses to ensure that the feeding of SH-POSS was more than that required for the POSS-bilayer-protected Au NPs to form a "pure" SH-POSS crystal. In addition to the four sharp diffraction bands for the hexagonal POSS crystal, the WAXS spectrum of POSS–Au1 displayed another four broad diffraction angles (2θ) and *d*-spacing distances (d_{hkl})—38.60° (2.33 Å), 44.43° (2.04 Å), 65.10° (1.43 Å), and 78.01° (1.22 Å)—corresponding to the (*hkl*) diffraction planes (111), (200), (220), and (311) for a face-centered cubic (FCC) lattice Au phase.[47] Thus, the excess SH-POSS colloids play an important role in the aggregation of the POSS–Au hybrid NPs. Moreover, the powder POSS–Au1 containing bulky POSS exhibited higher stability for long-term storage than did C12–Au because the dynamic nature of the Au–S bonds led to local aggregation through exchange of thiol-functional ligands (see the aggregation in Figures 4-7 and 4-8). The repulsion interaction between POSS colloids can prevent the exchange of Au-S bonds to stabilize Au NPs.

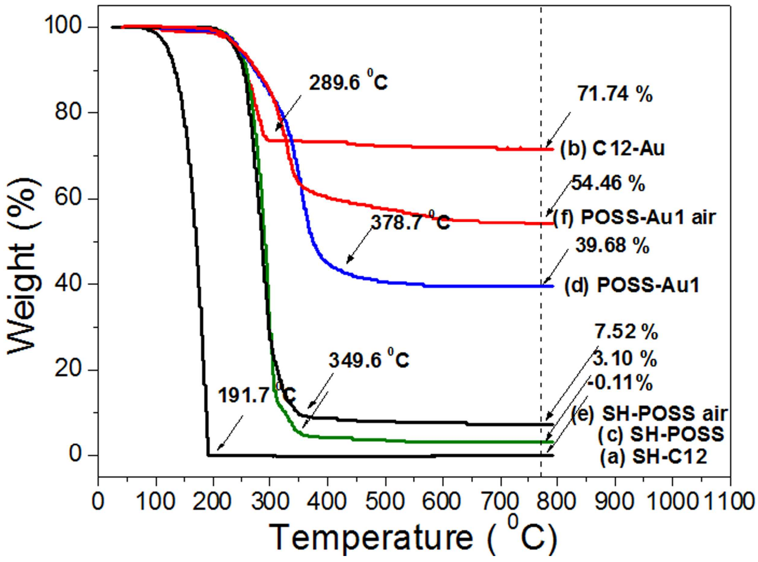

Figure 4-4. TGA thermograms of (a) SH-C12, (b) C12-Au, (c) SH-POSS, and (d) POSS-Au1 in N_2 and (e) SH-POSS air and (f) POSS-Au1 air in air.

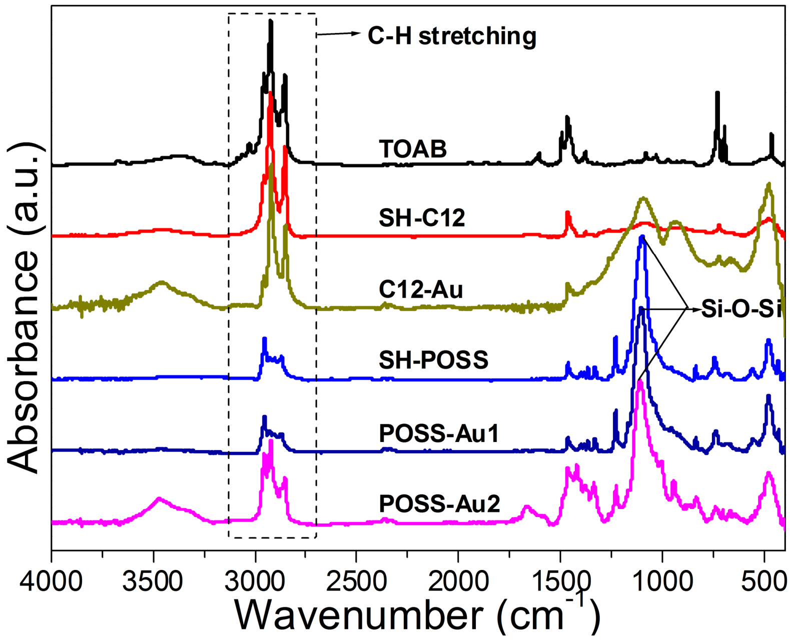

Figure 4-5. FTIR spectra of (a) TOAB, (b) SH-C12, (c) C12-Au, (d) SH-POSS, (e) POSS-Au1, and (f) POSS-Au2.

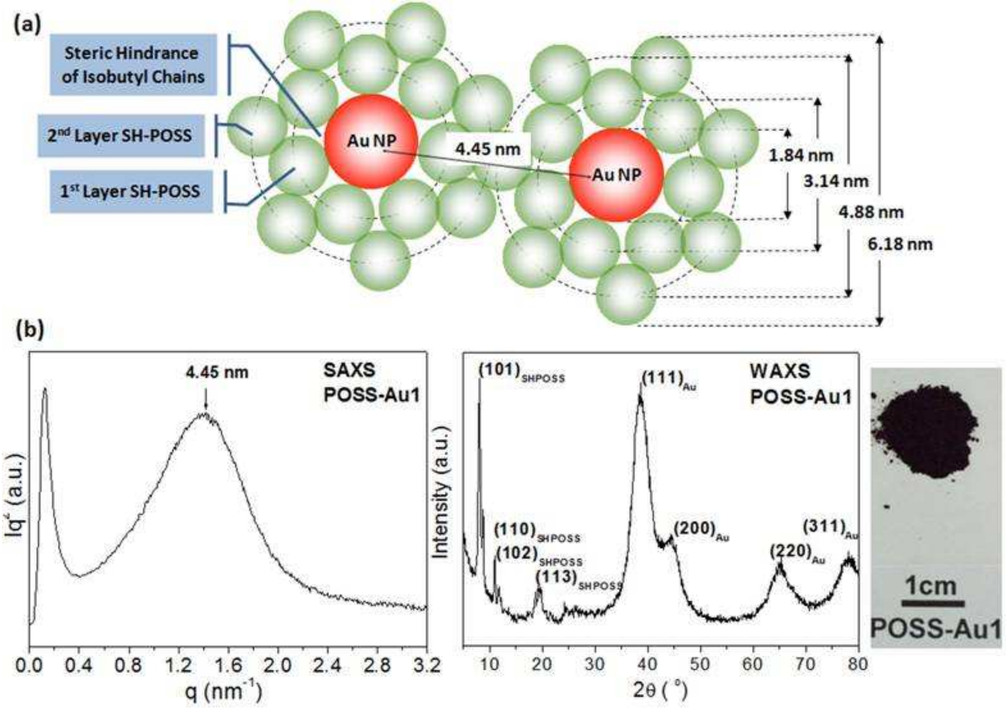

Figure 4-6. (a) cartoon representation of the molecular packing in the SH-POSS bilayer-protected POSS–Au1, with the center-to-center distance between two Au cores highlighted; (b) SAXS and WAXS spectra of POSS–Au1 powders. The insert photograph is a crystal powder of POSS–Au1.

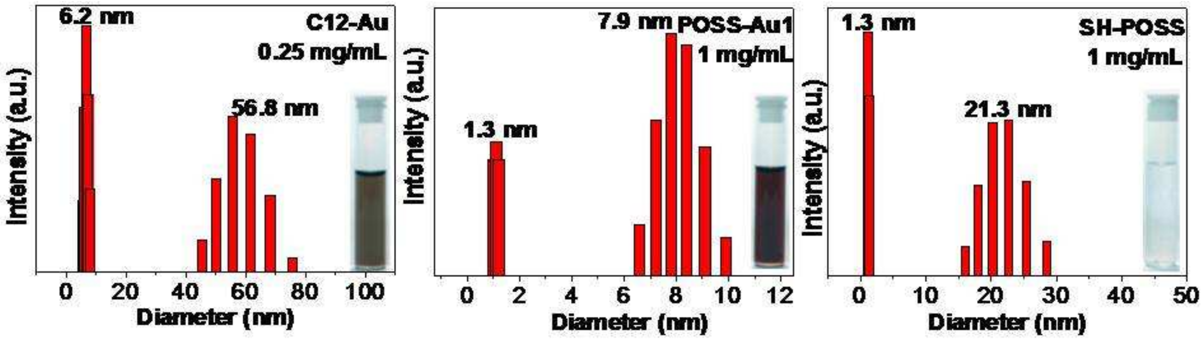

Figure 4-7. DLS analyses of (a) C12-Au, (b) POSS-Au1, and (c) SH-POSS.

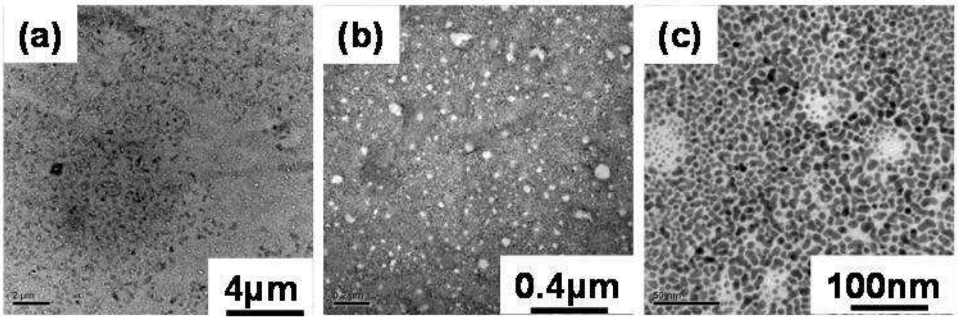

Figure 4-8. TEM images of C12-Au aggregations.

4-3.3 TEM and AFM Analyses of POSS–Au Micro- and Nanostructures

A spherical Au core with the diameter of 1.84 nm is composed of an average of 192.4 Au atoms based on the Au density of 19.3 g/cm^3 (POSS-Au1 in **Figure 4-9**). For the first layer, the centers of the 1.3-nm-diameter SH-POSS units are positioned on the spherical shell of 3.14 nm diameter (i.e., 1.84 + 1.3) occupying an area of 30.97 nm^2 to incorporate a maximum of 13.29 SH-POSS molecules (i.e., 30.97/2.33, where 2.33 [i.e., a^2sin60, where lattice constant a is equal to 16.4 Å for a hexagonal unit cell] is the area occupied by individual SH-POSS on the basal plane). The second layer can be covered by a maximum of 32.11 SH-POSS molecules on the spherical shell of 4.88 nm diameter [i.e., (1.84 + 1.3 + 2× 0.87), where 0.87 is the layer-to-layer distance (d_z) of the SH-POSS crystals]. Thus, the theoretical minimum n/m ratio of Au atoms to SH-POSS molecules would be 14.48 [i.e., 192.4/13.29] and 4.24 [i.e., 192.4/(13.29 + 32.11)] for a POSS protective monolayer and bilayer encapsulating 1.84-nm-diameter Au NPs (**Figure 4-9**). Because the theoretical n/m ratio was 4.24, the low experimental (TGA) ratio of 2.76 for POSS–Au1 indicates the presence of an excess of SH-POSS colloids. During solvent evaporation, excess SH-POSS colloids have a strong tendency to crystallize (thermodynamic first-order phase transition) prior to aggregation of the POSS–Au hybrid NPs. As mentioned above, the crystallization of SH-POSS colloids leads to fernlike or dendritic crystalline morphologies having lateral dimensions on the order of a few micrometers and thickness of a few hundred nanometers. Theoretically, the crystallization of excess SH-POSS colloids should lead toward macrophase separation from the POSS–Au hybrid NPs. We observe, however, fernlike microstructures for both SH-POSS and POSS–Au1 (feeding ratio, n:m = 1:1). Thus, we used TEM to investigate the condensed morphologies of SH-POSS and POSS–Au1 (because of the high contrast between Au and SH-POSS) and AFM to observe the 3D topologies of the crystalline microstructures (**Figure 4-10**). Samples were prepared by evaporating one drop of a dilute toluene solution (10 mg/mL for POSS–Au1; 50 mg/mL for SH-POSS) on a water surface (for TEM) and on a wafer (for AFM). After evaporating the toluene at 25 °C for 30 min, we transferred the samples to a carbon-coated Cu TEM grid for TEM analyses. At low magnification, individual micrometer-long and -wide ferns were visible for both SH-POSS and POSS–Au1 (**Figures 4-10a** and **4-10c**). At higher magnification of POSS–Au1, we could distinguish dark spots (Au cores), some of which were aggregated along the boundary of the fernlike microstructure, resulting in the dark boundary observed at low magnification. AFM analyses (sectional analyses and 2D images) revealed fernlike microstructures for SH-POSS and POSS–Au1 (**Figures 4-10b** and **4-10d**), similar to those observed by TEM (**Figures 4-10a** and **4-10c**). The fernlike microstructures of SH-POSS and POSS–Au1 were ca. 10.1 and 3.3 μm wide; the detected tapes heights were 324.5 and 166.5 nm, respectively. We attribute the smaller sizes of the fernlike microstructures for POSS–Au1 to suppressed SH-POSS crystallization with POSS–Au hybrid NPs. In addition, the rough surface of

POSS–Au1 (**Figure 4-10d**) indicates the incorporation of 6.23-nm-diameter Au NPs onto the surface of the crystalline POSS template. We suspect that the relatively large interstices on the surface of the SH-POSS fernlike template allow the incorporation of SH-POSS on the surface of the Au cores through POSS–POSS recognition processes.[35]

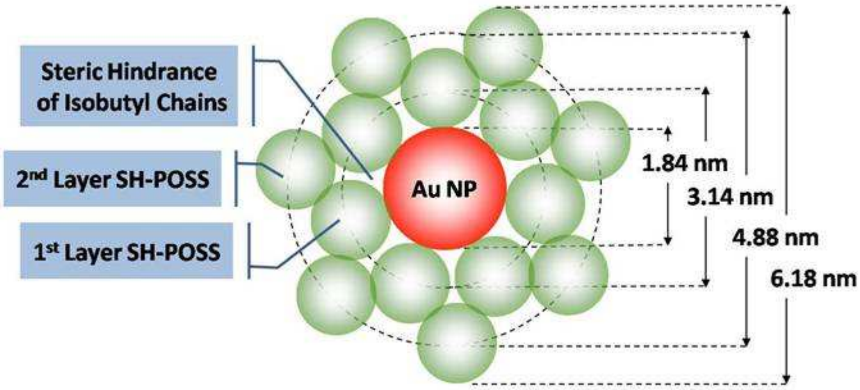

Figure 4-9. Schematic bilayer structure of 1.3-nm-diameter SH-POSS surrounding on a 1.84-nm-diameter Au NPs.

We used multifunctional high-resolution TEM (HRTEM) to investigate the elemental composition between the boundary and internal regions. The TEM image clearly displays a different distribution of Au cores in these two regions (**Figure 4-11a**). Analysis of TEM-assisted energy dispersive X-ray spectra (TEM-EDX) provided the resulting n/m ratios of Au atoms to SH-POSS molecules of 12.44 and 2.43 for the Au-rich boundary (region A) and Au-poor internal (region B) zones (**Figure 4-11b**). In comparison with the expected n/m ratios of 14.48 and 4.24 for monolayer and bilayer packing of SH-POSS spheres, we suspect that the packing of SH-POSS for the POSS–Au hybrid NPs should occur in the form of a monolayer in region A and a bilayer in region B. In addition, the relatively low n/m ratios in both regions A and B indicate that the interparticle region is filled with excess SH-POSS colloids. We recorded electron diffraction patterns at regions A and B to investigate the crystallization behavior of the Au atoms and SH-POSS colloids. In region A, four electron diffraction bands of Au NPs are visible (**Figure 4-11c**); they agree with our results from the powder WAXS analysis (**Figure 4-6b**). In region B, the relatively intense band at low diffraction angle corresponds to the (101) diffraction plane of the SH-POSS crystals and the (111) plane of the Au NPs. As a result, excess SH-POSS colloids in internal region B should form a crystal template for inserting POSS–Au hybrid NPs with bilayer POSS. Upon reducing the concentration of SH-POSS colloids to form the template of a SH-POSS crystal, physically absorbed SH-POSS on the second layer of the POSS–Au hybrid NPs would be released to form a POSS-protective monolayer encapsulating 1.84-nm-diameter Au NPs, followed by aggregation in region A.

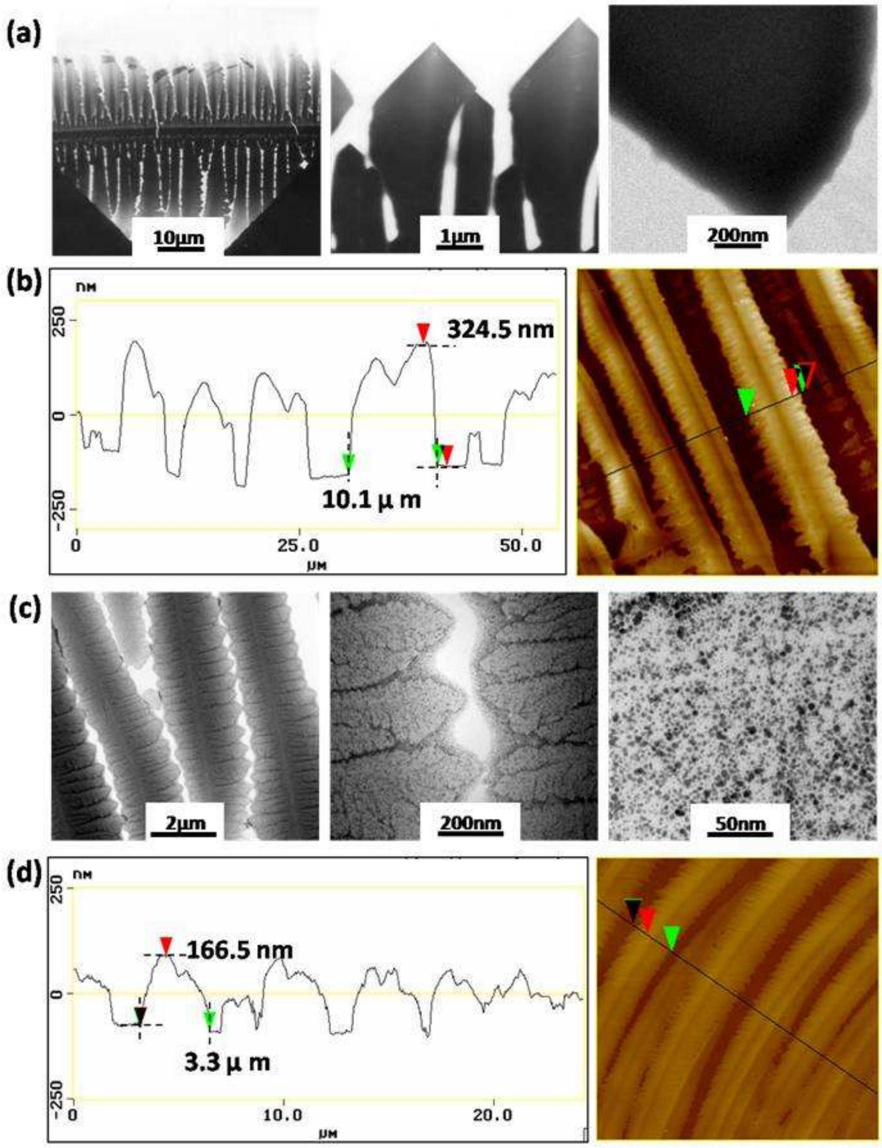

Figure 4-10. TEM images (various) magnifications and AFM sectional analyses of the (a, b) SH-POSS and (c, d) POSS–Au1 fernlike microstructures.

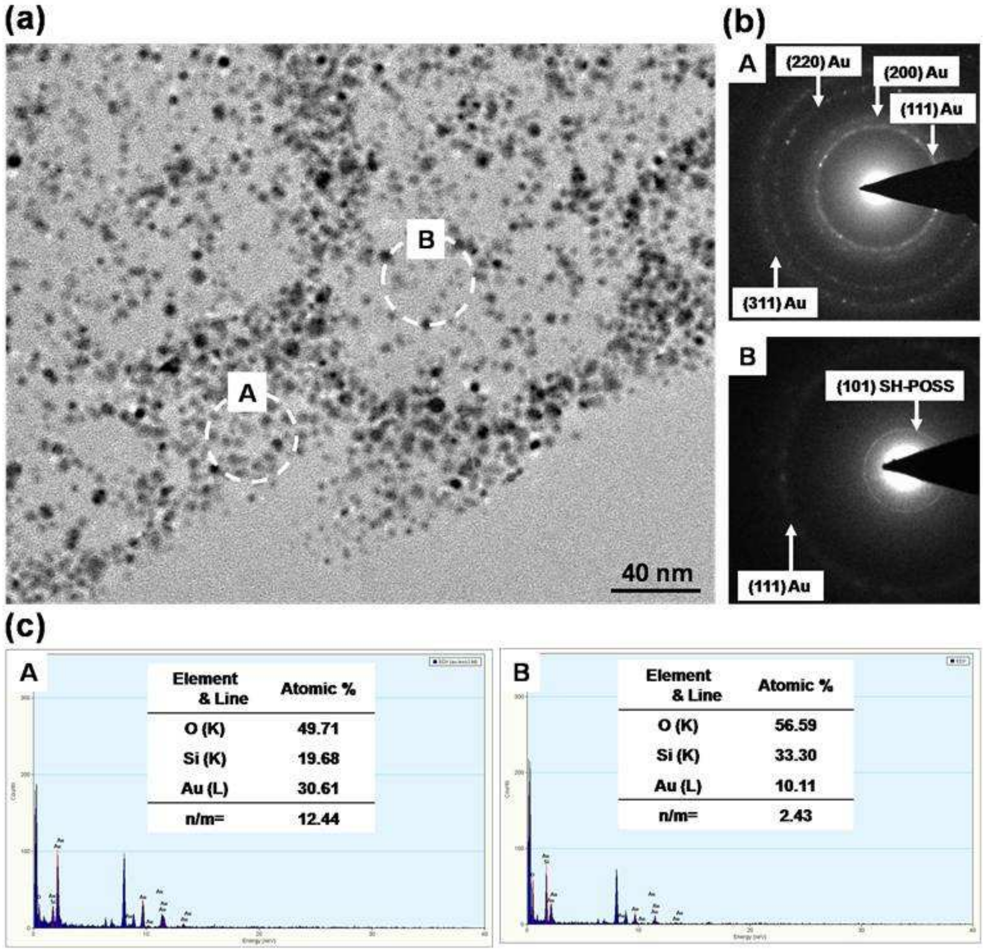

Figure 4-11. (a) HRTEM image, (b) energy dispersive X-ray spectra, and (c) electron diffraction patterns of the POSS–Au1 aggregate. Regions A and B are rich and poor in the Au component, respectively.

4-3.4 Thermal Sintering of POSS–Au Micro- and Nanostructures

This method using a POSS crystalline template is easy to scale up for bulk-quantity synthesis of POSS–Au microwires; these aggregated NPs can be fused together through thermal treatment. At temperatures above 250 °C, 92.5 wt% of the SH-POSS molecules undergo sublimation; the remaining molecules decompose and oxidize into a silica char with a network of POSS cages.[39,40] **Figure 4-12a** displays an OM image of the reddish fernlike microwires obtained after drying one drop of a dilute (10 mg/mL) POSS–Au1 (feeding ratio n:m = 1:1, with excess SH-POSS) solution on a glass slide. In contrast, POSS–Au2 (feeding ratio n:m = 1:0.5) was a droplike liquid because the number of SH-POSS colloids was insufficient to form the POSS crystal template. This observation also indicates that excess SH-POSS can disperse Au NPs onto the substrate. In contrast to the slight shrinkage that occurred when the Au film for POSS–Au2 when placed in an oven at 350 °C in air for 1 h, the resulting calcined POSS–Au1 turned purple and resembled metallic Au NPs (**Figure 4-12b**). In addition, the char yields of SH-POSS are 3.1 and 7.5 wt% in nitrogen and air, respectively (**Figure 4-4f**); in contrast, the char yields of POSS–Au1 were 39.7 and 54.5 wt%, respectively, suggesting that the greater silica char in air (oxidation by oxygen) constitutes larger interparticle grain boundaries between fused Au NPs (**Figure 4-12c**).[48,49] 2D AFM images of the large-scale aggregation (50 × 50 μm^2) of heat-fused POSS–Au1 revealed significant 11.8-nm-overall and 13.1-nm-local surface roughnesses. On the scale of 10 × 10 μm^2, individual fernlike microwires (ca. 3.3 μm wide) were also visible, corresponding to the POSS–Au1 fernlike microstructures in **Figure 4-10d**. The particle sizes of the fused Au NPs could also be calculated through sectional analyses on the scale of 2 × 2 μm^2; the films possessed nanoscale Au islands having thicknesses of 2–20 nm and diameters of 50–100 nm on the substrate resulting from fusion of dispersed Au NPs (**Figure 4-12d**). Moreover, the many cavities present in the Au-rich regions indicate that fusion of the Au NPs occurred to form a porous bulk Au network upon the sublimation of SH-POSS. Although similar Au-island films can be obtained through resistive thermal evaporation (physical vapor deposition) onto glass substrate,[50] our present technique (using a novel SH-POSS crystalline template) is a simpler and more effective method for preparing Au-island films.

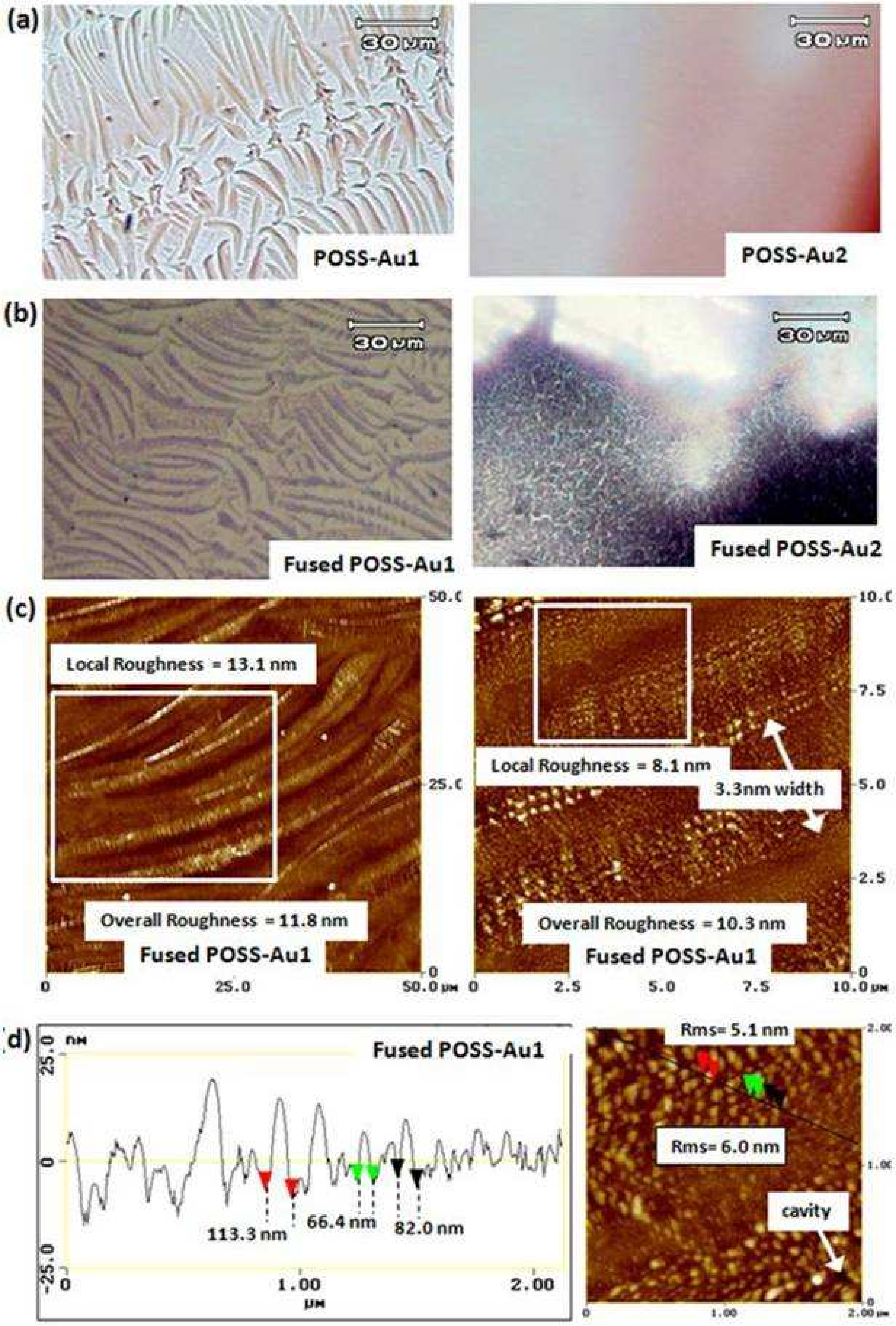

Figure 4-12. (a, b) OM images (× 500) of POSS–Au1 and POSS–Au2 (a) before and (b) after thermal fusion at 350 °C for 1 h. (c) AFM 2D images of heat-fused POSS–Au1 viewed at scales of 50 × 50 μm^2; 10 × 10 μm^2; (d) AFM sectional analysis of heat-fused POSS–Au1 viewed at a scale of 2 × 2 μm^2.

4-3.5 Mechanism of Formation of POSS–Au Hybrids

On the basis of the microscopic data and existing understanding of alkyl-POSS crystals, we propose the following structural model for the formation of the fernlike hybrid microstructures (**Figure 4-13**). As a result of steric interactions between its isobutyl side groups, SH-POSS pack into a bilayer shell on the surface of the Au cores, resulting in the high dispersion of the POSS–Au NPs in toluene. During the process of solvent evaporation, excess SH-POSS colloids (i.e., those not bound onto Au cores) tend to pack in the form of fern- and platelike crystals that function as templates for the self-assembly of POSS–Au NPs onto the surface interstices of the SH-POSS crystals (**Figure 4-13a**). Upon reducing the SH-POSS concentration in toluene, the SH-POSS colloids on the second layer of the bilayer of the POSS–Au NPs are released to fill the gaps between the incorporated Au NPs (**Figure 4-13b**). Finally, the monolayer-protected POSS–Au NPs aggregated at the boundaries of the fern micropatterns, resulting in the POSS–Au NP hybrid fernlike micropatterns (**Figure 4-13c**). When the samples were placed in an oven at 350 °C in air, the SH-POSS molecules either underwent sublimation or their organic alkyl chains decomposed, followed by oxidation and gelation into a silica char. As a result, a porous metallic network was obtained through the sintering of the Au NPs on the substrate (**Figure 4-13d**).

4-4 Conclusion

We have constructed organic/inorganic hybrid materials consisting of thiol-functionalized isobutyl-POSS colloids and Au NPs. The key feature of the self-assembly of the hybrid is the crystallization of excess SH-POSS colloids, which form a fernlike thin film, with relatively large surface interstices that incorporate the SH-POSS-protected Au NPs. This simple, rapid, droplet evaporation process allows thin films with ordered patterns to be prepared reproducibly with high quality. Moreover, Au NPs and SH-POSS colloids can be fused together through thermal treatment with essentially complete retention of the microwire structure—in this case forming an interconnected porous bulk Au network. Given the simplicity and diversity of this method, we suspect that it may have several potential applications.

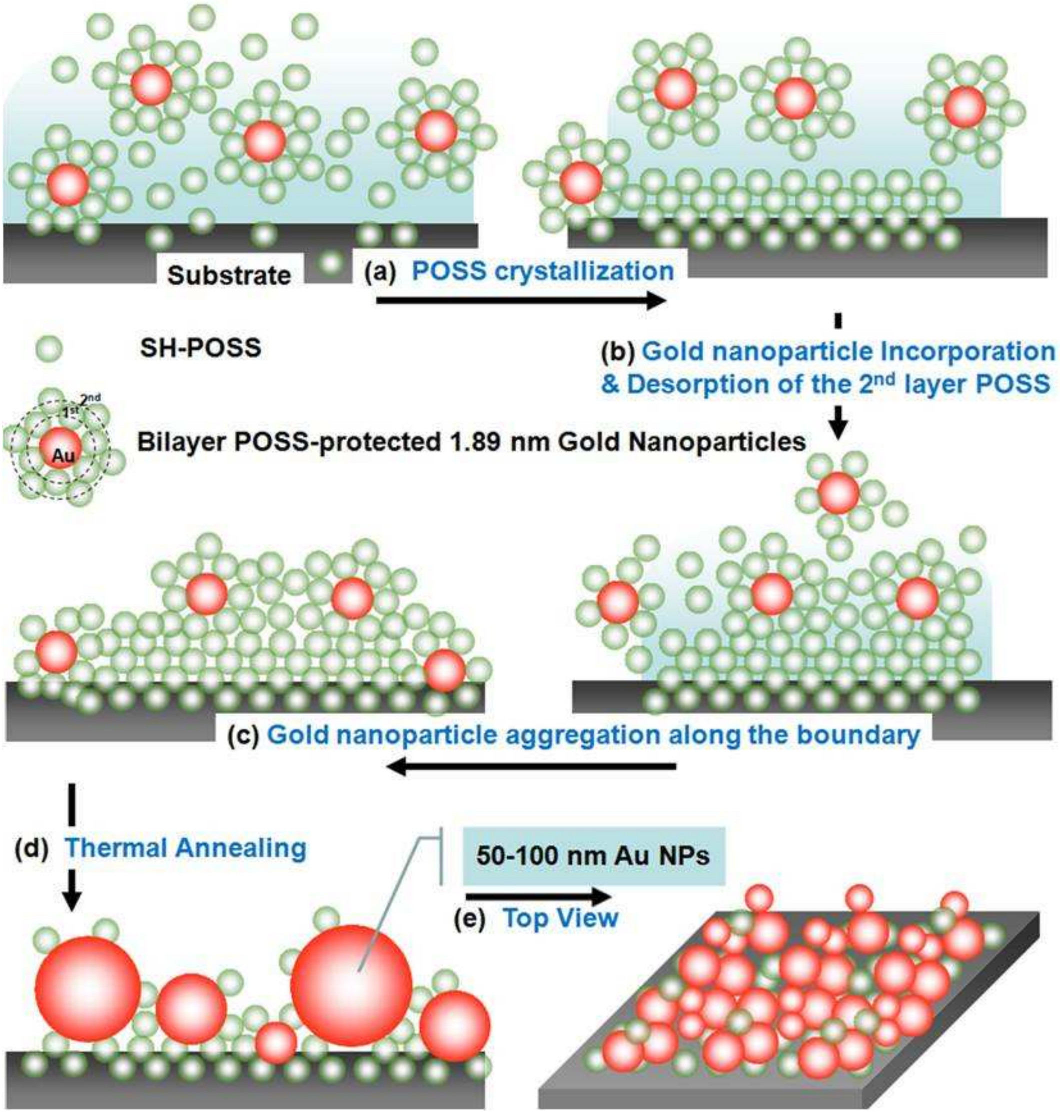

Figure 4-13. Schematic representation of the formation of fernlike POSS–Au1 microstructures.

4-5 Reference

1. Huynh, W. U.; Dittmer, J. J.; Alivisatos, A. P. *Science* **2002**, *295*, 2425.
2. Huang, X.; El-Sayed, I. H.; Qian, W.; El-Sayed, M. A. *J. Am. Chem. Soc.* **2006**, *128*, 2115.
3. Salem, A. K.; Searson, P. C.; Leong, K. W. *Nat. Mater.* **2003**, *2*, 668.
4. Patel, A. C.; Li, S.; Wang, C.; Zhang, W.; Wei, Y. *Chem. Mater.* **2007**, *19*, 1231.
5. Glotzer, S. C.; Solomon, M. J. *Nat. Mater.* **2007**, *6*, 557.
6. Love, J. C.; Urbach, A. R.; Prentiss, M. G.; Whitesides, G. M. *J. Am. Chem. Soc.* **2003**, *125*, 12696.
7. Salant, A.; Amitay-Sadovsky, E.; Banin, U. *J. Am. Chem. Soc.* **2006**, *128*, 10006.
8. Mokari, T.; Rothenberg, E.; Popov, I.; Costi, R.; Banin, U. *Science* **2004**, *304*, 1787.
9. Caswell, K. K.; Wilson, J. N.; Bunz, U. H. F.; Murphy, C. J. *J. Am. Chem. Soc.* **2003**, *125*, 13914.
10. Jackson, A. M.; Myerson, J. W.; Stellacci, F. *Nat. Mater.* **2004**, *3*, 330.
11. Roucoux, A.; Schulz, J.; Patin, H. *Chem. Rev.* **2002**, *102*, 3757.
12. Petit, C.; Taleb, A.; Pileni, M. P. *Adv. Mater.* **1998**, *10*, 259.
13. Murray, C. B.; Kagan, C. R.; Bawendi, M. G. *Annu. Rev. Mater. Sci.* **2000**, *30*, 545.
14. Andres, R. P.; Bielefeld, J. D.; Henderson, J. I.; Janes, D. B.; Kolagunta, V. R.; Kubiak, C. P.; Mahoney, W. J.; Osifchin, R. G. *Science* **1996**, *273*, 1690.
15. Markovich, G. *Acc. Chem. Res.* **1999**, *32*, 415.
16. Liu, J. *J. Am. Chem. Soc.* **1999**, *121*, 4340.
17. Marinakos, S. M.; Brousseau, L.C., III; Jones, A.; Feldheim, D. L. *Chem. Mater.* **1998**, *10*, 1214.
18. Whettern, R. L. *Acc. Chem. Res.* **1998**, *32*, 397.
19. Boal, A. K.; Iihan, F.; DeRouchey, J. E.; Thurn-Albrecht, T.; Russell, T. P.; Rotello, V. M. *Nature* **2000**, *404*, 746.

20. Li, B.; Ni, C.; Li, C. Y. *Macromolecules* **2008**, *41*, 149.

21. Wang, G.; Murray, R. W. *Nano Lett.* **2004**, *4*, 95.

22. Shenhar, S.; Rotello, V. M. *Acc. Chem. Res.* **2003**, *36*, 549.

23. Sato, T.; Hasko, D. G.; Ahmed. H. *J. Vac. Sci. Technol.***1997**, *B15*, 45.

24. Lin, X. M.; Pathasarathy, R.; Jaeger, H. M. *Appl. Phys. Lett.* **2001**, *78*, 1915.

25. Kannan, R. Y.; Salacinski, H. J.; Butler, P. E.; Seifalian, A. M. *Acc. Chem. Res.* **2005**, *38*, 879.

26. Larsson, K. *Ark. Kemi* **1960**, *16*, 209.

27. Waddon, A. J.; Coughlin, E. B. *Chem. Mater.* **2003**, *15*, 4555.

28. Cui, L.; Collet, J. P.; Xu, G.; Zhu, L. *Chem. Mater.* **2006**, *18*, 3503.

29. Miao, J.; Cui, L.; Lau, H. P.; Mather, P. T.; Zhu, L. *Macromolecules* **2007**, *40*, 5460.

30. Sanyal, A.; Norsten, T. B.; Rotello, V. M. Nanoparticle-Polymer Ensembles. In *Nanoparticles: Building Blocks for Nanotechnology*; Rotello, V. M., ed.; Kluwer: New York, 2004.

31. Schmid, G.; Pugin, R.; Malm, J. O.; Bovin, J. O. *Eur. J. Inorg. Chem.* **1998**, 813.

32. Wang, X.; Naka, K.; Itoh, H.; Chujo, Y. *Chem. Lett.* **2004**, *33*, 216.

33. Naka, K.; Itoh, H.; Chujo, Y. *Bull. Chem. Soc. Jpn.* **2006**, *77*, 1767.

34. Carroll, J. B.; Frankamp, B. L.; Srivastava, S.; Rotello, V. M. *J. Mater. Chem.* **2004**, *14*, 690.

35. Carroll, J. B.; Frankamp, B. L.; Rotello, V. M. *Chem. Commun.* **2002**, *17*, 1892.

36. van Herrikhuyzen, J.; George, S. J.; Vos, M. R. J.; Sommerdijk, N. A. J. M.; Ajayaghosh, A.; Meskers, S. C. J.; Schenning, A. P. H. J. *Angew. Chem. Int. Ed.* **2007**, *46*, 1825.

37. Brust, M.; Walker, M.; Bethell, D.; Schiffrin, D. J.; Whyman, R. *J. Chem. Soc. Chem. Commun.* **1994**, 801.

38. van Herrikhuyzen, J.; Janssen, R. A. J.; Meijer, E. W.; Meskers, S. C. J.; Schenning, A. P. H. J. *J. Am. Chem. Soc.* **2006**, *128*, 686.

39. Mantz, R. A.; Jones, P. F.; Chaffee, K. P.; Lichtenhan, J. D.; Gilman, J. W.; Ismail, I. M. K.; Burmeister, M. J. *Chem. Mater.* **1996**, *8*, 1250.

40. Liu, L.; Tian, M.; Zhang, W.; Zhang, L.; Mark, J. E. *Polymer* **2007**, *48*, 3201.

41. Shigematsu, K. Crystal Growth of Alkali Salts from Concentrated Aqueous Solutions. In *Crystallization Processes*; H. Ohtaki, ed.; John Wiley and Sons, New York, 1999; Vol. 3, pp 69–97.

42. Jeong, K. U.; Knapp, B. S.; Ge, J. J.; Graham, M. J.; Tu, Y.; Leng, S.; Xiong, H.; Harris, F. W.; Cheng, S. Z. D. *Polymer* **2006**, *47*, 3351.

43. Zhang, J. Z.; Wang, Z. L.; Liu, J.; Chen, S.; Liu, G. In *Self-Assembled Nanostructures*; Kluwer Academic: New York, 2003.

44. Krätschmer, W.; Lamb, L. D.; Fostiropoulos, K.; Huffman, D. R. *Nature* **1990**, *347*, 354.

45. Kroto, H. W.; Heath, J. R.; O'Brien, S. C.; Curl, R. F.; Smalley, R. E. *Nature* **1985**, *318*, 162.

46. K. Larsson, *Ark. Kemi* **1960**, *16*, 215.

47. Chunyan, B.; Ming, J.; Ran, L.; Tierui, Z.; Yingying, Z. *Mater. Chem. Phys.* **2003**, *82*, 812.

48. Fullam, S.; Cottell, D.; Rensmo, H.; Fitzmaurice, D. *Adv. Mater.* **2000**, *12*, 1430.

49. Prevo, B. G.; Fuller, J. C., III; Velev, O. D. *Chem. Mater.* **2005**, *17*, 28.

50. Xenogiannopoulou, E.; Iliopoulos, K.; Couris, S.; Karakouz, T.; Vaskevich, A.; Rubinstein, I. *Adv. Funct. Mater.* **2008**, *18*, 1281.

Chapter 5

Supramolecular Catalysts by Encapsulating Palladium Nanocrystals within POSS Colloids

Abstract

A very simple method to prepare POSS-protected palladium nanoparticles (POSS-Pd NPs) by reflux toluene solution containing palladium acetate ($Pd(OAc)_2$) and 3-mercaptopropylIsobutyl-polyhedral oligomeric silsesquioxane (SH-POSS) has been developed. POSS-Pd NPs were used to be metal catalysts in the Heck coupling with iodobenzene and methyl acrylate. The kinetic study by ^{1}H NMR spectra revealed this first order reaction and reached 99.7% conversion at 2.5h. In comparison with the conventional 1-dodecanthiol-protected palladium nanoparticles (C12-Pd NPs), the steric interaction between POSS colloids allows to the input of reactants and the output of products, indicating the higher reactivity than C12-Pd NPs.

5-1 Introduction

Palladium is among the most widely used transition metals in modern organic synthesis and synthetic transformations.[1] However, the separation of the Pd from the desired product, stability to retain its activity and reusability often complicates its applications. In this regard, there have been many efforts to immobilize Pd catalysts onto a support, such as charcoal, silica or alumina,[2] which may result in high catalytic activities but the stability to metal leaching is not satisfactory.[3] Alternatively, encapsulation of the metal particles by polymers[4] or dendrimers[5] have been reported, but these metal particles require further mechanical stabilization against being leaching out or the breakage of the host. Recently, a number of reports have been published on the immobilization of Pd particles via ligand/polymer anchoring[6] and layerby-layer assembly onto a solid support.[7] However, being a soft material, the ligand/polymer may not provide enough robustness against metal leaching, or for recyclability.[8]

The organic cluster consists of a cubical core and organic short arms stretched from eight corners of the core. The inorganic core structure functions as a stable spacer for separating organic arms to achieve organic/inorganic hybrid nanoparticles. Incorporating the small organic chains onto the cubical core could also maintain less steric hindrance to high reactivity. The polyhedral oligosilsesquioxanes (POSSs), cyclic oligomers of ladder-like poly(silsesquioxanes), are selected as the core due to its rigid cagelike structure (i.e., T8, T10, and T12 POSS). Especially, a T8 POSS molecule contains an inorganic cube (0.53 nm) with six identical siloxane planes and eight organic chains on eight points of a cube, being a molecular inorganic and organic hybrid nanoparticle. In organic solution, T8 POSSs can also be regarded as molecular colloids to disperse an inorganic core with soluble organic chains. Thus, the symmetric chemical structure of T8 POSS nanoparticles can pack into the ordered structures (colloidal crystals) after removal of solvent. The monofunctional POSS with the similar chemical structure to T8 POSS can also form a crystal. Herein, the thiol-functional POSS (SH-POSS) has been found to be an excellent metal nanoparticle stabilizer in solution or aggregation resulting from the steric hindrance between the outer alkyl chains. In addition, the thermogravity analysis showed that most SH-POSS were sublimated and others were decomposed into the silica char resulting in the low char yield.[9] Furthermore, the residual silica char is able to sinter metal nanoparticles on the substrate and holds the Pd nanoparticles in a well-defined structure.

Using nonionic stabilzers, a phase transfer agent is usually required to transfer water soluble metal salts for preparation of metal nanoparticles. The metal nanoparticles such as Ag, Au, Pd and Pd NPs can be prepared by chemical reduction or solvothermal reduction. For example, the chemical reduce agent of $NaBH_4$ is usually used to fabricate metal nanoparticles in the mild condition (25°C, 1atm). In contrast, Hyeon et al reported the synthesis of monodisperse Pd NPs by nonsolvent thermal aging of a Pd-surfactant complex at 300 °C for 30 min.[10] However, the temperatures higher than 200 °C may result in the evaporation of small molecules or the decomposition of oligomers. The current synthetic procedure is similar to the method developed by Hyeon's group for the synthesis of POSS-stabilized Pd nanoparticles which empolyed the formation of a metal-thiol complex followed by reflux of toluene solution. The detailed synthetic procedure to prepare 2.7-nm POSS-stabilzed and 2.5-nm 1-dodecanthiol-stabilized Pd NPs is shown in **Figure 5-1**.

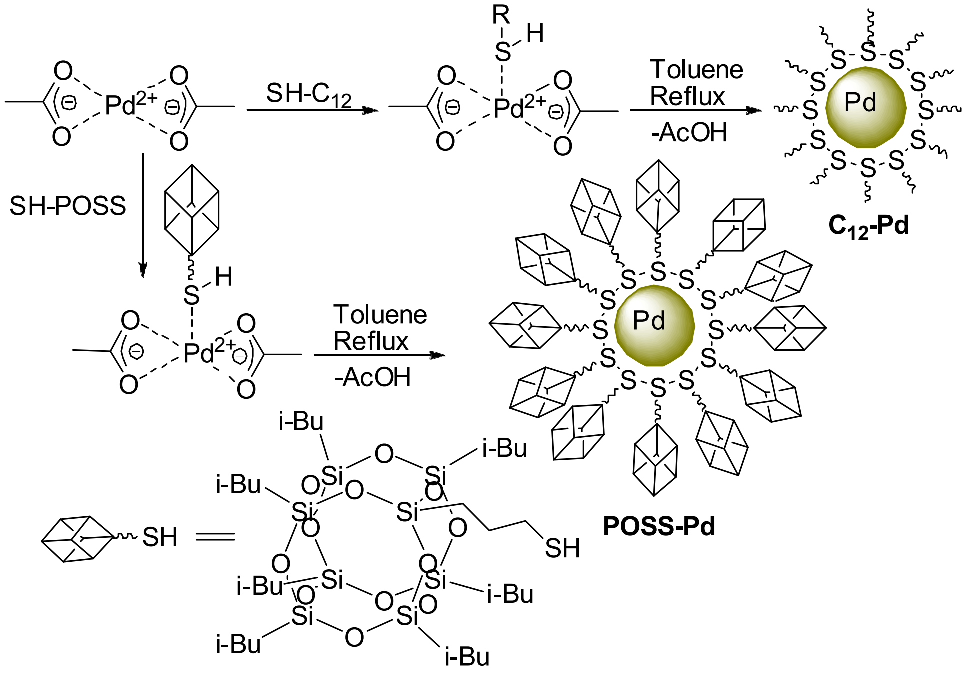

Figure 5-1. Direct synthesis of C_{12}-Pd and POSS-Pd.

5-2 Experimental Section

5-2.1 Materials.

3-Mercaptopropyl isobutyl-POSS (SH-POSS) was purchased from Hybrid Plastics, Inc. Palladium acetate ($Pd(OAc)_2$, Aldrich, 98%), 1-dodecanthiol (C12-SH, Aldrich, >98%), iodobenzene (IB, Aldrich, 98%), methyl acrylate (MA, Aldrich, 99%), tributylamine (TBA, Aldrich, >98%), and HPLC-grade solvents were used as received.

5-2.2 Syntheses of POSS-Pd or C12-Pd.

A mixture of $Pd(OAc)_2$ (0.112 g, 0.5 mmol) and SH-POSS (0.446 g, 0.5 mmol) or C12-SH (0.101 g, 0.5 mmol) in toluene (20 mL) was heated at 140 °C for 30 min. After toluene evaporation, the resulting concentrated reaction mixture was added with excess methanol to precipitate to afford a brown powder of POSS-Pd with the yield of 82% and a brown viscous liquid of C12-Pd with the yield of 76%.

5-2.3 Conditions of Heck coupling

The Heck reactions were carried out by mixture of POSS-Pd (0.1g, 0.128 mmol Pd) or C12-Pd (0.035g, 0.128 mmol Pd), iodobenzene (0.57 mL, 5 mmol) methyl acrylate (0.45 mL, 5 mmol), and tributylamine (1.79 mL, 7.5 mmol) in NMP (30 mL). The reactions were heated at 75 °C and a liquor of reaction solution are dissolved in CD_3OD at the given time interval for determination of methyl acrylate conversion by ^1H NMR spectra. The Pd catalysts were recovered by precipitation from methanol and were dried in the vacuum oven at 25 °C for 1d.

5-2.4 Measurements.

^1H spectra were recorded using a Varian Unityinova 500 NMR spectrometer. UV–Vis spectra were measured using a UV-1601 spectrophotometer (Shimadzu, Japan). A TA Instruments thermogravimetric analyzer, operated at a scan rate of 20 °C over temperatures ranging from 30 to

800 °C under a nitrogen purge of 40 mL/min, was used to record TGA thermograms of samples on a platinum holder. A Hitachi H-7500 transmission electron microscope (100 kV) was used to record TEM images of dilute solutions and aggregated POSS-Pd and C12-Pd. The XRD patterns were collected using a D8 Advance powder X-ray diffractometer (Cu K , 40 kV/40 mA; Bruker, Germany). Transmission electron microscopy (TEM) with electron diffraction analysis and energy dispersive X-ray spectra are performed by Philips Tecnai G2 F20 at 200 kV. All infrared spectra were recorded at 25 ^{o}C at a resolution of 1 cm^{-1} , over 32 scans on a Nicolet AVATAR 320 FTIR spectrometer and degassed with nitrogen.

5-3 Results and Discussion

5-3.1 Synthesis of POSS-Pd and C12-Pd

The Pd-thiol complex was prepared by dissolving $Pd(OAc)_2$ (0.11 g, 0.5 mmol) and 1-dodecanthiol (SH-C_{12}, 0.10 g, 0.5 mmol) or 3-mercaptopropyl isobutyl-polyhedral oligomeric silsesquioxane (SH-POSS, 0.45 g, 0.5 mmol) in toluene (20 mL) with argon purged. The color of the solution changed from yellow to orange as soon as mixing with the thiols (see the insert of **Figure 5-2**), demonstrating the formation of the Pd-thiol complex. The FT-IR spectrum of the complex shows a carbonyl stretching peaks at 1633.8 and 1601.4 cm^{-1}, indicating the release of metal-complex acetatic anion from the palladium center of the precursor (**Figure 5-2B**). The resulting solution was quickly imersed into a oil bath at 140 °C, and was further aged (toluene reflux) for 30 min to generate a black colloidal nanoparticle solution (see the inset of **Figure 5-2A**. The UV-vis spectra of C12-Pd and POSS-Pd NPs show an visible light abosorbance (400－800 nm), indicating the surface plasmon behavior of Pd nanoparticles (**Figure 5-2A**). Thiol anions generated in situ from the proton transfer from thiol to acetic anion induced the reduction of the Pd salt. This method is similar to alcohol reduction of silver nitrate at 120 °C by using ethylene glycol as a reducing agent.[11] After removal of the toluene, black precipitates were purified by washing acetic acid with 250 mL MeOH and gave yields of 76 and 82 % for C_{12}-Pd and POSS-Pd, respectively. The precipitate can be easily redispersed in nonpolar organic solvents such as toluene to yield a clear homogeneous solution. By thermogravity analyses, the inorganic composition of C12-Pd and POSS-Pd were 39.2 and 13.6 wt.%, respectively, in agreement with the expected values of 34.4 and 10.6 wt.% according to the feeding equimole of $Pd(OAc)_2$ and thiol compounds (**Figure 5-2C**). In comparison with $Pd(OAc)_2$ and SH-POSS crystals, XRD patterns of C_{12}-Pd and POSS-Pd exhibited two broad diffused rings, corresponding to (111) and (220) reflections of face centered cubic Pd (**Figure 5-2D**).[12]

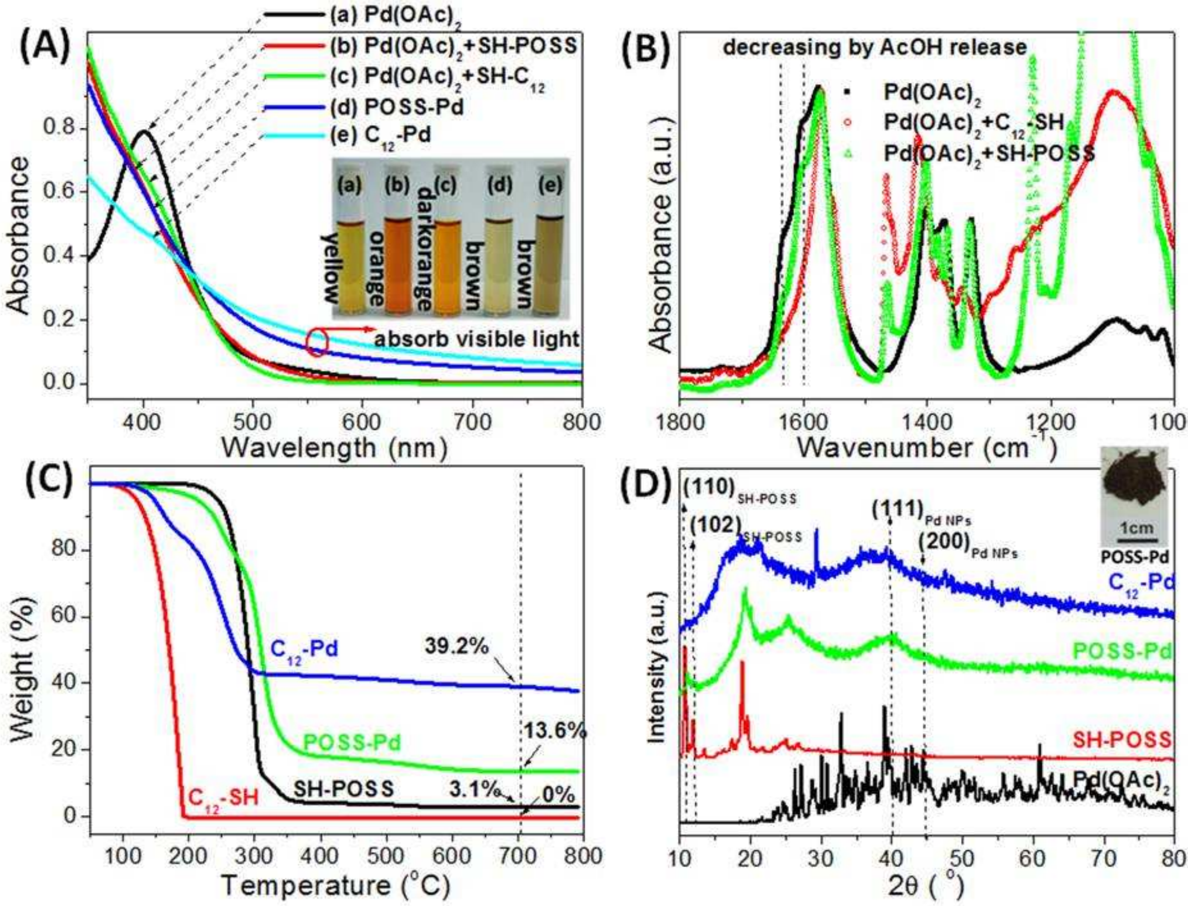

Figure 5-2. (A) UV-vis, (B) FTIR, (C) TGA, (D) XRD results of C_{12}-Pd, and POSS-Pd. Additional informations such as FTIR and UV-vis spectra of $Pd(OAc)_2$, $Pd(OAc)_2$+SH-C_{12}, $Pd(OAc)_2$+SH-POSS, TGA analyses of SH-C_{12}, SH-POSS, and XRD patterns of $Pd(OAc)_2$, SH-POSS.

5-3.2 Character of POSS-Pd and C12-Pd

The high-resolution transmission electron microscopic (HRTEM) image (**Figures 5-3A**) shows that 3.7-nm POSS-Pd and 2.5-nm C_{12}-Pd nanoparticles are well dispersed. These nanoparticles were obtained without any size selection process, which is important for the large-scale production. The electron diffraction patterns of C_{12}-Pd and POSS-Pd shown in the upper insets exhibit three diffused rings, confirming the face centered cubic structure of the metallic Pd (**Figure 5-3B**). The particle size calculated from the image process, matches well with broad XRD data (**Figure 5-3C**). A high-multiplication HRTEM of a single particle, shown in **Figure 5-3D** reveals atomic lattice fringe exhibiting the crystalline nature of the POSS-Pd nanoparticle.

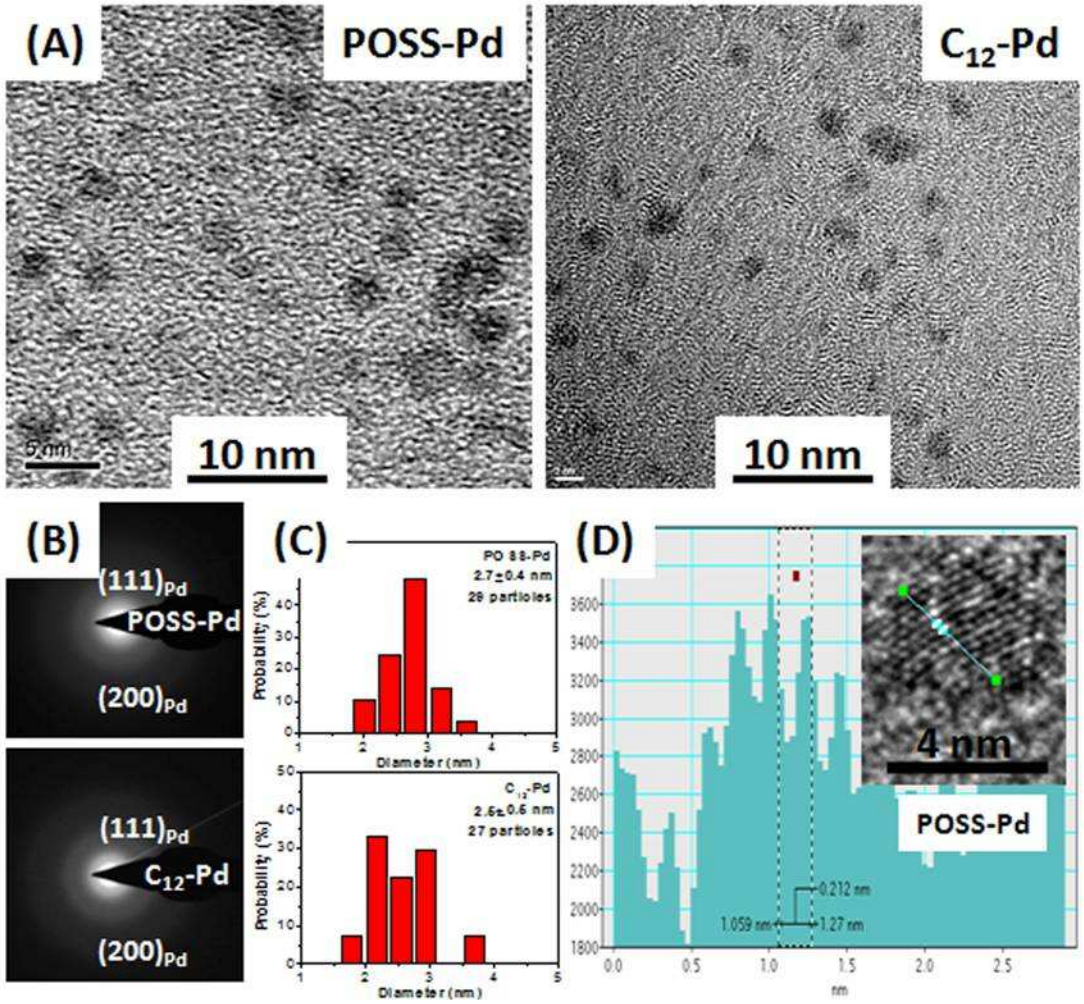

Figure 5-3. TEM images, electron diffraction pattern, and atomic lattice frigne of (a) C12-Pd and (b) POSS-Pd.

5-3.3 Heck coupling using POSS-Pd and C12-Pd

The POSS-protected Pd nanoparticles (POSS-Pd) can be applied to the Heck Reactions (**Figure 5-4**). Herein, we reported the Heck coupling between iodobenzene and methyl acrylate to give the methyl *trans*-cinnamate. In ^{1}H NMR spectra, vinyl protons of H_b and H_g are indicative of methyl acryalte and methyl *trans*-cinnamate (**Figure 5-5A**). In addition, the Heck coupling of methyl acrylate and iodobenzene into methyl *trans*-cinnamate can be observed from the increase of H_h and H_i and the decrease of H_a, H_b, H_c, H_d, and H_e. Under the conditions used, methyl trans-cinnamate was produced in 100% selectivity. **Figure 5-5B** shows time-conversion and time-ln($[M]_0/[M]$) curves at 75 °C for POSS-Pd or C12-Pd. The system using POSS-Pd was more active than the other, which needed the activation time of 1h. According the reaction mechanism of Heck coupling (**Figure 5-4**),[13] two key steps of oxidation addition and reduction elimination can dominate the catalyst activity and the catalyst recovery, respectively. Using colloidal Pd NCs (solid microdomains in solution), the protective groups such as C12-SH in the C12-Pd catalysts need to exchange with iodobenzene through oxidation addition. Therefore, the dense monolayer of C12-SH on the surface of Pd NCs needs the activation time of 1h to exchange the surface active site. In contrast, the interstices between bulk POSS groups allow the input of reactants and the output of products, showing the zero activation time and the linear time-conversion curves to 99.7% after 3h. Moreover, the linear time-ln($[M]_0/[M]$) curve indicates the first order reaction, meaning that the catalyst activity doesn't change during Heck coupling. In comparison, the S-shape time-conversion curve using C12-Pd indicates the reaction rate increased as the amount of leached Pd increase and decreased as the amount of reactants decease. The reaction mechanism of Heck coupling also reveals an important phenomenon of phase transfer from solid Pd(0) to liquid Pd(2+) to solid Pd(0). Therefore, the leached Pd NCs from the supporting matrices was still a serious problem due to the difficulty in forming Pd NCs again after reduction elimination. Thus, many conditions such as temperatures, base co-catalysts, and are developed by Zhao et al[14a] to overcome this drawback. This problem also happened in the Heck coupling using POSS-Pd NCs. We found the loss of around 45 wt% POSS-Pd NCs after recovering by precipitation from methanol. In addition, the thermogravity of recycled POSS-Pd NCs indicates the invariant fraction of inorganic Pd compositions, showing the conversion of POSS-Pd(0) NCs into POSS-Pd(2+) complexes. In the study by Zhao et al,[14a] the rate of reaction increased as the amount of leached Pd increased. This indicates that the Heck reactions are mainly homogeneously catalyzed by Pd species dissolved in the solution, in accordance with the results of Shmidt and Mametova.[14b] However, the 45 wt% loss of POSS-Pd NCs and the 99.7 % conversion of methyl acrylate indicate the Heck coupling shouldn't undergo through reduction elimination into Pd(0) NCs. In the further study, we will prove our suggestion that Heck coupling undergoes the favorable pathway (dash line in **Figure 5-4**) without phase transfer toward products. In this study, we found the solvothermal reduction (toluene reflux) of Pd(OAc)$_2$ to give Pd NCs in the presence of thiol-functional POSS. And, we will try to find a practical method to recover Pd catalysts according to this finding.

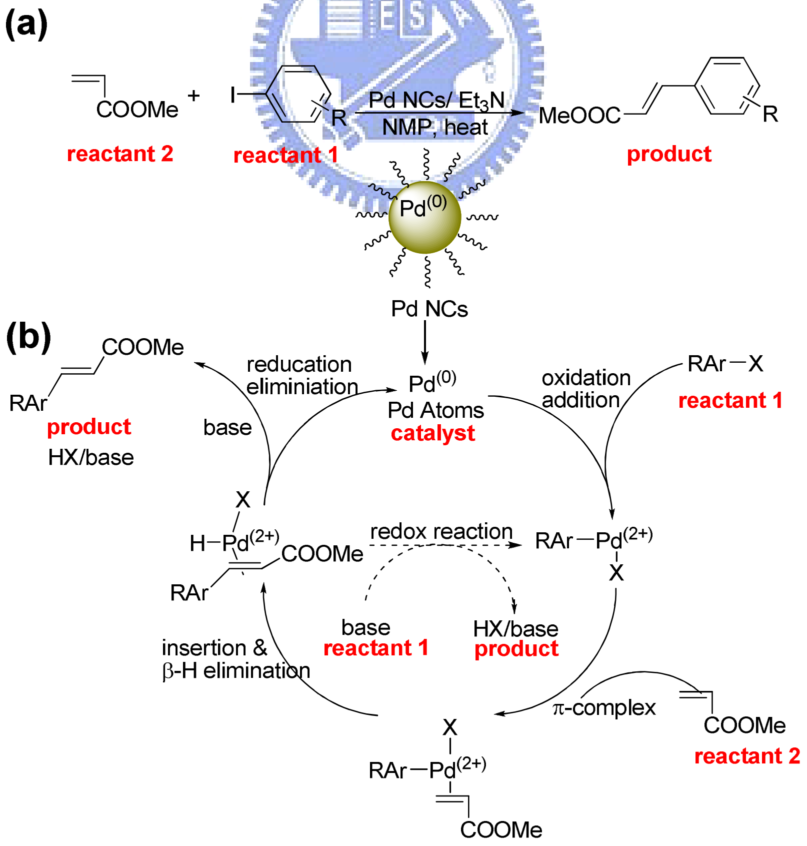

Figure 5-4. (a) Reaction scheme of Heck Coupling, which is the palladium-catalysed cross coupling between acrylate and halides and (b) reaction mechanism of Pd NCs-catalyzed Heck coupling with based-activation.[13] Herein, we proposed the favorable pathway (dash line) without phase transfer toward products.

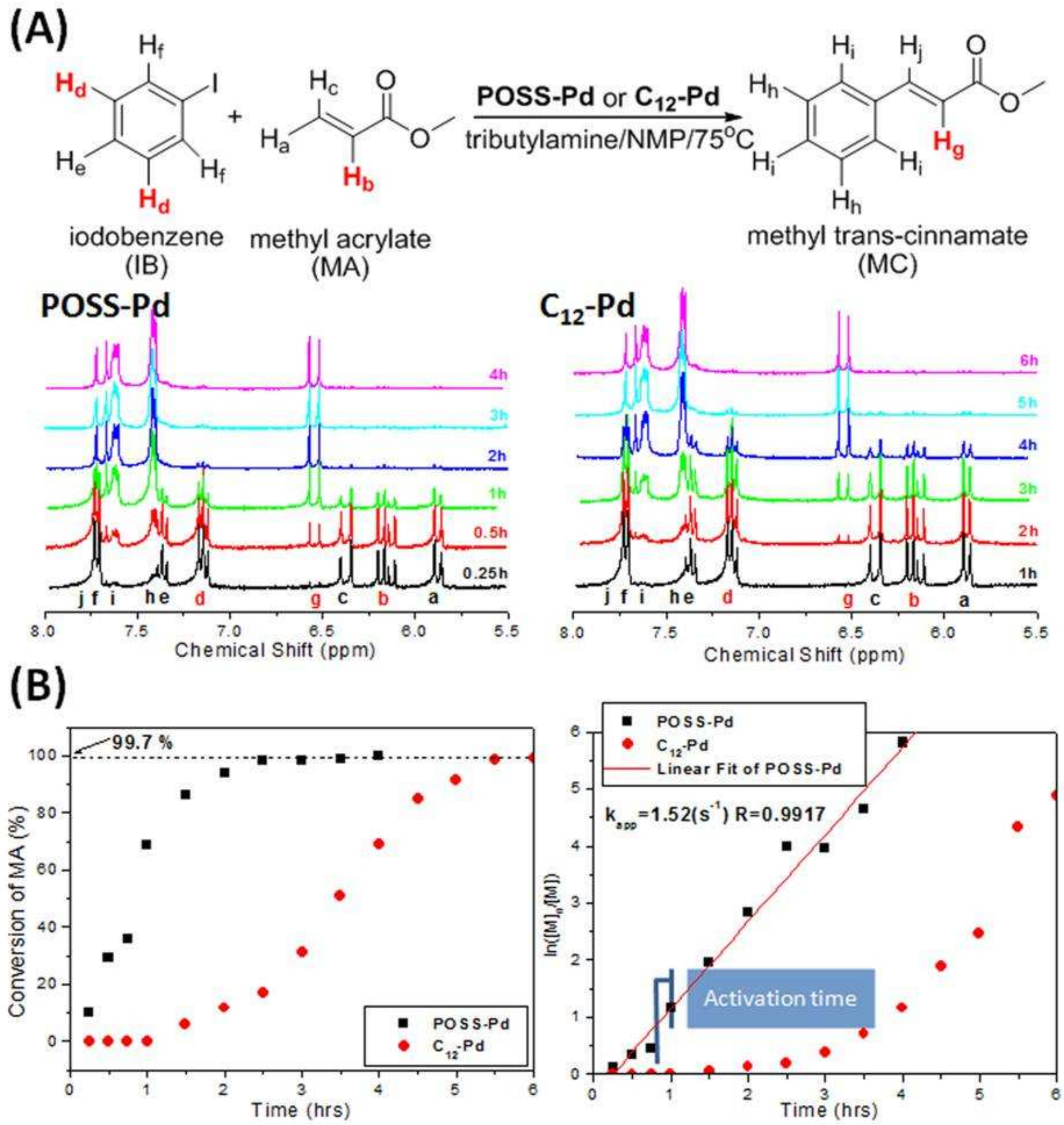

Figure 5-5. (A) ^{1}H NMR spectra of reaction mixture, (B) time-conversion and time-ln([M]$_0$/[M]) profiles of Heck reactions using catalysts of POSS-Pd and C12-Pd. Reaction conditions: 75 °C, catalysts 0.1 g POSS-Pd or 0.035 g C12-Pd (including 0.128 mmol Pd), NMP 30 mL, iodobenzene and methyl acrylate 5 mmol each, tributylamine 7.5 mmol.

5-4 Conclusions

We have synthesized well-dispersed 2~4 nm Pd nanoparticles from the redox of Pd-surfactant complexes without requiring any phase transfer agents or chemical reductants. The Heck coupling of methyl acrylate and iodobenzene using POSS-Pd NCs are investigated, showing the first-order reaction with high conversion up to 99.7%. In comparison with the dense monolayer of C12-SH on the surface of Pd NCs, the bulky POSS groups render relatively large interstices for supramolecular catalysts by encapsulating palladium nanocrystals within POSS colloids.

5-5 References

1. J. Tsuji, *Palladium Reagents and Catalysts*, Wiley, Chichester, 1995; J.-L. Malleron, J.-C. Fiaud and J.-Y. Legros, *Handbook of Palladium-Catalyzed Organic Reactions*, Academic Press, London, 2000.
2. (a) Marck, G.; Villiger, A.; Buchecker, R. *Tetrahedron Lett.* **1994**, *35*, 3277. (b) LeBlond, C. R.; Andrews, A. T.; Sun, Y.; Sowa, Jr J. R. *Org. Lett.* **2001**, *3*, 1555. (c) Choudary, B. M.; Madhi, S.; Chowdari, N. S.; Kantam, M. L.; Sreedhar, B. *J. Am. Chem. Soc.* **2002**, *124*, 14127. (d) Patel, A. C.; Li, S.; Wang, C.; Zhang, W.; Wei, Y. *Chem. Mater.* **2007**, *19*, 1231.
3. Raja, R.; Khimyak, T.; Thomas, J. M.; Herman, S.; Johnson, B. F. G. *Angew. Chem., Int. Ed.* **2001**, *40*, 4638.
4. (a) Akiyama, R.; Kobayashi, S. *Angew. Chem., Int. Ed.* **2001**, *40*, 3469. (b) Jansson, A. M.; Groti, M.; Halkes, K. M.; Meldal, M. *Org. Lett.* **2002**, *4*, 27. (c) Ramarao, C.; Ley, S. V.; Smith, S. C.; Shirley, I. M.; DeAlmeida, N. *Chem. Commun.* **2002**, 1132. (d) Lee, C. K. Y.; Holmes, A. B.; Ley, S. V.; McConvey, I. F.; Al-Duri, B.; Leeke, G. A.; Santos, R. C. D.; Seville, J. P. K. *Chem. Commun.* **2005**, 2175. (e) Okamoto, K.; Akiyama, R.; Yoshida, H.; Yoshida, T.; Kobayashi, S. *J. Am. Chem. Soc.* **2005**, *127*, 2125. (f) Oyamada, H.; Akiyama, R.; Hagio, H.; Naito, T.; Kobayashi, S. *Chem. Commun.* **2006**, 4297.

5. (a) Crooks, R. M.; Zhao, M.; Sun, L.; Chechik, V.; Yeung, L. K. *Acc. Chem. Res.* **2001**, *34*, 181. (b) Gopidas, R.; Whitesell, J. K.; Fox, M. A. *Nano Lett.* **2003**, *3*, 1757. (c) Ornelas, C.; Salmon, L.; Aranzaes, J. R.; Astruc, D. *Chem. Commun.*, **2007**, 4946.

6. (a) Hou, Z.; Theyssen, N.; Brinkmann, A.; Leitner, W. *Angew. Chem., Int. Ed.* **2005**, *44*, 1346. (b) Pathak, S.; Greci, M. T.; Kwong, R. C.; Mercado, K.; Prakash, G. K. S.; Olah, G. A.; Thompson, M. E. *Chem. Mater.* **2000**, *2*, 1985. (c) Shin, J. Y.; Lee, B. S.; Jung, Y.; Kim, S. J.; Lee, S. *Chem. Commun.* **2007**, 5238.

7. Kidambi, S.; Dai, J.; Li, J.; Bruening, M. L. *J. Am. Chem. Soc.* **2004**, *126*, 2658.

8. Li, Y.; El-Sayed, M. A. *J. Phys. Chem. B* **2001**, *105*, 8938.

9. (a) sumbitted work about POSS-Au nanoparticles (see the supporting information). (b) Sheen, Y. C.; Lu, C. H.; Huang, C. F.; Kuo, S. W.; Chang, F. C. *Polymer* **2008**, *49*, 4017. (c) Liu, L.; Tian, M.; Zhang, W.; Zhang, L.; Mark, J. E. *Polymer* **2007**, *48*, 3201. (d) Mantz, R. A.; Jones, P. F.; Chaffee, K. P.; Lichtenhan, J. D.; Gilman, J. W.; Ismail, I. M. K.; Burmeister, M. J. *Chem. Mater.* **1996**, *8*, 1250. (e) Naka, K.; Itoh, H.; Chujo, Y. *Bull. Chem. Soc. Jpn.* **2006**, *77*, 1767. (f) Carroll, J. B.; Frankamp, B. L.; Srivastava, S.; Rotello, V. M. *J. Mater. Chem.* **2004**, *14*, 690.(g) Carroll, J. B.; Frankamp, B. L.; Rotello, V. M. *Chem. Commun.* **2002**, *17*, 1892.

10. (a) Kim, S. W.; Park, J.; Jang, Y.; Chung, Y.; Hwang, S.; Hyeon, T. *Nano Lett.* **2003**, *3*, 1289. (b) Hyeon, T.; Lee, S. S.; Park, J.; Chung, Y.; Na, H. B. *J. Am. Chem. Soc.* **2001**, *123*, 12798. (c) Hyeon, T.; Chung, Y.; Park, J.; Lee, S. S.; Kim, Y.-W.; Park, B. H. *J. Phys. Chem. B* **2002**, *106*, 6831. (d) Joo, J.; Yu, T.; Kim, Y.-W.; Park, H. M.; Wu, F.; Zhang, J. Z.; Hyeon, T. *J. Am. Chem. Soc.* **2003**, *125*, 6553.

11. (a) Silvert, P. Y.; Urbina, R. H.; Duvauchelle, N.; Vijayakrishnan, V.; Elhsissen, K. T. *J. Mater. Chem.* **1996**, *6*, 573. (b) Silvert, P. Y.; Urbina, R. H.; Elhsissen, K. T. *J. Mater. Chem.* **1997**, *7*, 293.

12. Warren, S. C.; Banholzer, M. J.; Slaughter, L. S.; Gianneils, E. P.; DiSalvo, F. J.; Wiesner, U. B. *J. Am. Chem. Soc.*, **2006**, *128*, 12074.

13. (a) Miyaura, N.; Yamada, K.; Suzuki, A. *Tetrahedron Lett.* **1979**, 3437. (b) Miyaura, N.; Suzuki, A. *J. Chem. Soc, Chem. Commun.*, **1979**, 866.

14. (a) Zhao, F.; Bhanage, B. M.; Shirai, M.; Arai, M. *Chem. Eur. J.* **2000**, *6*, 843. (b) Shmidt, A. F.; Mametova, L. V. *Kinet. Katal.* **1996**, *37*, 431.

Chapter 6

Conclusions and Future Outlook

BPO, which decomposes into two benzoyloxyl radicals, is a well-known free radical precursor. The thermal decomposition of BPO is a first-order reaction; the time ($t_{1/2}$) required to decompose half the amount of BPO is given by $\ln 2/k_d$, where k_d is the rate constant. The values of k_d are 3.0×10^{-6} and 4.7×10^{-5} for the thermal decomposition of BPO in styrene at 50 and 70 °C, respectively, corresponding to values of $t_{1/2}$ of 64.2 and 4.1 h, respectively. BPO is thermally stable at 25 °C. In developing the nitroxide-mediated radical polymerization (NMRP) in 1994, Hawker et al. prepared an *N*-alkoxyamine adduct as a unimolecular initiator by heating mixture of BPO and TEMPO in styrene at 80 °C for 1 h. In 1998, Gravert and Janda prepared the same products at 50 °C for 16 h. At present, a temperature of 80 °C is regarded as the most suitable temperature for the preparation of *N*-alkoxyamine unimolecular initiators.

In **Chapter 2**, we find that this reaction proceeds at temperatures below 25 °C because the redox reaction between BPO and TEMPO is the one-electron oxidation of BPO, followed by decomposition into a benozyloxyl radical and a benzoate anion. An ice bath can be used to cool and suppress this exothermic reaction. After 24 h, we observed that the initially reddish brown solution (TEMPO color) had formed a pale green solution (nitroso compounds). In comparison with the studies reported by Hawker et al. and Gravert and Janda, we obtained the same product, 1-benzoyloxy-2-phenyl-2-(2′,2′,6′,6′-tetramethyl-1-piperidinyloxy)ethane. Using this low temperature method, we can easily purify the desired products without the need for complicated processes, making the reaction highly applicable to industrial NMRP. In addition, the ester groups on the products can be hydrolyzed into hydroxyl groups, which are initiators for the ring-opening polymerization of ε-caprolactone monomers to give *N*-alkoxyamine-terminated PCL. Using an excess of triethylaluminum to activate the hydroxyl groups in the preparation of PCL, the kinetics of the reaction (determined through GPC and ^{1}H NMR spectroscopic analyses) revealed that the living polymerization gave *N*-alkoxyamine-terminated PCL with conversions of up to 99.5% and polydispersities of less than 1.2. Herein, the macroinitiator of the *N*-alkoxyamine-terminated PCL was used directly in the NMRP of 4-vinylpyridine (4-VP). UV-RI dual-detection GPC analysis revealed evidence for the incorporation of 4-VP units at the chain end of the *N*-alkoxyamine-terminated PCL. In addition, TEM images revealed ordered (i.e., spherical and rodlike) micelles in toluene, a selective solvent. With an increase in the content of the P4VP block, the solution morphologies transformed from spheres to rods with a gradually increasing core size. Although PCL-*b*-P4VP diblock copolymers are hydrophobic polymers, the P4VP block could transfer gold ions ($HAuCl_4$) from water to an organic phase in the form of $NH^+Cl_4^-$. We obtained Au NC-incorporated micelles upon reduction with $NaBH_4$. In this two-phase preparation of Au NCs, the PCL-*b*-P4VP diblock copolymers play two roles: phase transfer agents and protective agents.

POSS derivatives are molecular inorganic/organic hybrid NPs having the chemical structure $(RSiO_{1.5})_8$, with eight organic groups presented from a siloxane cube. Monofunctional POSS derivatives are small molecular crystals, whereas octafunctional POSS derivatives are polymeric liquids exhibiting low glass transition temperatures. These different properties originate from (i) monofunctional POSS derivatives being regarded as spherical colloids that can pack into the ordered condensed structures (colloidal crystals) and (ii) octafunctional POSS derivatives having different geometries of their hydrosilylated linkages [i.e., β($-Si-CH_2-CH_2-R$) and α($-Si-CH(CH_3)-R$)], which suppresses their crystallization to give amorphous glass-like materials. Through simple hydrosilylation, the introduction of eight functional groups on a POSS cage results in poorer mechanical properties. Nevertheless, such compounds are interesting building blocks containing eight functional groups on the eight corners of a cube.

In **Chapter 3**, we describe the introduction of eight allyl-functional *N*-alkoxyamine units, derivatives of 1-benzoyloxy-2-phenyl-2-(2′,2′,6′,6′-tetramethyl-1-piperidinyloxy)ethane, onto a POSS cage through hydrosilylation at a molar ratio of 1:10. The ^{1}H NMR spectrum of this material displays an equimolar mixture of isomeric β and α linkages. In comparison with linear PS, kinetic studies (GPC and ^{1}H NMR spectroscopic analyses) revealed similar linear correlations between the molecular weight and the conversion and between the value of $\ln([M]_0/[M])$ and the time, indicating that a living and controlled star PS [POSS-(PS)$_8$] was formed from the multifunctional-initiator POSS cube. In addition, we prepared star-block POSS-(PS-*b*-P4VP)$_8$ and POSS-(PS-*b*-PAS)$_8$ polymers after adding the monomers 4-vinylpyridine (VP) and 4-acetoxystyrene (AS), respectively. From comparisons with POSS-(PS)$_8$, the shifts in the signals in the GPC traces of POSS-(PS-*b*-P4VP)$_8$ and POSS-(PS-*b*-PAS)$_8$ indicated the successful insertion of the VP and AS monomers from the macroinitiator of POSS-(PS)$_8$. The acetoxy groups of the PAS block were the removed through hydrazinolyzed to form POSS-(PS-*b*-PVPh)$_8$. These interesting star-block POSS-(PS-*b*-P4VP)$_8$ and POSS-(PS-*b*-PVPh)$_8$ polymers are potentially useful building blocks for the construction of more-ordered microstructures via intermolecular hydrogen bonding.

Chapter 4 describes the use of thiol-functional POSS colloids as protective agents in the preparation of Au NCs. Similar to the PCL-*b*-P4VP micelle-protected Au NCs, bulky POSS colloids disperse Au NCs well in organic solutions; in addition, the crystalline template allows the formation of dispersed condensed Au NCs on many substrates, such as glass slides and wafers. The crystallization of POSS colloids occurs through their deposition onto the surface, desorption of the solvent from the alkyl shell, and then packing along the z-direction. Because of the steric interactions of the alkyl chains on the POSS cages, the packing of the substrate-supported POSS colloids on the basal plane is looser than that of free POSS colloids in the z-direction. Therefore, large interstices on the basal plane (lattice a > the diameter of SH-POSS) and slightly overlapped colloids in the z-direction [dimension ratio (c/a) of 1.06 < that of 1.63 for HCP of hard spheres) can be observed. When an excess of SH-POSS is used in the preparation of POSS-Au hybrid NPs, the POSS colloids can form a crystalline template that incorporates POSS-Au units on its surface, mediated through favorable POSS–POSS interactions. In comparison, when a less-than-stoichiometric amount of SH-POSS is added, the POSS-Au hybrid NPs are viscous liquids, similar to the control (1-dodecanthiol-protective Au hybrid NPs). The use of POSS protective groups provides excellent properties to the materials: (i) powder POSS-Au hybrid crystals, (ii) high dispersion in organic solvents, and (iii) high dispersion on substrates. In addition, the silica char of SH-POSS (ca. 7 wt%) can function as a means of connecting Au NCs onto silica surfaces.

Chapter 5 describes a novel method of preparing POSS-protected Pd NPs (POSS-Pd hybrid NPs). In contrast to the chemical reduction of Au ions with $NaBH_4$ described in Chapters 2 and 4, here we found that thiol groups serve as reductants for the preparation of Pd NCs at 120 °C (i.e., solvothermal reduction). UV spectra of a mixture of SH-POSS and $Pd(OAc)_2$ revealed the formation of a metal complex prior to reduction and Pd NCs after reduction. The as-synthesized POSS-Pd hybrid NPs are catalysts for the Heck coupling of iodobenzene and methyl acrylate. From comparison with a control reaction using 1-dodecanthiol-protected Pd NCs, our kinetic study revealed that the presence of the bulky POSS protective groups provided nanosized gaps that allowed the reactants to approach, and the products to leave, the surface of the Pd NCs. In this Pd-catalyzed transformation, Pd(0) atoms are oxidized to Pd^{2+} through their reaction with iodobenzene and then couple with methyl acrylate to give the desire product. The average 45 wt% of POSS-Pd catalyst would be lost after catalyst recovery by precipitation from methanol. However, we found that the filtrate containing Pd^{2+} complex also activate the Heck coupling of iodobenzene and methyl acrylate. Herein, we suggested that the redox reaction combined of reduction elimination and oxidation addition would be a favor pathway to afford the desire product because of homogenous reaction. Therefore, the separation of the desire product plays a more important issue than the catalyst recovery.

LIST OF PUBLICATIONS

(A) Journal

1. **Chu-Hua Lu**, Shiao-Wei Kuo, Chih-Feng Huang, Feng-Chih Chang ***"Self-Assembled Fernlike Microstructures of POSS/Gold Nanoparticle Hybrids"*** *J. Phys. Chem. C* (**DOI**: 10.1021/jp808635j).
2. **Chu-Hua Lu**, Chih-Feng Huang, Shiao-Wei Kuo, Feng-Chih Chang ***"Synthesis and Characterization of Poly(ε-caprolactone-b-4-vinylpyridine): Initiation, Polymerization, Solution Morphology, and Gold Metalation"*** *Macromolecules*, (**DOI:** 10.1021/ma801413s).
3. **Chu-Hua Lu**, Yi-Che Su, Chih-Feng Wang, Chih-Feng Huang, Yuung-Ching Sheen, Feng-Chih Chang ***"Thermal properties and surface energy characteristics of interpenetrating polyacrylate and polybenzoxazine networks"*** *Polymer* **2008**, *49*, 4852.
4. Yuung-Ching Sheen, **Chu-Hua Lu**, Chih-Feng Huang, Shiao-Wei Kuo, Feng-Chih Chang ***"Synthesis and characterization of amorphous octakis-functionalized polyhedral oligomeric silsesquioxanes for polymer nanocomposites"*** *Polymer* **2008**, *49*, 4017-4024.
5. Shih-Chi Chan, Shiao-Wei Kuo, **Chu-Hua Lu**, Hsin-Fang Lee, Feng-Chih Chang ***"Syntheses and characterizations of the multiple morphologies formed by the self-assembly of the semicrystalline P4VP-b-PCL diblock copolymers"*** *Polymer* **2007**, *48*, 5059-5068.
6. Shiao-Wei Kuo, Chih-Feng Huang, **Chu-Hua Lu**, Ho-May Lin, Kwang-Un Jeong, Feng-Chih Chang ***"Syntheses and Specific Interactions of Poly(ε-caprolactone)-block-poly(vinyl phenol) Copolymers Obtained via a***

Combination of Ring-Opening and Atom-Transfer Radical Polymerizations" *Macromol. Chem. Phys.* **2006**, *207*, 2006-2016.

(B) Conference

1. 呂居樺、蘇一哲、王睿詡、張豐志***"Syntheses and Characterizations of Star Polymers and Star Block Copolymers from Polyhedral Oligomeric Silesesquioxane Core through Nitroxide-mediated Radical Polymerization"***2009 年第 32 屆高分子年會(Oral).
2. **Chu-Hua Lu**, Chih-Feng Huang, Feng-Chih Chang ***"Controllably Living Polymerizations of Poly(ε-caprolactone)-block-Poly(4-vinylpyridine) for Two-phase Extraction of Metal Ions"*** 236th ACS National Meeting & Expostion (POST).
3. **Chu-Hua Lu**, Chih-Feng Huang, Feng-Chih Chang ***"Synthesis and characteristics of hydrogen-bonding supramolecules composed of octaphenol functionalized polyhedral oligomeric silsesquioxane"*** 235th ACS National Meeting & Expostion (POST).
4. 呂居樺、詹師吉、郭紹偉、黃智峰、張豐志 ***"PCL-b-P4VP 團聯共聚物之製備及溶液態自組裝"*** 2007年第30屆高分子年會(POST佳作).
5. 呂居樺、黃智峰、郭紹偉、張豐志 ***"互溶型半結晶性團聯共聚物(PCL-b-PVPh)的合成及氫鍵作用力探討"*** 2006年第29屆高分子年會(Oral).
6. 呂居樺、杜成偉、詹師吉、張豐志 ***"BPO 和 TEMPO 在苯乙稀中发生的低温反應：氧化还原、自由基加成及抑制和醇基氧化"*** 兩岸三地全國博士生學術論壇(中國大陸, Oral)

Introduction to Author

English Name: Chu-Hua Lu

Chinese Name: 呂居樺

Birthday: 1980, 09, 08

Address: 500 彰化縣和美鎮月眉里和
厝路一段 232 巷 54 號

E-mail: luchuhua.ac93g@nctu.edu.tw

Cell Phone: 0952221517

Education:

1999.09～2004.06	**B.S.**, Department of Chemical Engineering, National Chung Hsing University, Taichung, Taiwan.
2004.09～2009.02	**Ph. D.**, Institute of Applied Chemistry, National Chiao Tung University, Hsinchu, Taiwan.